

POLITECNICO DI TORINO

Master's Thesis in

AEROSPACE ENGINEERING



Design and development of innovative asymmetry active monitoring techniques for high-lift actuation systems

Supervisors

Prof. Paolo MAGGIORE

Prof. Matteo D.L. DALLA VEDOVA

Candidate

José María CEJUDO RUIZ

March 2021



Abstract

The aim of this Master thesis is the innovative active monitoring techniques design and development that reduce the trailing edge high-lift devices asymmetry. Different system failures may cause the control surfaces asymmetry, such as the drive shaft torsion bar braking and the control surface actuators wear and tear.

The high-lift system is formed by a Power Drive Unit (PDU) that generates the power transmitted to the reversible actuators by a drive shaft torsion bar. In addition, a wingtip brakes system is implemented to meet the secondary flight controls design requirements considering reversible actuators.

The innovative asymmetry active monitoring techniques developed in this project both detect and identify the high-lift device (flap) position asymmetry. Once the failure side is known, the active techniques command the wingtip brakes to stop the failure surface. On the other hand, the operative surface is commanded to reach the failure surface braking position in order to minimize the flap asymmetry. Hence, the vehicle roll dynamic response will be more stable while the aircraft maneuverability after failure will be increased.

In particular, four active models have been developed in this project. The control logic inside each model is position-based. Moreover, the control algorithms are using either a differential position step-input algorithm or a relative position ramp-input logic. Furthermore, the active monitoring techniques may include an asymmetry anticipation logic by means of a “dynamic” position that allows an earlier asymmetry detection in case of high flap speeds after failure. The asymmetry active monitoring techniques have been widely tested in different external conditions, using either wear-free or wear-out actuators and considering every failure side scenario.

The external operating conditions consider either low or high aerodynamic loads, which significantly affect the high-lift actuation system dynamics. In consequence, the active models behaviour in terms of time response and stability margin under certain operating conditions depends on the asymmetry control algorithm. Several tests have been conducted to study the active monitoring techniques response on different operating conditions considering every failure side scenario.

In addition, certain aerodynamic borderline conditions have been tested. They consider high aerodynamic loads applied on the control surfaces when they deflect from a starting position that is too close to the mechanical lower limit switch of the flap. The combination of both high aerodynamic loads and little flap deflection starting positions may not occur on a regular commercial flight but it is useful to evaluate both the robustness and suitability of each new active model.

A general comparison of all four active monitoring techniques is performed for each operating condition, in which the most performing models are chosen in each case. Eventually, a single active model has been chosen for any operating scenario analyzed in this project due to either its acceptable or excellent behaviour according to the operating condition.

Contents

1	Flight controls and asymmetry	12
1.1	Flight controls definition and main classification	12
1.1.1	Flight control design requirements	13
1.2	The asymmetry problem	13
1.3	Position asymmetry monitoring techniques	15
2	Hydraulic drive systems for high-lift devices	17
2.1	Flight controls overview	17
2.1.1	Power source based flight controls classification	17
2.1.2	Current flight control systems	18
2.1.3	Design criteria for primary and secondary flight	20
2.2	High-lift devices architecture	20
2.2.1	Power Drive Unit architecture	21
2.2.2	Drive shaft design	21
2.2.3	Actuators and braked design configurations	21
3	System mathematical modeling	24
3.1	Mechanical subsystem mathematical modeling	24
3.1.1	Activation/deactivation logic	26
3.1.2	Shut-off valve mathematical modeling	26
3.1.3	Servovalve mathematical modeling	28
3.1.4	Hydraulic motor mathematical modeling	34
3.1.5	Position transducers mathematical modeling	37
3.1.6	Control surfaces dynamics mathematical modeling	38
3.2	Flight mechanics mathematical modeling	40
4	Reference monitoring techniques	42
4.1	General concepts	42
4.2	Monitoring device essential components	44
4.3	Passive reference monitoring techniques	45
4.3.1	Passive monitoring technique 1: differential position control	45
4.3.2	Passive monitoring technique 2: differential position & speed control	46
4.4	Active reference monitoring techniques	46
4.5	Non-asymmetry system failures	48
4.5.1	Wingtip brake system failure	48
4.5.2	Insufficient servovalve supply pressure failure	48
5	New asymmetry active monitoring techniques	50
5.1	Introduction to the new active monitoring techniques	50
5.1.1	Resistive constant torque considerations	51
5.2	Position anticipation or <i>dynamic position</i>	52
5.2.1	Non <i>dynamic position</i> active monitoring techniques	52
5.2.2	<i>Dynamic position</i> active monitoring techniques	53
5.3	New active monitoring algorithms	55
5.3.1	Step-input relative position control technique - model 3	55
5.3.2	Step-input relative dynamic position control technique - model 3D	57
5.3.3	Ramp-input relative position control technique - model 3C	58

5.3.4	Ramp-input relative dynamic position control technique - model 3E	59
5.4	The <i>Slow</i> parameter	59
6	Simulation results in regular conditions	62
6.1	New model 3 results	64
6.1.1	New model 3: origin and improvements	64
6.1.2	Low T_{RC} case results	67
6.1.3	High T_{RC} case results	68
6.2	Model 3D results	70
6.2.1	Low T_{RC} case results	70
6.2.2	High T_{RC} case results	71
6.3	Model 3C results	72
6.3.1	Ramp-input models: <i>Dem</i> slope fitting	72
6.3.2	Model 3C: origin and improvements	74
6.3.3	Low T_{RC} case results	76
6.3.4	High T_{RC} case results	78
6.4	Model 3E results	80
6.4.1	Low T_{RC} case results	81
6.4.2	High T_{RC} case results	82
6.5	Comparison of active models on regular conditions	83
6.5.1	General overview of low T_{RC} case results	84
6.5.2	General overview of high T_{RC} case results	85
6.5.3	Summary table of active models on regular wear-free conditions .	88
7	Aerodynamic wear-free borderline conditions	90
7.1	New model 3 results - wear-free borderline case	91
7.2	Model 3D results - wear-free borderline case	93
7.3	Model 3A results - wear-free borderline case	94
7.4	Model 3C results - wear-free borderline case	97
7.5	Model 3E results - wear-free borderline case	102
7.6	Comparison of active models on wear-free borderline conditions	104
7.6.1	Step-input models behaviour on wear-free borderline conditions	106
7.6.2	Ramp-input models behaviour on wear-free borderline conditions	107
7.6.3	Summary table of active models in wear-free borderline conditions	108
8	Simulation results on wear-out conditions	111
8.1	New model 3 results on wear-out conditions	112
8.1.1	Low T_{RC} case results	113
8.1.2	High T_{RC} case results	114
8.2	Model 3D results on wear-out conditions	116
8.2.1	Low T_{RC} case results	116
8.2.2	High T_{RC} case results	117
8.3	Model 3A results on wear-out conditions	120
8.4	Model 3C results on wear-out conditions	124
8.4.1	Low T_{RC} case results	124
8.4.2	High T_{RC} case results	127
8.5	Model 3E results on wear-out conditions	131
8.5.1	Low T_{RC} case results	131
8.5.2	High T_{RC} case results	133
8.6	Comparison of active models on wear-out conditions	135

8.6.1	General overview of low T_{RC} case results	135
8.6.2	General overview of high T_{RC} case results	136
8.6.3	Summary table of active models on worn-out conditions	139
9	Aerodynamic wear-out borderline conditions	142
9.1	Combined effect of aerodynamic load and friction force	142
9.2	New model 3 results - wear-out borderline case	144
9.3	Model 3D results - wear-out borderline case	147
9.3.1	Possible solutions to prevent the limit cycle instabilities	154
9.4	Model 3A results - wear-out borderline case	158
9.5	Model 3C results - wear-out borderline case	159
9.6	Model 3E results - wear-out borderline case	163
9.7	Comparison of active models on wear-out conditions	168
9.7.1	Step-input models behaviour on borderline wear-free conditions .	168
9.7.2	Ramp-input models behaviour on borderline wear-free conditions	169
9.7.3	Summary table of active models in wear-free borderline conditions	170
10	Conclusions	173
	Nomenclature	176
	Bibliography	184

List of Figures

1	Aircraft control surfaces	13
2	Oleodynamic servo-control configurations	17
3	Stability Augmentation System (SAS)	18
4	Control Augmentation System (CAS)	19
5	Fly By Wire (FBW)	19
6	Reversible actuators & wingtip brakes (WTB) configuration	22
7	Reversible actuators & self-acting brakes configuration	23
8	Actuation system mechanical model	25
9	Relation between the shut-off valve pressure and the spool displacement	27
10	Four way valve schematic	28
11	Servo valve fluid dynamic schamtic diagram	31
12	Servo valve control block diagram	34
13	Hydraulic motor block diagram	36
14	Right failure during extension from 0 to 0.07 rad at $T_{RC} = 0 Nm$. . .	65
15	Right failure during extension from 0.4 to 0.5 rad at $T_{RC} = 10000 Nm$	65
16	Left failure during extension from 0.4 to 0.5 rad at $T_{RC} = 10000 Nm$.	66
17	Left failure during retraction from 0.5 to 0.4 rad at $T_{RC} = 10000 Nm$.	67
18	New model 3 - failure extension from 0 to 0.07 rad at $T_{RC} = 0 Nm$. .	67
19	New model 3 - failure retraction from 0.07 to 0 rad at $T_{RC} = 0 Nm$. .	68
20	New model 3 - failure extension from 0.4 to 0.5 rad at $T_{RC} = 10000 Nm$	68
21	New model 3 - failure retraction from 0.5 to 0.4 rad at $T_{RC} = 10000 Nm$	69
22	Model 3D - failure extension from 0 to 0.07 rad at $T_{RC} = 0 Nm$	70
23	Model 3D - failure retraction from 0.07 to 0 rad at $T_{RC} = 0 Nm$	71
24	Model 3D - failure extension from 0.4 to 0.5 rad at $T_{RC} = 10000 Nm$.	71
25	Model 3D - failure retraction from 0.5 to 0.4 rad at $T_{RC} = 10000 Nm$.	72
26	Model 3C - False failures ramp slope 0.2 <i>rad/s</i> at $T_{RC} = 0 Nm$	73
27	Model 3C - No failure ramp slope 0.1 <i>rad/s</i> at $T_{RC} = 0 Nm$	74
28	Improvement model 3C - failure extension from 0 to 0.07 rad at $T_{RC} =$ $0Nm$	74
29	Improvement model 3C - failure retraction from 0.07 to 0 rad at $T_{RC} =$ $0Nm$	75
30	Improvement model 3C - failure extension from 0.4 to 0.5 rad at $T_{RC} =$ $10000Nm$	75
31	Improvement model 3C - failure retraction from 0.5 to 0.4 rad at $T_{RC} =$ $10000Nm$	76
32	Model 3C - failure extension from 0 to 0.07 rad at $T_{RC} = 0 Nm$	76
33	Model 3C - failure retraction from 0.07 to 0 rad at $T_{RC} = 0 Nm$	77
34	Comparison 3C & 3 left failure extension from 0 to 0.07 rad at $T_{RC} = 0Nm$	78
35	Comparison 3C & 3 right failure retraction from 0.07 to 0 rad at $T_{RC} =$ $0Nm$	78
36	Model 3C - failure extension from 0.4 to 0.5 rad at $T_{RC} = 10000 Nm$.	79
37	Model 3C - failure retraction from 0.5 to 0.4 rad at $T_{RC} = 10000 Nm$.	79
38	Comparison 3C & 3 left failure extension 0.4-0.5 rad at $T_{RC} = 10000Nm$	80
39	Comparison 3C & 3 right failure retraction 0.5-0.4 rad at $T_{RC} = 10000Nm$	80
40	Model 3E - failure extension from 0 to 0.07 rad at $T_{RC} = 0 Nm$	81
41	Model 3E - failure retraction from 0.07 to 0 rad at $T_{RC} = 0 Nm$	81
42	Model 3E - failure extension from 0.4 to 0.5 rad at $T_{RC} = 10000 Nm$.	82
43	Model 3E - failure retraction from 0.5 to 0.4 rad at $T_{RC} = 10000 Nm$.	82

44	Comparison 3E & 3D right failure extension 0.4-0.5 rad at $T_{RC} = 10000Nm$	83
45	Comparison 3E & 3D left failure retraction 0.5-0.4 rad at $T_{RC} = 10000Nm$	84
46	General overview at $T_{RC} = 0 Nm$ - failure extension from 0 to 0.07 rad	85
47	General overview at $T_{RC} = 0 Nm$ - failure retraction from 0.07 to 0 rad	85
48	Overview step-input at $T_{RC} = 10000Nm$ - failure extension 0.4-0.5 rad	86
49	Overview step-input at $T_{RC} = 10000Nm$ - failure retraction 0.5-0.4 rad	86
50	Overview ramp-input at $T_{RC} = 10000Nm$ - failure extension 0.4-0.5 rad	87
51	Overview ramp-input at $T_{RC} = 10000Nm$ - failure retraction 0.5-0.4 rad	87
52	New model 3 - bord. case wear-free failure ext 0-0.07 rad $T_{RC} = 10000Nm$	91
53	New model 3 - bord. case wear-free failure retr 0.07-0 rad $T_{RC} = 10000Nm$	92
54	Model 3D - bord. case wear-free failure ext 0-0.07 rad $T_{RC} = 10000Nm$	93
55	Model 3D - bord. case wear-free failure retr 0.07-0 rad $T_{RC} = 10000Nm$	93
56	Model 3A - bord. case wear-free right failure at $T_{RC} = 10000Nm$	94
57	Model 3A (electrical) lack of control right failure retraction (detail) . . .	96
58	Model 3A - bord. case wear-free left failure at $T_{RC} = 10000Nm$	97
59	Model 3C - bord. case wear-free failure ext 0-0.07 rad $T_{RC} = 10000Nm$	97
60	Model 3C - bord. case wear-free failure retr 0.07-0 rad $T_{RC} = 10000Nm$	98
61	Model 3C vs 3A $t_f = 0.4s$ right failure extension 0-0.07 rad $T_{RC} =$ $10000Nm$	98
62	Model 3C vs 3A general right failure retr 0.07-0 rad at $T_{RC} = 10000Nm$	99
63	Model 3C (electrical) general asymmetry I_A right failure retraction (detail)	100
64	Model 3C vs 3 - bord case wear-free failure at $T_{RC} = 10000Nm$ (detail)	101
65	Model 3E - bord. case wear-free failure ext 0-0.07 rad $T_{RC} = 10000Nm$	102
66	Model 3E - bord. case wear-free failure retr 0.07-0 rad $T_{RC} = 10000Nm$	103
67	Model 3E vs 3D bord case wear-free extension failure at $T_{RC} = 10000Nm$ (detail)	104
68	Model 3E vs 3D bord case wear-free extension failure at $T_{RC} = 10000Nm$ (detail)	105
69	Overview 3D vs 3 bord case wear-free extension failure at $T_{RC} = 10000Nm$ (detail)	106
70	Overview 3E vs 3C bord case wear-free extension failure at $T_{RC} =$ $10000Nm$ (detail)	108
71	New model 3 failure extension from 0-0.07 rad at $T_{RC} = 0Nm$ wear-out	113
72	New model 3 failure retraction from 0.07-0 rad at $T_{RC} = 0Nm$ wear-out	113
73	New model 3 failure extension from 0.4-0.5 rad $T_{RC} = 10000Nm$ wear- out	115
74	New model 3 failure retraction from 0.5-0.4 rad $T_{RC} = 10000Nm$ wear- out	115
75	Model 3D failure extension from 0-0.07 rad at $T_{RC} = 0Nm$ wear-out . .	116
76	Model 3D failure retraction from 0.07-0 rad at $T_{RC} = 0Nm$ wear-out . .	116
77	Model 3D extension from 0.4-0.5 rad $T_{RC} = 10000Nm$ wear-out	117
78	Model 3D retraction from 0.5-0.4 rad $T_{RC} = 10000Nm$ wear-out	117
79	Model 3D wear-out vs wear-free fail extension 0.4-0.5rad $T_{RC} = 10000Nm$	118
80	Model 3D wear-out vs wear-free fail retraction 0.5-0.4rad $T_{RC} = 10000Nm$	119
81	Model 3A satisfactory behaviour cases - wear-out failure $t_f = 0.4s$. . .	121
82	Model 3A (electrical) left failure retraction (detail) wear-out	122
83	Model 3A (electrical) right failure retraction (detail) wear-out	123
84	Model 3C failure extension from 0-0.07 rad at $T_{RC} = 0Nm$ wear-out . .	125
85	Model 3C failure retraction from 0.07-0 rad at $T_{RC} = 0Nm$ wear-out . .	125
86	Model 3C vs 3A wear-out failure $t_f = 0.4s$ at $T_{RC} = 0Nm$	126

87	Model 3C extension from 0.4-0.5 rad $T_{RC} = 10000Nm$ wear-out	127
88	Model 3C retraction from 0.5-0.4 rad $T_{RC} = 10000Nm$ wear-out	127
89	Model 3C vs 3A wear-out failure 0.4-0.5rad at $T_{RC} = 10000Nm$	128
90	Model 3C electric left & right failure retraction 0-0.07 rad $T_{RC} = 10000Nm$ wear-out	129
91	Model 3C vs 3A right failure retraction from 0.5-0.4 rad $T_{RC} = 10000Nm$ wear-out	130
92	Model 3C vs 3A right failure retraction from 0.5-0.4 rad $T_{RC} = 10000Nm$ wear-out	131
93	Model 3E failure extension from 0-0.07 rad at $T_{RC} = 0Nm$ wear-out . .	132
94	Model 3E failure retraction from 0.07-0 rad at $T_{RC} = 0Nm$ wear-out .	132
95	Model 3E extension from 0.4-0.5 rad $T_{RC} = 10000Nm$ wear-out	133
96	Model 3E retraction from 0.5-0.4 rad $T_{RC} = 10000Nm$ wear-out	133
97	Model 3E vs 3D wear-out failure retraction 0.5-0.4rad at $T_{RC} = 10000Nm$	134
98	General overview at $T_{RC} = 0 Nm$ - failure extension from 0 to 0.07 rad wear-out	135
99	General overview at $T_{RC} = 0 Nm$ - failure retraction from 0.07 to 0 rad wear-out	136
100	Overview step-input at $T_{RC} = 10000Nm$ - failure extension 0.4-0.5 rad wear-out	137
101	Overview step-input at $T_{RC} = 10000Nm$ - failure retraction 0.5-0.4 rad wear-out	138
102	Overview ramp-input at $T_{RC} = 10000Nm$ - failure extension 0.4-0.5 rad wear-out	138
103	Overview ramp-input at $T_{RC} = 10000Nm$ - failure retraction 0.5-0.4 rad wear-out	139
104	New model 3 - bord. case wear-out failure ext 0-0.07 rad $T_{RC} = 10000Nm$	145
105	New model 3 - bord. case wear-out failure retr 0.07-0 rad $T_{RC} = 10000Nm$	145
106	Model 3 wear-out vs wear-free borderline cond $t_f = 0.4s$ $T_{RC} = 10000Nm$	146
107	Model 3D - bord. case wear-out failure ext 0-0.07 rad $T_{RC} = 10000Nm$	147
108	Model 3D - bord. case wear-out failure retr 0.07-0 rad $T_{RC} = 10000Nm$	147
109	Model 3D (electrical) left fail extension 0-0.07 rad wear-out borderline .	149
110	Model 3D (electrical) left fail retraction 0.07-0 rad wear-out borderline .	150
111	Comparison model 3D vs new model 3 wear-out borderline $t_f = 0.4s$ $T_{RC} = 10000Nm$	152
112	Comparison model 3D wear-out vs wear-free borderline $t_f = 0.4s$ $T_{RC} =$ $10000Nm$	153
113	Model 3D - $T_i S_y = 0.03s$ bord. case wear-out ext 0-0.07rad $T_{RC} =$ $10000Nm$	155
114	Model 3D - $T_i S_y = 0.03s$ bord case wear-out retr 0.07-0rad $T_{RC} =$ $10000Nm$	155
115	Comparison model 3D $T_i S_y$ variation $t_f = 0.4s$ $T_{RC} = 10000Nm$	156
116	Model 3D multiple vs single failures wear-out bord $T_{RC} = 10000Nm$. .	157
117	Model 3A - bord. case wear-out failure ext 0-0.07 rad $T_{RC} = 10000Nm$	158
118	Model 3A - bord. case wear-out failure retr 0.07-0 rad $T_{RC} = 10000Nm$	158
119	Comparison model 3A wear-out vs wear-free borderline condition $t_f =$ $0.4s$ $T_{RC} = 10000Nm$	159
120	Model 3C - bord. case wear-out failure ext 0-0.07 rad $T_{RC} = 10000Nm$	160
121	Model 3C - bord. case wear-out failure retr 0.07-0 rad $T_{RC} = 10000Nm$	160

122	Comparison between models 3C, 3A, 3 wear-out borderline $t_f = 0.4s$ $T_{RC} = 10000Nm$	161
123	Model 3C wear-out vs wear-free borderline cond $t_f = 0.4s$ $T_{RC} = 10000Nm$	162
124	Model 3E - borderline case wear-out failure $t_f = 0.4s$ $T_{RC} = 10000Nm$.	164
125	Comparison model 3E vs 3D wear-out bord $t_f = 0.4s$ $T_{RC} = 10000Nm$.	165
126	Comparison model 3E vs 3 wear-out bord $t_f = 0.4s$ $T_{RC} = 10000Nm$. .	166
127	Comparison model 3E wear-out vs wear-free borderline $t_f = 0.4s$ $T_{RC} =$ $10000Nm$	167
128	Overview 3 vs 3D bord case wear-out failure $t_f = 0.4s$ at $T_{RC} = 10000Nm$	169
129	Overview 3E vs 3C bord case wear-out failure $t_f = 0.4s$ at $T_{RC} = 10000Nm$	170

List of Tables

1	Models efficiency classification on <i>regular wear-free conditions</i>	88
2	Models efficiency classification on aerodynamic wear-free borderline conditions	109
3	Friction force efficiencies of the original and the worn-out actuators . . .	111
4	Models efficiency classification on <i>wear-out conditions</i>	139
5	<i>Speed gain</i> $T_i S_y$ reduction	154
6	Models efficiency classification on aerodynamic wear-out borderline conditions	171

1 Flight controls and asymmetry

1.1 Flight controls definition and main classification

According to *SKYbrary*, the aircraft flight controls are “*the means by which a pilot controls the direction and attitude of an aircraft in flight*” (*Flight Controls - SKYbrary Aviation Safety*, n.d.). In particular, the vehicle flight controls are the set of elements, either mechanical or electromechanical, that allow the flight control surfaces maneuvers, such as the ailerons, elevator, rudder, high-lift devices (flaps), spoilers or lift sumpers, among others.

The flight controls may be classified as follows:

- **Primary flight controls.** These serve to control the aircraft motion in the six degrees of freedom:: three translational and three rotational (pitch, roll and yaw). They consist of:

- Ailerons.
- Elevators (or stabilator).
- Rudder.

Some authors consider that the *gas control lever* might be an additional primary flight control, since it controls the aircraft longitudinal accelerations. Nonetheless, only the control surfaces will be considered in this project. Moreover, the ailerons effect on the aircraft maneuverability will be discussed later on.

- **Secondary flight controls.** These modify the aircraft aerodynamic configuration in accordance with the flight conditions, guaranteeing the aircraft maneuverability of each flight phase. They consist of:

- High-lift devices. These may be divided in:
 - Leading-edge devices (slats & slots)
 - Trailing-edge devices (flaps)
- Spoilers (or lift dumpers).
- Aerodynamic brakes.
- Canard surface (if present)
- Trim systems.

The project study will focus on the high-lift devices performance regarding, in particular, the trailing-edge devices (flaps).

The high-lift devices increment the maximum lift coefficient C_{Lmax} , so they are useful in those flight phases in which both the aircraft speed V and incidence α would lead the aircraft that flies on a *clean configuration* to a stalled aerodynamic condition. Such flight phases are both the *take off* and *landing*, in which the aircraft speed V is too low enough to guarantee the safety of the flight operation performance.

Regarding the commercial aircrafts flight controls, the high-lift devices deflections are discrete. It means that only a limited number of final positions are considered for these devices, unlike the primary flight controls, which admit a continuous control surface deflection.

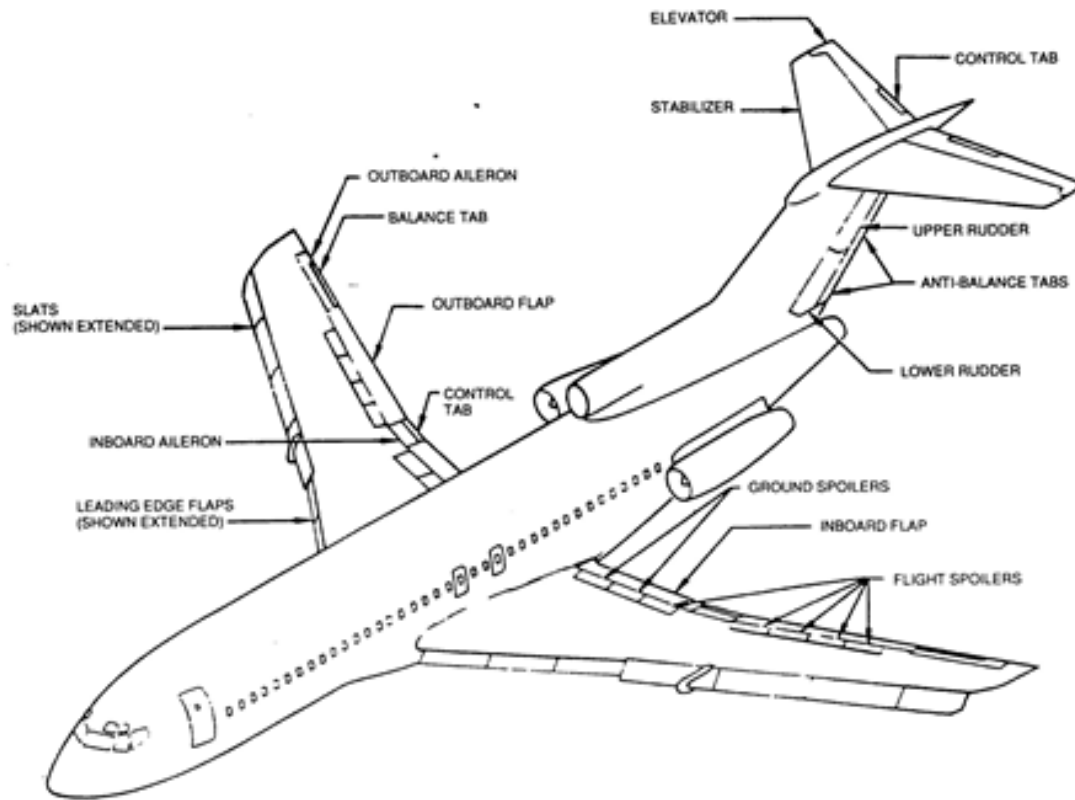


Figure 1: Aircraft control surfaces

1.1.1 Flight control design requirements

Different design requirements are applicable according to the flight control type.

The *primary flight controls* shall be designed according to these criteria:

1. Command input proportionality.
2. Reversibility.
3. Instinctivity.

The *secondary flight controls* and, in particular, the high-lift devices, should be designed according to the following criteria:

1. Stability.
2. Irreversibility.
3. Symmetrical deflection. This requirement will be essential in this work, in which several asymmetry failure situations will be analyzed.

1.2 The asymmetry problem

In regard to the *symmetrical deflection* requirement of the high-lift devices, follow a list of the possible failures that may affect these devices and, in particular, the trailing-edge devices (flaps).

- **Transmission line failure.** It is the secondary flight controls critical problem, which consequences will be carefully analyzed in this project. In effect, the *torsion bar breaking* will be the main flap asymmetry cause. While the transmission line part upstream the breaking point will rotate powered by the PDU, the motion of the part downstream of this point will depend on the kind of control surface linear actuators. These can be:
 - **Irreversible.** These actuators prevent the failure control surface back-drive the by the effect of the aerodynamic torque. To that end, the high friction forces inside the irreversible actuators compensate the aerodynamic torques, preventing any the failure flap retraction. On the other hand, the remaining rotational kinetic energy of the torque transmission line will be dissipated by the tare losses of the rotating shafts. In consequence, the control surface would remain braked almost instantaneously after failure.
 - **Reversible.** In this case, the actuators allow the failure surface retraction by the effect of the aerodynamic load (which would be translated into an aerodynamic torque on the control surface). Consequently, the failure surface may suffer great accelerations, especially considering the low rotational inertia J_S of the high-lift device system. Hence, a braking system will be necessary to stop the failure flap if reversible actuators are used. The braking systems considered are:
 - **Wingtip brakes.** They are installed close to the electrical flap position transducer, one per flap.
 - **Self-acting brakes.** They enable an effective control of the inoperative control surface deflection sense after failure whenever the surface speed differ from the engine rotation speed.
- **Final control surface actuators failure.** This failure may be caused by actuators asymmetric galling, or even the actuators breaking. Galled actuators present high internal friction forces which determine the failure surface dynamics. Nevertheless, the actuators failure due to wear and tear is critical on primary flight controls. In effect, the high friction forces inside the actuators may deteriorate their performance and could even compromise the aircraft maneuverability and/or flight safety in certain borderline high friction force scenarios. Only actuators symmetric galling conditions will be carefully studied in this project (see sections 8 and 9), since the combination of both the torsion bar failure and the actuators symmetric wear and tear conditions may be critical in some particular cases.

A mathematical definition of both reversible and irreversible actuators will be given in section 3.

Follow the system architecture used for this project:

- Transmission line with torsion bars.
- Wingtip brakes.
- Ball screw actuators.

Nevertheless, a deep high-lift devices architecture analysis will be performed in section 2.2.

Note that high lift devices position asymmetry failures may cause relevant roll and yaw moments on the vehicle, which may compromise the controllability and maneuverability after failure. The lateral-directional aircraft time response is simulated by a simple program that reproduces the vehicle flight mechanics considering the combined effect of the primary and secondary flight controls together with the autopilot.

The aforementioned failures are managed by the *asymmetry monitoring techniques*, which try to minimize detrimental consequences of the control surface position asymmetry after failure.

1.3 Position asymmetry monitoring techniques

As mentioned above, the aim of the position asymmetry monitoring techniques is to minimize the detrimental effects the high-lift devices asymmetry may produce on both the aircraft controllability and maneuverability after failure. In addition, important reductions of the aircraft roll time response stability margin may happen as a result of the aforementioned asymmetry cases.

In this project, the control surface analyzed will be the trailing-edge high-lift devices: flaps.

There are different types of control surfaces asymmetry monitoring techniques. The two main categories of these techniques are:

- **Passive asymmetry monitoring techniques.** A passive asymmetry monitoring technique only detects the *position asymmetry failure condition*, after which it brakes both flaps, regardless their position in that moment. The *passive* techniques prevent the flap position asymmetry by the control surfaces deflection at the expense of maintaining such asymmetry on steady state, entailing negative consequences regarding the aircraft controllability and maneuverability. However, these techniques happen to be simpler and easier to implement than the active ones.
- **Active asymmetry monitoring techniques.** An active asymmetry monitoring technique both detects the position asymmetry failure, identifying the failure side, and corrects it. Once the asymmetry failure arises, the failure surface is braked as soon as possible while the operative flap tries to reach position of the failure surface. In consequence, the control surface position asymmetry on steady state will be minimal, which increases the aforementioned stability, controllability and the symmetrical maneuverability after failure. These models happen to be more complex than the previous ones but preserve the dynamic system response stability, as well as both the aircraft controllability and maneuverability after failure.

In other words, the *active* asymmetry monitoring techniques seek an increase in flight safety maintaining acceptable levels of reliability with respect to the passive monitoring models.

In general, every position asymmetry monitoring technique follows a similar logic both to detect the asymmetry failure condition and to brake the failure surface. Follows

the simplified explanation of how these two are performed by asymmetry monitoring models, which is may be used both for leading-edge and trailing-edge high-lift devices.

Fistly, the asymmetry failure is detected for comparison using the electrical signal of the each control surface electrical transducer, placed control surface actuators. These positions are called *electrical control surface (flap) positions*, or simply *electrical positions*. Should the aforementioned comparison¹ exceed a certain asymmetry threshold for a certain time, the position asymmetry failure is declared. All this is possible using specific counters, as will be discussed later on.

Once the asymmetry failure is detected, the power pressure of the hydraulic unit is depressurized and, consequently, the wingtip brakes will stop the failure surface.

To that end, the following parameters should be set:

- The asymmetry threshold beyond which the asymmetry failure condition is declared.
- Asymmetry confirmation time. It is properly defined in section 5.1.
- The failure surface deflection between the failure instant and the beginning of the braking action (hydraulic unit depressurization & beginning of the failure surface braking).

Moreover, these models may consider either the control surfaces electrical position only or both the flaps electrical position and electrical speed. While the former only considers an electrical position asymmetry to define and declare the asymmetry failure, the latter exploits the position variation with time, which is relevant to determine the *potential* failure condition.

The control surfaces speed may be provided of:

- a. *Ad hoc additional transducers*. These would provide an analogic signal, proportional to the aforementioned flap speed. Nonetheless, additional components would be introduced, compromising the system reliability.
- b. *A numerical integration of the electrical transducers output signal*. No additional components would be added to the system in this case, which increase the system reliability. However, the speed data precision would be lower, since a numerical integration takes time and the electrical signal is sensitive to electromagnetic disturbances.

In particular, considering both the flap position and speed inside the asymmetry monitoring models leads to an earlier position asymmetry failure declaration in those scenarios in which the failure surface experiments high speeds after failure. This is quite common with *reversible* actuators, with which the failure surface will experiment high retraction speeds when operating under high aerodynamic load scenarios. A deep analysis of these considerations will be performed from section 6 to 9, when the flap position asymmetry test results will be discussed.

Different **active asymmetry monitoring techniques** have been fully designed and developed in this project.

¹This comparison may be done either comparing the electrical position signals to each other or to a previously set *reference position*.

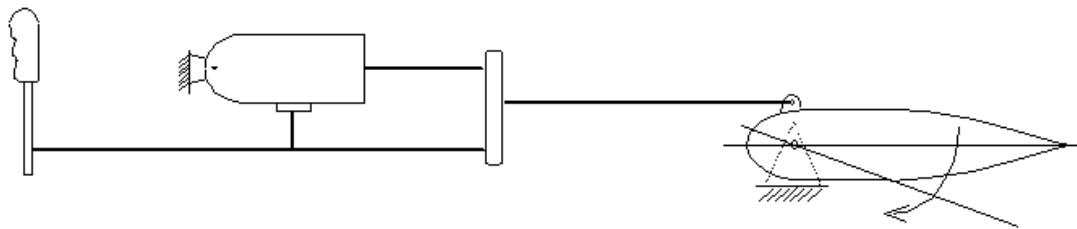
2 Hydraulic drive systems for high-lift devices

2.1 Flight controls overview

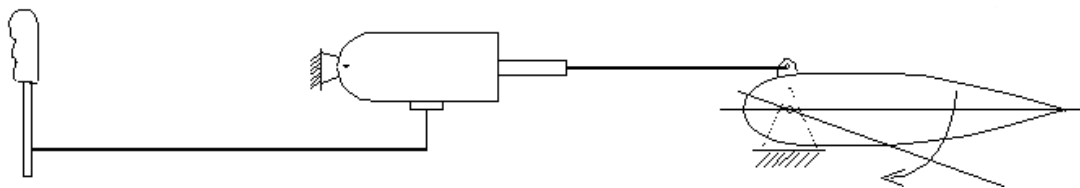
2.1.1 Power source based flight controls classification

An additional flight controls classification may be done according to the power generation, regarding the primary flight controls. Therefore, the flight controls can be:

- a. *Manual*. The control surfaces are powered by the pilots physical strength by means of a series of rods, cables, levers and pulleys. In other words, from the *manual* flight controls perspective, the pilot would command the control signal and produce the power needed to make it effective. Nowadays, the *manual* flight controls are exclusively used on small aircrafts.
- b. *Servo-assisted* or *power-assisted*. The pilot is “assisted” by *force enhancers* to deflect the control surfaces. Therefore, the physical strength required to the pilot is lower. As illustrated in Figure 2a, the *servo-assisted* flight controls preser a torque summing configuration, which can be noted on the vertical element than combines both the output of both the pilot physical input and the enhanced power input. It is the predecessor of the current *power-operated* flight controls.
- c. *Power-operated*. They are powered by an artifitial power source. The *power-oerated* flight contols are the sucessor of the *servo-assisted* controls mentioned above. Nowadays, they are used both in large vehicles and high performance aircrafts.



(a) Servo-assisted control



(b) Power operated control

Figure 2: Oleodynamic servo-control configurations

Regarding the drive system power source, the most common wither partial or complete artifitial power generation servo-controls (*servo-assisted* and *power-operated*, respectively), are :

- *Electromechanic* servo-control
- *Oleodynamic* servo-control. These can be divided in:

- *Hydromechanical*. The pilot command is mechanically transmitted to the servovalve, in charge of the hydraulic power regulation.
- *Electro-hydraulic*. The pilot command is transmitted via electrical signal to the electro-hydraulic servovalve.

The evolution of the *oleodynamic* servo-control was determined both by the technology progress of the last forty years and the technological evolution of the flight controls used to govern the aircraft flight, such as autopilot, stability augmentation systems (SAS)...., which demands best-performing systems.

Summarizing, the *manual* flight controls evolved into *servo-assisted*, which used an oleodynamic servo to enhance the pilot direct action on the control surfaces (see Figure 2a).

Then, the current *power-operated* flight controls manage the pilot command as an input command signal, while power source that deflects the control surface is totally artificial (see Figure 2b).

In general, the power-operated configuration is used on secondary flight controls, since it meets the secondary flight controls design criteria. Since neither instinctivity nor command input proportionality problems concern the secondary flight controls, they generally present power-operated configurations.

On the other hand, the primary flight controls may present any of the aforementioned flight control configurations. Nonetheless, these flight controls nowadays tend to incorporate innovative architectures that make them more performing guaranteeing acceptable levels both of safety and reliability.

2.1.2 Current flight control systems

There are different flight control systems (FCS) configurations that determined the evolution of the *oleodynamic power-operated* servo-controls.

Firstly, the Stability Augmentation System (SAS) generates a high frequency low authority command added to the low frequency high authority pilot command.

The Stability Augmentation System is schematized in Figure 3.

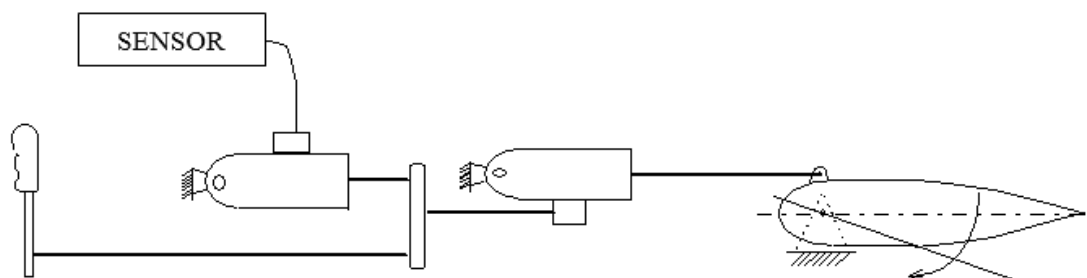


Figure 3: Stability Augmentation System (SAS)

Secondly, the Control Augmentation System (CAS) manage both a mechanical and an electrical command signals. A schematization of the CAS system is illustrated in

Figure 4.

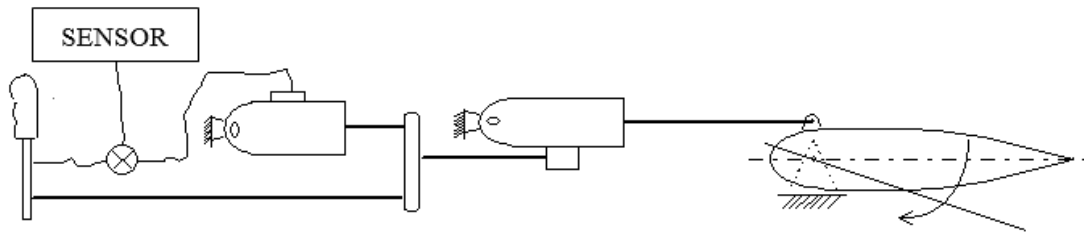


Figure 4: Control Augmentation System (CAS)

Then, the Fly By Wire (FBW) system only manages an electrical command signal. The FBW schematic is shown in Figure 5.

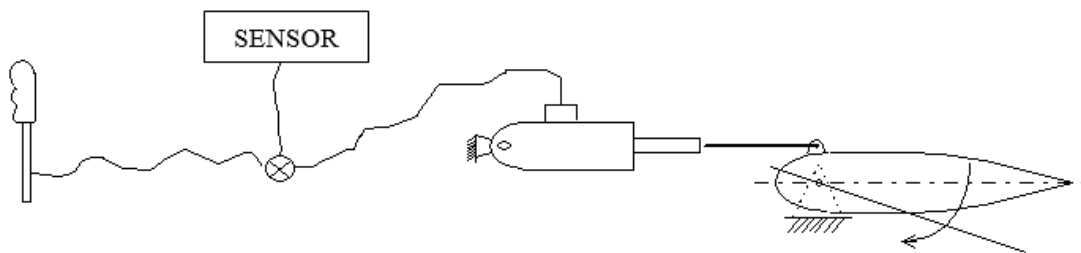


Figure 5: Fly By Wire (FBW)

The main advantages of the FBW systems regard their exclusively electric input signal. It allows an ideal interfacing with other aircraft systems and reduces the FCS encumbrance, facilitating its installation on board. In addition, the FBW system improves the overall system weight and dimensions with respect to the previous flight control systems.

In contrast, the FBW system is sensitive to electromagnetic disturbances due to the electrical command signal nature. It deteriorates the FCS reliability.

In consequence, hybrid solutions seek to exploit the benefits of the aforementioned configuration without compromising the FCS reliability. For that purpose, the hybrid Control and Stability Augmentation Systems (CSAS) consider both electrical and mechanical transmission lines installed in parallel. In contrast to the CAS, only the electrical transmission lines are active to prevent interferences. Nonetheless, the mechanical lines would be activated in case of electrical system general failure.

Therefore, the hybrid CSAS does not exploit all the advantages of the FBW systems but maintains an acceptable FCS reliability.

An additional *fly-by-wire* system advantage is the pilot input signal filtering to guarantee an acceptable aircraft stick-free stability. In addition, the FBW systems may perform a flight external loads control, guaranteeing the aircraft operation inside the flight envelope and allowing the pilot to focus on its mission.

2.1.3 Design criteria for primary and secondary flight

Different design criteria are considered on the flight controls design, according to their specific requirements. Indeed, the primary flight controls design requirements are more demanding than those of the secondary flight controls.

In regard to the *primary* flight controls, they are proportional to the pilot continuous command input. To that end, they shall provide either a real or an artificial feel to the pilot and be instinctive.

In addition, they shall have an accurate high frequency response, as well as being high reliability systems. This last requirement is very important, since a primary flight control failure should not compromise the aircraft controllability.

Hence, ***damage tolerance*** is the primary flight control design criterion. In effect, the primary flight controls shall remain operative should a system failure arise.

In contrast to the primary flight controls, a less accurate low frequency response is required to the *secondary* flight controls, since the flight conditions more slowly than the aircraft attitude. In addition, the secondary flight controls deflection is discrete, unlike the primary flight controls, in which it is a continuous function of the pilot command input.

Therefore, the secondary flight controls design criterion is less demanding. In fact, a secondary flight controls functionality loss deteriorates the aircraft performances but neither the flight safety nor the aircraft controllability would be compromised.

Consequently, the ***fail safe*** design criterion would be used on secondary flight controls, with which the aircraft safe operation is guaranteed after failure.

2.2 High-lift devices architecture

In general, the high-lift devices architecture is the following:

- *Power Drive Unit (PDU)*. It is the mechanical power unit, placed centrally. This unit is powered by hydraulic motors.
- *Power Control Unit (PCU)*. In general, it is integrated together with the PCU, forming the single unit PDCU.
- *Drive shafts*
- *Actuators*. Redundancy criteria would define the amount of actuators that allows a uniform high-lift device deflection.
- *Servovalves, solenoid and shut-off valve*, which regulate the power.

Regarding the drive system design, different configurations have been implemented to meet the system response requirements, such as speed and actuation time, while allowing a correct and efficient interfacing with the other aircraft systems and subsystems.

2.2.1 Power Drive Unit architecture

While this PDU is generally powered by hydraulic motors, electrical engines may also be used. Nonetheless, the *all electric aircraft* configurations may not perform as wanted on high lift-devices drive systems, due the inefficient high power management of the electrical systems. Moreover, these are lower specific power systems due to the electrical generator high weight. Note that the hydraulic systems allow smaller and lighter actuators to manage large amounts of power (very high working pressures).

In addition, the PDU may consist in either one or two engines. In the last case, there are two different design philosophies. These are:

- a. *Velocity summing architecture.* Both are interfaced to an intermediate stage, from a single output arrives to the drift shaft. This engine configuration provides both engines average velocity and a final torque equal to a single engine torque. Should single engine failure arise, the final velocity would be the half of the operative engine speed and the final torque would be equal to the operative engine torque. This PDU engine architecture is generally used on commercial aircrafts, in which the PDU architecture reliability is guaranteed by the engine torque redundance in terms of final torque, especially under the unaltered aerodynamic load applied on the control surface. In consequence, the control surface deflection time would be double, which is still acceptable on commercial aircrafts.
- b. *Torque summing architecture.* In this case, both engines are interfaced directly to the drift shaft. This engine configuration provides the sum of each engine resulting torque and the final velocity would be the speed of a single engine. This might be considered a high-performance PDU architecture when both engines are operative. However, the overall torque transmitted to the drive shaft may be halved should a single engine failure arise. Thus, the PDU torque summing architecture is less reliable than the velocity summing one, but it allows a very high aircraft controllability and maneuverability in regular operating conditions. In consequence, the control surface deflection time would be double, which is still acceptable on fighter aircrafts.

The PDU localization inside the high lift device system is shown in figures 6 and 7.

2.2.2 Drive shaft design

The drive shaft system consists in torsion bars in charge of the torque transmission from the PDU to the high-lift device utilities (control surfaces) by means of the actuators placed in the wingtip.

In general, the high lift devices drive shaft bars present a certain degree of torsional flexibility on commercial aircrafts. In effect, the slow and rigid torsion bars are being replaced by flexible drive shaft bars with high operational rotation speeds.

The drive shaft torsion bars are schematized in figures 6 and 7.

2.2.3 Actuators and braked design configurations

In general, the actuators used on high-lift devices drive systems are *linear*. As discussed in section 1.2, the linear actuators might be:

- a. **Irreversible.** These actuators prevent the control surface deflection after failure by the effect of the aerodynamic torque. The *screw-and-nut* actuators are an example of this kind.
- b. **Reversible.** In this case, the actuators allow the failure surface retraction by the effect of the aerodynamic torque. The *ballscrew* actuators are an example of this kind.

The actuators internal friction forces determine the actuators performance in terms of reversibility. In effect, the high internal friction forces that characterize the *irreversible* actuators prevent the inoperative surface retraction after failure when operating under high aerodynamic loads. On the contrary, the *reversible* actuators internal friction forces allow the failure surface retraction on high aerodynamic load conditions. Nonetheless, the reversible actuators will be more efficient than the irreversible ones in terms of energy dissipation before failure.

The linear actuators should used on high-lift devices drive shall always meet the flap asymmetry specifications. These state that the flap position asymmetry should be limited, both in case of drift shaft failure and in case o drive system depressurization once the commanded flap position is reached.

In general, the *ballscrew* actuators are used on high-lift devices drive systems.

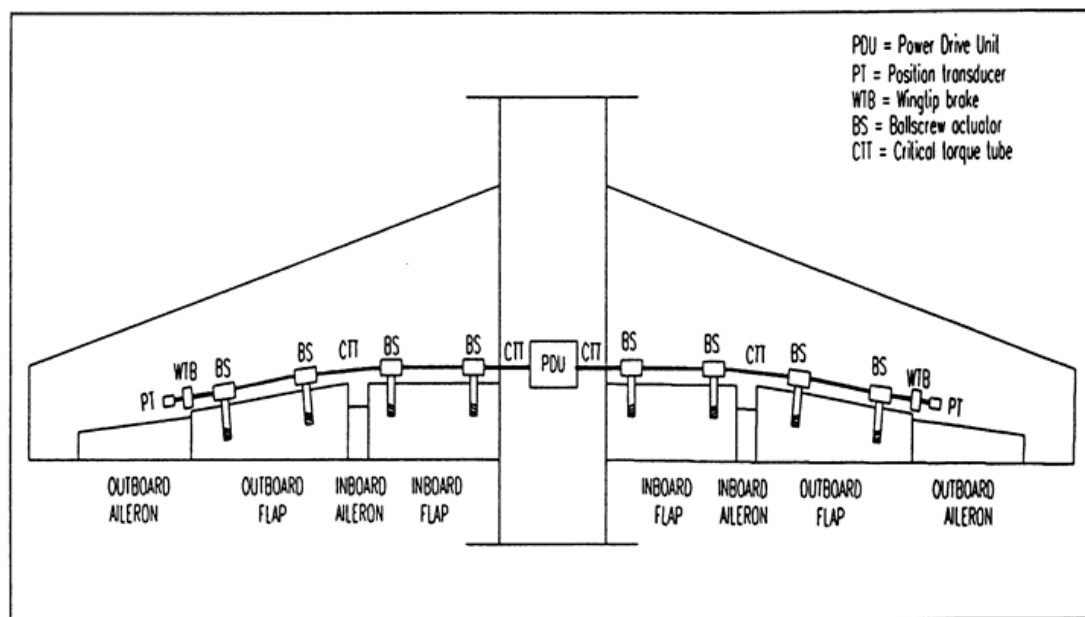


Figure 6: Reversible actuators & wingtip brakes (WTB) configuration

The non-reversible actuators always meet the aforementioned conditions, while the drive system should activate the braking system to guarantee the flap commanded position after depressurization in the last scenario in case of using reversible actuators. The braking system configurations are two:

- a. **Wingtip brakes.** They are installed on the transmission line, close to the electrical flap position transducer (one per flap). The wingtip brakes are controlled by the

activation and deactivation unit, which is commanded by the asymmetry monitoring techniques. The wingtip brakes are schematized in Figure 6.

- b. **Self-acting brakes.** They are installed inside each actuator, enabling an effective control on the failure surface in case the flap speed differ from the engine rotation speed. Should the flap rotating sense differ from the commanded rotation (previously converted on *output* flap motion), the self-acting brakes automatically brake the failure flap. The self-acting brakes are schematized in Figure 7.

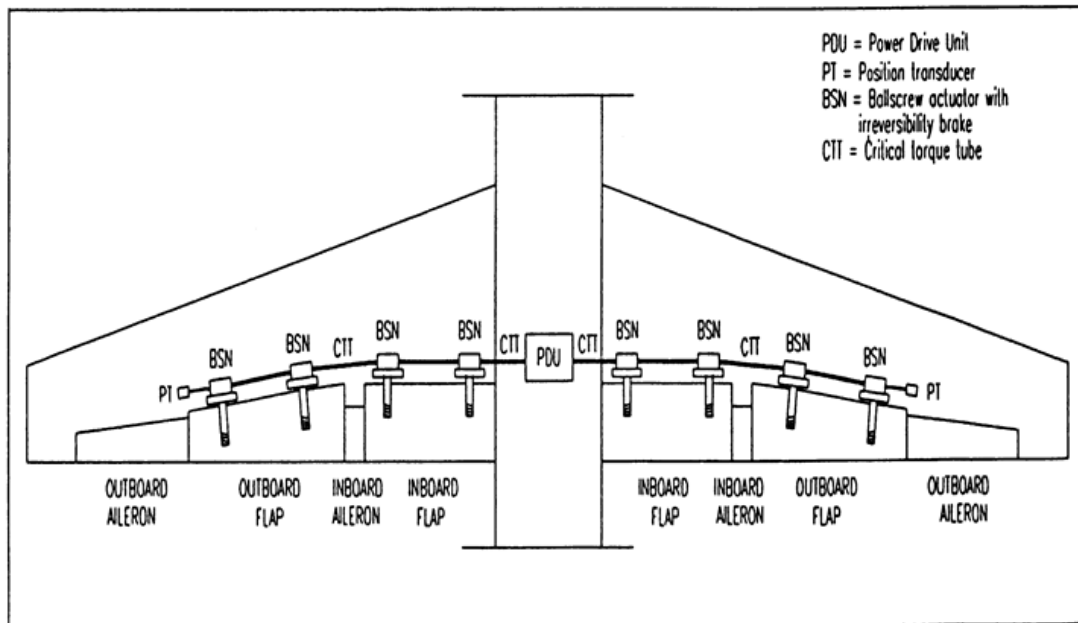


Figure 7: Reversible actuators & self-acting brakes configuration

The flap asymmetry on regular operating conditions (no failures), would be less than 0.05% of the total flap travel and the drive shaft torsion bar deformation by the aerodynamic load of the control surface would not exceed the 0.4% total control surface travel.

Notice that only the angular measures inside the closed loop (up to the drive shaft torsion bars) can be detected by the electrical position transducers. Nevertheless, the actuator angular position measures in open loop may not be detected by the position transducers.

Moreover, should the mechanical transmission fail, a great position asymmetry may arise between the left and the right flap. It should be corrected as soon as possible to guarantee the flight safety, as well as the aircraft controllability and maneuverability after failure.

For that purpose, four different active monitoring techniques have been both designed and developed from zero. These will be explained in section 5 and tested in different conditions from section 6 to section 9. In this project, the mechanical transmission failure concerns the drive shaft torsion bar breaking.

3 System mathematical modeling

The high-lift devices system modeling and simulation has been done through a computer program that reproduces the trailing-edge devices (flaps) behaviour when commanded. In addition, both the aircraft roll dynamics and the autopilot behaviour are also reproduced. The aircraft lateral-directional modelling reproduces the vehicle roll dynamics considering the flap position asymmetry and the autopilot controls the aircraft rolling moment.

3.1 Mechanical subsystem mathematical modeling

The physical model of the reversible actuators with wingtip brakes configuration of Figure 6 is discussed in this section, focusing on the mechanical modeling schematized in Figure 8.

The mechanical system architecture is formed by the aforementioned Power Drive Unit (PDU), which generates the power that is transmitted to the ballscrew actuators (BS) by means of the drive shaft torque tube (CTB). These bars, set between the PDU and the final actuators, are designed according to frangibility criteria to increase operation safety. The engine torque reduction is essential to guarantee the actuators correct performance. To that end, a motor (or intermediate) gear reducer Z_M will reduce the engine torque before the drive shaft torsion bar. Then, a second torque reduction stage will be performed by the actuator (or final) gear reducer Z_S before the ballscrew actuators.

In addition, both the wingtip brakes (WTB) and the position transducers (PT) are placed at the drive shaft end. The electrical velocities are obtained by numerical integration of the position transmission output (see section see section 1.3), so no velocity transducers will be used. Nonetheless, these would also have been placed at the drive shaft end if present.

The Electrical Control Unit (ECU), not illustrated in Figure 8, commands the entire mechanical subsystem. Both the left and right position transducers provide both flaps electrical position. These are evaluated to determine the control surfaces position asymmetry. Should the position asymmetry exceed certain limits, it would be corrected by the asymmetry monitoring techniques.

As shown in Figure 8, the PDU is composed of:

1. Hydraulic motor.
2. Motor gear reducers, characterized its gear ratio Z_M .
3. Servovalves.
4. Solenoid and shut-off valves.

Note that the control surface gear reducers ratio are written as $Z_S + \Delta Z_S$ in the schematic diagram in Figure 8. The component ΔZ_S considers all which may affect the gear reducer ratio, such as thermal loads, possible manufacturing defects, possible actuators travel changes, etc. All these considerations may be interesting in a second approximation approach to raise the model accuracy. However, $\Delta Z_S = 0$ in the current

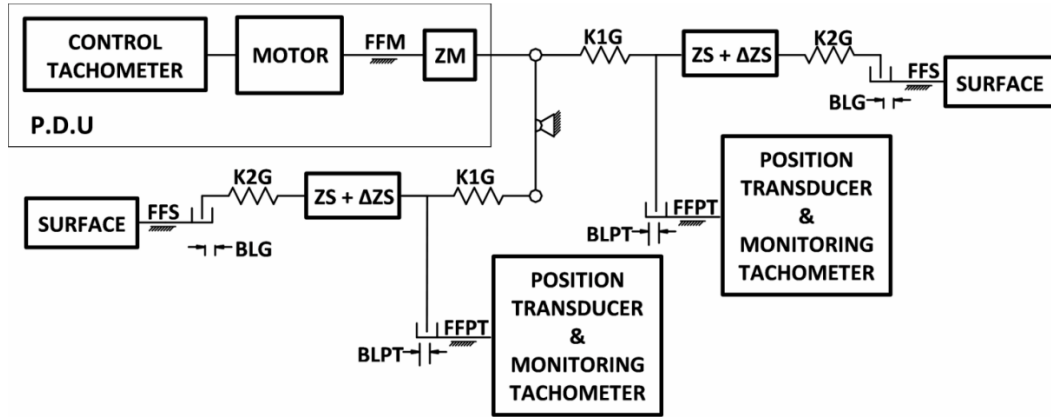


Figure 8: Actuation system mechanical model

design phase, since the error margin in this phase would be notably higher than the model second order efficiency improvement.

Further components would be added torque *torque summing architectures*. Nevertheless, these on commercial aircrafts, *velocity summing architectures* are used, so no additional elements are needed (see section 2.2.1).

In particular, the mechanical subsystem scheme in Figure 8, contains the following:

- Dry (or Coulomb) friction that affects the PDU $F_{f,M}$, the control surfaces $F_{f,S}$ and the position transducers $F_{f,PT}$.
- Drive shaft torsion bar torsional stiffness on *closed* loop K_{1G} , both of the left and right bar.
- Position transducers backlash (BLPT) and other errors due to the transducers thermal loads on closed loop.
- Drive shaft torsion bar torsional stiffness on *open* loop K_{2G} , both of the left and right bar. They regard the torsion bar stiffness downstream of the position transducer.
- The third-order valve model with position and velocity saturations, together with the servovalve fluid dynamics modeling for hydraulic drive system
- Both the hydraulic motor and its gear reducer mechanical and fluid dynamics modeling. In addition to dry friction, both viscous friction and the leakage losses are considered in the model.
- Reversible actuators modeling, considering different friction efficiencies in case the aerodynamic load against opposes the flap extension (in *opposing*) η_{OS} or favours it (in *aiding*) η_{AS} . These two efficiencies will be discussed later on.

The flap commanded position is compared with the angular position detector by the transducers on closed loop. The difference between these two is called *position error*, which should be minimized by the controller. The current mechanical model uses a *proportional controller* (“P” controller). The corrective action passes through an amplification gain G_A that amplifies the electric signal to minimize the aforementioned

error. This position controlled is possible due to the closed loop that is formed with the sensors (transducers) placed on the torsion bar, as shown in figures 6 and 7. In consequence, the closed loop allows the initial commanded position track.

The higher the amplification gain is, the lower the position error will be. However, larger gains may lead to lower system stability margins for many reasons: the loop feedback delays, the torsion bars mechanical complacance, the non-linearities due to backlash, friction...

3.1.1 Activation/deactivation logic

The secondary flight controls and, in particular, the high-lift devices are be pressurized when they a new angular position is commanded. There is no need to maintain indefinitely such pressurization due to their occasional actuation. Moreover, significant oleodynamic energy losses would be produced due to both the hydraulic motor and the servovalve second stage oil leakage, as well as the servovalve first stage continuous oil demand to drive the second stage.

Hence, an the high-lift device system should be pressurized before every actuation and depressurized after it has finished, braking the flaps with the wingtip brakes. The high-lift device system is activated in case of a flap command over $0.8 - 1.2$ degrees for at least $150ms$, in order to prevent possible “false flap commands” due to electric and/or magnetic disturbances.

The activation mechanism sends an electric current to the solenoid valve coil that drives the shut-off valve, in charge of pressurizing both the servovalve and the hydraulic motor (the so-called *actuation group*). On the other hand, the group depressurization is possible cutting off the current Cor .

The activation sequence is correctly executed once the system pressure exceeds the minimum acuation pressure. After the correct pressure execution confirmation time, set in $180 - 200ms$ from the flap command instant, the flap is deflected by the electrohydraulic servovalve.

Once the flap commanded position is reached, the electric current the current is interrupted and the flight control is deactivated. As mentioned before, the flap final position would be maintained by the brakeing system, which stops the control surfaces in the desired position.

3.1.2 Shut-off valve mathematical modeling

The shut-off valve is in charge of the servovalve pressure supply/removal. It is always activated by a solenoid valve, which responds to the electrical on/off inputs, while the shut-off valve manages the pressure. In effect, once the solenoid valve receives an electric input, it drives the spool to open/close the ports, wither increasing or decreasing the pressure downstream of the shut-off valve.

This valves configuration allows a high pressure management with moderate input signals.

The mathematical modelling does not consider both valves separately but analyzes

their combined effect, which simplifies the system modeling.

It should be noted that the spool commutation times are different whether the shut-off valve opening or closing are commanded, especially in the latter, due to the coil electrical inductance.

In addition, the spool travel is limited by both an upper and lower end of travel, which determines both the maximum and minimum servovalve pressure, respectively. This is physically represented by both the spool travel and the servovalve pressure saturation, as illustrated in Figure 9.

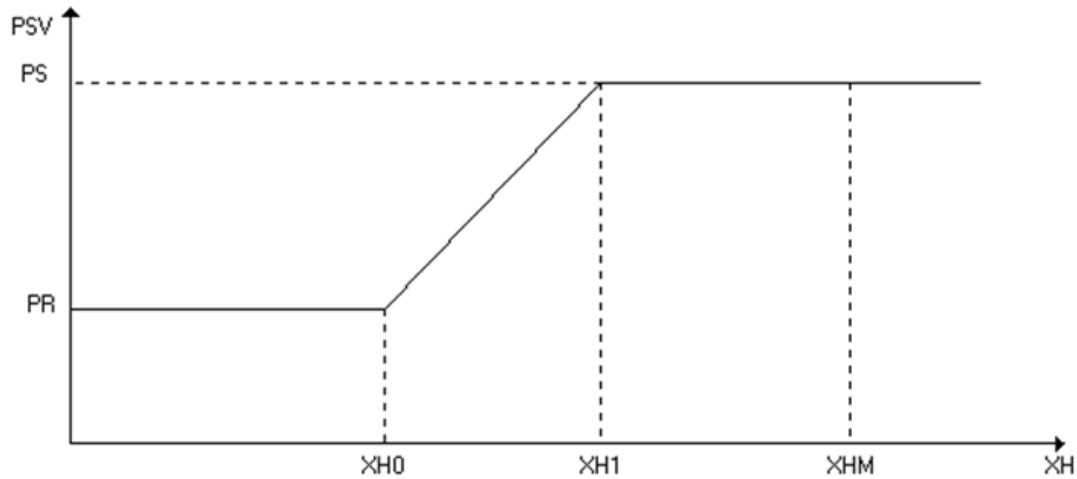


Figure 9: Relation between the shut-off valve pressure and the spool displacement

where X_H is the shutoff valve spool displacement, P_{SV} is the servovalve pressure downstream of the shut-off valve (between shutoff valve and servovalve). Moreover, X_{H1} and X_{H0} determine the maximum and minimum shutoff spool displacements, respectively, between which the shut-off valve pressure varies linearly with X_H . On the other hand, the maximum and minimum servovalve pressures are the *supply pressure* $P_S \equiv P_{SV_{max}}$, and the return pressure $P_R \equiv P_{SV_{min}}$ (also named tank pressure P_T), respectively.

The Figure 9 shows a first order shut-off valve fluid dynamics between X_{H0} and X_{H1} (linear relation $P_{SV} = f(X_H)$). However, the saturation non-linear effect is evident beyond the maximum and minimum spool travel thresholds. Notice that X_{HM} determines the spool upper end of travel, but no pressure increments can be noted beyond X_{H1} . In fact, $P_{SV}(X_{H1}) = P_{SV}(X_{HM}) = P_S$.

It should be noted that the leakage losses are negligible, since they shut-off valve orifices are big enough.

Once the electric current Cor is cut off, the shut-off valve is closed with a second-order differential equation. Nonetheless, the shut-off system dynamics is very fast, so it seems to close (quasi) instantaneously. Hence, the servovalve pressure P_{SV} drops rapidly according to its linear relation with the servovalve spool displacement X_H .

Thus, the servovalve will be be depressurized rapidly by the once the shut-off valve

is closed, which is produced once the electric current C_{or} is cut off.

3.1.3 Servovalve mathematical modeling

Two different approaches are possible when modeling the servovalve fluid dynamics:

- Calculate the pressure variation from the volumetric flow rate ΔQ difference between the supply and return (tank) passages for a given spool displacement

$$\Delta P = \Delta P(Q_S - Q_R) \text{ for a given } X_S$$

- Calculate the volumetric flow rate variation from the pressure difference between the supply and return (tank) passages for a given spool displacement.

$$\Delta Q = \Delta Q(P_S - P_R) \text{ for a given } X_S$$

The last approach was chosen to reproduce the servovalve behaviour in this project.

The servovalve model is generally valid for hydromechanic valves, electrohydraulic servovalves and the aforementioned direct drive control valves (solenoid + shut-off valves). In effect, the valve input could be understood either as a spool displacement or an electric signal input and the valve servovalve model could be used without loss of generality.

The valve used in this project is a *flapper-nozzle* servovalve, a *electrohydraulic* four ways servovalve with two stages.

A four way valve schematic is illustrated in Figure 10. Note that the ports named as “1” and “2” connect the flapper-nozzle second stage to the hydraulic motor, providing it the necessary oil pressure to produce the required torque. On the other hand, the other two passages named as “S” (supply) and “R” (return or tank) provide the necessary pressure difference to move the servovalve spool and guarantee the oil volumetric flow rate through “1” and “2”.

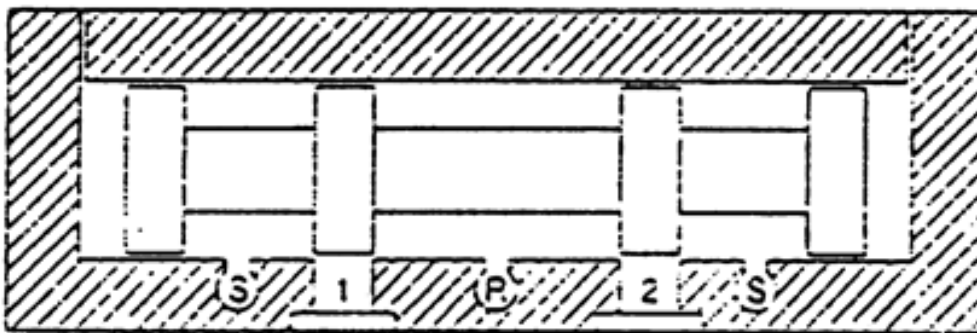


Figure 10: Four way valve schematic

In regard to the servovalve dynamics, the mathematical model is different on each stage:

- A *first stage* non-linear (position saturation) second-order (mass-spring-damper) dynamics.
- A *second stage* non-linear (position saturation) first-order dynamics.

Moreover, the fluid dynamics model calculates the pressure drop by the sum of both a linear and a quadratic term, so the volumetric flow rate through each valve port would be a function of both the pressure drop and each edge gap geometry.

As indicated above, the servovalve second stage presents four way architecture. It is composed by the following ports, as illustrated in Figure 10:

- Supply and “1”.
- “1” and return.
- Supply and “2”.
- “2” and return.

The correct design of the edge gap geometries is essential to minimize the leakage losses and maximize both the *actuation group* (servovalve and hydraulic motor) performances.

Thus, a correct modelling of the aforementioned four valve ways is essential. This will be discussed later on.

The relation between the pressure differential and the volumetric flow rate may be written as follows:

$$\Delta P = \Delta P_{lin} + \Delta P_{quad} \quad (3.1)$$

where

$$\Delta P_{lin} = R_{lin} \cdot Q \quad (3.2)$$

$$\Delta P_{quad} = R_{quad} \cdot Q \cdot |Q| \quad (3.3)$$

where R_{lin} and R_{quad} are the linear and quadratic coefficients, respectively. They can be written as follows:

$$R_{lin} = \frac{12\mu X_O}{\varphi \Delta r^3} \frac{1}{1 + \frac{3 \left(\frac{e}{\Delta r} \right)^2}{2}} \quad (3.4)$$

$$R_{quad} = \frac{\rho}{2C_d^2 A^2} \quad (3.5)$$

where

μ = oil dynamic viscosity
 X_O = servovalve orifice regulation length
 φ = orifice circumferencial amplitude
 Δr = servovalve radial clearance
 e = maximum radial eccentricity
 ρ = oil dynamic viscosity
 C_d = servovalve discharge coefficient (also efflux coefficient)
 A = passage area

Notice that R_{lin} depends on the servovalve orifice geometry, which is carefully studied hereunder, where the different servovalve orifices regulation lengths X_O will be calculated.

Let the spool position X_S be centered when $X_S = 0$, which entails both the servovalve ports complete coverage as well as an additional overlap as illustrated in Figure 11. These overlaps may concern the supply ΔX_S (also named OSSV) and/or the return ΔX_R (also named ORSV) side of the valve.

The geometrical magnitudes are represented in Figure 11, as well as the directions of both the spool displacement and the oil volumetric flow rates.

where the different volumetric flow rates represented are:

Q_{1S} = volumetric flow rate from the *supply* passage and port 1
 Q_{1R} = volumetric flow rate oil flow from port 1 to the *return* passage
 Q_{2S} = volumetric flow rate oil flow from the *supply* passage and port 2
 Q_{2R} = volumetric flow rate oil flow from port 2 to the *return* passage
 Q_{1L} = maximum volumetric flow rate through the port 1 (to the hydraulic motor)
 Q_{2L} = maximum volumetric flow rate through the port 2 (back from the hydraulic motor)

Hence, the non-zero length of the different orifices X_O can be calculated from Figure 11 as:

$$\begin{aligned}
 X_{O1S} &= \Delta X_S - X_S \\
 X_{O1R} &= \Delta X_R + X_S \\
 X_{O2R} &= \Delta X_R - X_S \\
 X_{O2S} &= \Delta X_S + X_S
 \end{aligned} \tag{3.6}$$

where:

X_{O1S} = from *supply* passage to port 1
 X_{O1R} = from port 1 to *return* passage
 X_{O2R} = from port 2 to *return* passage
 X_{O2S} = from *supply* passage to port 2

considering that $X_O \geq 0$. Note that X_O should not be negative, so $X_{Omin} = 0$. Notice that the indices “S” and “R” refer to the *supply side* and the *return side* of the servovalve, respectively.

In the light of the above, two different scenarios can be studied according to the orifice regulation length values:

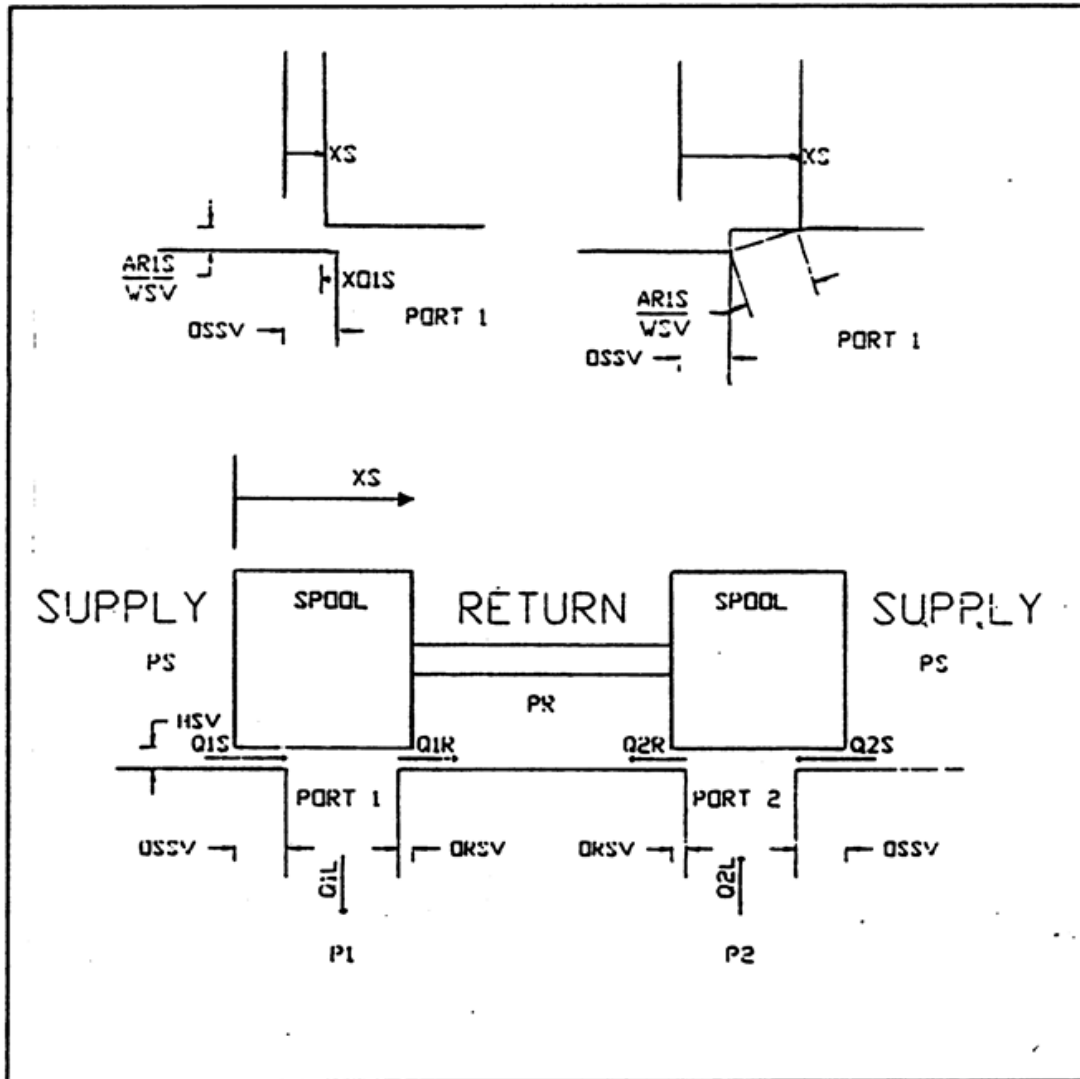


Figure 11: Servovalve fluid dynamic schematic diagram

- a. *Underlapped case.* The orifice length is zero considering either $\Delta X_S < X_S$ on the *supply side* or $\Delta X_R < X_S$ on the *return side*. Hence, $X_O = X_{Omin} = 0$, so the linear coefficient would be zero $R_{lin} = 0$ and the pressure differential can be written as:

$$\Delta P = \Delta P_{quad} \quad (3.7)$$

The underlapped case only considers turbulent flow to calculate the pressure differential ΔP through the passage area A .

- b. *Overlapped case.* The orifice length is positive considering either $\Delta X_S > X_S$ on the *supply side* or $\Delta X_R > X_S$ on the *return side*. Hence, $X_O > X_{Omin}$, so the linear coefficient would not be zero anymore $R_{lin} \neq 0$ and the pressure differential can be written as:

$$\Delta P = \Delta P_{lin} + \Delta P_{quad} \quad (3.8)$$

The overlapped case considers also the laminar flow represented by a low Reynolds number Re through the radial clearance. In effect, the current scenario calculates the pressure differential as the sum of both the linear and quadratic component with respect to the volumetric flow rate Q .

In regard to the passage area A , these can be calculated as:

$$A = \begin{cases} \varphi \cdot \Delta r & \text{if } X_S < \Delta X_{S,R} \\ A_{mn} & \text{if } X_S > \Delta X_{S,R} \end{cases} \quad (3.9)$$

In case of $\Delta X_{S,R} < X_S$, the passage area would be calculated as the conical surface area, as illustrated in Figure 11.

$$\begin{aligned} A_{1S} &= \varphi \cdot \sqrt{\Delta r^2 + (X_S - \Delta X_S)^2} \\ A_{1R} &= \varphi \cdot \sqrt{\Delta r^2 + (X_S + \Delta X_R)^2} \\ A_{2R} &= \varphi \cdot \sqrt{\Delta r^2 + (X_S - \Delta X_R)^2} \\ A_{2S} &= \varphi \cdot \sqrt{\Delta r^2 + (X_S + \Delta X_S)^2} \end{aligned} \quad (3.10)$$

where:

A_{1S} = from *supply* passage to port 1

A_{1R} = from port 1 to *return* passage

A_{2R} = from port 2 to *return* passage

A_{2S} = from *supply* passage to port 2

considering $X_S > \Delta X_{S,R}$, hence $A > \varphi \cdot \Delta r = A_{min}$.

Regarding the *discharge coefficient* (also named *efflux coefficient*) C_d considered in the different passages and ports, it depends both on the Reynolds number Re and the passage area $C_d = C_d(Re, A)$. In particular, the C_d variation with Re presents an horizontal asymptote when Re is large enough:

$$\lim_{Re \rightarrow \infty} C_d = 0.61 \quad (3.11)$$

In this project, the discharge coefficient has been set equal to the asymptotic value $C_d = 0.61$ since large Reynolds numbers are present when the spool displacements are large enough ($X_S \sim 25\Delta r$).

Once all these have been calculated, the oil volumetric flow rates can be obtained as a function of the pressure difference through the valve ports.

Note the pressure difference is calculated as the sum of the linear and the quadratic term $\Delta P = \Delta P_{lin} + \Delta P_{quad}$. Hence, the aforementioned volumetric flow are:

$$\begin{aligned}
Q_{1S} &= \frac{\sqrt{R_{lin1S}^2 + 4 \cdot R_{quad1S} \cdot |P_S - P_1|} - R_{lin1S}}{2 \cdot R_{quad1S}} \cdot \text{sgn}(P_S - P_1) \\
Q_{1R} &= \frac{\sqrt{R_{lin1R}^2 + 4 \cdot R_{quad1R} \cdot |P_1 - P_R|} - R_{lin1R}}{2 \cdot R_{quad1R}} \cdot \text{sgn}(P_S - P_R) \\
Q_{2R} &= \frac{\sqrt{R_{lin2R}^2 + 4 \cdot R_{quad2R} \cdot |P_2 - P_R|} - R_{lin2R}}{2 \cdot R_{quad2R}} \cdot \text{sgn}(P_2 - P_R) \\
Q_{2S} &= \frac{\sqrt{R_{lin2S}^2 + 4 \cdot R_{quad2S} \cdot |P_S - P_2|} - R_{lin2S}}{2 \cdot R_{quad2S}} \cdot \text{sgn}(P_S - P_2)
\end{aligned} \tag{3.12}$$

where the oil volumetric flow rates, analogously to the passage areas, are:

Q_{1S} = from *supply* passage to port 1

Q_{1R} = from port 1 to *return* passage

Q_{2R} = from port 2 to *return* passage

Q_{2S} = from *supply* passage to port 2

Note that the coefficients R_{lin} and R_{quad} regard both the laminar (linear) and the turbulent (quadratic) contributes of the differential pressure that affect the oil volumetric flow rates on each servovalve port.

Finally, the net oil volumetric flow rate either to or from the hydraulic motor can be written as:

$$\begin{aligned}
Q_{1L} &= Q_{1S} - Q_{1R} \\
Q_{2L} &= Q_{2R} - Q_{2S}
\end{aligned} \tag{3.13}$$

where:

Q_{1L} = net volumetric flow rate *to*² the hydraulic motor

Q_{2L} = new volumetric flow rate *from* the hydraulic motor

Thus, the aforementioned net volumetric flow rates can be obtained from the electric input that arrives to the servovalve, once calculated the spool displacement X_S .

To show this, the model represented in Figure 12 schematizes the servovalve spool displacement output X_S obtained from the electric input Cor which arrives to the flapper-nozzle. Once obtained X_S , the net volumetric flow rates can be calculates as indicated above.

As illustrated in Figure 12, the electric input Cor that arrives to the flapper-nozzle valve, which is limited to the maximum electric current Cor_{max} , produces a torque on the first servovavle stage by means of the torque-motor gain G_M . The combined effect of both the aforementioned torque and the feedback effect, represented by K_{SF} , that comes from the spool position X_S in the second state determines the flapper position X_F in the first stage, which is also limited according to the end top limit switch. The second-order system that determines the flapper motion is governed by the first stage elastic hinge stiffness K_F , the flapper natural frequency ω_{nF} and the flapper dimensional dumping ζ_F . Note that the flapper position is limited by the mechanical top

²The definition *to* or *from* is given to the positive value of the magnitude accoring to the sign convention illustrated in Figure 11

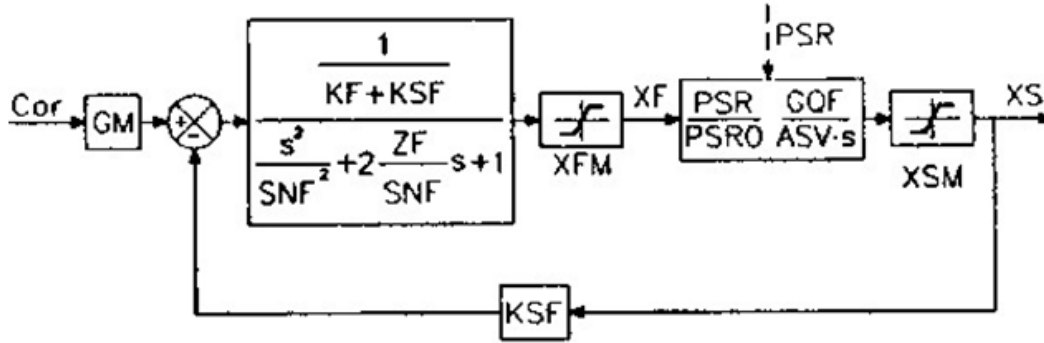


Figure 12: Servovalve control block diagram

limit switch X_{Fmax} .

The second stage spool speed $\frac{d}{dt}(X_S)$ depends on the flapper position X_F by means of the servovalve volumetric flow rate gain G_{QF} and the second stage end faces A_{SV} . The spool position is calculated via the numerical integration of $\frac{d}{dt}(X_S)$. Analogously to the flapper saturation, the spool position is also limited by its mechanical top limit switch X_{Smax} .

3.1.4 Hydraulic motor mathematical modeling

The hydraulic engine produces mechanical power from the differential pressure that arrives to the engine. Follow the mathematical relations that are generally applicable to an hydraulic motor.

$$P_M = 2\pi C_M \frac{n}{60} = C_M \omega_M \quad (3.14)$$

$$Q = \frac{Dn}{60\eta_v} = \frac{D\omega_M}{2\pi\eta_v} \quad (3.15)$$

where:

P_M = mechanical power

T_M = mechanical torque

Q = volumetric flow rate

D = displacement

n = angular velocity in r.p.m

ω_M = angular velocity in rad/s

η_v = volumetric efficiency

In addition, considering that the hydraulic motor inlet pressure the hydraulic motor mechanical power can be written as:

$$P_M = \eta_v \eta_m P_i \quad (3.16)$$

where the inlet pressure P_i is:

$$P_i = Q(P_1 - P_2) \quad (3.17)$$

hence, the mechanical pressure can be written as a function of the pressure difference as:

$$P_M = \eta_m D \frac{n}{60} (P_1 - P_2) = \eta_v \eta_m \frac{D}{2\pi} \frac{\omega_M}{60\eta_v} (P_1 - P_2) \quad (3.18)$$

where:

- P_i = pressure differential between the inlet and the outlet port
- P_1 = inlet pressure
- P_2 = outlet pressure
- η_m = mechanical efficiency

Substituting Equation (3.16) into Equation (3.18), the latter will be transformed to:

$$T_M = \frac{\eta_m D (P_1 - P_2)}{2\pi} = f(P_1 - P_2) \quad (3.19)$$

which shows the relation between the mechanical torque T_M and the pressure differential ($P_1 - P_2$)

Regarding the hydraulic motor dynamics, there are several torques that the engine would compensate. The momentum equation can be written as:

$$T_M - T_R - T_{visc} - T_{FF,M} - T_{in} = 0 \quad (3.20)$$

where:

- T_R = resistive torque from the external (aerodynamic) loads
- T_{visc} = viscous torque, proportional engine angular velocity ω_M
- $T_{FF,M}$ = friction force torque
- T_{in} = inertial torque

In turn the torques that the hydraulic motor has to compensate can be written as follows:

$$\begin{aligned} T_R &= (T_{GL} + T_{GR}) Z_M \\ T_{visc} &= c_M \dot{\theta}_M \\ T_{FF,M} &= F_{f,M} \\ T_{in} &= J_M \ddot{\theta}_M \end{aligned} \quad (3.21)$$

where:

- T_{GL} = torque transmitted to the left actuator
- T_{GR} = torque transmitted to the right actuator
- Z_M = gear ratio, between the hydraulic motor and the drive shaft
- c_M = motor damping coefficient
- $\dot{\theta}_M$ = motor angular speed
- $T_{FF,M}$ = engine friction force torque $F_{f,M}$ according to the Coulomb friction model.
- J_M = engine moment of inertia
- $\ddot{\theta}_M$ = motor angular acceleration

Substituting Equation (3.23) into Equation (3.19), shows the second-order differential equation that represents the hydraulic motor dynamics. Therefore, the hydraulic engine angular position can be obtained integrating the resulting equation. It has

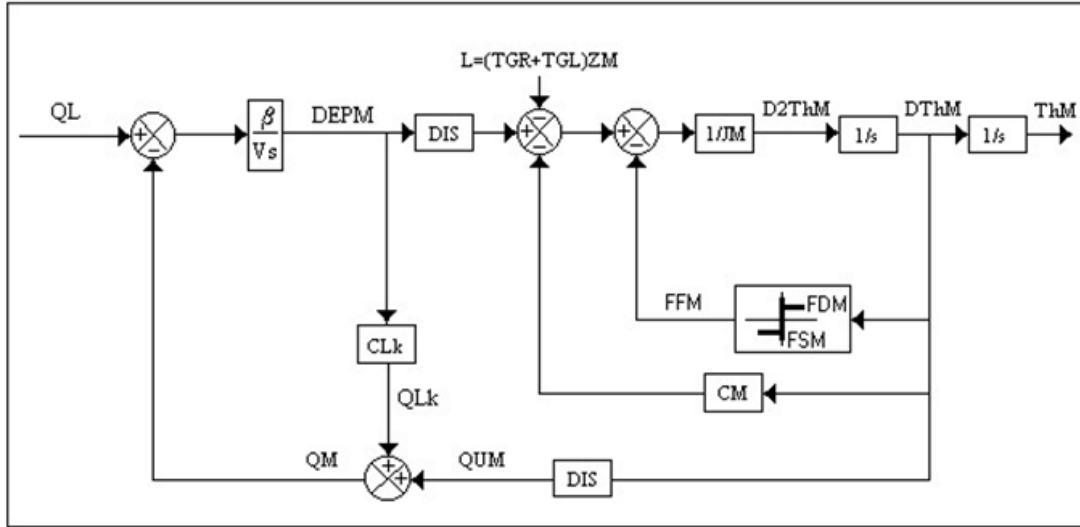


Figure 13: Hydraulic motor block diagram

schematized in the block diagram illustrated in Figure 13.

The block diagram shown in Figure 13 considers the servovalve both pressure drops and the volumetric flow rate leakage.

The net servovalve volumetric flow rate between the what sent to the hydraulic motor from the servovalve Q_{1L} and what demanded by the engine Q_M determines the time variation of the hydraulic motor supply pressure $\frac{dP_M}{dt}$.

In regard to the volumetric flow rate through the engine Q_M , it is the sum of the leakage term and the engine speed proportional term Q_{UM} :

$$Q_M = Q_{leak} + Q_{UM} \quad (3.22)$$

in which:

$$\begin{aligned} Q_{M,leak} &= c_{M,leak} \frac{dP_M}{dt} \\ Q_{UM} &= D\dot{\theta}_M \end{aligned} \quad (3.23)$$

where $c_{M,leak}$ is the engine leakage coefficient. Do not mistake the volume inside the term $\frac{\beta}{Vol}$ with the vehicle airspeed V .

Regarding the momentum equation shown in Equation 3.20, notice the different torque summing points in Figure 13. In the first one, both the resistive torque (both left and right) T_R and the inertial torque T_{in} would be deducted from the engine torque T_M . In the second summing point, the friction force torque $T_{FF,M}$ would be deducted from the resultant torque. It should be reiterated that $T_{FF,M}$ is obtained from the Coulomb friction model, considering either the static T_{FSM} or dynamic T_{FDM} friction force when appropriate. The new resultant torque might be considered the *hydraulic engine net torque*.

The hydraulic motor angular acceleration $\ddot{\theta}_M$ is calculated dividing the aforementioned net engine torque by the engine moment of inertia J_M . Hence, the hydraulic motor angular position θ_M would be obtained from integrating twice the engine angular acceleration.

Finally, notice that the viscous torque component T_{visc} is calculated as:

$$T_{visc} = c_M \dot{\theta}_M \quad (3.24)$$

where c_M is the engine damping coefficient. Thus, T_{visc} needs the first integration of engine angular acceleration, closing the loop.

3.1.5 Position transducers mathematical modeling

The engine position θ_M is the feedback loop input. It is composed by both a reducer with backlash and the angular position electrical transducer that produces an electrical position signal $\theta_{E,i}$, which will be the feedback loop output. Both the left and right electrical positions are then used in every position comparison to determine the control surfaces position asymmetry. In fact, the electrical positions $\theta_{E,i}$ will be essential to develop the asymmetry logic inside the asymmetry monitoring techniques.

Firstly, the angular position upstream of the position transducer (on intermediate shaft) reduced on shaft-surface or “slow” shaft, θ_{IT} . To that end, the angular position on intermediate shaft will be reduced by means of the actuator gear reducer Z_S .

Notice that the angular position downstream of the position the position transducer reducer cannot be calculated directly since it is part of an open loop and no device would measure it.

Two different scenarios are possible when calculating the position θ_{IT} on intermediate shaft: either operating or broken transmission line:

a. *Operative transmission line.* In this scenario, θ_{IT} can be written as:

$$\theta_{IT} = \left(\theta_M Z_M - \frac{K_G}{K_{1G}} \theta_G \right) Z_S \quad (3.25)$$

b. *Broken transmission line.* In this scenario, θ_{IT} can be written as:

$$\theta_{IT} = (\theta_M Z_M - \theta_G) Z_S \quad (3.26)$$

where the closed loop torsional stiffness is not considered, since the drive shaft is broken

where:

- θ_M = engine angular position (on fast shaft)
- Z_M = actuator gear reducer ratio
- K_G = drive shaft torsional stiffness
- K_{1G} = closed loop drive shaft torsional stiffness
- θ_G = drive shaft torsional deformation
- Z_S = actuator gear reducer ratio

Notice that the angular position θ_{IT} in case of broken drive shaft shown in Equation (3.26) is not very rigorous but simple. In fact, θ_{IT} should be calculated similarly to the previous case and considering the drive shaft backlash (or gear backlash, $\Delta\theta_{BL}$), considering both the applied load and the rotation sense. Nonetheless this would complicate significantly the position transducers mathematical modeling, which is not essential in the current design phase.

Once obtained the angular position upstream of the position transducer θ_{IT} , the mechanical position θ_T considering the position transducer backlash $\Delta\theta_{BL}$ can be written as:

$$\theta_{IT} - \Delta\theta_{BL} \leq \theta_T \leq \theta_{IT} + \Delta\theta_{BL} \quad (3.27)$$

Finally, the electrical position θ_E can be obtained considering both the transducers angular position non-zero offset $\theta_{Os,Ti}$ and the position transducer scale factor FST , which are characteristic of each device. Hence, θ_E can be written as:

$$\theta_E = FST \cdot \theta_T + \theta_{Os,Ti} \quad (3.28)$$

The electrical speed $\dot{\theta}_E$ can be obtained with electrical position first time-derivative.

Both the electrical position and speed will be compared with the real (physical) magnitudes. In addition, the electrical magnitudes are useful to develop the asymmetry logic inside the asymmetry monitoring techniques.

3.1.6 Control surfaces dynamics mathematical modeling

The mechanical system presents ball screw actuators and wingtip brakes, as indicated in section 1.2 and illustrated in Figure 6.

The control surface dynamics mathematical modeling considers all the forces (torques) applied to each surface. In particular, the engine torque applied to each flap would be named differently according to the control surface side: left T_{GL} and right T_{GR} .

Regarding each flap dynamics, the corresponding momentum equations are:

1. *Left flap.* The momentum equation can be written as:

$$\frac{T_{GL}}{ZS} - T_{RL} - c_S \dot{\theta}_L - T_{fL} = J_S \ddot{\theta}_L \quad (3.29)$$

2. *Right flap.* The momentum equation can be written as:

$$\frac{T_{GR}}{ZS} - T_{RR} - c_S \dot{\theta}_R - T_{fR} = J_S \ddot{\theta}_R \quad (3.30)$$

where:

- $T_{GL,R}$ = torque transmitted to the left/right actuator
 Z_S = actuator gear reducer ratio
 $T_{RL,R}$ = resistive torque from the external (aerodynamic) loads applied on the left/right surface
 c_S = control surface damping coefficient
 $\dot{\theta}_{L,R}$ = left/right control surface speed
 $T_{fL,R}$ = friction torque³ on the left/right control surface
 J_S = control surface moment of inertia
 $\ddot{\theta}_{L,R}$ = left/right control surface acceleration

In regard to the resistive torque from the external (aerodynamic) loads applied on the left/right surface $T_{RL,R}$, it is formed by four components. These are: a constant term, a first-order time-dependant term, a control deflection dependant term and a sinusoidal term.

As will be discussed in section 5.1.1, only the constant term of the external (aerodynamic) loads applied will be considered in this project. This simplifies the study cases as will be discussed in greater detail later.

Regarding the friction torque $T_{f,i}$, there are two different operative scenarios according to the aerodynamic load with respect to the control surface deflection sense. In effect, the aerodynamic load may be classified as follows:

- a. *In opposing*: the aerodynamic load opposes the control surface deflection. Therefore, the actuators friction efficiency *in opposing* considering dynamic conditions is η_{OS} . The dynamic friction *in opposing* F_{DO} can be written as:

$$F_{DO} = F_{DS} + \left(\frac{1}{\eta_{OS}} - 1 \right) |T_{RL,R}| + T_{brL,R} \left[\frac{DIM(P_{SV,c}, P_{brL,R})}{P_{SV,c} - P_R} \right] \quad (3.31)$$

- b. *In aiding*: the aerodynamic load favours the control surface deflection. Analogously, the actuators friction efficiency *in aiding* considering dynamic conditions is η_{AS} . The dynamic friction *in aiding* F_{DA} can be written as:

$$F_{DA} = F_{DS} + (1 - \eta_{AS}) |T_{RL,R}| + T_{brL,R} \left[\frac{DIM(P_{SV,c}, P_{brL,R})}{P_{SV,c} - P_R} \right] \quad (3.32)$$

where:

- F_{DO} = net dynamic friction force (torque) *in opposing*
 F_{DA} = net dynamic friction force (torque) *in aiding*
 F_{DS} = control surface constant component of the dynamic friction force (torque)
 η_{OS} = friction efficiency *in opposing*
 η_{AS} = friction efficiency *in aiding*
 $T_{RL,R}$ = resistive torque from the external (aerodynamic) loads applied on the left/right surface
 $T_{brL,R}$ = braking torque from the wingtip brakes applied on the left/right surface
 $P_{SV,c}$ = minimum permissible system pressure
 $P_{brL,R}$ = minimum brake releasing pressure
 P_R = system return pressure (also named *tank* pressure)

³It should be said that the friction force torque $T_{fL,R}$ is written in its vectorial form in section 9 as $\vec{F}_{f,i}$, referring to the friction torque vector referenced to the control surface i .

The control surfaces physical (real) angular acceleration $\ddot{\theta}_{SL,R}$ can be obtained from the equations (3.31) and (3.32). The surfaces physical (real) angular position $\theta_{L,R}$ can be calculated from integrating twice the acceleration.

Notice that these expressions can be used both for left and right surfaces. Nonetheless, the torque values may be different on each surfaces.

The braking torques are considered inside the dynamic friction force formulation. It can be noted that the braking system performance depends on the system hydraulic pressure. The wingtip brakes braking action is explained in detail below.

1. Once finished the system action, the pressure downstream of the shutoff valve point $P_{brL,R}$ drops. Nonetheless, the wingtip brakes will not break the control surface while $P_{brL,R}$ is higher than the minimum permissible servovalve pressure: $P_{brL,R} \geq P_{SV,c}$.
2. The braking action starts when the pressure downstream of the shutoff valve drops under the minimum permissible: $P_{brL,R} < P_{SV,c}$. The lower $P_{brL,R}$ is, the higher the braking torque will be.
3. The control surface will be stopped once the braking torque dissipates the flap torsional kinetic energy.

For that purpose, the mathematical function that reproduces the wingtip brakes behaviour is:

$$T_{brL,R} \left[\frac{DIM(P_{SV,c}, P_{brL,R})}{P_{SV,c} - P_R} \right]$$

Firstly, the function $DIM(x, y)$ is defined in the programming language FORTRAN[®] as follows:

$$DIM(P_{SV,c}, P_{brL,R}) = \begin{cases} 0 & \text{if } P_{SV,c} < P_{brL,R} \\ (P_{SV,c} - P_{brL,R}) & \text{if } P_{SV,c} > P_{brL,R} \end{cases} \quad (3.33)$$

Therefore, the breaking torque term will be zero before crossing the minimum permissible servovalve pressure $P_{SV,c} < P_{brL,R}$ and it will grow linearly when the pressure drops under the aforementioned permissible threshold, $P_{SV,c} > P_{brL,R}$. In particular, $DIM(P_{SV,c}, P_{brL,R})$ grows linearly from 0 to 1 as the pressure downstream of the shutoff valve $P_{brL,R}$ decreases from the minimum permissible servovalve pressure $P_{SV,c}$ to the return pressure P_R .

Both the left and the right flap physical angular position $\theta_{L,R}$ are essential to determine the aircraft flight mechanics. These will be discussed in the following section.

3.2 Flight mechanics mathematical modeling

Both the aircraft lateral-directional flight mechanics and the autopilot are reproduced using simplified models. These are able to reproduce the aircraft time response regarding the control surfaces physical (real) position.

It should be reiterated that the aim of this project is the design and development of asymmetry active monitoring techniques that reduce the control surfaces asymmetry

after failure. Hence, both the aircraft roll dynamics and the autopilot control logic are modeled to provide acceptable aircraft time responses given the control surfaces position asymmetry. To that end, simple but effective mathematical models have been developed to guarantee a realistic aircraft roll behaviour.

Firstly, the aircraft roll angle ϕ_A is obtained from a second-order differential equation. It considers the aileron position θ_A , aileron speed $\dot{\theta}_A$ and the flap asymmetry measure as:

$$\Delta\theta_{asym} = \frac{\theta_L - \theta_R}{2} \quad (3.34)$$

The differential equation output is the aircraft roll angle ϕ_A , which will be controlled by the autopilot.

Secondly, the autopilot commands the ailerons asymmetrical deflection to compensate the aircraft roll angle ϕ_A induced by the control surfaces asymmetry. In particular, the autopilot follows a *PID* control logic. It is a simple but effective way to reduce the roll moment in case of flap failure during deflection. The autopilot considers both the roll angle ϕ_A and its first derivative $\frac{d}{dt}(\phi_A)$ to control the aircraft roll time response.

The autopilot command will determine the calculation of the aileron deflection θ_A , as discussed below.

Finally, the aileron deflection θ_A is obtained from a second-order differential equation, similarly to the roll angle case. It should be noted that the aileron deflection and the aileron speed $\dot{\theta}_A$ are limited by the mechanical end stops. In effect, the aileron speed deflection would be set equal to zero $\dot{\theta}_A$ should the aileron position reach either the upper or lower mechanical limit switch, $\theta_{A,max}$ and $\theta_{A,min}$.

4 Reference monitoring techniques

4.1 General concepts

A monitoring technique is an studied procedure with which the proper functioning of an onboard system can be verified. In particular, the *asymmetry* monitoring techniques analyzed in this project study the flap position asymmetry, which is detected and either prevented from growing (passive techniques) or identified the failure side after which the asymmetry is corrected and minimized (active techniques).

In general, the monitoring techniques need to interface with other algorithm logics. This is essential since a correct algorithm interfacing onboard improves the entire system performance.

The trailing-edge devices may fail due to different reasons. Some of them are listed hereunder:

- **Transmission line failure.** It is the secondary flight controls critical problem, which consequences will be carefully analyzed in this project. In effect, the *torsion bar breaking* will be the main flap asymmetry cause.
- **Final control surface actuators failure.** This failure may be caused by actuators galling, or even the actuators breaking. Galled actuators present high internal friction forces which determines the failure surface dynamics.
- **Wingtip brakes failure.** This failure may not necessarily lead to position asymmetry scenarios but the control surface final position will not be reached and maintained properly, which may affect the normal aircraft operation and even compromise the flight safety in extreme cases.
- **Power plant failure.** A Power Drive Unit (PDU) failure, such as a pressure drop, may reduce the power that arrives to the control surface by means of the transmission line. Consequently, the control surface may not reach the commanded position or even may remain undeflected. This kind of failure has not been tested in this project.

The first two have been discussed in section 1.2, while the last two affect the flaps but they may not necessarily cause a position asymmetry problem.

It should be said that only *single failure* scenarios can be managed. This means that only one failure type can be managed.

The asymmetry monitoring techniques can be classified according different criteria:

- *Asymmetry identification, detection and correction.* It focus on the asymmetry detection and the possible failure side identification, as well as the asymmetry failure correction to that minimizes it. In this regard, the monitoring techniques can be:
 - *Passive monitoring techniques.* These only detect the flap position asymmetry and prevent it from growing. However, they do not reduce the asymmetry failure when produced: the *asymmetry failure is not corrected but limited.*

In addition, the failure may not be identified in some cases⁴, so they stop both flaps in case of failure detected to stop the asymmetry from growing (asymmetry divergence), regardless which is the failure and the operative flap. In consequence, the passive monitoring techniques will be more simple and the asymmetry will not keep growing but will be limited during the rest of the flight, which means a significant flap position steady state error ϵ_{ss} .

- *Active monitoring techniques.* They both detect and identify the failure side, after which the flap position asymmetry will be minimized: the *asymmetry failure is detected and corrected (minimized) regarding always the failure side.* In effect, the operative surface will be commanded to reach the failure flap and remain in that position during the rest of the flight. Consequently, the active monitoring techniques algorithm logics are more complex by they reduce the flap position asymmetry improving the aircraft lateral-directional performance after failure. In other words, the steady state error will be reduced since the asymmetry is not only limited but minimized.

In addition, both flaps may be stopped in case of emergency without a previous position asymmetry reduction. In this case, the active monitoring techniques behave as the passive models.

- *Demand input signal.* The asymmetry monitoring techniques behave differently depending the demand input signal. In any case, the *command input Com* is always a step signal that starts on the flap initial position and arrives to the commanded position. On the other hand, the demand input *Dem* is the signal with which the control surfaces reaches the commanded position. In other words, the demand input signal defines the *path* that the control surfaces follow to reach the command step input signal, ergo the flap commanded position.

This distinction is characteristic of the active monitoring techniques. The two different demand input signals studied in this project are:

- *Step input signal.* The demand input signal will be identical to the command input signal $Dem = Com$.
- *Ramp input signal.* The demand input signal will tend to the command input signal following a ramp input signal. Consequently, the control surface deflection will be slower but more controlled, since the ramp input is determined by a maximum *ramp slope*, which is empirically defined and limits the flap maximum deflection speed, as follows:

$$Dem = \min \left[\max \left(Dem - \frac{d Dem}{dt} \Big|_{max}, Com \right), Dem + \frac{d Dem}{dt} \Big|_{max} \right] \quad (4.1)$$

- *Asymmetry measurement.* It is the way in which the asymmetry is measured using the electric positions $\theta_{E,i}$. In this regard, the monitoring techniques can be:
 - *Differential position monitoring techniques.* They use the difference between both flap position to define the asymmetry failure condition. Once this

⁴Note that the new versions of the passive asymmetry monitoring techniques differentiate between the failure side, improving the asymmetry limitation, as well as the aircraft roll performance after failure.

difference exceeds a certain threshold, the asymmetry failure condition is met.

- *Relative position monitoring techniques.* They use the flap position with respect to a common reference position to define the asymmetry failure condition. The reference position will depend on the demand input signal. Analogously to the previous case, once this difference exceeds a certain threshold, the asymmetry failure condition is met.

These two will be discussed in detail in section 5.2.

4.2 Monitoring device essential components

The monitoring device monitors the control surfaces position and commands the flap braking in case the asymmetry failure condition is met.

The monitoring device essential components are:

- The control unit (ECU). It controls the surfaces.
- The angular position transducers (RVDT). The final RVDT number will be discussed below.
- Both the solenoid and the shutoff valve, with which the control unit can be stopped braking the control surfaces if necessary.

Further consideration should be given to the angular position transducers (RVDT final number and disposition).

The position transducers final number is determined by:

- The system redundancy.
- The control surface speed monitoring criteria. As discussed in section 1.3, the flap asymmetry speed can be obtained installing additional transducers. Nonetheless, a numerical integration of the electrical transducers output signal is chosen since no significant disadvantages will result from it while guaranteeing an acceptable system reliability for a given effective system redundancy.

On the other hand, the position transducers may be disposed in different ways:

- a. Placed both in the PDU, connected with the surface (slow) shaft, and at the end of the transmission line, which will work as “asymmetry indicators”. This disposition meets the secondary flight controls stability requirement while simplifying the asymmetry monitoring technique logics. In effect, this is a closed loop configuration that can detect the control surfaces angular position, helping the asymmetry detection. Nonetheless, this design philosophy will increase excessively the RVDT final number for a given effective system redundancy.
- b. Placed at the end to the transmission line to close the loop, renouncing to the PDU position transducers. This RVDT disposition complicates the asymmetry monitoring logics but increases the system reliability for a given effective system redundancy. Nevertheless, the control surfaces actuators will not be monitored, since the the position transducers will be placed upstream of the actuators installation point.

This system architecture is acceptable since mechanical system critical braking point is the drive shaft torsion bar, which is inside the closed loop, so it will be monitored. In addition, the actuators failures happen to be less critical than the drive shaft failure.

The aforementioned monitoring device should be governed by a dedicated software which should differentiate between all the possible control surface failures listed above in section 4.1 in order to optimize the monitoring action. However only the transmission line failure and the final control surface actuators wear are considered in this project.

As mentioned in section 1.1, both a complete and symmetrical control surfaces deflection is necessary on those flight phases in which the high-lift devices are essential: *take off* and *landing*.

It should be said that all the asymmetry monitoring techniques logics include certain *asymmetry counters*. These counters increase in case the *asymmetry threshold* is exceeded and decrease in case the flap asymmetry drops under the aforementioned threshold. In other words, the asymmetry counters measure the *time that a certain asymmetry condition is verified*.

Follow a general overview of the asymmetry monitoring techniques developed in the past, which were the reference models to entirely develop the asymmetry active monitoring techniques described in section 5.3.

4.3 Passive reference monitoring techniques

The asymmetry passive monitoring techniques are those that detect the flap position asymmetry without identifying the failure side. Hence, the asymmetry corrective maneuver consists in braking both control surface once the asymmetry failure condition is met.

There are two main passive monitoring techniques design philosophies developed in the past. These are discussed below.

4.3.1 Passive monitoring technique 1: differential position control

In general, the passive asymmetry monitoring techniques named as “1”, establish the asymmetry failure condition once any flap electrical position exceeds a position asymmetry threshold, which is empirically set, during a certain time, measured by a specific *time counter*. The passive model 1 is based on a differential position step-input control logic.

Should the flaps present a position asymmetry during the empirically prefixed time, the wingtip brakes would stop the *both* flaps to both limit the asymmetry and prevent it from increasing. This flaps braked conditions will be maintained during the rest of the flight, which means that the system position steady state error will be high and constant. In other words, the flap asymmetry condition will be limited and constant but not reduced during the rest of the flight, which induces significant rolling moments that should be compensated with the corresponding aileron deflection, reducing the aircraft maneuverability after failure.

The more developed differential position control algorithms, named as 1A, differentiate the failure side, which improves the behaviour of the passive model type “1”, as well as the aircraft roll performance after failure. This is possible on ramp-input models, since they use the demand input signal Dem as a common reference position to identify the failure side. Thus, the passive model 1A is based on a relative position ramp-input control logic.

4.3.2 Passive monitoring technique 2: differential position & speed control

The main difference between the *differential position and speed* passive control (type “2”) and the *differential position* passive control (type “1”) is that the former introduces the failure surface speed inside the asymmetry algorithm logic. In effect, either a position asymmetry or a “speed asymmetry” may cause the asymmetry failure condition declaration.

The passive asymmetry models type “2” behave similarly to the previous models in terms of both the asymmetry detection and the asymmetry failure condition verification. In effect, this condition is again determined by an empirically set electrical position asymmetry threshold, which should be exceeded during a certain time, (measured by a specific *time counter*) to declare the failure condition. Analogously to the previous passive model type, the model 2 are based on a differential position step-input control logic.

However, the main problem of the passive model 2 is the “speed asymmetry” failure declarations when the system still does not present a flap “position asymmetry”. This may occur in some particular operating scenarios with considerably high aerodynamic loads which might cause a fast failure flap retraction. This effect is called *position asymmetry anticipation*, which is the main disadvantage of model 2.

In this case, the more developed monitoring techniques of this kind, named from 2A to 2E, present one of the following improvements:

- a. Analogously to the previous passive model improvements, some of them differentiate the failure side, which improves the behaviour of the passive model type “1”, as well as the aircraft roll performance after failure.
- b. Some model improvements give preference to the position asymmetry over the “speed asymmetry” when defining the asymmetry failure condition. These would improve the model 2 behaviour when failure under high aerodynamic loads, as discussed above. In fact, these models take advantage of the *position asymmetry anticipation* effect, which is introduced to anticipate the position asymmetry failure declaration and start the flap braking maneuver earlier.

These will be the first *dynamic position* active monitoring techniques, which will be deeply discussed in section 5.2.2 regarding the new asymmetry active monitoring techniques, which have been both entirely developed and widely tested in this project.

4.4 Active reference monitoring techniques

As discussed above, the asymmetry active monitoring techniques both detect and identify the failure side, after which the flap position asymmetry will be minimized: the

asymmetry failure is detected and corrected (minimized) regarding always the failure side. This is possible by means of specific asymmetry counters that, similarly to what discussed on the passive asymmetry models, that measure the “time” in which the position asymmetry threshold has been exceeded. Should the counter increase over a certain empirical threshold, the asymmetry failure is declared.

Nonetheless, the main difference between the active and the passive monitoring techniques is the asymmetry correction after the failure declaration. While the passive techniques brake both control surface in case of failure, maintaining large current asymmetries, the active techniques minimize the flap position difference on steady state.

To that end, the failure surface is braked once the asymmetry failure is declared. Meanwhile, the operative flap is commanded to reach the failure surface position. In other words, the operative surface new command input will be the failure surface braked position $Com = \theta_{E,i}$, where i identifies the failure side: either left or right. Thus, the flap position asymmetry on steady state will be minimized, and so will be the position error, since the average electrical position $\theta_{E,av}$ that defined it will become the failure surface braked position:

$$\epsilon = Dem - \theta_{E,av} \quad (4.2)$$

while

$$\theta_{E,av} = \begin{cases} \frac{\theta_{E,L} + \theta_{E,R}}{2} & \text{if } t < t_f \\ \theta_{E,i} & \text{if } t > t_f \end{cases} \quad (4.3)$$

This positiona symmetry failure correction will be discussed when the new active asymmetry monitoring techniques will be deeply discussed and tested.

All these was implemented on model 3 and its variants 3A and 3B.

In particular, the first two active models, both 3 and 3A, consider a position asymmetry, while 3B also considers the “speed asymmetry” variant. Moreover, the model 3 is a differential position step-input, while both 3A and 3B present relative position step-input control logics.

The reference active monitoring techniques for this project are both the active model 3 and 3A, since the *new* active monitoring techniques developed in this project are position-based. Therefore, the active model 3B was not considered.

Nonetheless, both 3 and 3A present significant deficiencies in their position asymmetry control algorithms, especially the active model 3, which always declare a *left* failure, regardless the real failure side. These definciciencies will be discussed in the following sections.

In this project four *new* asymmetry active monitoring techniques have been developed from zero, which correct the behaviour deficiencies that both 3 and 3A present, while improving considerably the monitoring system performance, as well as the aircraft lateral-directional dynamics. Such improvements will be both discussed and tested from the next section.

4.5 Non-asymmetry system failures

The system monitoring logic was developed to detect further system failures apart from those that regard the flap asymmetry. These will not be studied in detail in this project. Nonetheless, a general overview can be found below.

In effect, the monitoring algorithm logic can also manage the two system failures that do not concern the flap asymmetry, discussed above in section 4.1.

- *Wingtip brakes failure*
- *Power plant failure.*

4.5.1 Wingtip brake system failure

The wingtip brakes failure does not necessarily cause flap position asymmetry but it may affect the aircraft flight operation, or even compromise the flight safety on certain extreme conditions.

The wingtip braking system may fail due to wear and tear conditions or high thermal loads, among others.

The braking system failure concerns the flight controls with reversible actuators. In particular, this kind of failures might be:

- a. *Latent.* The braking system failure arises while both flaps are being deflected towards the commanded position. Hence, the failure is not detected until the wingtip brakes try to stop the control surfaces and these do not maintain a fixed position.
- b. *Evident.* The braking system cannot fix the control surfaces position, which varies when no input has been commanded. Hence, the failure is detected when either one or both control surface do no maintain a constant position. In particular, a specific counter will be increased in case the flaps position differ significantly from the braking position. The evident wingtip brake system failure will be declared in case the aforementioned counter exceed certain empirical threshold. The monitoring system shall reactivate the hydraulic system which will be operative during the rest of the flight, since the wingtip brakes cannot maintain the flap position.

4.5.2 Insufficient servovalve supply pressure failure

The servovalve supply pressure P_{SV} is always monitored by a specific pressure transducer. Should P_{SV} drop under the minimum permissible (critical) servovalve pressure $P_{SV,c}$, a specific pressure counter increases. Analogously to the asymmetry failure procedure, the insufficient servovalve supply pressure failure will be declared if the pressure counter exceeds a certain empirical threshold.

Once the pressure failure is declared, the mechanical system will be depressurized by closing the shutoff valve. This will activate the wingtip brakes that stop the control surfaces.

On the contrary, it will decrease should the P_{SV} exceeds the minimum pressure $P_{SV,c}$. This may happen if the P_{SV} drops under the critical pressure for a short time, which happens when too many utilities should be contemporaneously managed.

In case of pressure failure, the hydraulic system will be depressurized and reactivated after some time. This procedure will be repeated until either acceptable levels of P_{SV} are maintained or the pilot depressurizes the hydraulic system manually.

5 New asymmetry active monitoring techniques

5.1 Introduction to the new active monitoring techniques

The active monitoring techniques improve the type 1 and 2 monitoring techniques performances since they both limit the asymmetry between the both flaps and distinguish which surface presents the failure. Once identified which transmission is broken, the corresponding flap is braked and a new command governs the motion of the operative surface so as to reach the position of the inoperative one. Thus, the asymmetry is significantly reduced and little aileron deflection is used to correct the eventual asymmetry produced by the failure.

Once the operative flap reaches the failure flap electrical position, the braking system stops the flap motion during the rest of the simulation. This is one of the reasons why the asymmetry should be minimized, since the ailerons would have to compensate indefinitely the rolling moment and the aircraft, and the aircraft maneuverability might be compromised.

It should be noted that both the passive and the active asymmetry monitoring techniques share the following assumptions:

- The aerodynamic surfaces are considered infinitely rigid. Hence, no aeroelastic effects such as divergence, control reversal and flutter, would be considered.
- Linear aerodynamics. The nonlinear aerodynamic effects, such as stall or wing-tip vortex, and the nonlinear formulation would be dismissed.

The new active monitoring techniques exploit all the benefits of the old active models and improve the code to correct the main errors that take place in certain ambiental and failure conditions.

Different active monitoring techniques have been tested and analyzed considering the following factors:

- Asymmetry confirmation time: should a failure take place on any surface, the asymmetry confirmation time is an important parameter. This time should not be too small since false failures would not be detected, so those would be considered as real system failures. It is measured by means of an increasing counter on the code. Moreover, the confirmation time should not be too big to prevent from big surface position shifts, especially when big torque constant component is applied. The false failure declaration may be the result of:
 - Electric power line disturbances: disturbances of electromagnetic nature could cause a momentary asymmetry (milliseconds). These could load the counter so, once the disturbances disappear, the counter should be unloaded.
 - Aerodynamic torque perturbations: punctual variation of the aerodynamic loads applied to the system may cause a momentary asymmetry, even though no failure has been produced. Similarly, the “time counter” should be unloaded whenever the torque perturbation disappears.

The asymmetry confirmation time can be seen as a failure declaration delay Δt_{fail} . In effect, from this perspective it would measure the time between

the asymmetry declaration and the beginning of failure surface braking correction. As mentioned in section 1.3, this is possible by means of a *partial or general asymmetry counter* before it reaches a certain asymmetry threshold, together with the integration time step $\Delta\tau$. In effect, $\Delta t_{fail} = \frac{N}{\Delta N} \cdot \Delta\tau$ after failure but before its detection, where N is the number of steps of the counter and ΔN is the step increment/decrement, a design parameter empirically set.

- Asymmetry anticipation time $T_i S_y$: characteristic time that allows to anticipate the asymmetry failure detection on certain active monitoring techniques. In fact, it is the “weight” of the *speed term* (also called *anticipation term*) that conforms the so-called *dynamic position* which anticipates the asymmetry failure declaration allowing an earlier correction on certain active models (see section 5.2.1).

In addition, it seems evident that the asymmetry anticipation time $T_i S_y$ affects the failure declaration delay. In effect, $T_i S_y$ anticipates the *asymmetry failure condition* verification, which is different in each active model. In consequence, this anticipates the moment in which the *asymmetry counter* starts increasing, which reduces the asymmetry confirmation time. This leads to an anticipated failure flap braking action for a given failure instant without varying the design parameter ΔN but anticipating the *asymmetry failure condition* verification.

- Deceleration time, t_{dec} : regarding the inoperative surface, it measures the time between the power shut off and the braking instant. In other words, it measures the time necessary to brake the surface after the failure declaration delay. It the time-evolution of the servo-valve hydraulic parameters.
- Braking time after failure, t_{br} : it is braking time once the asymmetry failure arises. It can be mathematically expressed as $t_{br} = t_{dec} + \Delta t_{dec}$. It is used in the following sections to analyze the *efficiency* of the asymmetry active monitoring techniques.
- Resistive torque: torque applied on the surface that should be overcome by the hinge moment to properly extend or retract the flap. It represents the aerodynamic torque on the aerodynamic surface. Only the *constant* component of the resistive torque T_{RC} has been considered in this work which notably simplifies the simulations and the results and allows to better understand the asymmetry problem, even though these might not be realistic. The resistive torque is the basis to design the dynamic position asymmetry active monitoring techniques (see subsection 5.2).

5.1.1 Resistive constant torque considerations

It should be noted that considering constant the resistive (aerodynamic) torque is far from reality since, in general, the aerodynamic torque does not remain constant when extending/retracting the flaps. Indeed, let consider a representative wing section with a control surface of its leading edge. Considering linear aerodynamics, the aerodynamic torque may be written in its asimensional form as:

$$C_m = C_{m_0} + C_{m_\alpha}\alpha + C_{m_\theta}\theta \quad (5.1)$$

where $C_{m_\alpha} < 0$ to guarantee the static stability of the aircraft and $C_{m_\theta} < 0$ on regular NACA aerodynamic profiles, where θ is the control surface deflection angle. Hence,

if the aerodynamic torque is constant, C_m remains constant whilst δ varies, either growing if extending or decreasing if retracting the flap. Hence, the function $C_{m\alpha}\alpha + C_{m\theta}\theta = f(\alpha, \theta)$ should be constant, which is only verified for a negative angle of attack α that is never achieved during any flight phase.

Since this might not occur during an extending/retracting flap maneuver, the simulation results would not be realistic. However, a constant moment dimensionless coefficient C_m is interesting to study in a first approximation what would it be the controlling system response when varying the aerodynamic torque on the surface, as commented before.

Four innovative active monitoring techniques have been developed, either with step or ramp input analyze the effect of such element inside the control law. However, new control aspects were introduced in relation to previous active monitoring techniques developed in the past in order to improve the monitoring performance.

An interesting approach for future research projects may be the analysis of the system response with a time-dependant resistive torque (according to a ramp function, for instance).

The new asymmetry active monitoring techniques are divided in two categories according to:

1. Input signal: it could be a step demand or a ramp demand to follow the command set by the user. In this work, only constant commands to be reached by step or ramp demand signals were considered. It may be interesting in future research projects to study how the system would respond to a time-dependant command (according to a ramp or sinusoidal function, for instance).
2. Position anticipation or *dynamic position*: the system may include an extra position term called “anticipated electrical position” added to the actual electrical position.

5.2 Position anticipation or *dynamic position*

5.2.1 Non *dynamic position* active monitoring techniques

Regarding the asymmetry active monitoring techniques without a *dynamic position* logic, the algorithms always use the surface relative electrical position in relation to a common position reference to detect eventual asymmetry failure conditions. This is done comparing the relative position reference of either the left or right surface with a *angular position threshold* $\Delta\theta_E$ which in earlier works was empirically set as $\Delta\theta_E = 0.02 \text{ rad}$. As described further on, whenever the position threshold is exceeded, the asymmetry is declared.

This marks an improvement respect the *passive* asymmetry monitoring techniques, in particular the *differential position control techniques* (models 1 and 1a), from which these *active* non dynamic position models come. Whereas the *passive* techniques use a differential position logic to detect the asymmetry failure conditions, the *active* models use a relative position based algorithms which reference position is common both for the left and the right surface.

Since *active* non dynamic position models introduce the relative position in their algorithms, there will be named as ***relative position control techniques***.

5.2.2 *Dynamic position active monitoring techniques*

The anticipated position, which could also be named as *dynamic position*, is calculated by means of the first derivative of the differential position ($\theta_M Z_M Z_S - \theta_i$) and the mathematical expression changes depending on the input signal.

In particular, the position anticipation term of the *dynamic position* is useful in high constant resistive torque scenarios T_{RC} , in which the failure surface reaches very high retraction speeds. In those cases, it is essential to anticipate the asymmetry failure declaration as soon as possible before the inoperative flap reaches an excessively retracted braking position after failure $\theta_i(t = t_{br})$. Consequently, the failure surface speed should be considered in the active model algorithm in order to anticipate the asymmetry failure declaration that activates the braking system before the surface accelerates excessively.

It should be noted that the position anticipation term should be expressed as a position magnitude. Since it is calculated with using the differential velocity, a reference time magnitude is needed in the *dynamic position* expression. As considered in previous *passive* monitoring techniques, in particular on the *differential dynamic position control technique* (model 2C), the *asymmetry anticipation time* $T_i S_y$ was used. As previously mentioned, $T_i S_y$ is the characteristic time that allows to anticipate the asymmetry failure detection on certain active monitoring techniques, in particular those that include the *dynamic position* logic.

Notice that the differential dynamic *active* model shares the time $T_i S_y$ with its corresponding passive monitoring technique and the main difference between both models lies in the speed calculus. In effect, the *active* model always refers to the ***relative speed*** by means of a common velocity for both the left and right flap instead of calculating the ***differential speed*** of both flaps.

In a similar fashion to the previous case, in order to detect eventual asymmetry failure conditions, the algorithms compare the relative dynamic position reference of either the left or right surface with the same *angular position threshold*, empirically set as $\Delta\theta_E = 0.02 \text{ rad}$. Similarly, whenever the position threshold is exceeded, the asymmetry failure is declared.

Since the anticipating position *active* models consider the relative velocity to calculate the dynamic position, there will be named as ***relative dynamic position control techniques***.

However, the anticipation logic does not always behave as expected. In regard to how the variations of the constant component of the resistive (aerodynamic) torque T_{RC} may affect the system response, two different scenarios might be considered: *high* T_{RC} and *low* T_{RC} .

On the one hand, if T_{RC} is small enough (no big friction forces considered)⁵, the *dy-*

⁵Big friction forces will be considered with *worn out actuators* in sections 8 and 9

dynamic position reduces the dynamic stability of the entire system. In some cases, this may cause a limit cycle of the electric current Cor current that feeds the servo-valve, affecting the engine rotating speed $\dot{\theta}_M$. In consequence, the electrical and real surface position will also suffer from such dynamic limit cycle.

On the other hand, if T_{RC} is big, a dynamic position logic is needed to anticipate the corrective action on the failure surface before it reaches high retraction non-commanded speed values due to the aerodynamic torque. Thus, the dynamic position should be composed by the failure speed to increase the relative position term and anticipate the corrective action.

Hence, in order to active or cancel the dynamic position effect, this kind of active monitoring techniques include a control parameter ξ . It is a boolean variable that activates or cancels the position anticipating term according to T_{RC} .

Thus, the boolean ξ is empirically set as follows:

$$\xi = \begin{cases} 0 & \text{if } T_{RC} < T_{RC}^{thr} \text{ Nm} \\ 1 & \text{if } T_{RC} \geq T_{RC}^{thr} \text{ Nm} \end{cases} \quad (5.2)$$

where T_{RC}^{thr} is the aerodynamic constant torque threshold to activate/deactivate the anticipating term.

Several cases have tested with different active monitoring techniques that include the anticipation logic (no big friction forces considered), varying the demand input (step/ramp and extraction/retraction) and failure surface(left/right). The threshold empirically established for the resistive torque is $T_{RC}^{thr} = 4000 \text{ Nm}$, over which no instability effects appear(no big friction forces considered).

In fact, the control parameter ξ is activated when the aerodynamic load is “high enough”. Such load is empirically set considering an aircraft speed V and angle of attack α that lead to a high T_{RC} (linear aerodynamics may be considered in a first approximation). It may cause high retraction surface speeds in case of flap failure, so the *dynamic position* is required to both detect and correct the asymmetry failure.

It should be noted the control remains *proportional* (P control), since the control output is proportional to the error signal ϵ . In fact,

$$Cor = G_A \cdot \epsilon \quad (5.3)$$

where Cor is the output electric current, which is the result of the amplified error signal ϵ with the current gain G_A .

Furthermore, the position error could be written as:

$$\epsilon = Dem - \theta_{E,av} \quad (5.4)$$

where $\theta_{E,av} = \frac{\theta_{E,L} + \theta_{E,R}}{2}$ is the average electrical position.

However, the *dynamic position* considers a speed loop activated with the control parameter ξ . This entails an overall proportional control logic enhanced with an extra

speed component in the position loop. Hence, this might be a *proportional speed control* “PS”. In fact, the *asymmetry anticipation time* $T_i S_y$ works as a proportional speed control gain, *weighing* the effect of the speed term inside the *dynamic position* logic.

A deep comparison between the different active monitoring techniques will be performed in the following pages. The improvements achieved with these new active monitoring techniques will be described in relation to the active models developed in the past and the passive techniques.

It should be noted that the following asymmetry active monitoring models have been entirely designed on this project. The main characteristics and improvements of these seek to solve the main problems of the past models as well as exploiting their benefits.

5.3 New active monitoring algorithms

In this section, the completely new asymmetry active monitoring techniques developed on this project are explained regarding the control algorithm. The simulation results will be discussed in the following sections.

It should be noted that both the angular position and the angular speed variables used to develop the new active models are *electrical* magnitudes, measured by the electrical angular position transducer. Consequently, the electrical position may slightly differ from the real (physical) position but they are close to one another. The electrical speeds are obtained by a numerical integration of the electrical positions.

Nonetheless, the simulation results are mainly plotted using real (physical) magnitudes, since these represent the real time output of the system. This is because the system time response will be evaluated according to physical variables. In effect, both the aircraft rolling response and the maneuverability after failure make use of the physical position.

Therefore, the electrical variables are only used by the asymmetry active monitoring techniques to both detect and correct the eventual asymmetry problems, but the dynamic system response makes use of the physical magnitudes that are calculated from the external torques applied on the surfaces (mechanical, resistive (aerodynamic)...).

This is why the *electrical* suffix will only be written in this section. From section 6, in which the time results of the active models will be discussed on different operating conditions, it should be borne in mind that those *positions* and *speeds* would be electrical magnitudes if they refer to the control algorithms of the active models.

5.3.1 Step-input relative position control technique - model 3

The model 3 is the most basic step input active monitoring technique. It was developed to both detect the failure surface and to activate the braking system of the inoperative surface when a failure happens. This model improves the previous model 3 which always considered the left failure, regardless the particular case study. The new developed model improves the control algorithm behaviour since it both detects the failure side and corrects it, regardless whether the failure arise either on the left or the right surface.

Firstly, the partial asymmetry detection differentiates between left and right failure

with the following logic.

$$\left. \begin{array}{l} |\theta_M Z_M Z_S - \theta_{E,i}| > |\theta_M Z_M Z_S - \theta_{E,j}| \\ |\theta_M Z_M Z_S - \theta_{E,i}| > \Delta\theta_E \end{array} \right\} \mathbf{i \text{ surface failure}} \quad (5.5)$$

$\forall i = 1, 2$ where i stands for *left* and *right* surface respectively.

Whenever this condition is met, either for the left or the right surface, the *partial asymmetry counter* $I_{W_{rn},i}$ increases. When it reaches $I_{W_{rn},i}^{thr}$ ⁶, the *partial asymmetry indicator* I_{A_i} is activated. This is a boolean variable set as 1 “on” or 0 “off” whether there is a failure or not.

Here there is the main advantage regarding the previous version of this active monitoring technique, since the partial asymmetry could be identified and declared both on the left and right surface.

However, the system failure architecture only manages one partial failure on one surface, either left or right, in order to set the failure surface position as the new command for the operative flap. Furthermore, its logic is *exclusive with left reference*, which means that if both partial indicators are active, the reference to become the new position command will always be given to the left surface (see section 7). These two aspects might lead to an inappropriate behaviour in case both surfaces fail.

Another great improvement of model 3 is the introduction of a *general asymmetry detection logic*, which was conceived to solve the eventual multiple failure problem. In general, this extreme condition may not be met in step-input models but on some borderline cases can be crucial, especially on right failure scenarios with a ramp-input model (see model 3C in 5.3.3). Borderline cases will be deeply analyzed in section 7. This relevant logic states the following:

$$\left. \begin{array}{l} |\theta_M Z_M Z_S - \theta_{E,i}| > \Delta\theta_E \\ |\theta_M Z_M Z_S - \theta_{E,j}| > \Delta\theta_E \end{array} \right\} \mathbf{i \text{ surface failure}} \quad (5.6)$$

$\forall i = 1, 2$ where i stands for *left* and *right* surface respectively.

This algorithm manages the general asymmetry scenario as *independent* from both partial asymmetry cases, which makes the model more robust and reliable (as shown on borderline cases in subsection ??).

Similarly, whenever this condition is met, the *general asymmetry counter* $I_{W_{rn}}$ increases and when it reaches $I_{W_{rn}}^u$ ⁷, which doubles the *partial asymmetry counter* to ensure that no false failure declaration cause the emergency situation. Again, once such threshold is reached, the *general asymmetry indicator* I_A is activated in case of failure.

Nonetheless, it should be reiterated that both counters could be unloaded if the asymmetry failure conditions are not maintained during the entire asymmetry confirmation time, which dismisses any false declaration due to an electrical or aerodynamic punctual perturbation.

⁶ $I_{W_{rn},i}^{thr}$ is the partial asymmetry upper counter threshold, empirically set as $I_{W_{rn},i}^{thr} = 5000$

⁷ $I_{W_{rn}}^{thr}$ is the general upper asymmetry counter threshold, empirically set as $I_{W_{rn}}^{thr} = 10000$

Moreover, as the algorithm shows, no position anticipation is considered in this model.

5.3.2 Step-input relative dynamic position control technique - model 3D

The model 3D is a variation of the previous model 3 that introduces the position anticipation term in the monitoring technique logic. Hence, it both improves the surface failure detection with the dynamic position term and activates the braking system of the inoperative surface when a failure happens.

In regard to the partial asymmetry detection, the algorithm includes the position anticipation term as follows:

$$|\theta_M Z_M Z_S - \theta_{E,i}| + \xi \left(\dot{\theta}_M Z_M Z_S - \dot{\theta}_{E,i} \right) T_i S_y > \Delta\theta_E \implies \mathbf{i \text{ surface failure}} \quad (5.7)$$

$\forall i = 1, 2$ where i stands for *left* and *right* surface respectively.

As with model 3, whenever this condition is met, either for the left or the right surface, the *partial asymmetry counter* $I_{Wrn,i}$ increases. When it reaches the threshold $I_{Wrn,i}^{thr}$, the *partial asymmetry indicator* I_{Ai} is activated.

Here there is the main advantage regarding the previous version of this active monitoring technique, since the partial asymmetry failure could be identified and declared both on the left and right surface.

On the other hand, similarly to the previous case, a *general asymmetry* detection logic, independent of the *partial asymmetry* logic, was added to the control algorithm in order to prevent from a multiple surface failure. It brings excellent benefits in terms of system stability and robustness. The algorithm states the following:

$$|\theta_M Z_M Z_S - \theta_{E,i}| + \left(\dot{\theta}_M Z_M Z_S - \dot{\theta}_{E,i} \right) T_i S_y > \Delta\theta_E \implies \mathbf{i \text{ surface failure}} \quad (5.8)$$

$\forall i = 1, 2$ where i stands for *left* and *right* surface respectively.

Regarding both the dynamic stability of the system under “low” constant resistive (aerodynamic) torques and the use of the resistive torque threshold, empirically established as $T_{RC}^{thr} = 4000Nm$, they will be discussed at the end of section 5.4.

Note that no control parameter was used in the general failure algorithm, which is always set $\xi = 1$. Whereas the partial asymmetry detection needs such parameter to stabilize the position dynamics downstream the failure time according to the applied aerodynamic torque, no control parameter is needed in case of a general failure. In fact, the braking system stops any surface motion once the failure is detected so no dynamic instability is expected.

Furthermore, the position anticipation term should always be active to brake as soon as possible both flaps, preventing serious asymmetry consequences during the rest of the flight.

5.3.3 Ramp-input relative position control technique - model 3C

The first ramp-input asymmetry monitoring technique is the model 3C, which is considered the most simple of its kind since no anticipation logic (speed loop) is considered.

The model 3C derives from the active model 3A, which is significantly improved by the introduction of a *general failure* routine with which the system behaves correctly in case of multiple failure (see 7.4). This catastrophic scenario could either be produced by a mechanical failure or an detrimental *partial failure* correction (see subsection ??).

Again, 3C manages the general asymmetry scenario as *independent* from both partial asymmetry cases, which makes the model more robust and reliable (as shown on borderline cases in section 7).

As with the case 3, the partial asymmetry detection differentiates between left and right failure with the following logic:

$$\left. \begin{array}{l} |Dem - \theta_{E,i}| > |Dem - \theta_{E,j}| \\ |Dem - \theta_{E,i}| > \Delta\theta_E \end{array} \right\} \mathbf{i \ surface \ failure} \quad (5.9)$$

$\forall i = 1, 2$ where i stands for *left* and *right* surface respectively.

Analogously, should this condition is met, $I_{Wrn,i}$ increases and the asymmetry failure is declared if $I_{Wrn,i} = I_{Wrn,i}^{thr}$ ⁸

In regard to the *general asymmetry* detection logic, also conceived to solve the multiple failure problem, the algorithm is:

$$\left. \begin{array}{l} |Dem - \theta_{E,i}| > \Delta\theta_E \\ |Dem - \theta_{E,j}| > \Delta\theta_E \end{array} \right\} \mathbf{i \ surface \ failure} \quad (5.10)$$

$\forall i = 1, 2$ where i stands for *left* and *right* surface respectively.

Similarly, whenever this condition is met, the *general asymmetry counter* I_{Wrn} increases and when it reaches I_{Wrn}^{thr} ⁹, which doubles the *partial asymmetry counter* to ensure that no false failure declaration cause the emergency situation. Again, once such threshold is reached, the *general asymmetry indicator* I_A is activated in case of failure.

Nonetheless, it should be reiterated that both counters could be unloaded if the asymmetry failure conditions are not maintained during the entire asymmetry confirmation time (which dismisses any false asymmetry failure declaration).

The main difference between the active models 3C and 3 is the kind of input signal they manage, which plays an important role in monitoring and declaring the asymmetry failure. Whereas on model3 $Dem = Com$, on model3C Dem tends to the Com following a fixed linear path defined by a prefixed *ramp slope*. Hence, the ascending/descending trajectory of each surface is much more restricted to the desired path which, in general, leads to a better asymmetry control, especially under failure conditions.

⁸ $I_{Wrn,i}^{thr}$ was empirically set as $I_{Wrn,i}^{thr} = 5000$, as on model3

⁹ I_{Wrn}^{thr} was empirically set as $I_{Wrn}^{thr} = 10000$, as on model3

5.3.4 Ramp-input relative dynamic position control technique - model 3E

The model 3E, is a variation of the previous model 3C considering the *dynamic position*, analogously to model 3D, improving the surface failure detection favouring a quick response of the braking system when a failure happens.

Similarly to model 3D, the partial asymmetry detection algorithm was conceived as follows:

$$|Dem - \theta_{E,i}| + \xi \left(\frac{d Dem}{dt} - \dot{\theta}_{E,i} \right) T_i S_y > \Delta \theta_E \implies \mathbf{i \text{ surface failure}} \quad (5.11)$$

$\forall i = 1, 2$ where i stands for *left* and *right* surface respectively

It should be noted that $\frac{d Dem}{dt}$ is the ramp *slope*, essential in ramp-input models. The model lets the ramp slope vary between zero to a maximum ramp slope, which is empirically set as $\left| \left(\frac{d Dem}{dt} \right)_{max} \right| = 0.1 \text{ rad/s}$.

As with model 3, whenever this condition is met, either for the left or the right surface, the *partial asymmetry counter* $I_{Wrn,i}$ increases. When it reaches the threshold $I_{Wrn,i}^{thr}$, the *partial asymmetry indicator* I_{Ai} is activated. This is the main advantage regarding the previous version of this active monitoring technique, since the partial asymmetry failure could be identified and declared both on the left and right surface.

Similarly, to prevent the multiple surface failure problem, a *general asymmetry detection logic*. This complementary logic states the following:

$$|\theta_M Z_M Z_S - \theta_{E,i}| + \left(\dot{\theta}_M Z_M Z_S - \dot{\theta}_{E,i} \right) T_i S_y > \Delta \theta_E \implies \mathbf{i \text{ surface failure}} \quad (5.12)$$

$\forall i = 1, 2$ where i stands for *left* and *right* surface respectively.

As mentioned on model 3D, no control parameter was used in the general failure algorithm, which is always set $\xi = 1$ (see subsection 5.3.2).

5.4 The *Slow* parameter

The *Slow* parameter is a boolean that stops the engine when the *partial asymmetry counter* $I_{Wrn,i}$ reaches a certain value after a failure that is not yet detected. This helps to prevent the operative surface from an over-acceleration when correcting the asymmetry once the failure occurs and this is why this parameter is only considered with *active* asymmetry monitoring techniques under *high load* conditions.

In particular, $Slow = 1$ when there is no failure. whenever $I_{Wrn,i}$ reaches certain new threshold $I_{Wrn,i}^{thr,S} < I_{Wrn,i}^{thr}$,¹⁰ the *Slow* parameter becomes zero, deactivating the current *Cor* that drops to zero instantaneously which progressively stops the engine. Meanwhile, $I_{Wrn,i}$ continues increasing and when $I_{Wrn,i} = I_{Wrn,i}^{thr}$ the *partial asymmetry indicator* is activated $I_{Ai} = 1$ and *Slow* parameter becomes 1 again. From that moment on, the current *Cor* is reactivated and the engine lets the operative surface reach the failure flap, which is braked by then.

¹⁰The new threshold $I_{Wrn,i}^{thr,S}$ was empirically set as $I_{Wrn,i}^{thr,S} = 1000 < I_{Wrn,i}^{thr}$

$$Slow = \begin{cases} 1 & \text{if } I_{Wrn,i} < I_{Wrn,i}^{thr,S} \oplus I_{Wrn,i} \leq I_{Wrn,i}^{thr} \\ 0 & \text{if } I_{Wrn,i}^{thr,S} \leq I_{Wrn,i} < I_{Wrn,i}^{thr} \end{cases} \quad (5.13)$$

Should the *Slow* parameter do not “shut” the electric current *Cor*, the correction maneuver would ead to an over-acceleration of the operative surface when trying to reach the failure surface on a non-braked position, fastly retracting due to the effect of the high aerodynamic forces. The consequences could be catastrophic when $I_{Ai} = 1$ and the braking system stops the failure surface given that the extremly high velocity of the operative surface would not let it stop on the filure surface position but continue retracting, which might cause a *second failure* scenario that the asymmetry algorithm cannot manage properly.

In regard to the dynamic stability of the system under “low” constant resistive (aerodynamic) torques T_{RC} , always present in the active model *3D*, eventual limit cycles may arise on *dynamic position* active models. The inoperative surface would not speed up after failure under low resistive torques, since the friction would stop it almost immediately, becoming $\dot{\theta}_{fail}(t > t_f) = 0$. Consequently, the dynamic system response would be slower under “low” constant resistive (aerodynamic) torques, so the speed term of the position control logic will not be necessary. In fact, speed control may cause dynamic instabilities in slow dynamic systems.

In particular, the *Slow* parameter may either become 1 in case of high $\dot{\theta}_M Z_M Z_S$ or 0 when in case of low $\dot{\theta}_M Z_M Z_S$. This flipping between 0 to 1 activates and deactivates the electric current *Cor* of the valve, which may cause a limit cycle of the engine speed time output that affects both the electrical and physical surface angular positions.

Fortunately, the control parameter ξ may be used to differentiate between “high” and “low” resistive (aerodynamic) torques T_{RC} , activating the position anticipation term of the *dynamic position* logic in only high T_{RC} scenarios (regular wear-free actuators considered). In effect, wear-free actuators lead to regular friction forces¹¹ $F_f \ll T_{RC}$, so ξ differentiates according to the T_{RC} . This resistive (aerodynamic) torque differentiation was empirically established with the resistive torque threshold equal to $T_{RC}^{thr} = 4000Nm$:

- In case of $T_{RC} < T_{RC}^{thr} = 4000Nm$, the engine speed may manifest limit cycle instabilities for the extension/retraction tests conducted. These values of T_{RC} are considered as *low aerodynamic torques*, for which $\xi = 0$.
- In case of $T_{RC} > T_{RC}^{thr} = 4000Nm$, the engine speed does **not** manifest limit cycle instabilities for the extension/retraction tests conducted. These values of T_{RC} are considered as *high aerodynamic torques*, for which $\xi = 1$.

Indeed, $\xi = 1$ only in “high” T_{RC} scenarios, in which both the failure surface and the engine speeds will be dominant and the *dynamic position* algorithm, in general, would not present a limit cycle. Particular exceptions will be discussed in section 9, considering aerodynamic borderline cases on wear-out conditions, with very high friction forces due to both actuators wear and tear conditions.

¹¹The effect of high friction forces due to worn out actuators when using dynamic position activel models will be discussed in section 9.

In conclusion, the *Slow* parameter facilitates the asymmetry correction by cutting off the electric current *Cor* after failure $t > t_f$ but before the asymmetry failure declaration $I_{Ai} = 0$. This makes the asymmetry correction easier once the failure is detected $I_{Ai} = 1$ and the inoperative surface is braked.

6 Simulation results in regular conditions

Once the models have been developed, they should be tested to study the effect they have on the overall system response on the so-called *regular wear-free conditions* (also *regular conditions*).

These are those that consider:

- Reversible wear-free actuators.
- Low external (aerodynamic) loads when deflecting from an angular position that is close from the maximum flap retraction.

The second condition can be expressed when T_{RC} is small enough as:

$$\theta_i(t = t_f) \ll \theta_{max} \wedge \theta_i(t = t_f) \gg \theta_{min} \quad (6.1)$$

where θ_{max} and θ_{min} are the maximum and minimum angular position respectively that constitute the flap mechanical limit switch.

Thus, no “extreme conditions” have been tested yet. These issues will be discussed in the relevant sections below (see sections 7 and 9).

Several tests were performed to study the system behaviour and detecting the main advantages and weaknesses of each active monitoring technique. To that end, a test campaign was followed, which consisted in testing the following variables on each model:

- Failure side: each test was performed considering the failure either on the right or the left surface. The system, far from behaving symmetrically, presented some significant differences depending on the failure side.
- Aerodynamic constant torque T_{RC} : the torque caused by the resultant aerodynamic force on the flap notably affects the test results. Since T_{RC} is constant during the whole simulation, it may represent the aerodynamic torque on flight conditions. Thus, different flight phases could be tested in a first approximation varying T_{RC} , included ground tests with no aerodynamic forces.

Therefore:

- A low T_{RC} value may represent either on ground conditions (ground tests) or on flight conditions with low speed and high pitch angle.
- A high T_{RC} value may represent on flight conditions with high speed and/or high pitch angle.
- Flap extension or retraction: the motion sense, combined with the aerodynamic constant torque T_{RC} , might be essential when detecting and controlling the asymmetry. In particular, the speed of the failure surface might increase considerably in certain T_{RC} - retraction cases. In effect, these will be considered as the critical cases, which will be studied in the following section (see the wear-free borderline cases in section 7).
- Failure time t_f : the moment in which the failure occurs might be an interesting parameter to consider on the test campaign. The failure time remained constant

in almost all the tests $t_f = 0.4$ s since the system single-failure scenario was considered ¹².

A system double-failure scenario would be an interesting next step on the high-lift devices asymmetry field of study, especially from the active asymmetry control techniques perspective.

In addition, the test campaign performed to study the active models behaviour in these conditions considers the following actions, either for left and right surface failures:

- Extraction from 0 to 0.07 rad at $T_{RC} = 0Nm$.
- Retraction from 0.07 to 0 rad at $T_{RC} = 0Nm$.
- Extraction from 0.4 to 0.5 rad at $T_{RC} = 10000Nm$.
- Retraction from 0.5 to 0.4 rad at $T_{RC} = 10000Nm$.

The first two cases are considered to be *maneuvers at low aerodynamic load*. On the other hand, the last two cases are considered to be *maneuvers at high aerodynamic load*.

In regard to the high aerodynamic load cases, two different scenarios may happen:

1. Both flaps remain braked on the same position during the rest of the flight. In this case, two different subcases should be considered:
 - a. Both flaps are “too extended”: the lift-induced drag would be very high during the rest of the flight. In contrast, the landing field length would be shorter.
 - b. Both flaps are “too retracted”: the lift-induced drag would be reduced but the landing field length would increase significantly.
2. The operative flap deflects again and the aircraft rolling moment induced is compensated by the ailerons. This may in part solve part of the problems commented before but the maneuverability would be considerably reduced since the aileron would need a constant non-zero deflection to compensate such rolling moment. Should any adverse condition may arise (lateral gust, crosswind landing...) the aircraft maneuverability could be seriously compromised.

The simulation results of each active model described on section 5.3 will be described analyzed, the ultimate being to study the system response stability and the aircraft maneuverability after the flap asymmetry failure.

In other words, the active techniques effectiveness will be evaluated according to the following aspects:

1. The system stability: the stability margin is analyzed measuring the system response overshoot and time-to-peak, two essential system dynamic stability indicators in the time domain. In particular, the overshoot presents appreciable differences from one model to another so it is determinant to evaluate the active techniques efficiency. Thus, the overshoot of either ϕ_A or θ_A determine the system stability and the model efficiency.

¹²A double-failure case was considered in the last borderline tests with a reversible wear out actuation

2. The aircraft maneuverability after failure: maneuverability is conditioned by the failure surface braking position when $t > t_f$. It is characteristic of the high aerodynamic load scenarios. The sooner the failure surface brakes, the less retraction due to aerodynamic drag is produced and less aileron deflection would be necessary to compensate the rolling moments, for example when on the landing phase.

In regard to the aircraft maneuverability, such braking position of the failure surface can be mathematically represented as $\theta_{i,br} \equiv \theta(t = t_{br})$, where t_{br} is the *braking time after failure* (see definition on section 5).

Let τ_{br} define the dimensionless braking time, when the broken surface is braked, referenced to the braking time t_f :

$$\tau_{br} = \frac{t_{br}}{t_f} \quad (6.2)$$

Thus, the less τ_{br} is, the higher the aircraft maneuverability will be. In effect, the less deflected is the failure flap, the less the rolling moment will be due to the aerodynamic configuration asymmetry and the less the aileron compensation will be to maintain the aircraft trim position. Although the aerodynamic drag might be notably bigger than in no-failure conditions, the landing field length would be considerably reduced maintaining an acceptable maneuverability during the (emergency) landing phase.

Both the response stability and the aircraft maneuverability after failure will define the active model *efficiency*, which will be treated in 6.5.

In the following pages, the test results of the asymmetry active monitoring techniques on *regular conditions* will be studied.

6.1 New model 3 results

6.1.1 New model 3: origin and improvements

As mentioned in 5.3.1, the *new* asymmetry active monitoring technique 3 improves the *previous* model 3 (see Figures 14 and 15) since the latter does not differentiate between left and right failure. Indeed, it only declares the failure on the *left* surface in any case. This leads to detrimental effects when controlling the asymmetry with this model in particular for two reasons:

1. No right failures will be correctly detected and fixed.
2. Unstable position control (divergence) when controlling the asymmetry happens in case of right failure. Not even the benefits of the passive monitoring techniques can be exploited in this case since the divergence makes the system unstable, regardless the initial stability margin of the system.

In case of right surface failure, the *previous* model 3 shows that its position could evolve in two ways after the failure:

- a. Remains constant: in case of high friction force (worn out actuators, analyzed in sections 8 and 9) or regular reversible actuators under low T_{RC} , the right surface stops shortly after the failure time t_f due to the friction.

- b. Quickly drops to the end-of-travel: in case of high T_{RC} with a wear-free actuator, the right surface suddenly varies and stops once reached the flap mechanical end-of-travel. No other mechanism would stop the failure surface since the control algorithm does not consider the right failure.

It should be noted an important control effect that emerges in the *previous* model 3. In this model, *operative* (left) surface diverges since the model erroneously believes that the failure was detected on the left surface (which is false) and tries to correct the asymmetry extending (raising) the “operative right surface”, which is not because that is the failure one. Thus, the controlling effect is detrimental since the identification of the failure surface side is completely wrong, which leads to a asymmetry correction based on the wrong surface (see Figures 14b and 15b of the extension cases).

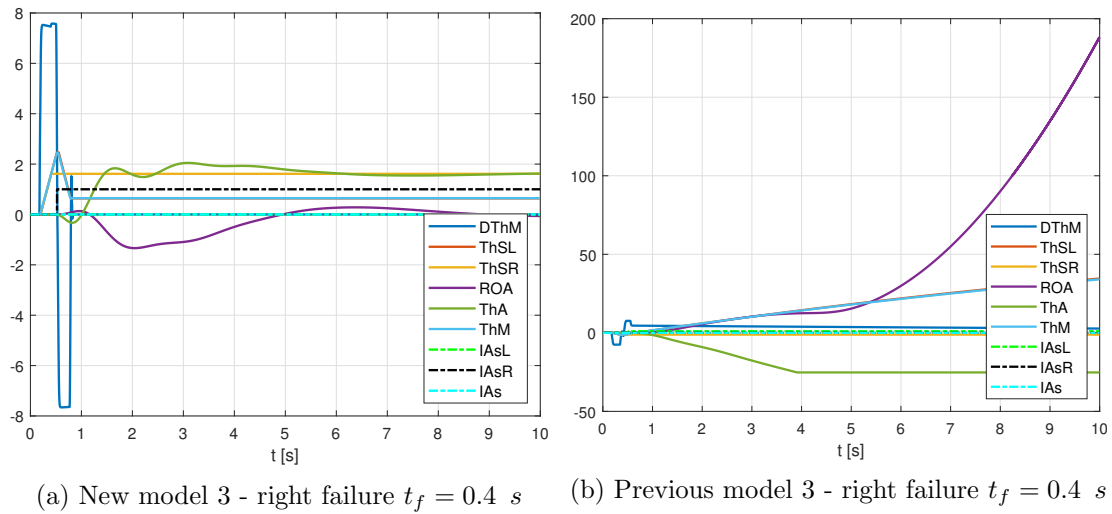


Figure 14: Right failure during extension from 0 to 0.07 rad at $T_{RC} = 0$ Nm

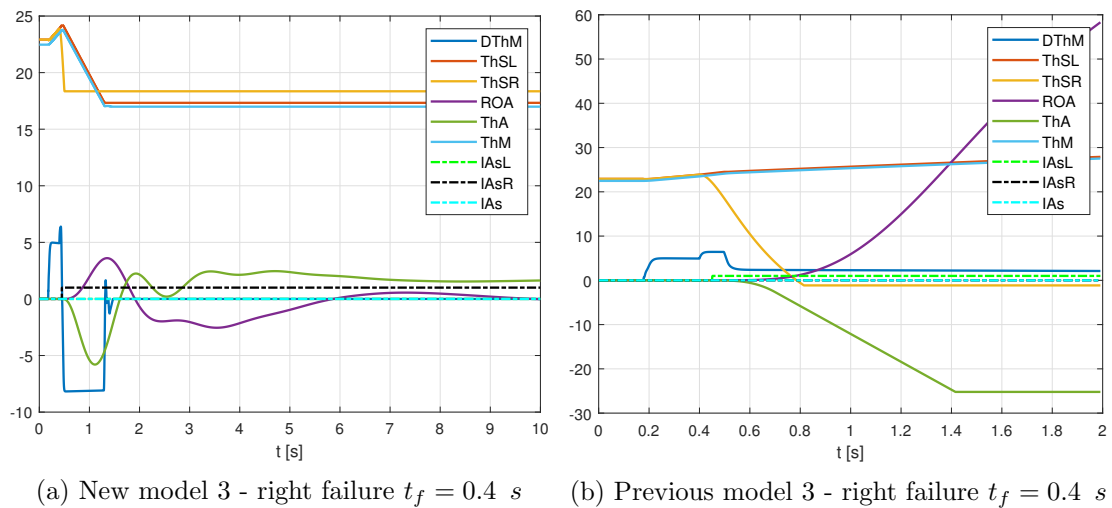


Figure 15: Right failure during extension from 0.4 to 0.5 rad at $T_{RC} = 10000$ Nm

This effect is shown both with high T_{RC} (wear-free actuators), where the divergence is slow (due to high T_{RC}), and with low T_{RC} ¹³, where the divergence is fast (steep

¹³Is also possible the case of high T_{RC} with worn out actuators, see section 9

position variation of the *operative* surface, due to low T_{RC}).

In any case, the detrimental control behaviour of the previous model 3 when the right failure arises, causes a divergence of the aircraft roll angle ϕ_A , which leads to a high loss of the aircraft lateral-directional stability and makes the aircraft unstable.

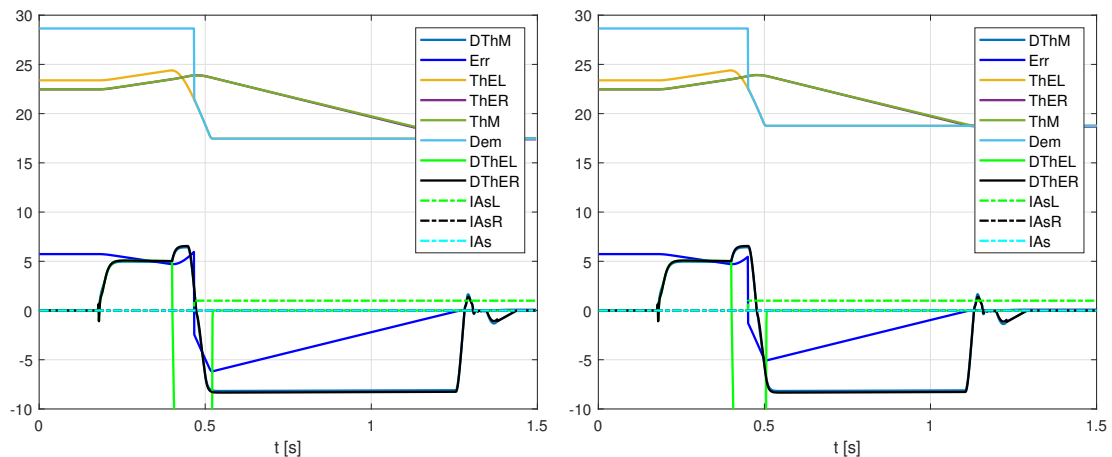
However, the right failure would be detected with the *new* active model 3. Hence, should a failure arise, either on the left or the right surface, it would be detected and controlled. This would lead to a better control of the aircraft roll angle ϕ_A evolution, which would not diverge with the new active model 3, so the aircraft turns to be lateral-directional stable. Furthermore, the new model improves the aircraft controllability and maneuverability.

Analogously, the divergent behaviour of the extension cases is also present on the retraction cases, both with high and low aerodynamic loads.

Regarding to the left failure, both models respond correctly to it but in different ways:

- The *previous* model 3 only detects the left failures correctly by means of either a *differential* position or a *differential* speed, each of them greater than a position or speed threshold respectively. Consequently, this model brakes the left surface faster, reducing the failure declaration delay.
- The *new* active monitoring technique 3 uses the the *relative* position respect the engine angular position θ_M which is the reference in all the step input models. However, this model does not consider any surface speed, which means a simpler asymmetry control algorithm but entails a slightly bigger failure declaration delay.

As shown in figures 16 and 17, the surface electrical positions show clearly these effects.

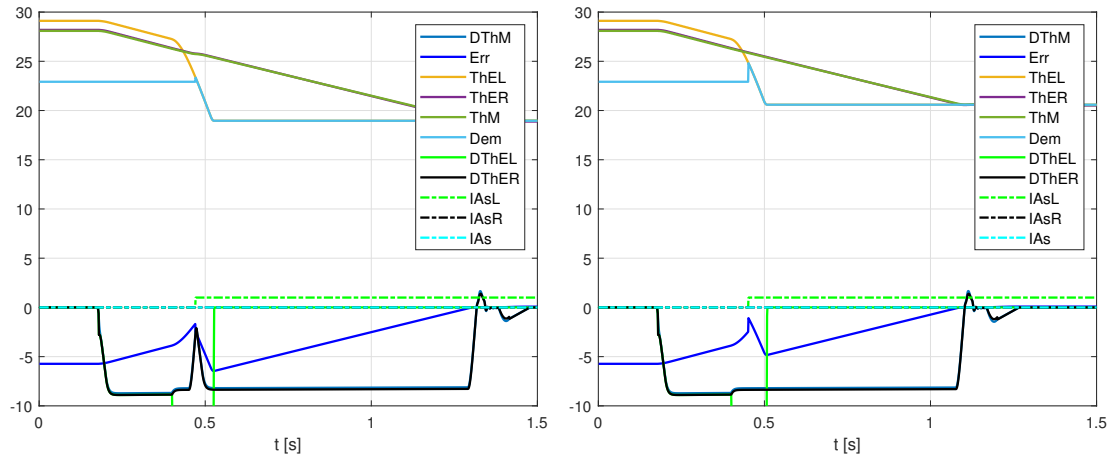


(a) New model 3 - left failure $t_f = 0.4$ s

(b) Previous model 3 - left failure $t_f = 0.4$ s

Figure 16: Left failure during extension from 0.4 to 0.5 rad at $T_{RC} = 10000$ Nm

Obviously, the failure declaration delay consideration applies only if the aerodynamic load is high, since the failure surface stops immediately if T_{RC} is small enough by the action of the friction force.



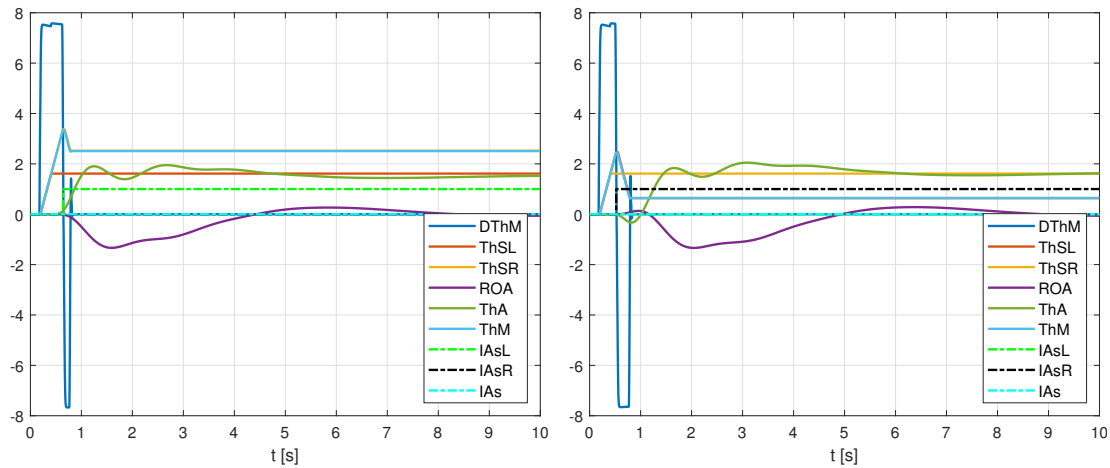
(a) New model 3 - left failure $t_f = 0.4$ s

(b) Previous model 3 - left failure $t_f = 0.4$ s

Figure 17: Left failure during retraction from 0.5 to 0.4 rad at $T_{RC} = 10000$ Nm

6.1.2 Low T_{RC} case results

Considering low T_{RC} , the results of both extension and retraction for both surfaces are shown in Figures 18 and 19



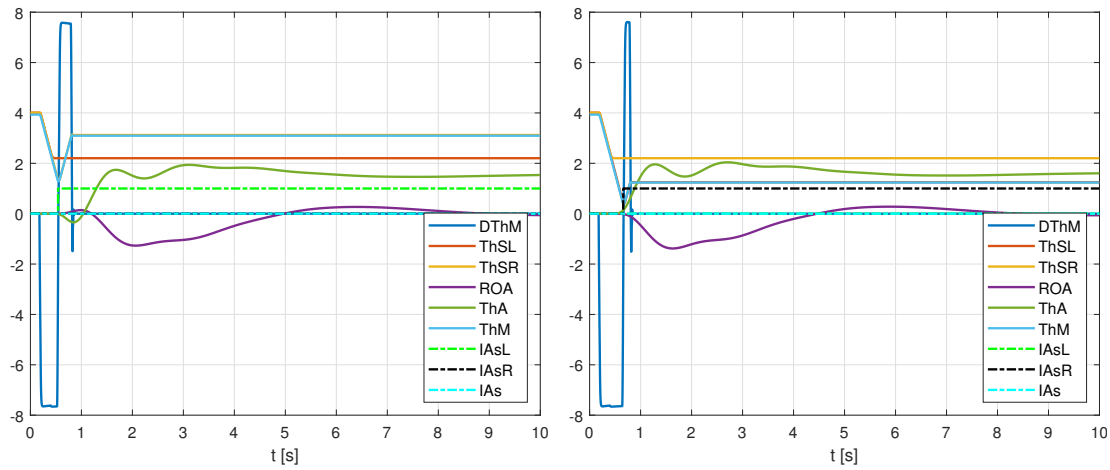
(a) Left failure $t_f = 0.4$ s during extension

(b) Right failure $t_f = 0.4$ s during extension

Figure 18: New model 3 - failure extension from 0 to 0.07 rad at $T_{RC} = 0$ Nm

The main characteristics of the low resistive torque T_{RC} of the new model 3 are:

1. The failure side is correctly detected, regardless of whether the surface is extending or retracting.
2. The failure surface stops shortly after the failure time t_f due to the high friction force and the low T_{RC} .
3. The operative surface does not reach exactly the failure surface in the asymmetry correction due to the position offset $\theta_{Os, Ti}$, which is intrinsic to the electrical position transducers. $\theta_{Os, Ti}$ is set antisymmetrical in relation to the null-offset position and always affects the asymmetry correction of the active models since it is done by the electrical position transducers.



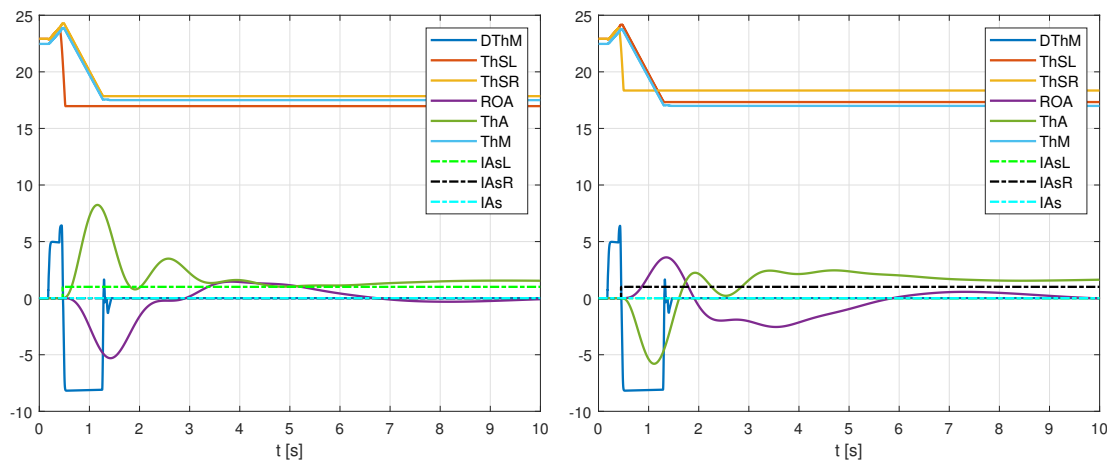
(a) Left failure $t_f = 0.4$ s during retraction (b) Right failure $t_f = 0.4$ s during retraction

Figure 19: New model 3 - failure retraction from 0.07 to 0 rad at $T_{RC} = 0$ Nm

4. The asymmetry correction, based on a *reference* position given by the engine θ_M , makes the controlling response more fast and accurate, raising the stability margin of the system which positively affects the full aircraft stability and control.

6.1.3 High T_{RC} case results

In regard to the high T_{RC} cases, the extension and retraction results for both surfaces are shown in Figures 20 and 21



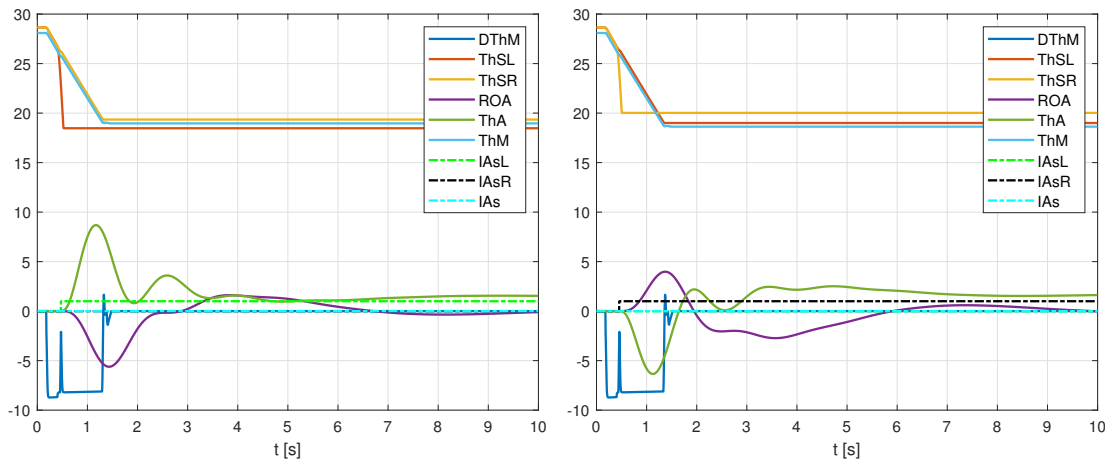
(a) Left failure $t_f = 0.4$ s during extension (b) Right failure $t_f = 0.4$ s during extension

Figure 20: New model 3 - failure extension from 0.4 to 0.5 rad at $T_{RC} = 10000$ Nm

The main characteristics of the low resistive torque T_{RC} of the new model 3 are:

1. As in the previous case, the failure side is correctly detected, regardless of whether the surface is extending or retracting.
2. The failure surface does **not** stop after the failure time t_f but it quickly retracts due to the high T_{RC} , since the engine force does not compensate the aerodynamic torque anymore (the hinge torque drops to zero after failure).

3. The simulations show that the braking time of the failure surface when extending is slightly less than in retracting cases. This seems to be caused by the high speed that the failure surface gains when retracting (see Figure 21) in contrast to the extending case, in which the inoperative surface has to stop before accelerating aided by the aerodynamic force (Figure 20).
4. In case of an extending maneuver, shortly after the failure time t_f , the engine rotating speed $\dot{\theta}_M$ slightly increases. This is caused by the loss of the failure surface transmission, which means that half of the aerodynamic load is no longer compensated by the engine power (only remains the aerodynamic torque of the operative surface), so the power supply needed drops. The engine speed regulation is not instantaneous: at first $\dot{\theta}_M$ grows due to the inertia of the engine and then it drops to the steady value.
5. Again, the operative surface does not reach exactly the failure surface in the asymmetry correction due to the position offset θ_{O_s, T_i} , intrinsic to the electrical position transducers.
6. As commented in the previous case, the asymmetry correction, based on a *reference* position given by the engine θ_M , makes the controlling response more fast and accurate, raising the stability margin of the system which positively affects the full aircraft stability and control.



(a) Left failure $t_f = 0.4$ s during retraction (b) Right failure $t_f = 0.4$ s during retraction

Figure 21: New model 3 - failure retraction from 0.5 to 0.4 rad at $T_{RC} = 10000$ Nm

In addition, the Figures 20 and 21 show that the system remains under control on the steady state, since the braked position of the failure surface is reached by the operative flap, so the aircraft stability is guaranteed. However, the the lateral-directional stability would improve is further control action are considered in the algorithm control logic, such as considering a *dynamic position*, like model 3D (see 6.2)

The main reason to introduce an anticipation term on the control algorithms is to reduce as much as possible the inoperative surface braking time. This term will be essential to anticipate the asymmetry failure declaration in the *high* aerodynamic load cases, specially in flap retracting maneuvers.

The Figures 20 and 21 show how the anticipation term that considers the *relative* speed of the surface would improve the aircraft lateral-directional stability. However,

the aircraft steady state response does not significantly improve, since $\phi_{A,ss}$ remains (quasi) constant due to the transducers intrinsic offset.

6.2 Model 3D results

The asymmetry active monitoring technique *3D* was conceived as an interesting variant of the new model 3, in which a position anticipation logic was added in the control algorithm. This seems to be an interesting way to solve the main asymmetry problems under high aerodynamic loads. In effect, the *dynamic position* “anticipates” the failure in case of high T_{RC} since the inoperative surface speed rapidly grows after t_f , which reduces the failure confirmation delay. Hence, the higher the retracting speed is, the faster the *dynamic position* grows and the earlier the partial asymmetry failure condition is met.

Therefore, the braking time of the inoperative surface decreases and the aircraft lateral-directional stability is better than on model3.

It should be reiterated that, as commented in 5.3.2, the anticipation term of the dynamic position is cancelled. In effect, there is no need of the anticipation term since the failure surface speed after failure is null due to the high friction force.

Thus, the main difference between the asymmetry active monitoring techniques 3 and *3D* will be appreciated in case of high T_{RC} , when the *dynamic position* will make the difference between both models.

6.2.1 Low T_{RC} case results

As commented in 5.2.2, the effect of the high friction load and the little (null) aerodynamic load, makes the anticipation term completely useless. In fact, the control parameter is $\xi = 0$, which cancels the anticipation effect of the *dynamic position*.

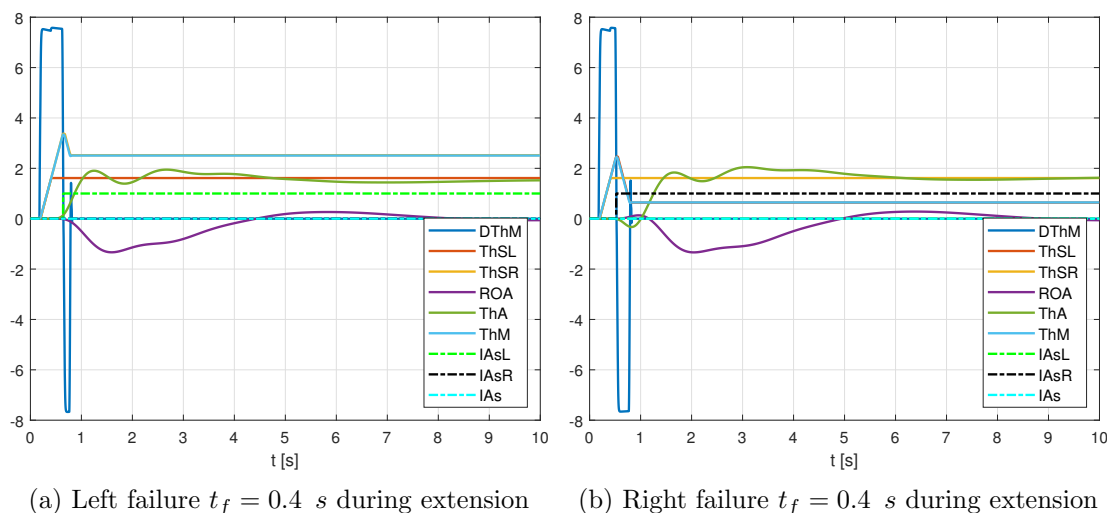
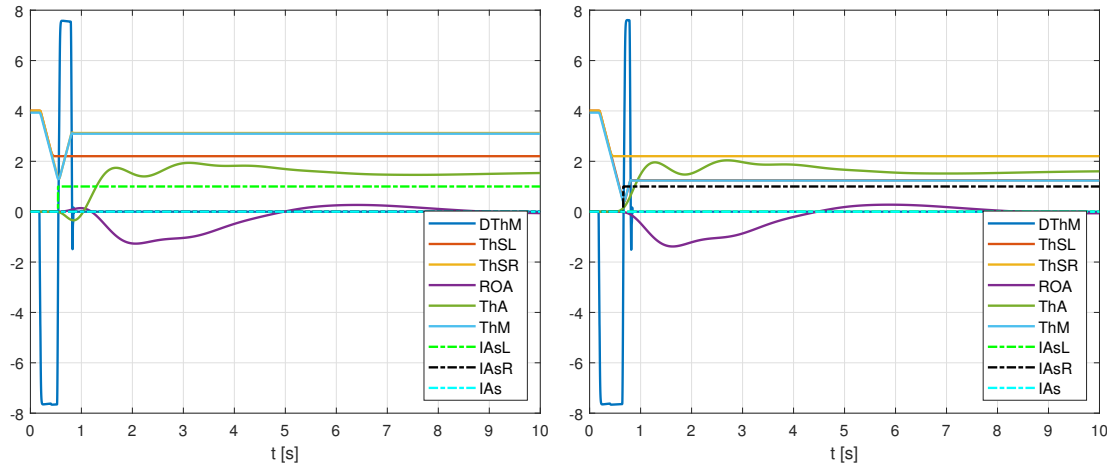


Figure 22: Model 3D - failure extension from 0 to 0.07 rad at $T_{RC} = 0$ Nm

Therefore, in case of low T_{RC} , the test results of models 3 and *3D* will be exactly the same (see Figures 22 and 23) and so will be the main characteristics of those results.

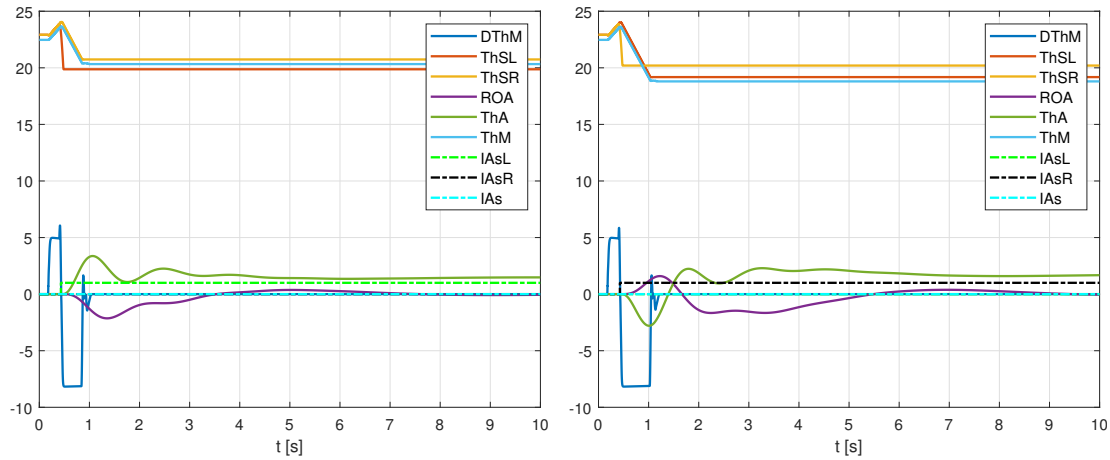


(a) Left failure $t_f = 0.4$ s during retraction (b) Right failure $t_f = 0.4$ s during retraction

Figure 23: Model 3D - failure retraction from 0.07 to 0 rad at $T_{RC} = 0$ Nm

6.2.2 High T_{RC} case results

In regard to the high T_{RC} cases, the effect of the “dynamic position” improves the dynamic response in terms of failure surface braking time and exploits all the advantages of model 3 in terms of reducing the asymmetry. The improved extension and retraction results for both surfaces are shown in Figures 24 and 25.

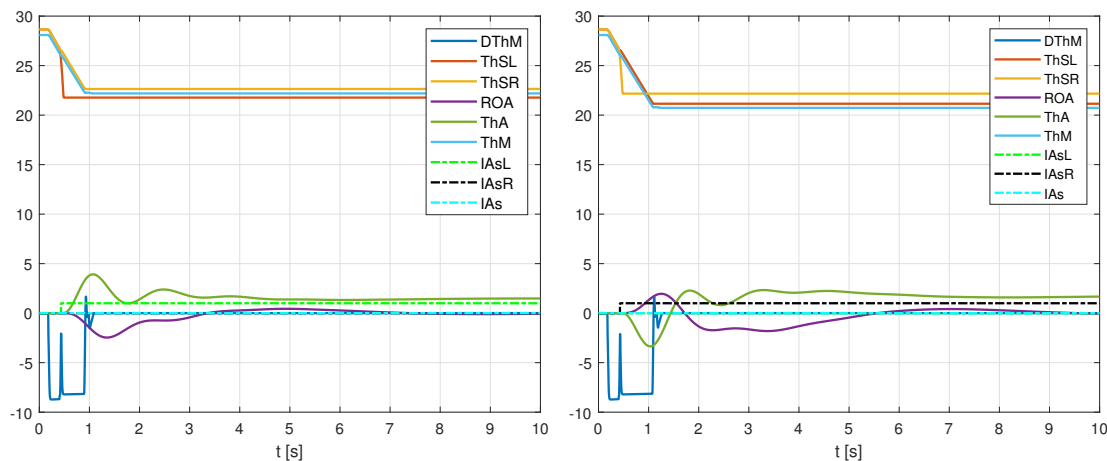


(a) Left failure $t_f = 0.4$ s during extension (b) Right failure $t_f = 0.4$ s during extension

Figure 24: Model 3D - failure extension from 0.4 to 0.5 rad at $T_{RC} = 10000$ Nm

The high T_{RC} of model 3D share the same main characteristics (and benefits) of model 3. However, further comments should be done:

1. The braking time is considerably reduced. This reduces both the roll angle ϕ_A overshoot and time-to-peak, two essential system dynamic stability indicators in the time domain. Hence, this improves the aircraft lateral-directional stability. However, $\phi_{A,ss}$ does not change significantly.
2. The flaps final position after the asymmetry correcting maneuver is determining for aircraft behaviour during the rest of the flight, as indicated in the introduction of section 6.



(a) Left failure $t_f = 0.4$ s during retraction (b) Right failure $t_f = 0.4$ s during retraction

Figure 25: Model 3D - failure retraction from 0.5 to 0.4 rad at $T_{RC} = 10000$ Nm

6.3 Model 3C results

In regard to the asymmetry active monitoring techniques with ramp inputs, they exploit the benefits of a ramp input, which they take as a the position reference to build the control algorithm.

6.3.1 Ramp-input models: *Dem* slope fitting

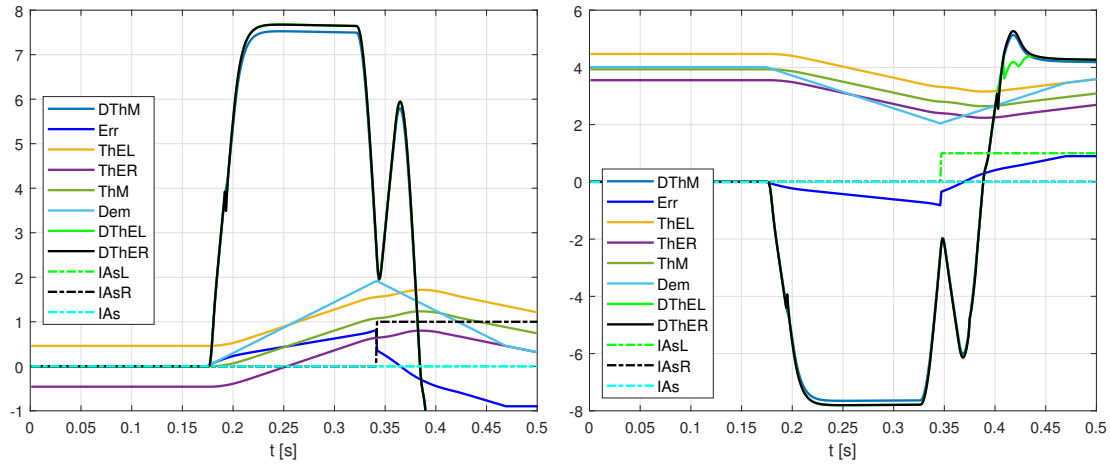
The main reason is that ramp-input models use Dem instead of θ_M as reference position, which seems to be more effective to detect asymmetry failure conditions since Dem does not suffer from the engine speed variations. In addition, the Dem slope (ramp slope) could be varied which directly on both surfaces time evolution. In effect, the average electrical position should always follow Dem to minimize the position error ϵ .

These advantages are essential when studying any ramp-input model, in particular 3C, with which the input command could be reached varying the Dem slope. However, there are some limits on both flaps maximum speed, which is given by the engine. Hence the demand slope cannot be too steep in order to prevent from inexistent failure declarations.

In effect, an inexistent failure could be “detected” using an excessive ramp slope. The Figure 26 shows this effect at low aerodynamic load both on extension and retraction without testing any failure $\nexists t_f$ and

$$\left| \left(\frac{d Dem}{dt} \right)_{max} \right| = 0.2 \text{ rad/s}$$

Although no failure time t_f was considered, the steep ramp slope separates the reference agunal position Dem from both surfaces electrical position. Hence at some point one flap meets the failure declaration conditions depending on the deflection sense (extension or retraction), even though $\nexists t_f$ and the corresponding *partial asymmetry counter* $I_{Wrn,i}$ increases. In each deflection, the surface i that will present the “false asymmetry” is the furthest with respect to the demand Dem . Mathematically, it corresponds to the surface that meets the following sign condition:



(a) False failure extension 0 to 0.07 rad ∇t_f (b) False failure retraction 0.07 to 0 rad ∇t_f

Figure 26: Model 3C - False failures ramp slope 0.2 rad/s at $T_{RC} = 0$ Nm

$$\theta_{Os,Ti} \cdot \left. \frac{d Dem}{dt} \right|_{max} < 0 \quad (6.3)$$

Thus, the sign of these two variables should be different to identify which surface would suffer the “false asymmetry”.

The strange behaviour of the engine could be explained as follows:

1. When the position difference between Dem and the electrical position of the furthest surface $\theta_{E,i}$, the “false asymmetry failure” is declared and the corresponding *partial asymmetry counter* $I_{Wrn,i}$ increases.
2. Once $I_{Wrn,i} = I_{Wrn,i}^{thr,S}$, the *Slow* parameter becomes zero shuts the current. Therefore, $Cor = 0$ and $\dot{\theta}_M$ decreases. When $I_{Wrn,i} = I_{Wrn,i}^{thr}$ the “false failure” is detected $I_{Ai} = 1$ and $Slow = 1$, reactivating $Cor = 0$ and the engine accelerates again. In addition, $\left. \frac{d Dem}{dt} \right|_{max}$ changes sign to reach the new command: the “false failure surface”.
3. After $I_{Ai} = 1$, both surface try to reach the demand which now follows the “false failure surface” position. Hence, the engine acceleration varies speed $\dot{\theta}_M$ to achieve that.

Consequently, $\dot{\theta}_M$ accelerates and decelerates when $t \approx t_f$, which is a characteristic phenomenon of ramp-input models. It may appear in excessive ramp slope cases (see Figure 26) or in some retraction cases with high aerodynamic load (see Figure 38a).

The detrimental asymmetry failure detection and control would be easily corrected by lowering the ramp slop. The test results shown in Figure 27 correspond to:

$$\left| \left(\frac{d Dem}{dt} \right)_{max} \right| = 0.1 \text{ rad/s}$$

With $\left| \left(\frac{d Dem}{dt} \right)_{max} \right| = 0.1 \text{ rad/s}$ both surface can follow the demand Dem correctly and no false asymmetry failures arise.

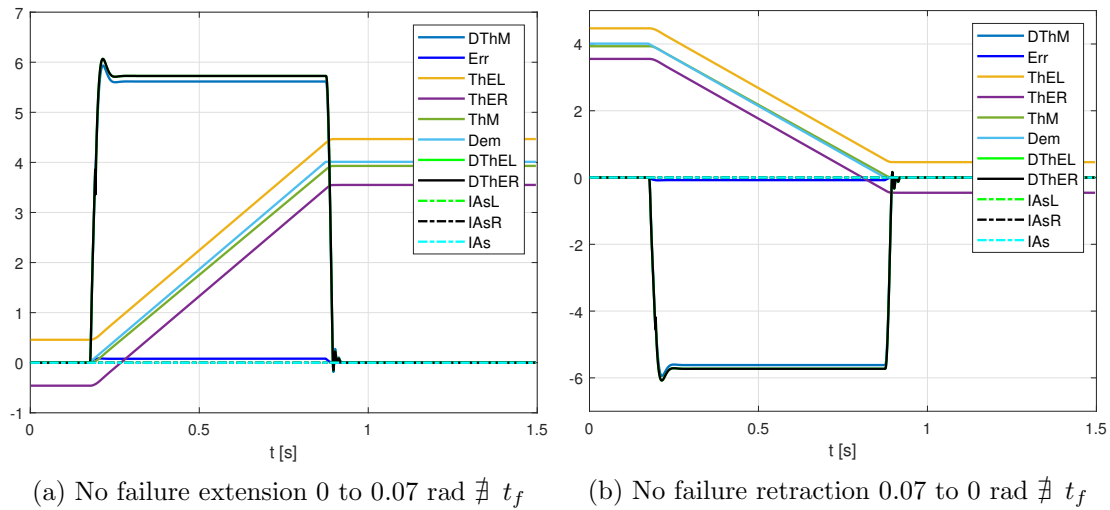


Figure 27: Model 3C - No failure ramp slope 0.1 rad/s at $T_{RC} = 0 Nm$

Thus, the maximum surface actuation speed cannot be lower¹⁴ than the fixed ramp slope while deflecting the flaps (either extension or retraction), otherwise a false asymmetry failure detection will be declared as illustrated in Figure 26.

All these considerations apply both on high and low aerodynamic load cases. Only low aerodynamic load figures were included in this project given their clarity.

6.3.2 Model 3C: origin and improvements

As mentioned in 5.3.3, the model 3C was created to improve the model old model 3A. In contrast to the *previous* model 3, 3A behaves correctly either with a left or a right asymmetry failure.

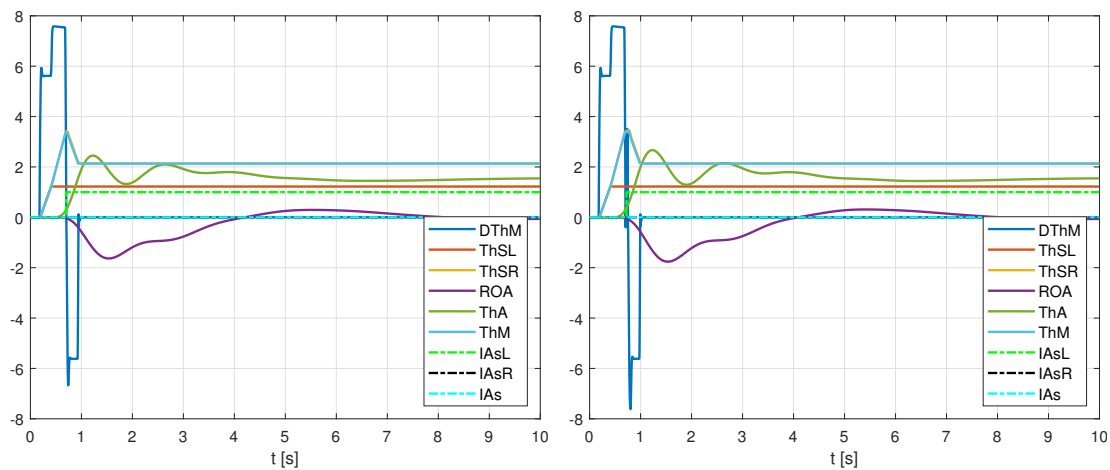
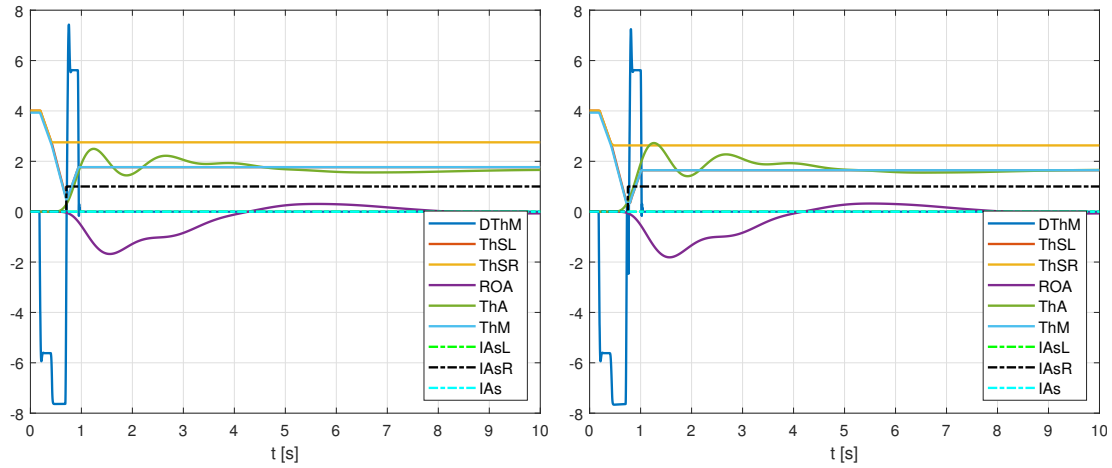


Figure 28: Improvement model 3C - failure extension from 0 to 0.07 rad at $T_{RC} = 0 Nm$

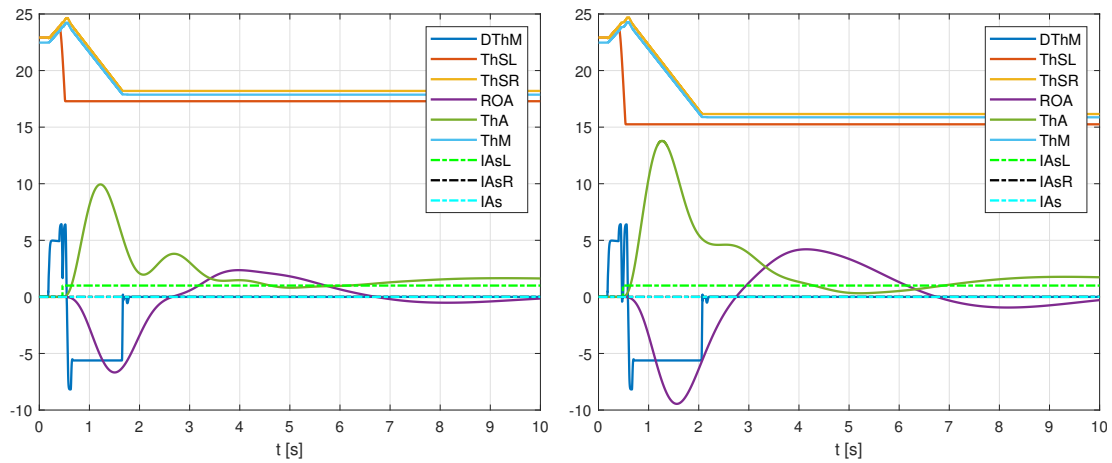
However, the model 3A presents a couple of weaknesses that the new developed model 3C tries to correct:

¹⁴a sudden oil pressure drop may momentary decrease the maximum surface actuation speed.



(a) Model 3C right failure $t_f = 0.4s$ retraction (b) Model 3A right failure $t_f = 0.4s$ retraction

Figure 29: Improvement model 3C - failure retraction from 0.07 to 0 rad at $T_{RC} = 0Nm$



(a) Model 3C left failure $t_f = 0.4s$ extension (b) Model 3A left failure $t_f = 0.4s$ extension

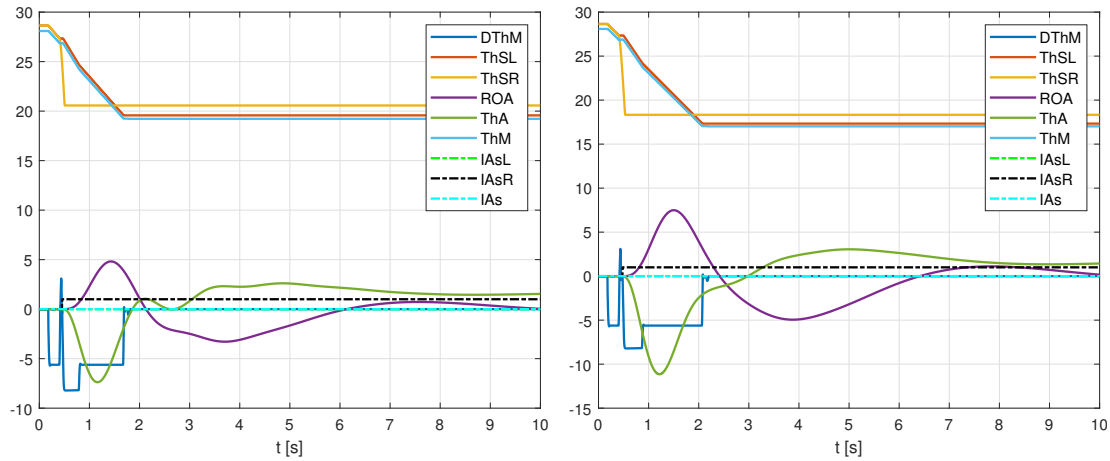
Figure 30: Improvement model 3C - failure extension from 0.4 to 0.5 rad at $T_{RC} = 10000Nm$

1. No *general* asymmetry detection is considered. Thus, 3C presents a detrimental behaviour when controlling the asymmetry in certain borderline cases, in which it seriously compromise the flight safety. Such borderline cases will be discussed in the relevant sections below (see sections 7 and 9).
2. The *partial* asymmetry confirmation time is too large. This is not critical but affects both the aircraft stability and controllability.

Consequently, the developed ramp-input active technique 3C integrates a *general* asymmetry detection logic and the threshold of the *partial asymmetry counter* $I_{Wrn,i}^{thr}$ has been halved to reduce the *partial* asymmetry confirmation time.

The main improvements of model 3C with respect to model 3A are shown from Figure 28 to 31 (no borderline cases considered).

Some considerations for model 3C compared with 3A are given below:



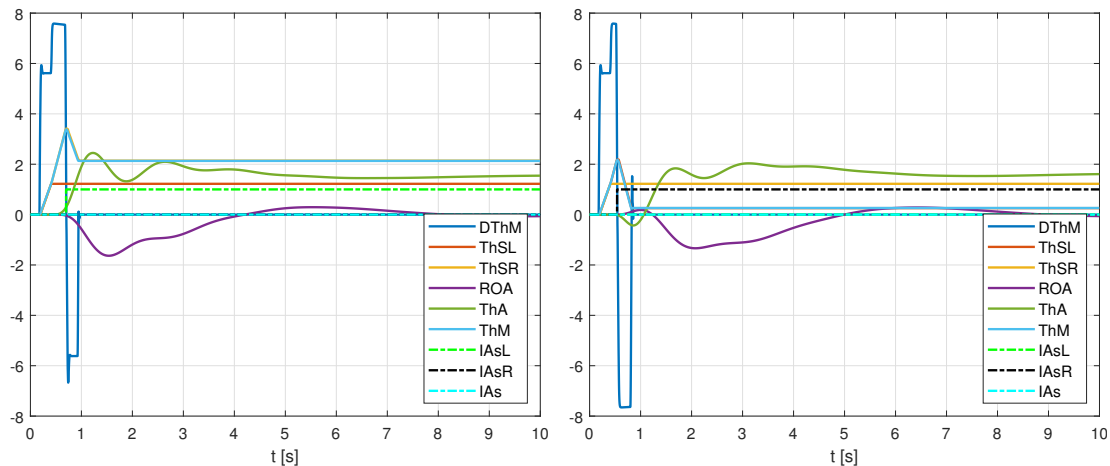
(a) Model 3C right failure $t_f = 0.4s$ retraction (b) Model 3A right failure $t_f = 0.4s$ retraction

Figure 31: Improvement model 3C - failure retraction from 0.5 to 0.4 rad at $T_{RC} = 10000Nm$

- Minor differences can be noted between both active models in case of low aerodynamic load.
- 3C presents great improvements in case of high aerodynamic load.
- The early *partial* asymmetry detection of model 3C, improves the aircraft stability and controllability in any case.
- The *general* asymmetry failure is never verified in any case study.

6.3.3 Low T_{RC} case results

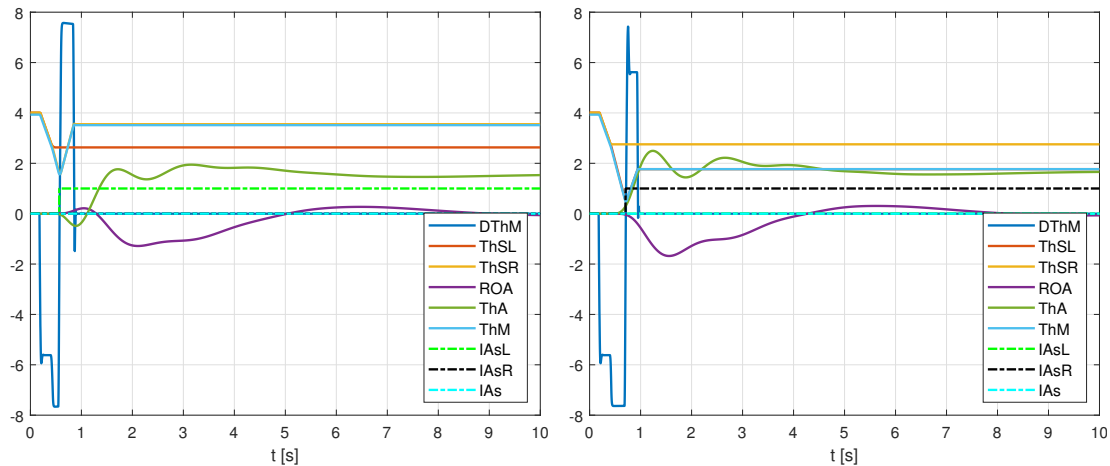
Considering low T_{RC} , the results of both extension and retraction for both surfaces are shown in figures 32 and 33.



(a) Left failure $t_f = 0.4 s$ during extension (b) Right failure $t_f = 0.4 s$ during extension

Figure 32: Model 3C - failure extension from 0 to 0.07 rad at $T_{RC} = 0 Nm$

The model 3C presents some significant differences when either extending or retracting the flaps when comparing with model 3 when the aerodynamic load is small enough.



(a) Left failure $t_f = 0.4$ s during retraction (b) Right failure $t_f = 0.4$ s during retraction

Figure 33: Model 3C - failure retraction from 0.07 to 0 rad at $T_{RC} = 0$ Nm

- The surface initial speed before failure can be easily controlled by means of the Dem slope, which indirectly affects the engine speed $\dot{\theta}_M$ that governs both surfaces time evolution. This entails that the failure position $\theta_i(t = t_f)$ can be modified within certain limits (no excessive Dem slope is allowed), empirically set as $\left| \left(\frac{dDem}{dt} \right)_{max} \right| = 0.1$ rad/s as mentioned on 5.3.4. In effect, the flap deflection when $t = t_f$ is smaller on model 3C than on model 3.
- The surface speed increases after failure and before the asymmetry detection $I_{As} = 0$. This is because the position error should not increase after failure so the operative surface should accelerate considering that the failure surface stops immediately due to the presence of the friction force and the low aerodynamic load. In effect, $\theta_{E,av} \simeq Dem$ to minimize the position error ϵ , where the average electrical position is still calculated as $\theta_{E,av} = \frac{\theta_{EL} + \theta_{ER}}{2}$.
- When $I_{As} = 1$, the failure is detected and the correction maneuver starts. The model 3C needs more time to reach the failure position given that it stopped before with respect to model 3 due to the ramp slope.

These differences can be noted in Figures 34 and 35.

Consequently, the behaviour of model 3C with respect to the new model 3 on *regular conditions*, both on flap extension and retraction maneuvers, is governed by the effect of the ramp slope. It delays both the inoperative surface braking position $\theta_i(t = t_{br})$ and the instant in which the operative surface reaches the failure surface position. Furthermore, the final position of both surfaces using the active technique 3C will be more closer to the initial flap position little and controlled ramp slope. All these increases the time-to-peak of the aircraft response, reducing the stability margin.

On the other hand, the aircraft maneuverability after failure of model 3C in the aforementioned cases has slightly increased due to the less deflected stopping position of the inoperative surface $\theta_i(t = t_{br})$.

Nonetheless, no significant overshoot and time-to-peak variations are present neither on right failures during extension nor on left failures during retraction. Hence, no

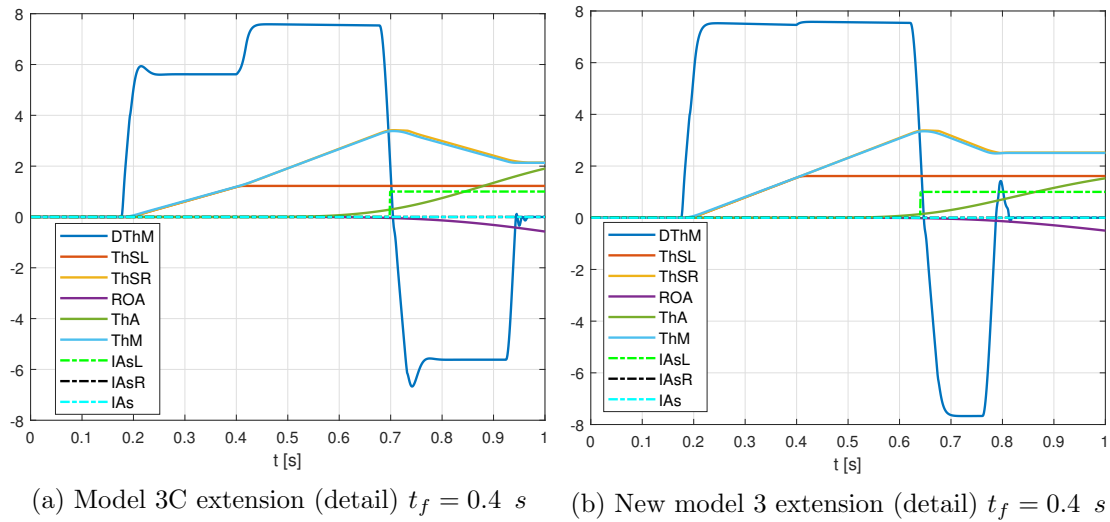


Figure 34: Comparison 3C & 3 left failure extension from 0 to 0.07 rad at $T_{RC} = 0Nm$

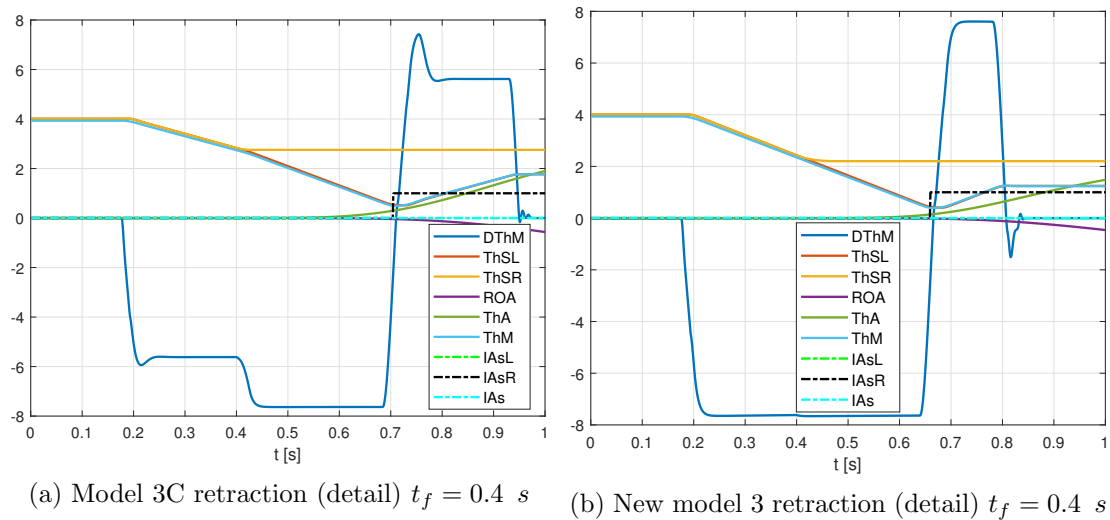


Figure 35: Comparison 3C & 3 right failure retraction from 0.07 to 0 rad at $T_{RC} = 0Nm$

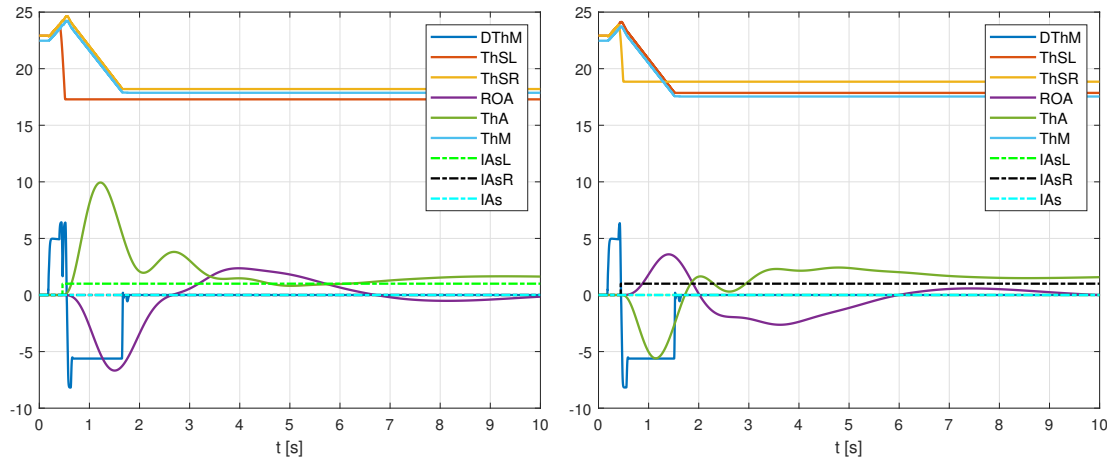
significant stability and maneuverability differences will be noted in the aforementioned flap maneuvers.

6.3.4 High T_{RC} case results

Regarding the high T_{RC} cases, the extension and retraction results for both surfaces are shown in Figures 36 and 37.

Similarly, some particular differences could be noted on model 3C when comparing it with model 3 in case of high aerodynamic load depending on the deflection case: extension or retraction.

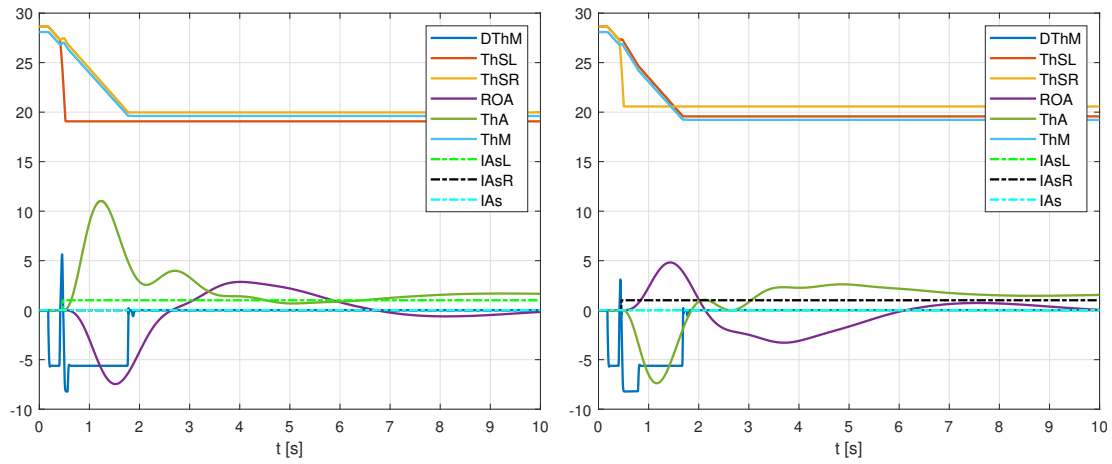
- On the one hand, in case of extending both flaps, the surface initial speed before failure cannot be fully controlled by the ramp slope since the “opposing” aerodynamic load determines the flap extension, affecting the engine speed and the whole system performance. Hence, the extension rate of both model 3 and 3C are quite similar. However, once the failure is detected, the engine powers only



(a) Left failure $t_f = 0.4$ s during extension

(b) Right failure $t_f = 0.4$ s during extension

Figure 36: Model 3C - failure extension from 0.4 to 0.5 rad at $T_{RC} = 10000$ Nm



(a) Left failure $t_f = 0.4$ s during retraction

(b) Right failure $t_f = 0.4$ s during retraction

Figure 37: Model 3C - failure retraction from 0.5 to 0.4 rad at $T_{RC} = 10000$ Nm

the operative surface and the *effective* aerodynamic load halved, so the effect of the ramp slope becomes relevant to control the flap deflection. In consequence, the operative surface takes more to reach the failure one on model 3C (Figure 38).

- On the other hand, in case of flap retraction, the “aiding” aerodynamic load lets the engine follow the ramp demand. Consequently, the failure position $\theta_i(t = t_f)$ can be easily controlled by $\left. \frac{dDem}{dt} \right|_{max}$. The subsequent system time evolution is analogous to what studied on low aerodynamic load case of 3C model (see Figure 39).

These particularities can be noted in Figures 38 and 39.

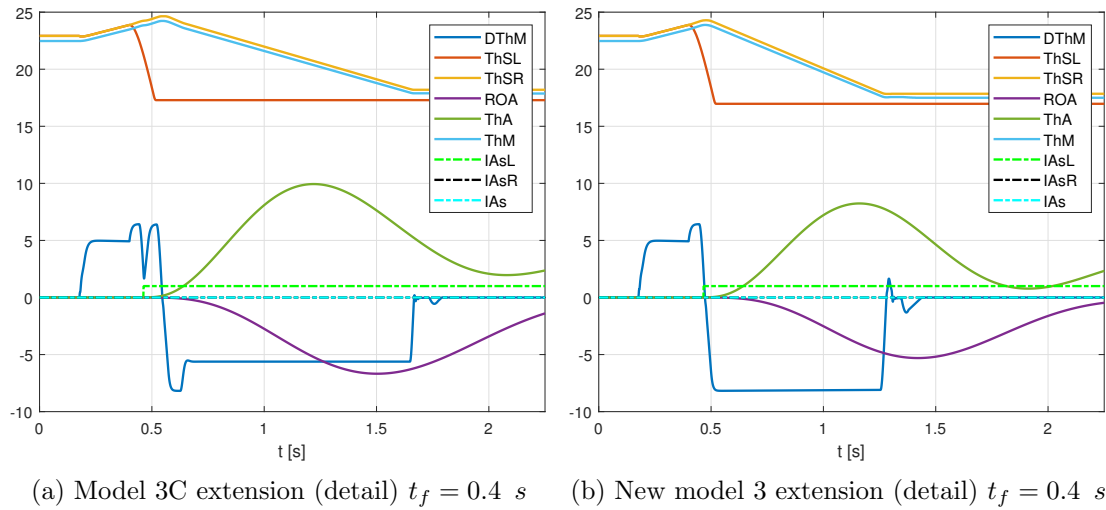


Figure 38: Comparison 3C & 3 left failure extension 0.4-0.5 rad at $T_{RC} = 10000Nm$

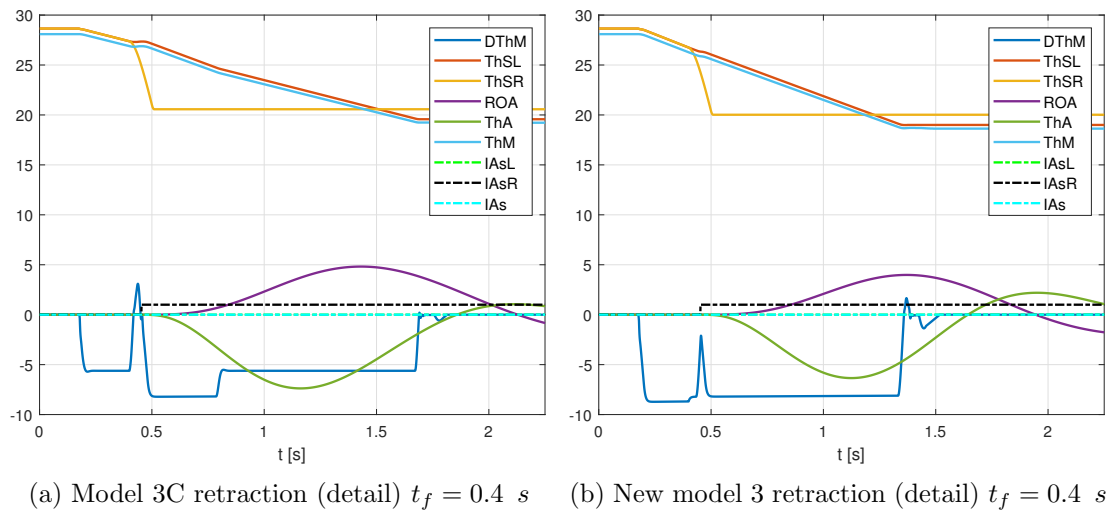


Figure 39: Comparison 3C & 3 right failure retraction 0.5-0.4 rad at $T_{RC} = 10000Nm$

6.4 Model 3E results

The asymmetry active monitoring technique 3D was conceived to improve model 3C at high aerodynamic loads by adding an anticipation logic. In effect, the *dynamic position* “anticipates” the failure in case of high T_{RC} since the inoperative surface speed rapidly grows after t_f , which reduces the failure confirmation delay.

Again, the higher the retracting speed is, the faster the *dynamic position* grows and the earlier the partial asymmetry failure condition is met. However, the anticipation term is cancelled in case of low T_{RC} cases, since the failure surface presents no big retraction speeds after failure as with high aerodynamic load.

Once again, the *dynamic position* will improve the aircraft stability and maneuverability after failure with respect to model 3C.

In what follows, the main improvements of model 3E are commented.

6.4.1 Low T_{RC} case results

As commented before, $\xi = 0$ in low aerodynamic load cases, so the tests results of both model 3E and 3C will be identical, as shown in figures 40 and 41.

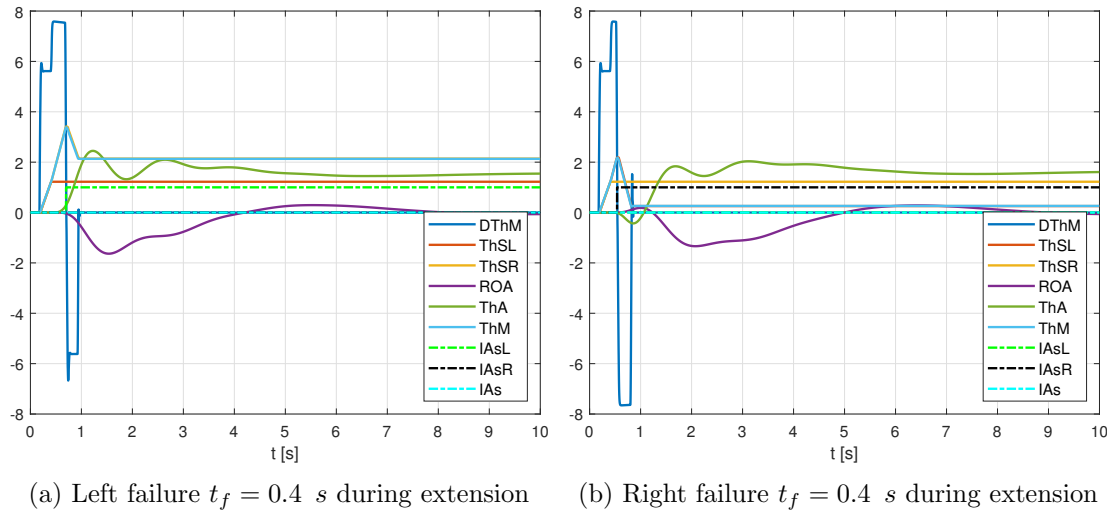


Figure 40: Model 3E - failure extension from 0 to 0.07 rad at $T_{RC} = 0$ Nm

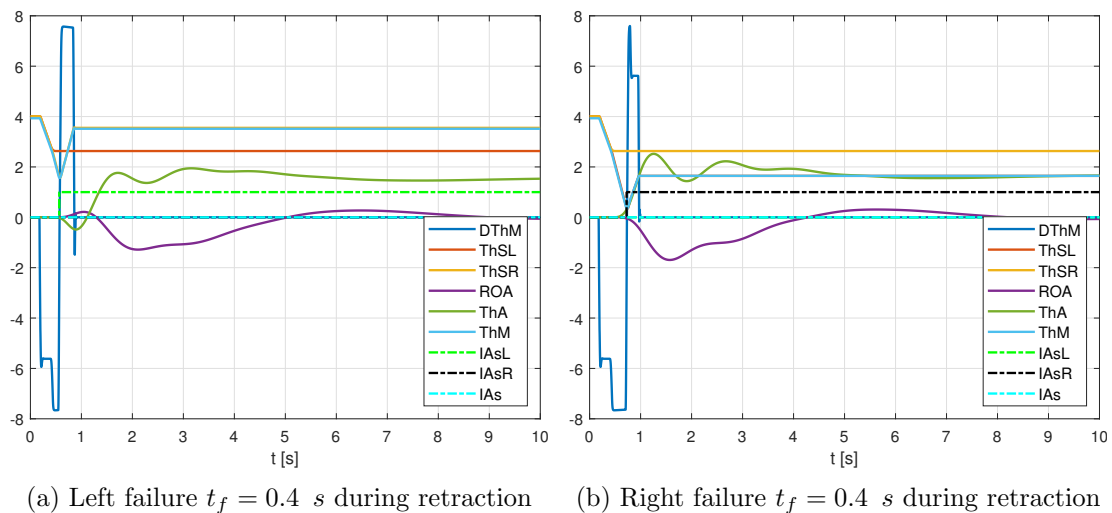


Figure 41: Model 3E - failure retraction from 0.07 to 0 rad at $T_{RC} = 0$ Nm

As illustrated in the aforementioned figures, the behaviour of model 3E with respect to the model 3D on *regular conditions*, both on flap extension and retraction maneuvers, is governed again by the effect of the ramp slope. It delays both the inoperative surface braking position $\theta_i(t = t_{br})$ and the instant in which the operative surface reaches the failure surface position. Furthermore, the final position of both surfaces using the active model 3E will be closer to the initial flap position due to the little and controlled demand slope of the ramp-inpt models. All these increases the time-to-peak of the aircraft response, reducing the stability margin.

Similarly to what discussed above for model 3C, all these variations are present both in left failure during extension and right failure during extraction. These contribute to reduce the stability margin.

On the other hand, the aircraft maneuverability after failure of model 3E in the aforementioned cases has slightly increased due to the less deflected stopping position of the failure surface $\theta_i(t = t_{br})$.

However, no significant overshoot and time-to-peak variations are present neither on right failures during extension nor on left failures during retraction. Therefore, no significant stability and maneuverability differences will be noted in the aforementioned flap maneuvers.

6.4.2 High T_{RC} case results

The major differences between both active ramp-input models lies in the *dynamic position* effect on high T_{RC} cases, where the control parameter $\xi = 1$. These are shown in figures 42 and 43.

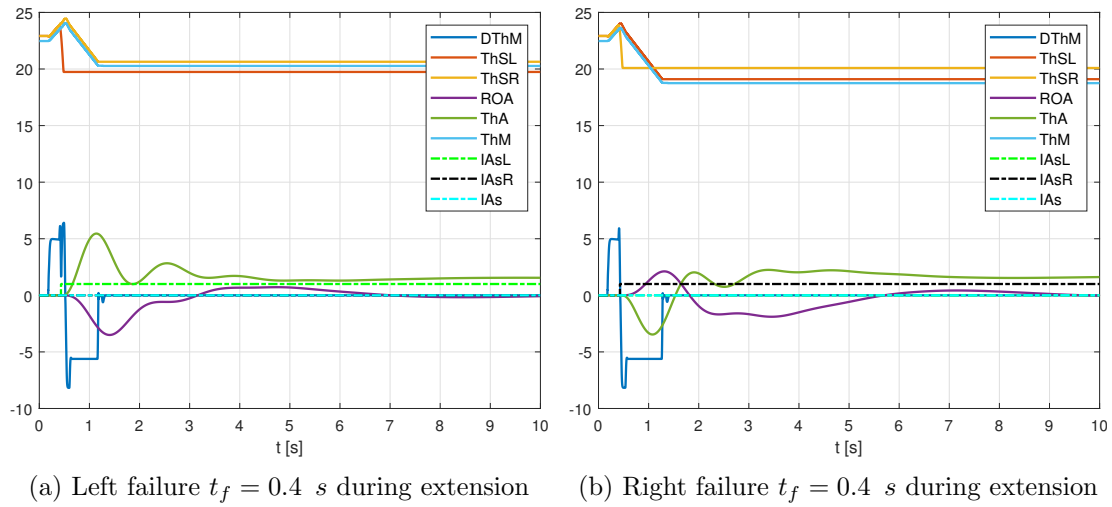


Figure 42: Model 3E - failure extension from 0.4 to 0.5 rad at $T_{RC} = 10000$ Nm

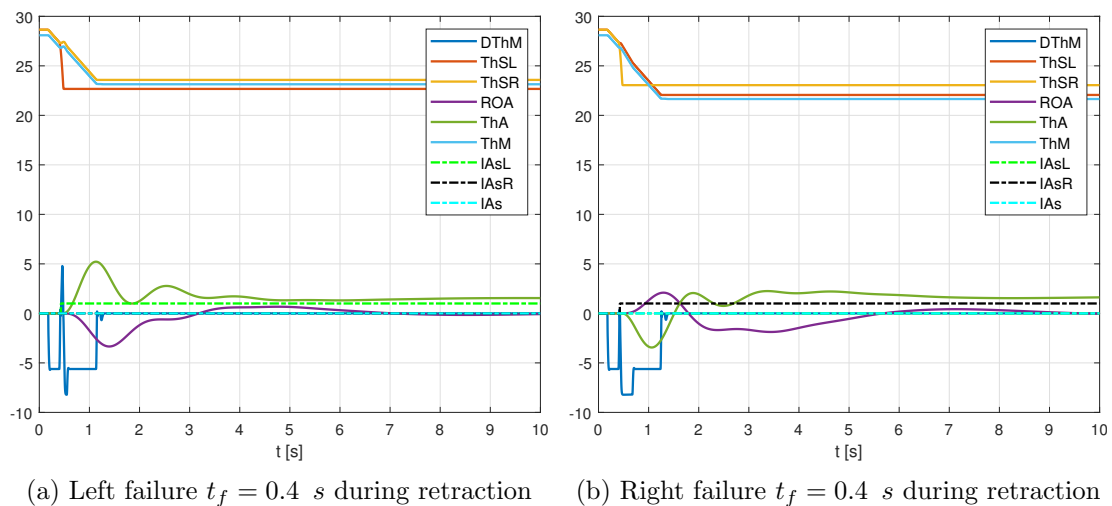


Figure 43: Model 3E - failure retraction from 0.5 to 0.4 rad at $T_{RC} = 10000$ Nm

The active technique 3E shares the same advantages than model 3C when T_{RC} is big

enough (see the comparison between model 3C and new model 3 in 6.3.4). However, the former improves the aircraft stability and maneuverability after the flap asymmetry failure. Following are detailed such considerations.

1. The operative flap takes more time to reach the failure surface on model 3E. Since the ramp slope governs the operative flap time evolution after failure, the surface speed is significantly reduced. This reduces the stability of the system response, raising the overshoot both of the aileron deflection θ_A and the aircraft roll angle ϕ_A .
2. The braking time after failure t_{br} of model 3E decreases with respect to model 3D, which improves the aircraft maneuverability after failure.

Thus, it seems that model 3E improves model 3C in case of high aerodynamic loads, as well as model 3D did with respect to new model 3.

Analogously, some particular differences could be noted on model 3E when comparing it with model 3C in the same aerodynamic conditions. Both models contain a *dynamic position* which anticipation effect applies only when T_{RC} is big enough, so the kind of input signal would make the difference. The considerations about the aerodynamic load effect when either extending or retracting the surfaces also apply here (see 6.3.4).

These particularities can be noted in Figures 44 and 45.

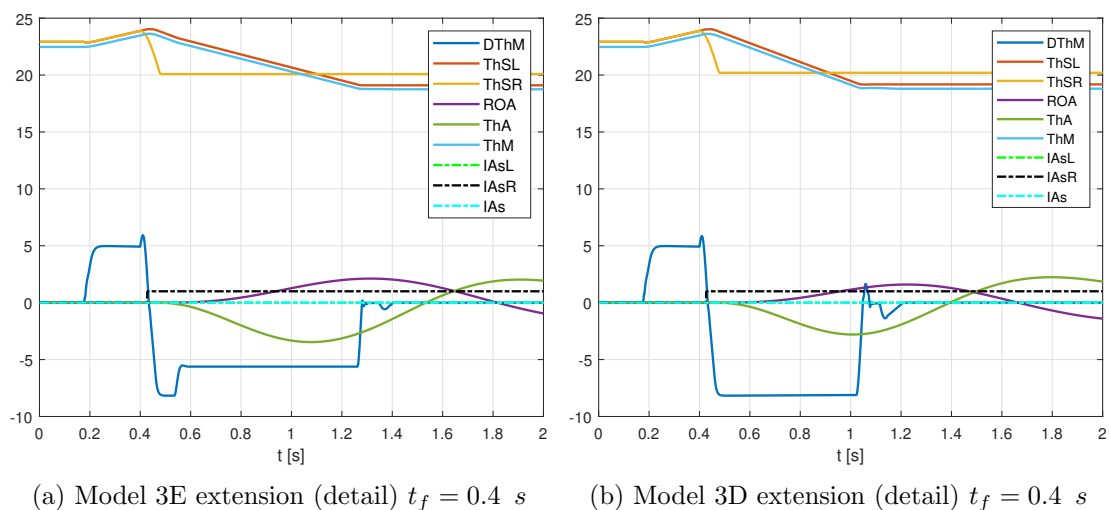
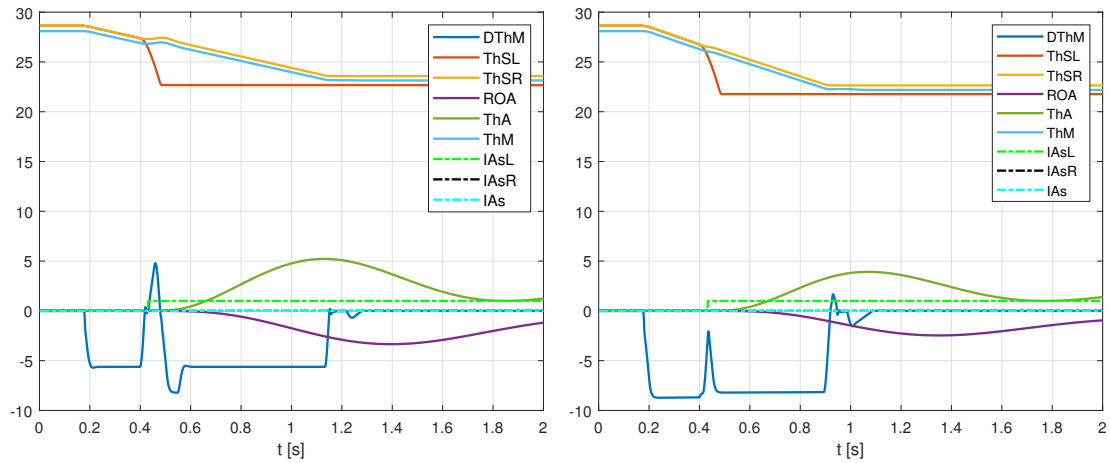


Figure 44: Comparison 3E & 3D right failure extension 0.4-0.5 rad at $T_{RC} = 10000Nm$

6.5 Comparison of active models on regular conditions

In general, the asymmetry active monitoring techniques seem to behave correctly in regular conditions.

In the previous pages, a deep comparison analysis of the active monitoring techniques was performed according to the input signal: either step input or ramp input models, since their characteristics were similar with the only difference of the input signal peculiarities. The aim was to better understand the effect of the input signal



(a) Model 3E retraction (detail) $t_f = 0.4$ s (b) Model 3D retraction (detail) $t_f = 0.4$ s

Figure 45: Comparison 3E & 3D left failure retraction 0.5-0.4 rad at $T_{RC} = 10000Nm$

and the reference position considered to perform the asymmetry control, regardless the *dynamic position* effect.

Nonetheless, is also important to analyze the active techniques behaviour according to the effect of the position anticipation term, considering models with the same input signal. This is the next step to identify the most efficient active model for each case, since the *dynamic position* implementation aimed to improve active model performances regardless the input signal. Therefore, a comparison of the active models behaviour on *regular wear-free conditions* according to the *dynamic position* effect for equal input signal models will be performed in the following pages.

6.5.1 General overview of low T_{RC} case results

The asymmetry active monitoring techniques can be grouped in two big categories when comparing their behaviour on *regular wear-free conditions* in low aerodynamic load scenarios.

- Step-input monitoring techniques (3 & 3D)
- Ramp-input monitoring techniques (3C & 3E)

In fact, the anticipation logics do not apply when considering low T_{RC} since the control parameter cancels the anticipation term, $\xi = 0$.

In general, the behaviour of the active models under low aerodynamic load is satisfactory.

As shown in figures 46 and 47:

- The step-input models responses are slightly more stable since their overshoot is a bit more dumped.
- The ramp-input models responses lead to slightly more maneuverable aircrafts. This is because the position at the failure time $\theta_i(t = t_f)$ is reached with little flap deflections, which entails a smaller τ_{br} .

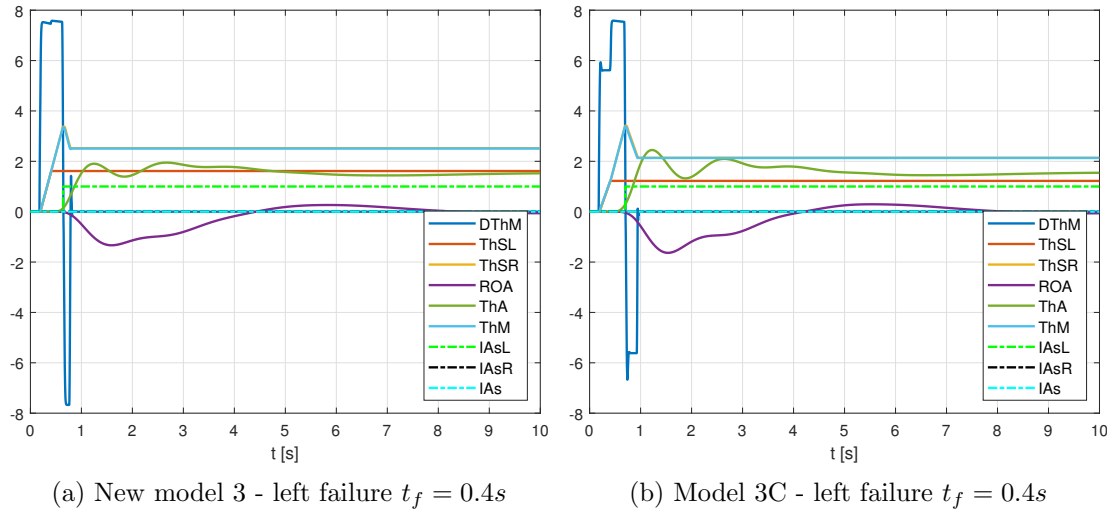


Figure 46: General overview at $T_{RC} = 0$ Nm - failure extension from 0 to 0.07 rad

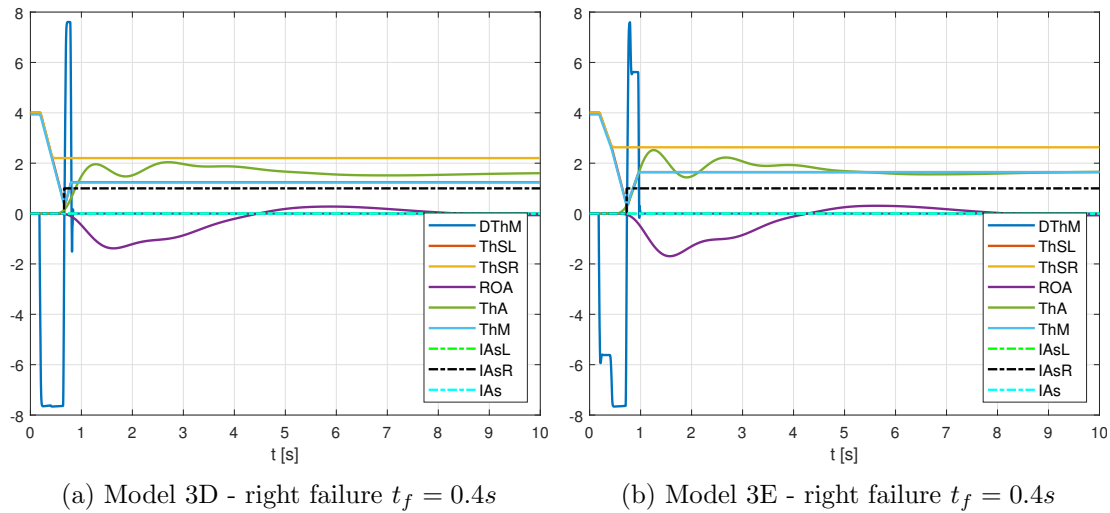


Figure 47: General overview at $T_{RC} = 0$ Nm - failure retraction from 0.07 to 0 rad

In any case, the response difference between active models is minimal. Thus, all the asymmetry active monitoring techniques are satisfactory in regular conditions.

6.5.2 General overview of high T_{RC} case results

Regarding the system response under high aerodynamic loads, a deep analysis has been done in 6.3.4 and 6.4.2 between active monitoring techniques with the same input signal, showing that there is little response difference in terms of stability and maneuverability.

However, in contrast to the low T_{RC} scenarios, the *dynamic position* is relevant to determine the system response, since $\xi = 1$ when T_{RC} is high enough. In fact, the main response difference between models lies in the position anticipation logic.

Hence, similarly to the previous load scenario, the asymmetry active monitoring techniques could be grouped in two big categories, regardless the input signal:

- *Dynamic-position* active monitoring techniques (3D & 3E).

- *Non dynamic-position* active monitoring techniques (3 & 3C).

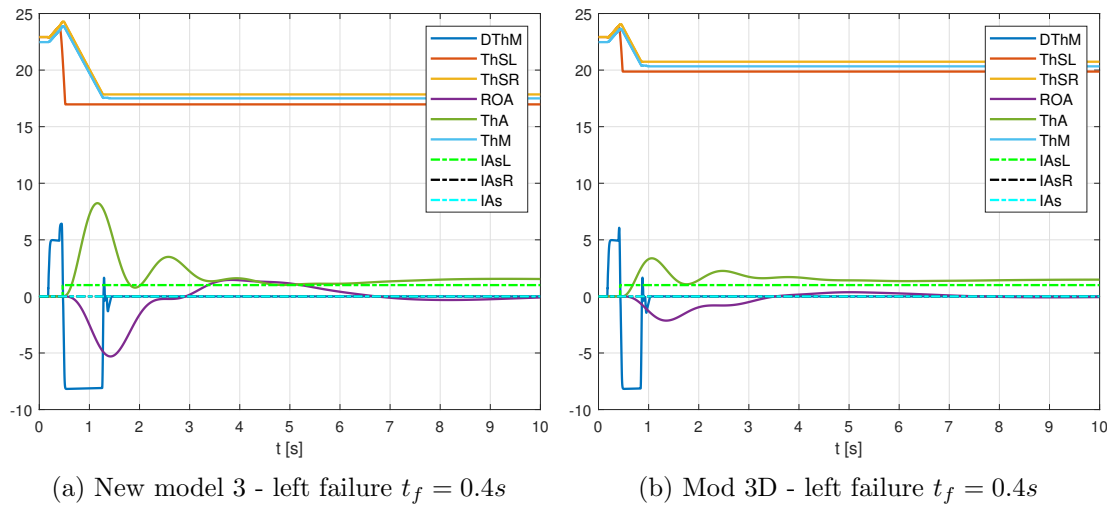


Figure 48: Overview step-input at $T_{RC} = 10000Nm$ - failure extension 0.4-0.5 rad

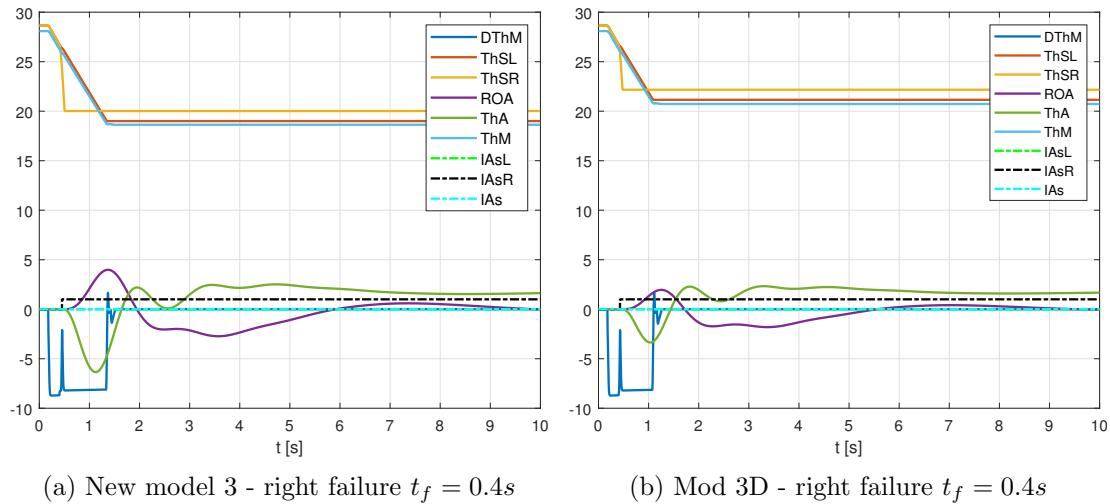


Figure 49: Overview step-input at $T_{RC} = 10000Nm$ - failure retraction 0.5-0.4 rad

In general, the behaviour of the active models under low aerodynamic loads is acceptable. Nonetheless, the response of the dynamic-position active monitoring techniques is much better than those that do not consider any position anticipation logic.

As shown in figures 48 and 49, there is a clear response improvement between the step-input models due to the effect of the *dynamic position*. In effect, it could be noted that:

- The response stability is much better of both of the aileron deflection θ_A and the aircraft roll angle ϕ_A , since the overshoot is notably damped. Such effect is more evident in extension than in retraction cases.
- The aircraft maneuverability after failure significantly increases given that the reduced $\theta_i(t = t_f)$ due to a smaller τ_{br} . Again, such effect is more relevant in extension than in retraction scenarios.

The same improvements are present in the ramp-input active monitoring techniques. As shown in figures 50 and 51, the system response stability is much better on model 3E than on model 3C (especially in the extension cases), as well as the aircraft maneuverability after failure.

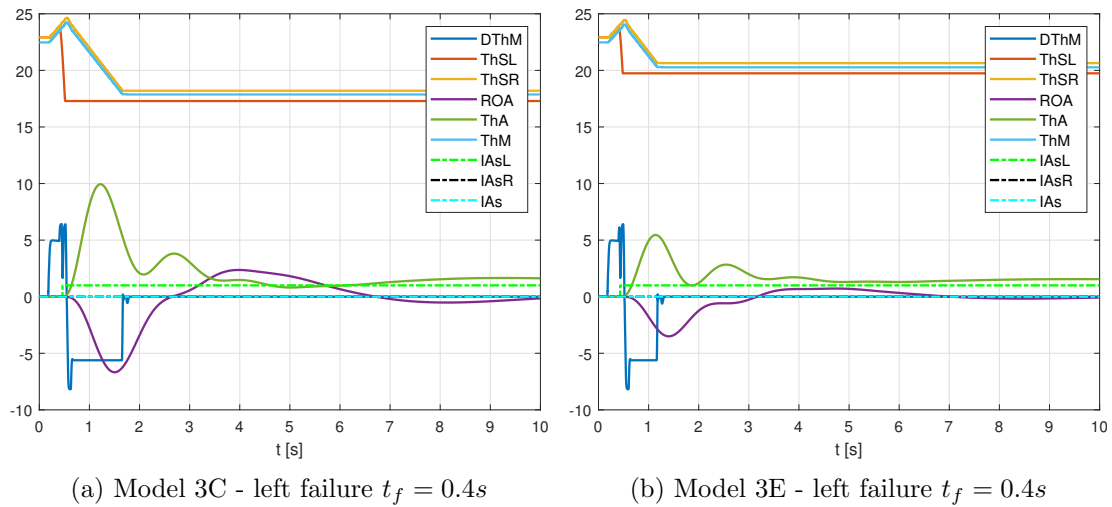


Figure 50: Overview ramp-input at $T_{RC} = 10000Nm$ - failure extension 0.4-0.5 rad

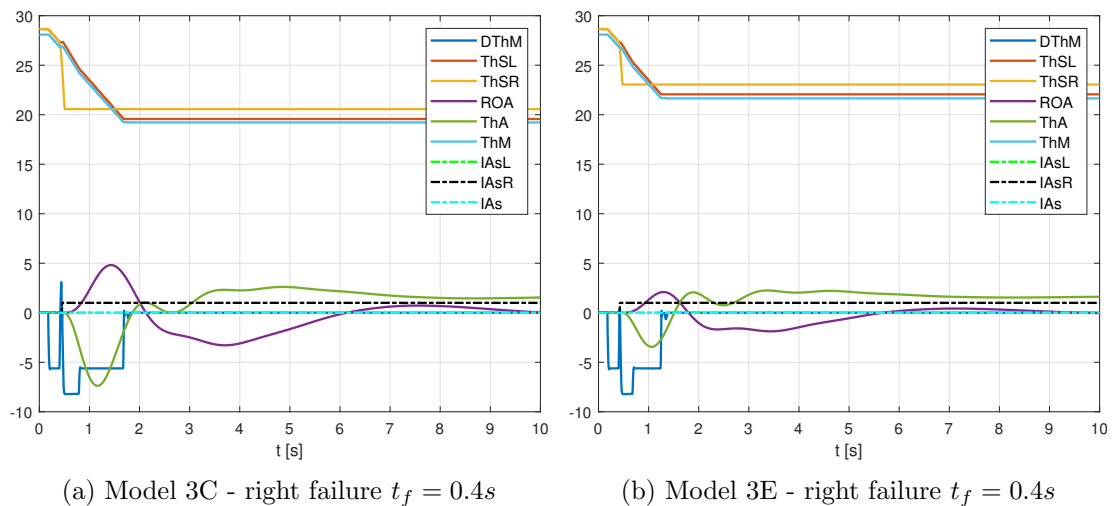


Figure 51: Overview ramp-input at $T_{RC} = 10000Nm$ - failure retraction 0.5-0.4 rad

In addition, as commented in 6.4.2, the effect of the Dem delays the steady-state conditions (reaching the failure surface) due to the little ramp slope that controls the operative surface deflection after failure. Therefore, the aircraft stability decreases. However, the aircraft maneuverability is better in the ramp-input models due to the τ_{br} reduction.

These considerations, together with the *dynamic position* improvements, will define the best models for high aerodynamic loads in regular conditions.

6.5.3 Summary table of active models on regular wear-free conditions

Finally, it follows a summary table that compares all the active models on the *regular wear-free conditions* studied in this chapter in order to analyze which behaves better in each situation (see Table 1). This table classifies both the active step-input and ramp-input monitoring techniques on *regular wear-free conditions* according to the different aerodynamic load cases, either in extension or retraction cases.

	Step-input models		Ramp-input models		
	3	3D	3C	3E	
Low T_{RC}	2	2	1	1	Extension
	2	2	1	1	Retraction
High T_{RC}	3	1	4	2	Extension
	3	1	4	2	Retraction

Table 1: Models efficiency classification on *regular wear-free conditions*

For that purpose, a numerical classification was used to quantitatively evaluate these models. These are ranked on a scale 1 to 5, 1 being the most efficient model and 5 the less efficient one. These numbers indicate the best-intermediate-worst model comparing all the active techniques according both to their dynamic response stability and the aircraft maneuverability after failure. Since the number is the result of the crossed comparison of all the active monitoring techniques, this is considered to be a numerical **relative** scale.

In addition, a color coding was also implemented to give a general overview of the active models behaviour in the considered regular conditions. Similarly, the color coding is based on three colors, green, orange and red. Green represents the most efficient models, orange the less efficient models, in both cases with satisfactory results, and red being the insatisfactory models in terms of efficiency, always for the current regular conditions.

In the light of the test results on *regular conditions*, some additional comments should be made:

1. The active monitoring techniques that consider an anticipation term by means of the *dynamic position*, behave much better than the non *dynamic position* active models in case of high aerodynamic loads.
2. Minor differences can be noted between the active models according to the input signal in case of low aerodynamic loads.
3. There are no differences between the same input-signal models in case of low aerodynamic load.
4. Great improvements can be noted between the active models marked in green and orange. Similarly, minor differences can be noted between the active models marked with the same color.

It seems that the models that behave better on *regular conditions* are:

- The *models 3D and 3E* in low aerodynamic load cases.

- The *model 3D* in high aerodynamic load cases.

Thus, in general, the *model 3D* is considered the *best* model to manage any load and deflection scenario due to two main characteristics:

- **The reference position θ_M varies according to a non-constant engine speed $\dot{\theta}_M$ which allows a fast and reliable asymmetry control.** It leads to a faster response in reaching the commanded position, increasing the system stability without compromising the aircraft maneuverability after failure. Therefore, it is not necessary to depend on a reference position based on constant ramp slope in regular conditions, which would delay reaching commanded position, decreasing the response stability.
- **The dynamic stability of the engine speed $\dot{\theta}_M$.** In fact, $\dot{\theta}_M$ is always stable in regular conditions, preventing from limit-cycle instability that may affect the position time evolution response.

Nonetheless, if the regular conditions are not always met, and the $\dot{\theta}_M$ dynamic stability is not always guaranteed. This issue, among others, will be analyzed in the following section, where the *borderline cases* will be discussed.

7 Aerodynamic wear-free borderline conditions

The *borderline cases* study the *extreme conditions* that affect the system either reducing the stability/manueverability onboard or compromising the flight safety, in the worst of cases.

These scenarios are called *aerodynamic wear-free borderline conditions*. These include:

- High external (aerodynamic) loads when deflecting from an angular position that is close to the minimum flap retraction. This operating condition considers a combination of both the aircraft speed V and angle of attack α that leads to a high T_{RC} ¹⁵.
- Reversible wear-free actuators.

It should be said that these conditions are not frequent on a normal flight. In fact, they assume a flight with a high speed at a high incidence before either extending or retracting the flaps from an angular position close to θ_{min} . This borderline case is quite unlikely since the aircraft clean configuration does not consider high angles of attack (cruise phase). On the other hand, high angle of attack with zero flap deflection does not consider high flight speeds due to both high lift-induced drag (landing phase) and the idle speed of the aircraft engines (commercial flight are considered).

Nonetheless, this aerodynamic wear-free borderline scenario allows to test the active asymmetry monitoring techniques in different aerodynamic *extreme conditions*.

Different critical scenarios arise from the combination of the extreme cases mentioned above.

In this section, a deep analysis of the extreme conditions effect on the asymmetry active techniques will be performed. It should be noted that the so-called “borderline conditions”, far from being rarely verified, may occur on a normal flight but they are extreme (more or less critical) regarding the active techniques asymmetry detection and/or correction.

Regarding the borderline case studied on this section, the extreme condition that harms the asymmetry control is the effect of high aerodynamic loads when deflecting the surface from an angular position that is close from the maximum flap retraction.

Should T_{RC} be high enough, the failure surface may quickly retract by the effect of the aerodynamic load. When regular conditions are considered, the failure surface failed far from the both the maximum and minimum flap deflection (see 6.5). Therefore, no position saturation was noted in regular conditions.

Nonetheless, the saturation position might be reached under high aerodynamic loads since:

$$\theta_i(t = t_f) \geq \theta_{min} \quad (7.1)$$

¹⁵linear aerodynamics may be considered in a first approximation

Therefore, position saturations might arise in some active models.

Consequently, a test campaign was performed to study the active models behaviour in these conditions considers the following actions, either for left and right surface failures:

- Extraction from 0 to 0.07 rad at $T_{RC} = 10000Nm$: extraction from a retarded position in flight.
- Retraction from 0.07 to 0 rad at $T_{RC} = 10000Nm$: retraction from a retarded position in flight.

Both cases are considered *maneuvers under high aerodynamic loads*, which was one of the two assumption of the *aerodynamic wear-free borderline conditions*.

In the following pages, the behaviour of the active monitoring techniques under aerodynamic borderline conditions with wear-free actuators will be analyzed.

7.1 New model 3 results - wear-free borderline case

In general, the non *dynamic position* asymmetry active monitoring techniques always present saturation on borderline cases with wear-free actuators. This is because they cannot anticipate the asymmetry failure with the inoperative surface speed, which increases considerably on high aerodynamic load scenarios, as mentioned earlier.

In fact, these models take too much time to react and stop the broken surface. In addition, when the failure position is close to the minimum angular position of the flap $\theta_i(t = t_f) \simeq \theta_{min}$ in case of high T_{RC} , the dimensionless braking time is too big to let the braking system stop the surface after failure before it reaches saturation. Such effect is present both with left and right failures.

In particular, the new model 3 results in the *extreme conditions* considering wear-free actuators are shown in figures 52 and 53.

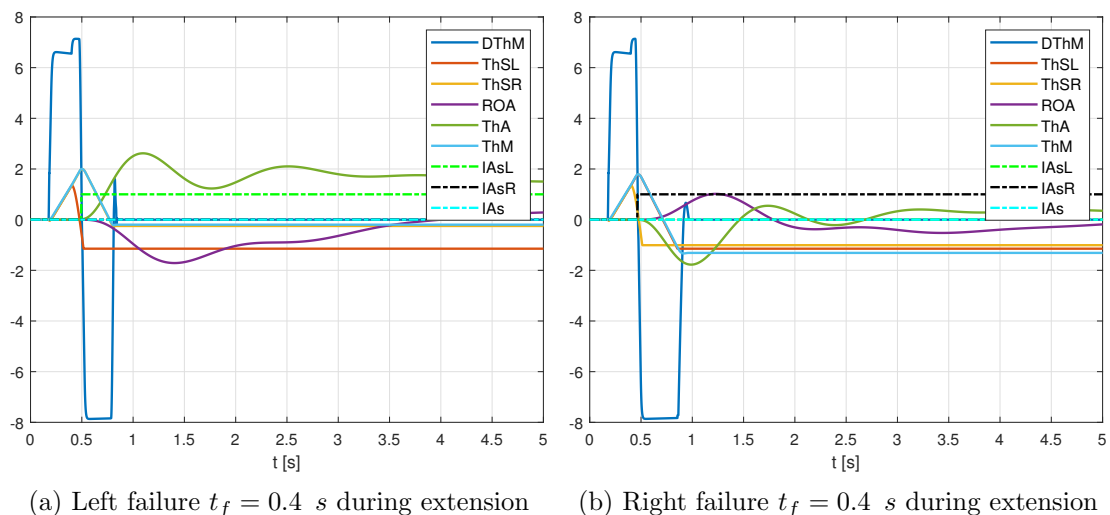


Figure 52: New model 3 - bord. case wear-free failure ext 0-0.07 rad $T_{RC} = 10000Nm$

It seems that the left surface reaches the lower position limit switch in every case by different reasons:

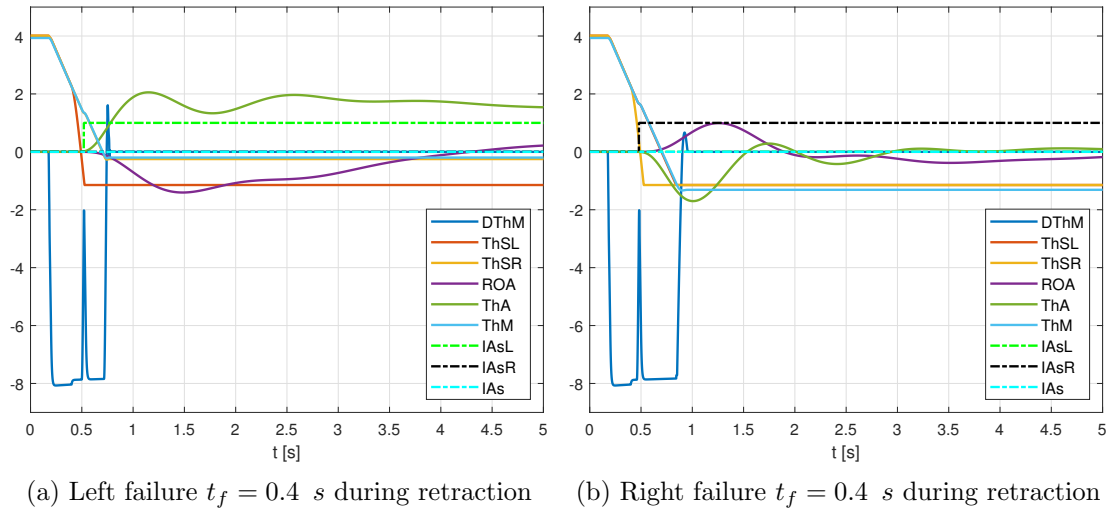


Figure 53: New model 3 - bord. case wear-free failure retr 0.07-0 rad $T_{RC} = 10000Nm$

- In case of left failure, the braking system cannot stop it before it reaches θ_{min} , especially in retraction scenarios, where the surface speed after failure is extremely high, which is particularly critical in left failure during retraction.
- In case of right failure, such surface is braked before reaching θ_{min} . Nonetheless, the left surface reaches the lower limit switch when correcting the asymmetry, due to the transducers offset.

In regard to the transducers offset $\theta_{Os, Ti}$ in surface saturation cases, the it always disadvantages the left surface.

$$\theta_{Os, Ti} = \begin{cases} +0.008 \text{ rad} & \text{if } i \equiv \text{left} \\ -0.008 \text{ rad} & \text{if } i \equiv \text{right} \end{cases} \quad (7.2)$$

Therefore, the right surface always stops in advance $\theta_{Os, Ti} < 0$ and the left surface always stops in arrears $\theta_{Os, Ti} > 0$. This causes the left surface saturation also in the right failure cases if it happens to stop close enough to θ_{min}

It should be noted that reaching the mechanical limit switch carries important consequences:

- Should a failure arise when extending the flaps, no surface would reach any extended position after failure. In fact, both flaps stop on retracted “hidden” positions $\theta_{i, ss} < 0$, which is critical in flight phases where high-lift devices are needed (i.e. landing phase).
- Should a failure arise when retracting the surfaces, the steady-state position consequences might be less critical but also important, especially if very small flap retraction were commanded.
- The failure surface is forced to reach such position by an impact that brakes instantaneously the flap retraction. This could damage the flap, the mechanical transmission and even the internal structure, compromising the flight safety in the worst cases.

To solve this problem, a *dynamic position* logic should be considered to anticipate the failure especially in such borderline conditions.

7.2 Model 3D results - wear-free borderline case

In regard to the *dynamic position* asymmetry active monitoring techniques on borderline cases due to high aerodynamic loads, the anticipation term is always active on models 3D and 3E. In effect, the control parameter is always $\xi = 1$ since the aerodynamic load is always high enough to activate the speed term of the *dynamic position*. This is a great advantage of the borderline cases, in which the anticipation term is always needed due to the high retraction speed of the inoperative surface after failure.

In addition, the model 3D does not present saturation with the extension/retraction maneuvers considered in this project. This is the consequence of the combined effect of both the “dynamic” term that anticipates the asymmetry failure and the reference position θ_M , which varies according to the engine speed $\dot{\theta}_M$, which are key to prevent the surfaces from reaching the mechanical lower limit switch θ_{min} .

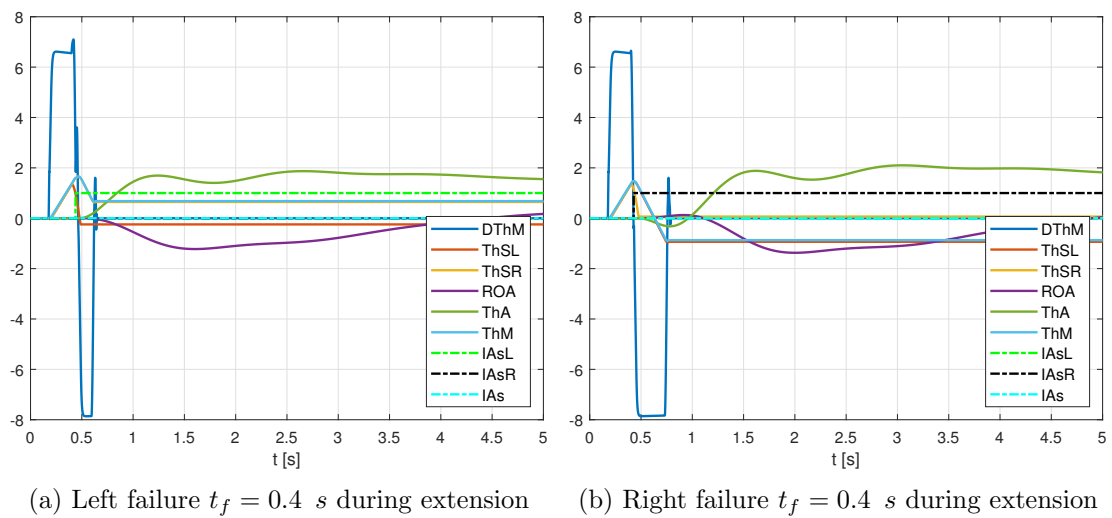


Figure 54: Model 3D - bord. case wear-free failure ext 0-0.07 rad $T_{RC} = 10000Nm$

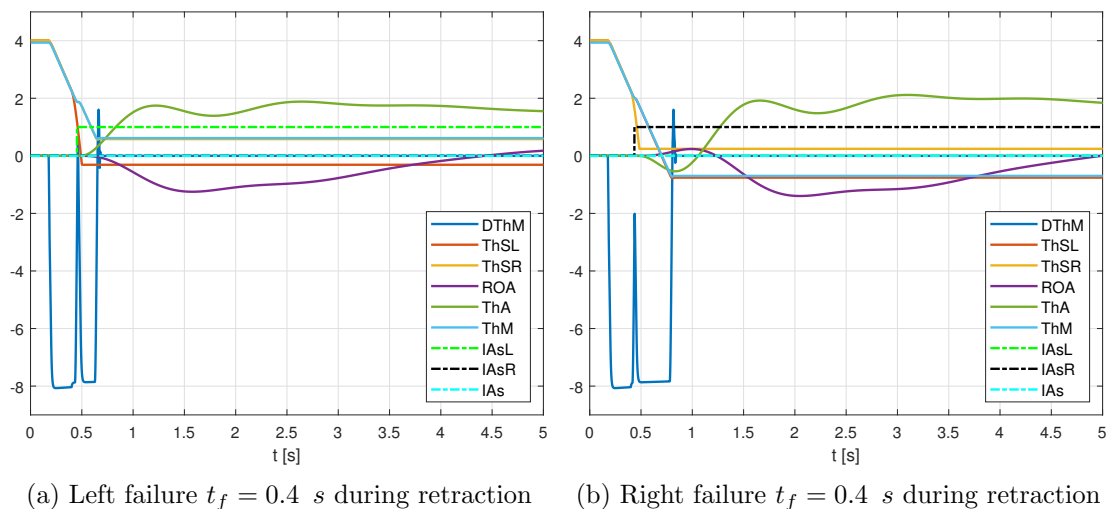


Figure 55: Model 3D - bord. case wear-free failure retr 0.07-0 rad $T_{RC} = 10000Nm$

As seen in figures 54 and 55, neither the failure surface nor the operative one reach

θ_{min} when correcting the asymmetry.

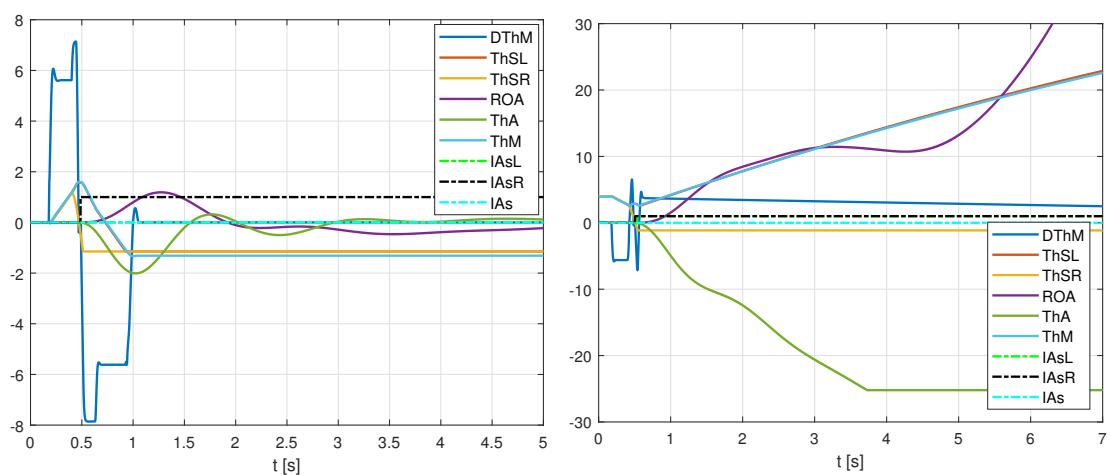
Model 3D improves all the negative consequences the new model 3 faced:

- Should a failure arise when extending the flaps, at least the operative surface would reach an extended position after failure, $\theta > 0$. This solves part of the problem that arose in the previous model since some lift will be provided by the high-lift devices during landing. Nonetheless, the ailerons would both correct the rolling moment and provide the extra lift necessary for landing if possible. Otherwise, longer landing field lengths would be necessary.
- Should a failure arise when retracting the surfaces, the steady-state position consequences might be less critical than in the previous model. This improvement is especially important if very small flap retraction are commanded, in which case the right surface may reach not significantly differ from commanded position (see figures 55a and 55b).
- Regarding the system structural integrity (aerodynamic surfaces, mechanical transmissions...), there will be no impacts if the mechanical lower limit switch of the flap is reached. Therefore, no further damages critical condition will be added to the position asymmetry problem.

7.3 Model 3A results - wear-free borderline case

The behaviour of the active monitoring technique 3A in aerodynamic borderline cases with wear-free actuators is decisive to understand the main improvements of model 3C on such conditions.

Firstly, the model 3A presents a detrimental behaviour in these conditions, especially in right failure scenarios. In fact, the model 3A presents a double-surface saturation in retraction and a completely *lack* of control in case of retraction, both when the right surface fails. Both cases are illustrated in Figure 56.



(a) Right failure $t_f = 0.4s$ extension 0-0.07 rad (b) Right failure $t_f = 0.4s$ retraction 0.07-0 rad

Figure 56: Model 3A - bord. case wear-free right failure at $T_{RC} = 10000Nm$

The first and most important problem of model 3A on aerodynamic borderline conditions is the *lack* of control in retraction should a right failure arise (Figure 62b).

This scenario is extremely critical because:

- The model correctly detects the *partial asymmetry* of both the left and the right surface.
- The combination of high aerodynamic load and flap retraction from an angular position that is close to θ_{min} is not uncommon in a real flight.

The description of such critical and dangerous failure is detailed hereunder:

1. The right failure is produced at $t_f = 0.4 s$
2. An inexistent left failure is detected shortly after the previous one. It is produced by the operative surface position fast deviation due to the engine speed peak $\dot{\theta}_{M,max}$ caused by the failure surface loss and the consequent reduction of the effective aerodynamic load on the system. In fact, T_{RC} halves and the operative surface, powered by the engine, deviates from the reference position Dem , which charges the *partial asymmetry counter* until the failure declaration.
3. The system cannot manage two *partial failures*, since it follows an exclusive algorithm logic that only considers single-failure scenarios. Hence, the algorithm always chooses the left failure over the right one, which leads to a detrimental behaviour since the active model will try to correct an asymmetry that does not even exist. Consequently, the active technique commands confuses both the operative and the inoperative flap.
4. The control algorithm tries to command the failure “right” surface to reach the operative “left” surface by increasing the engine speed to extend the right flap. Nonetheless, the effect is completely the opposite: the left surface is the one powered by the engine, which should be retracted to reach the failure flap, but it is extended instead, diverging indefinitely from the inoperative flap tending to the θ_{max} .
5. The left brake is activated once the left failure failure is detected, which should stop the flap, preventing the divergence problem. However, this surface is also powered by the engine to perform the correction maneuver. Unfortunately, the engine torque applied to the surface is greater than the braking torque of the braking system. Hence, the left surface diverges even though the left brake is active.

The braking system could be designed to perform greater torques to avoid this left flap divergence problem. Nonetheless, this would become the design point for the braking system, oversizing it.

These effects are illustrated in Figure 57, where the electrical variables are plotted.

The main flaws of model 3A that cause this situation are:

- The absence of a *general failure* declaration. This would stop the divergence of the operative surface, braking both flaps. Such emergency action is included on model 3C.

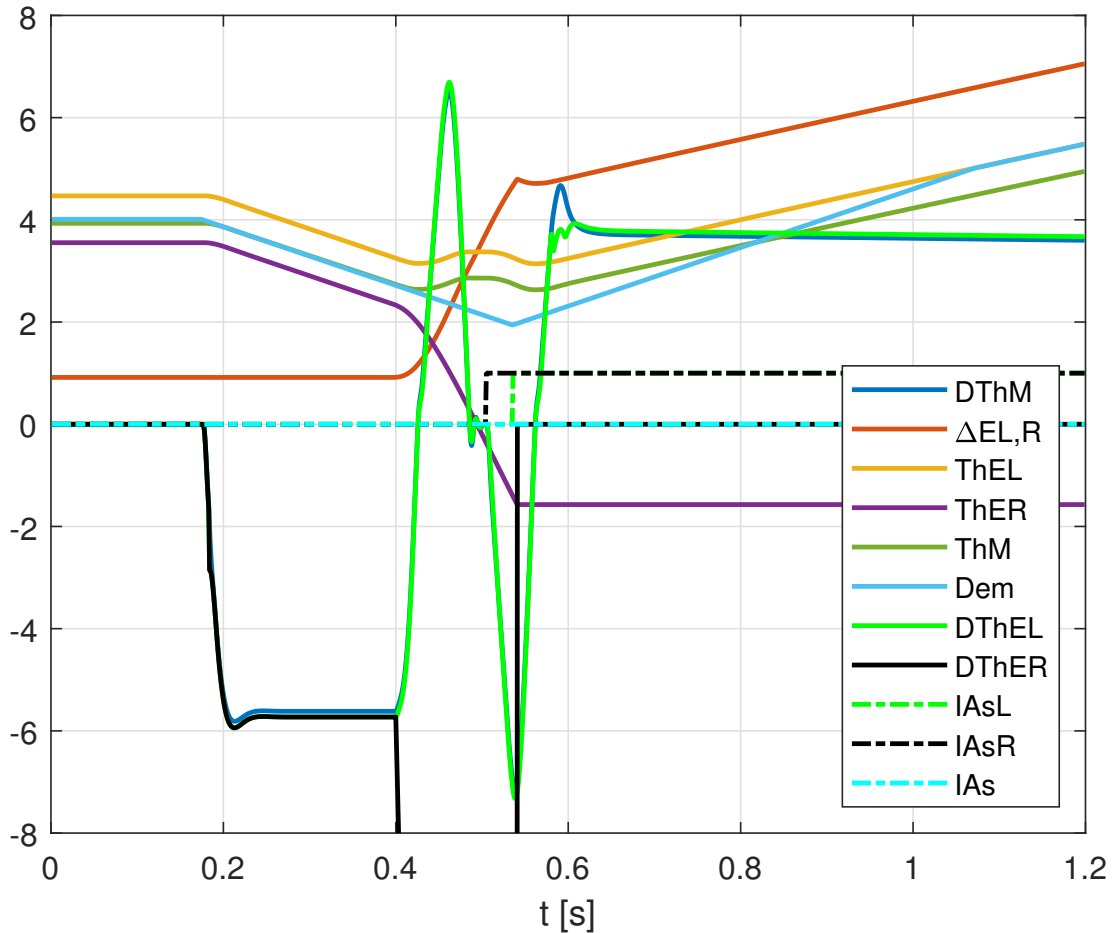


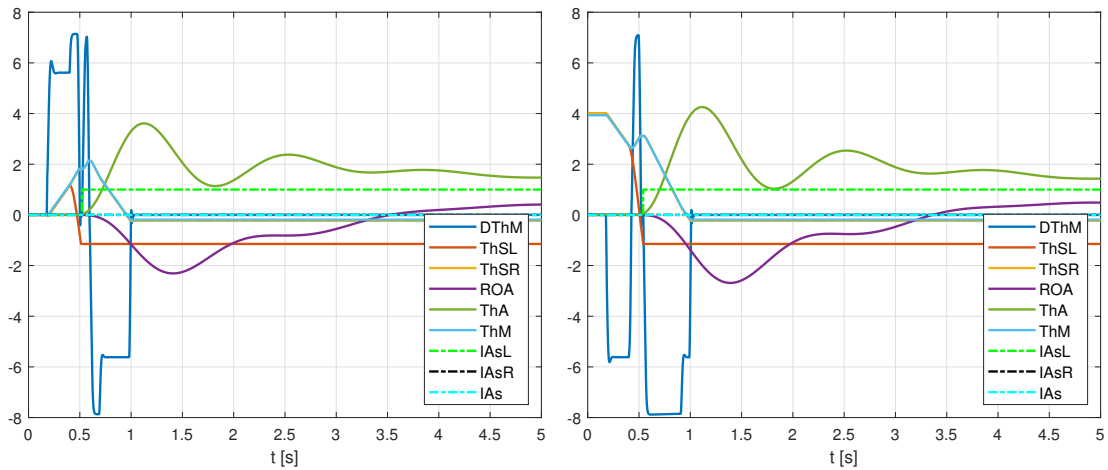
Figure 57: Model 3A (electrical) lack of control right failure retraction (detail)

- The asymmetry management only considers a single-failure scenario by means of a sequential exclusive logic. It always gives preference to the left failure instead of analyzing which is the present situation. Therefore, a double-failure scenario in which the first failure happen to be on the right transmission will always manifest a complete lack of control, as described above.

It should be reiterated that the asymmetry monitoring techniques are not designed to manage a multiple asymmetry scenario. In fact, the sequential exclusive logic of the control algorithm seems valid for single failure scenarios. Nonetheless, should a multiple failure case arise, this logic leads to divergent system responses, as mentioned above. Future research projects may study the asymmetry correction algorithm in case of either false or real double asymmetry failure scenarios.

On the contrary, the left failure scenarios of model 3A present the same saturation problems than model 3, but with an additional *partial failure* declaration delay. In effect, the upper threshold of the partial asymmetry counter detector is too high, doubling the threshold value of model 3. This effect is shown in Figure 58.

Moreover, should the right failure arise during extension (Figure 56a), the inoperative (right) surface reaches the mechanical lower limit switch, which never happened on model 3. Therefore, the left surface will impact such mechanical limit as well due to the transducers offset setting, which always happened on model3. Thus, a double-



(a) Left failure $t_f = 0.4s$ extension 0-0.07 rad (b) Left failure $t_f = 0.4s$ retraction 0.07-0 rad

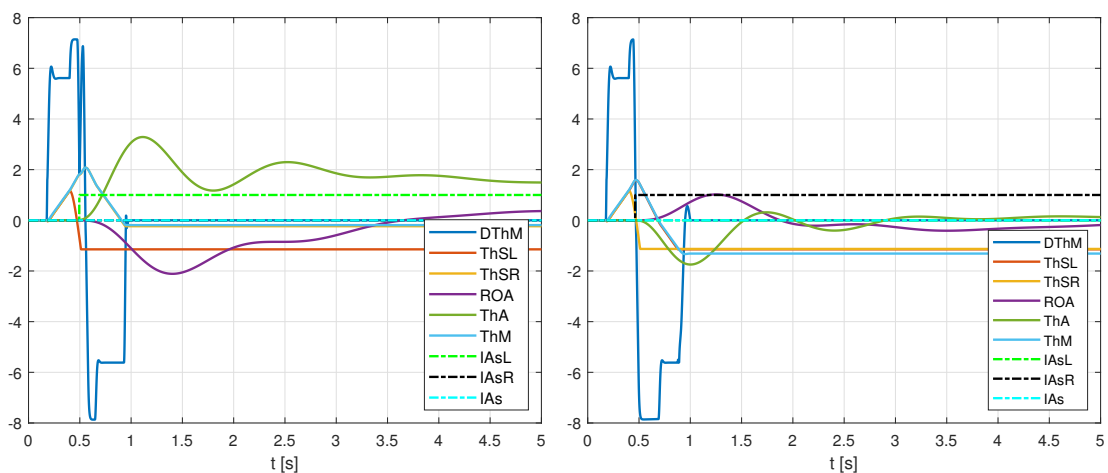
Figure 58: Model 3A - bord. case wear-free left failure at $T_{RC} = 10000Nm$

surface saturation is produced, which never happened before, but it can happen also on model 3 if the aerodynamic load increases.

7.4 Model 3C results - wear-free borderline case

As mentioned in 5.3.3 and 6.3.2, the active monitoring technique 3C improves behaviour of the old model 3A, also in aerodynamic borderline cases with wear-free actuators. In effect, the model 3C improves the aircraft stability and maneuverability in any case, as happened in regular conditions. In addition, the aircraft controllability in case of right failure during retraction is clearly higher on model 3C with respect to model 3A, in which the aircraft was uncontrollable. Nonetheless, 3C works worse than model 3 on the current extreme conditions.

Follow the test results of model 3C in aerodynamic borderline cases with wear-free actuators, shown in figures 59 and 60.



(a) Left failure $t_f = 0.4 s$ during extension (b) Right failure $t_f = 0.4 s$ during extension

Figure 59: Model 3C - bord. case wear-free failure ext 0-0.07 rad $T_{RC} = 10000Nm$

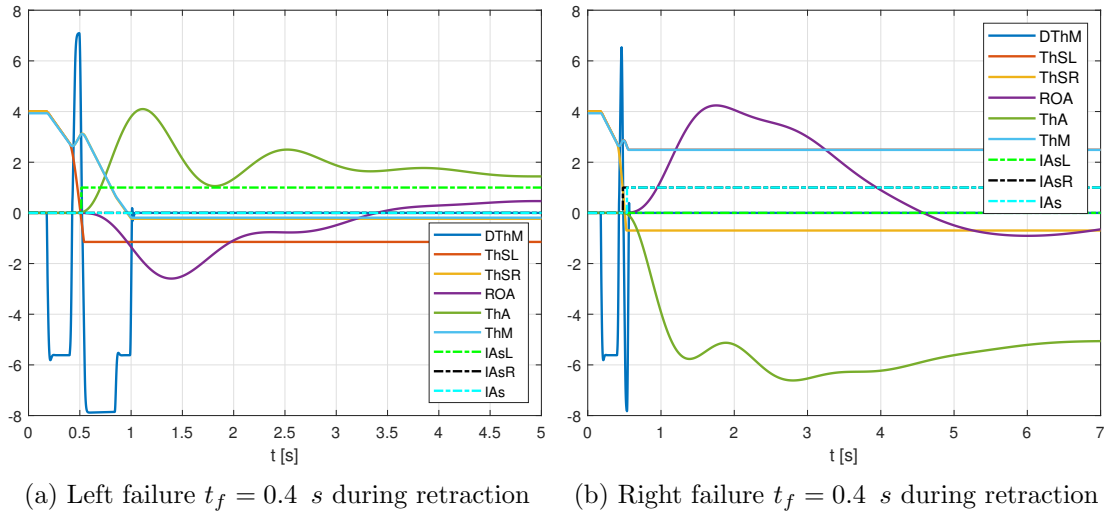


Figure 60: Model 3C - bord. case wear-free failure retr 0.07-0 rad $T_{RC} = 10000Nm$

On the one hand, the model 3C slightly improves the behaviour model 3A in terms of response stability and the aircraft maneuverability. Indeed, the effect of the lower threshold of the *partial asymmetry* counter $I_{Wrn,i}^{thr}$ “anticipates” the *partial asymmetry failure* declaration, slightly reducing the time braking after failure t_{br} . The best proof of this behaviour of 3C is that it corrects the double-surface saturation illustrated in Figure 56a. In fact, only the left surface saturates in 3C as happened in 3 due to the transducers offset θ_{O_s, T_i} . Such improvements are shown in Figure 61.

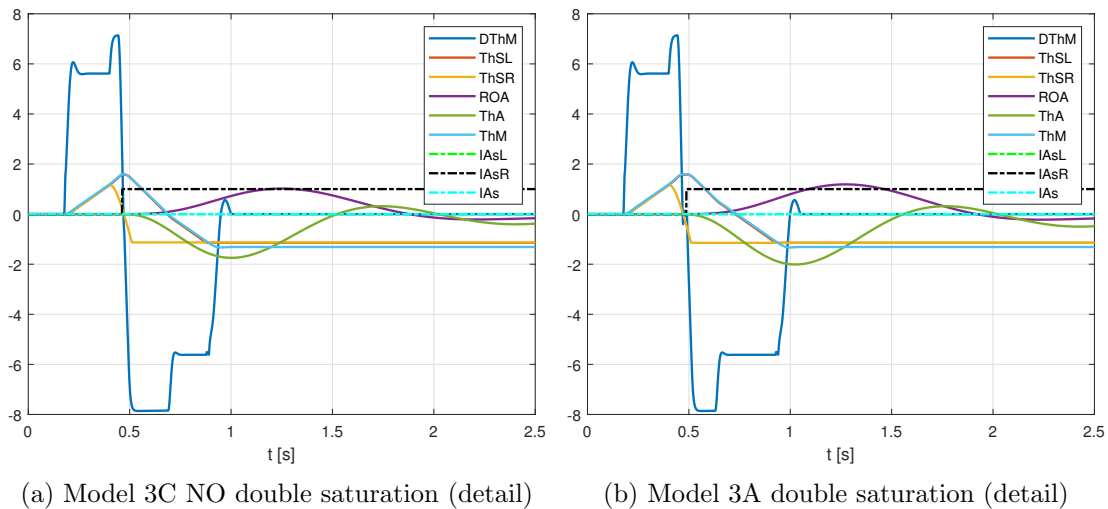


Figure 61: Model 3C vs 3A $t_f = 0.4s$ right failure extension 0-0.07 rad $T_{RC} = 10000Nm$

In regard to the improvement of the aforementioned model 3A in the lack of control scenario (right failure during retraction), the active monitoring technique 3C considers a general asymmetry case adding the corresponding indicator I_A . Hence, the model brakes both flaps in case of operative surface divergence. This is considered as an emergency measure that prevents the system from compromising the flight safety.

Thus, although the false multiple failure is not managed correctly, (the preference is always given to the left surface), the general failure declaration increases the system

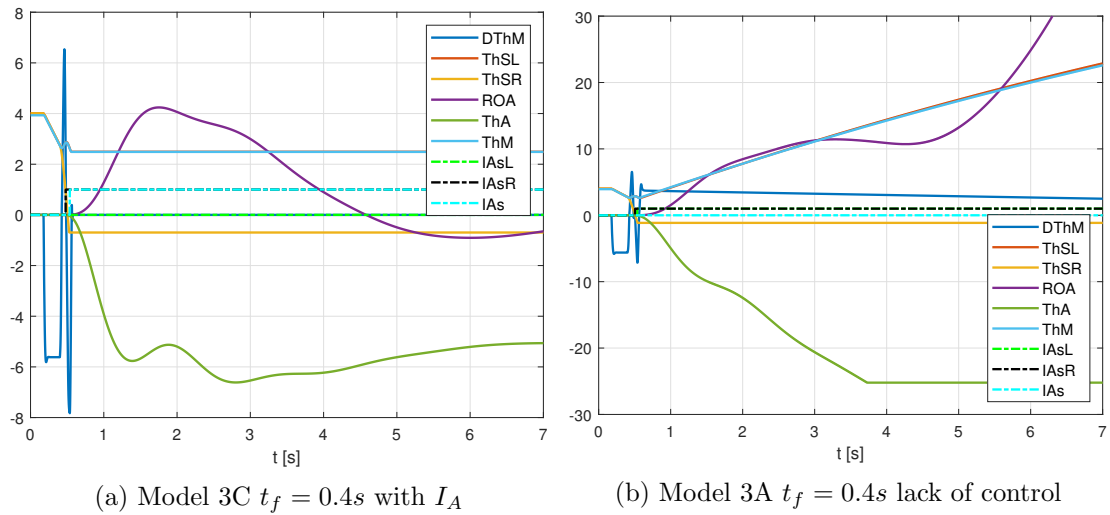


Figure 62: Model 3C vs 3A general right failure retr 0.07-0 rad at $T_{RC} = 10000Nm$

reliability and robustness. In addition, it both prevents from any surface saturation and contributes to the model consistence with the purpose of declaring either the partial or the general asymmetry failure.

Nonetheless the aircraft maneuverability the stability margin of the response decrease since the failure is not mitigated but contained. Therefore:

- The differential position between both flaps is too big affecting the aircraft maneuverability
- The divergence period before the *general failure* declaration reduces the stability margin of the aircraft dynamic response.

All this is illustrated in Figure 62. Moreover, the effect of the *general asymmetry failure* logic, by means of I_A is shown in Figure 63, where the electrical variables are plotted.

Future lines of research might study different ways of solving the false multiple failure scenarios, such as identifying which surface is still powered by the engine, even though both *partial asymmetry failures* have been declared, and correct the right asymmetry.

On the other hand, the model 3C, in general, behaves worse than the new model 3 in aerodynamic borderline condition with wear-free actuators, especially in retraction cases, affecting the aircraft response stability. Nonetheless, the maneuverability remains almost unaltered except in the lack of control correction case (right failure during retraction scenario), where both stability and maneuverability are seriously affected, always preserving the flight safety.

- On extension maneuvers, the effect of the ramp slope delays the instant in which the operative surface reaches the inoperative surface position, which decreases the stability margin of the aircraft rolling response. Nonetheless these effects do not seriously compromise the aircraft lateral-directional stability.
- On retraction maneuvers, the control effect of model 3C increases significantly the overshoot of the roll angle ϕ_A , which decreases the stability margin of the

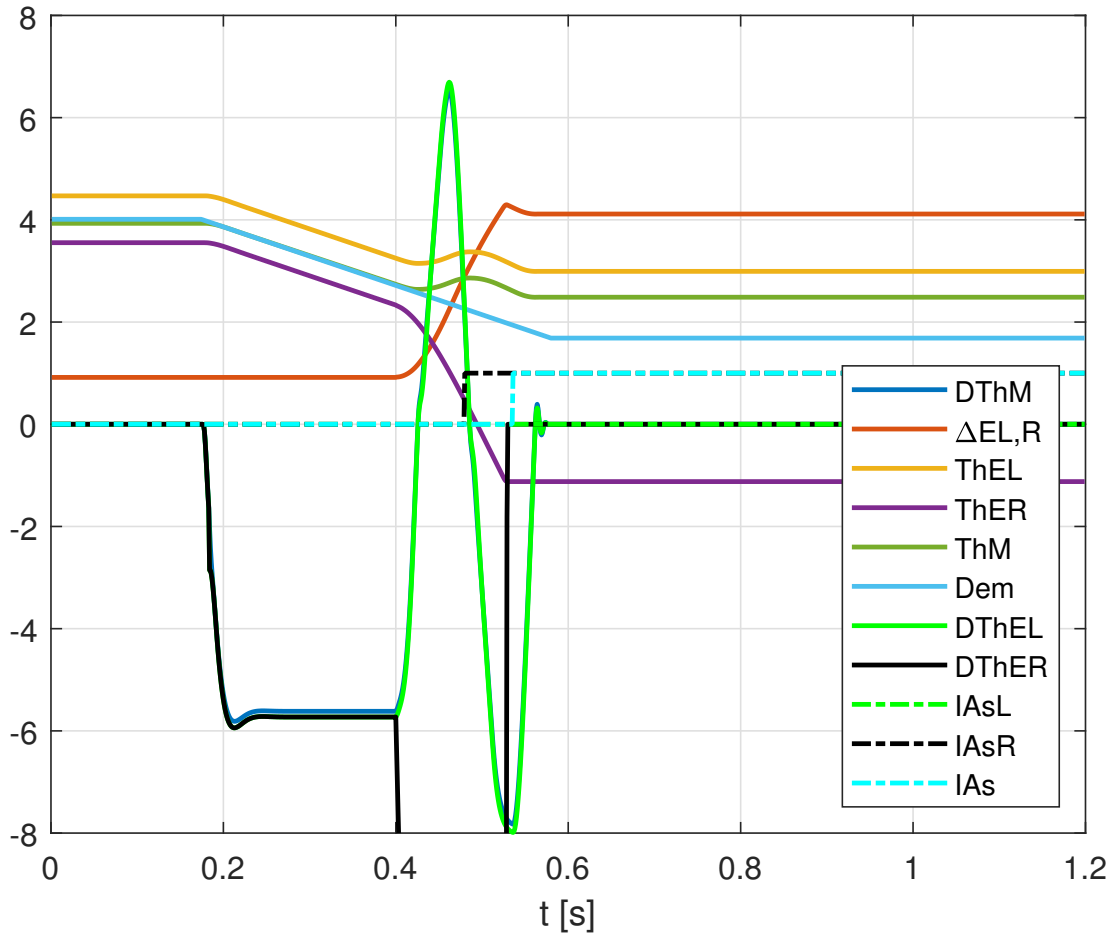


Figure 63: Model 3C (electrical) general asymmetry I_A right failure retraction (detail)

aircraft lateral-directional response. In addition, the aircraft maneuverability after failure of model 3C decreases in case of right failure during retracting, when the *general asymmetry failure* brakes both flaps to preserve the aircraft flight safety, regardless their notably different angular position.

- Little oscillations before the failure declaration can be noted on model 3C results, unlike on model 3. These are caused by the combined effect of the constant ramp slope of the reference position Dem and the engine speed peak $\dot{\theta}_{M,max}$ after failure. In effect, the lack of peak in the reference position Dem delays the failure declaration, while the $\dot{\theta}_{M,max}$ activates/deactivates the *Slow* parameter, causing little oscillations that disappear once any failure is declared. These do not appear on model 3, since its reference position θ_M varies according the $\dot{\theta}_M$, increasing the difference between the failure surface and the reference position, which leads to an earlier failure declaration, increasing the dynamic stability of the rolling response.

All these is shown in Figures 64.

In conclusion the asymmetry active monitoring technique 3C:

1. Behaves better than model 3A concerning the stability and maneuverability of the aircraft after failure. In addition, the model 3C is a reliable a robust model

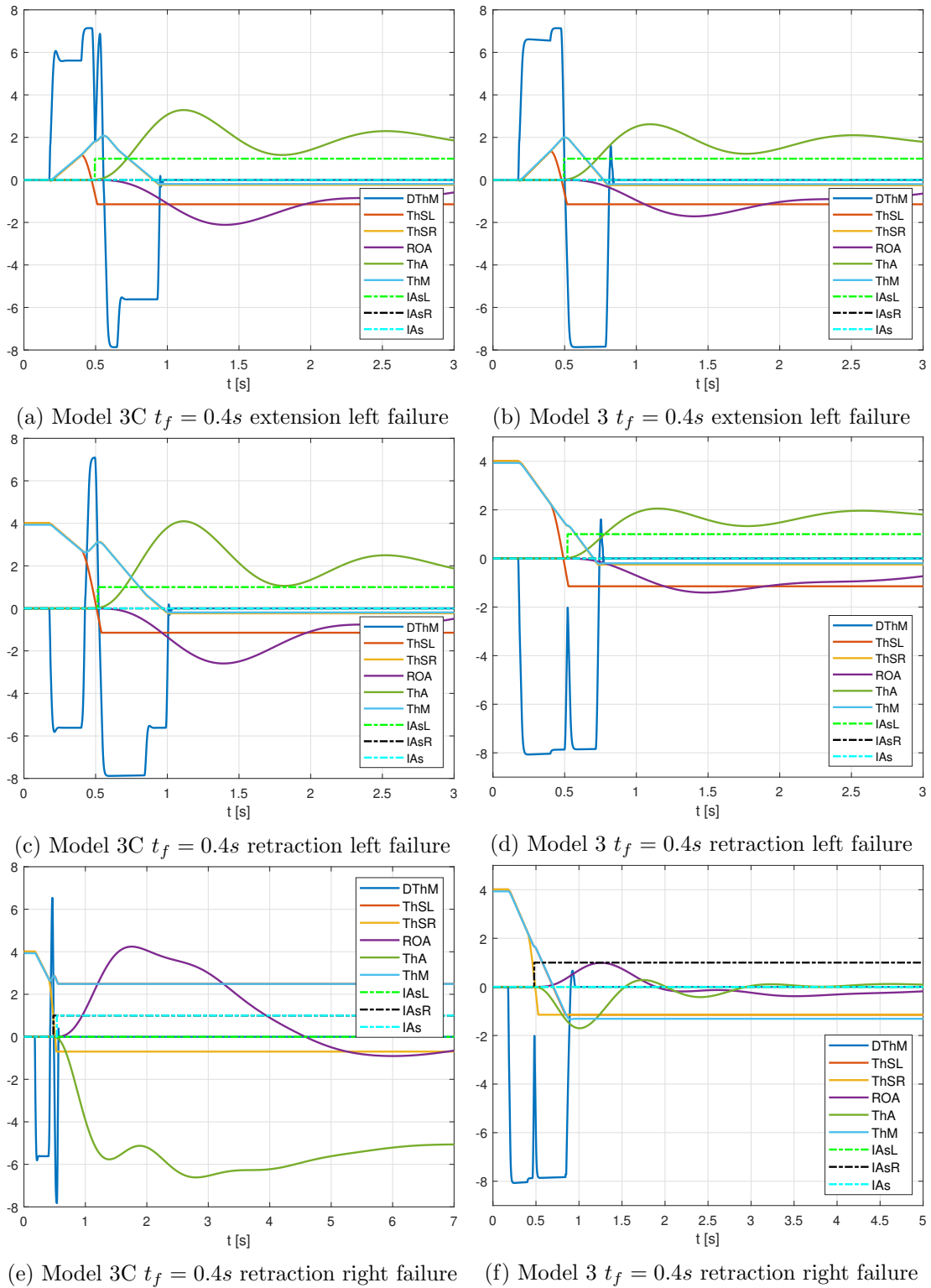


Figure 64: Model 3C vs 3 - bord case wear-free failure at $T_{RC} = 10000Nm$ (detail)

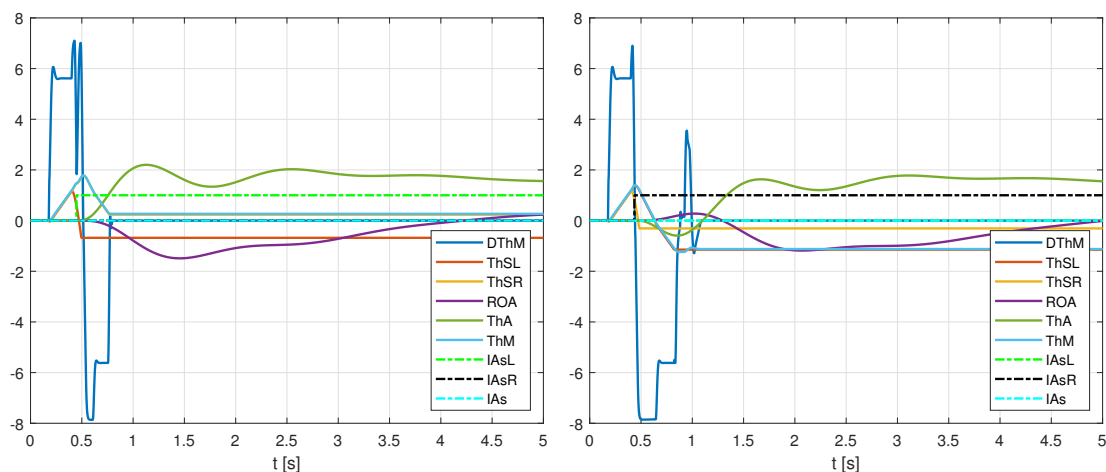
that prevents from a detrimental correction behaviour regarding both the surfaces saturation and preserving the flight safety.

2. Leads to a lower stability and maneuverability after failure compared with model 3 due to the reference position Dem . Such demand signal Dem causes both a significant delay when reaching the failure surface (affecting the reponse stability) and a delay when declaring the *partial asymmetry failure* (especially in retraction compared with 3), since Dem is independent from the engine variation.
3. Little oscillations before the failure declaration can be noted on model 3C results, unlike on model 3, due to the combined effect of the constant ramp slope of the reference position Dem and the engine speed peak $\dot{\theta}_{M,max}$ after failure.

Thus, model 3 seems to be better than model 3C in aerodynamic borderline cases with wear-free actuators, where the engine speed $\dot{\theta}_M$ variations are “stable” (no limit-cycle effects are present on $\dot{\theta}_M$).

7.5 Model 3E results - wear-free borderline case

The asymmetry active monitoring technique 3E in aerodynamic borderline cases with wear-free actuators shares the benefits of model 3C and improves the asymmetry correction response exploiting the high retraction speed after failure of the inoperative surface. This is key to anticipate the asymmetry detection and improve consequently both the stability of the aircraft response and the vehicle maneuverability after failure.

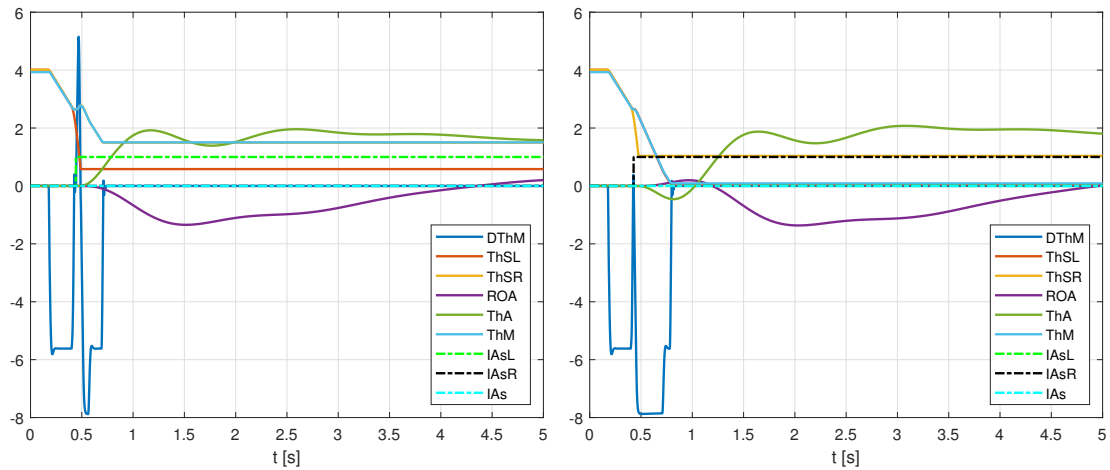


(a) Left failure $t_f = 0.4$ s during extension (b) Right failure $t_f = 0.4$ s during extension

Figure 65: Model 3E - bord. case wear-free failure ext 0-0.07 rad $T_{RC} = 10000Nm$

The anticipation effect of the *dynamic position* is particularly important on ramp-input models regarding the little oscillations of model 3C, which are either mitigated or cancelled on the active model 3E. In fact, anticipating the failure has a similar effect than the reference position peak of model 3 $\theta_{M,max}$ according to the same peak of $\dot{\theta}_{M,max}$, always present after failure when T_{RC} is high enough.

Regarding the surface saturation phenomena, the model 3E only presents saturation on the right failure during extension scenario due to the adverse effect of the transducers offset θ_{O_s, T_i} .



(a) Left failure $t_f = 0.4$ s during retraction (b) Right failure $t_f = 0.4$ s during retraction

Figure 66: Model 3E - bord. case wear-free failure retr 0.07-0 rad $T_{RC} = 10000Nm$

Moreover, the false multiple asymmetry failure declaration disappears with the anticipating effect of the *dynamic position*.

These results are illustrated in figures 65 and 66.

Nonetheless, the behaviour of the active model 3E compared with the corresponding *dynamic position* step-input technique 3D depends on the maneuver performed with the flaps, always considering aerodynamic borderline conditions with wear-free actuators :

- Should a failure arise during extension, the active model 3E behaves slightly worse than 3D, regarding both the rolling response stability and aircraft maneuverability after failure. The slow reference position Dem is responsible of a more retracted failure position $\theta_i(t = t_f)$ leading to higher time to break after failure t_{br} , which implies both a greater surface saturation risk due to its proximity to θ_{min} and a lower the aircraft maneuverability after failure. In addition, the effect of the slow reference position Dem delays the operative surface correcting maneuver of reaching the inoperative flap, which reduces the stability margin of the aircraft rolling response. All these is illustrated in Figure 67.
- Should a failure arise when retracting the surfaces, 3E behaves better than 3D and, consequently, notably better than 3, regarding both the rolling response stability and aircraft maneuverability after failure. In this case, the slow and more controlled ramp slope Dem reduces the surface speed before failure, which increases the speed difference between the failure surface and the reference position after failure. Hence, the asymmetry failure is declared earlier on the ramp-input model 3E than in the active step-input models, in which the retraction engine speed is so high that the reference position peak after failure $\theta_{M,max}$ is too small or even inexistent, which causes a larger delay in asymmetry detection, affecting stability and maneuverability. Thus, the active technique 3E presents higher rolling response stability and aircraft maneuverability after failure than both step-input models 3D and 3. These considerations can be noted in Figure 68.
- Regarding the system structural integrity (aerodynamic surfaces, mechanical transmissions...) on extension failures, the only aggressive impact would be on the left

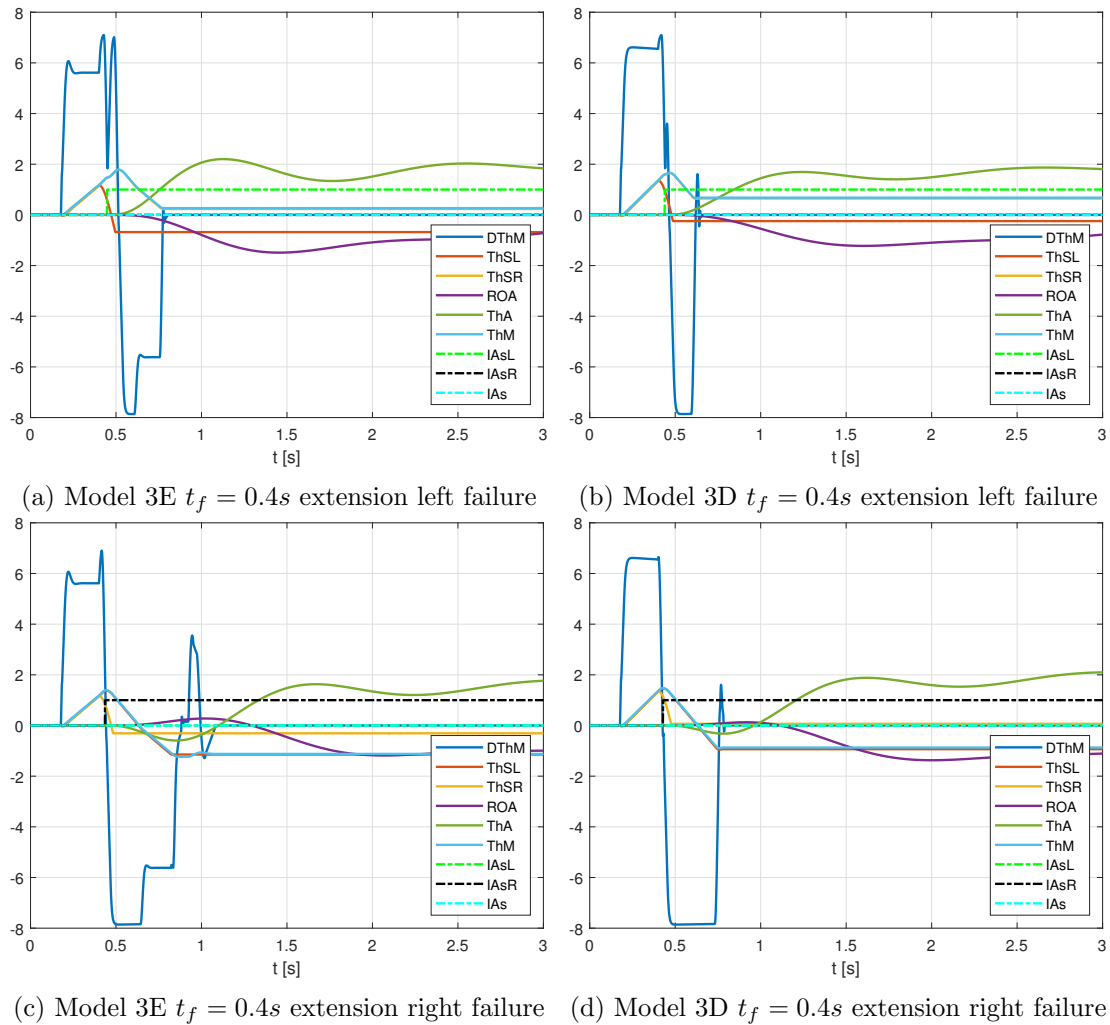


Figure 67: Model 3E vs 3D bord case wear-free extension failure at $T_{RC} = 10000Nm$ (detail)

failure case due to the high left surface speed right before reaching the mechanical θ_{min} . Nonetheless, in the right failure surface scenario, the Dem slope would decrease the left operative surface speed during correction, so the impact would be less critical once it reaches the the mechanical lower limit switch θ_{min} .

Thus, the behaviour of the active technique $3E$ compared with the $3D$ can be summarized as follows:

1. In case of asymmetry failure during extension, the stability margin of the aircraft rolling dynamic response is a slightly lower on $3E$ than on $3D$. Furthermore, the maneuverability after failure using model $3E$ is lower than in case of model $3D$.
2. In case of asymmetry failure during extension, the aircraft rolling dynamic response of $3E$ is more stable than the corresponding response of model $3D$. Furthermore, the maneuverability after failure using model $3E$ is higher than in case of model $3D$.

7.6 Comparison of active models on wear-free borderline conditions

In general, the asymmetry active monitoring techniques seem to behave correctly in aerodynamic wear-free borderline cases.

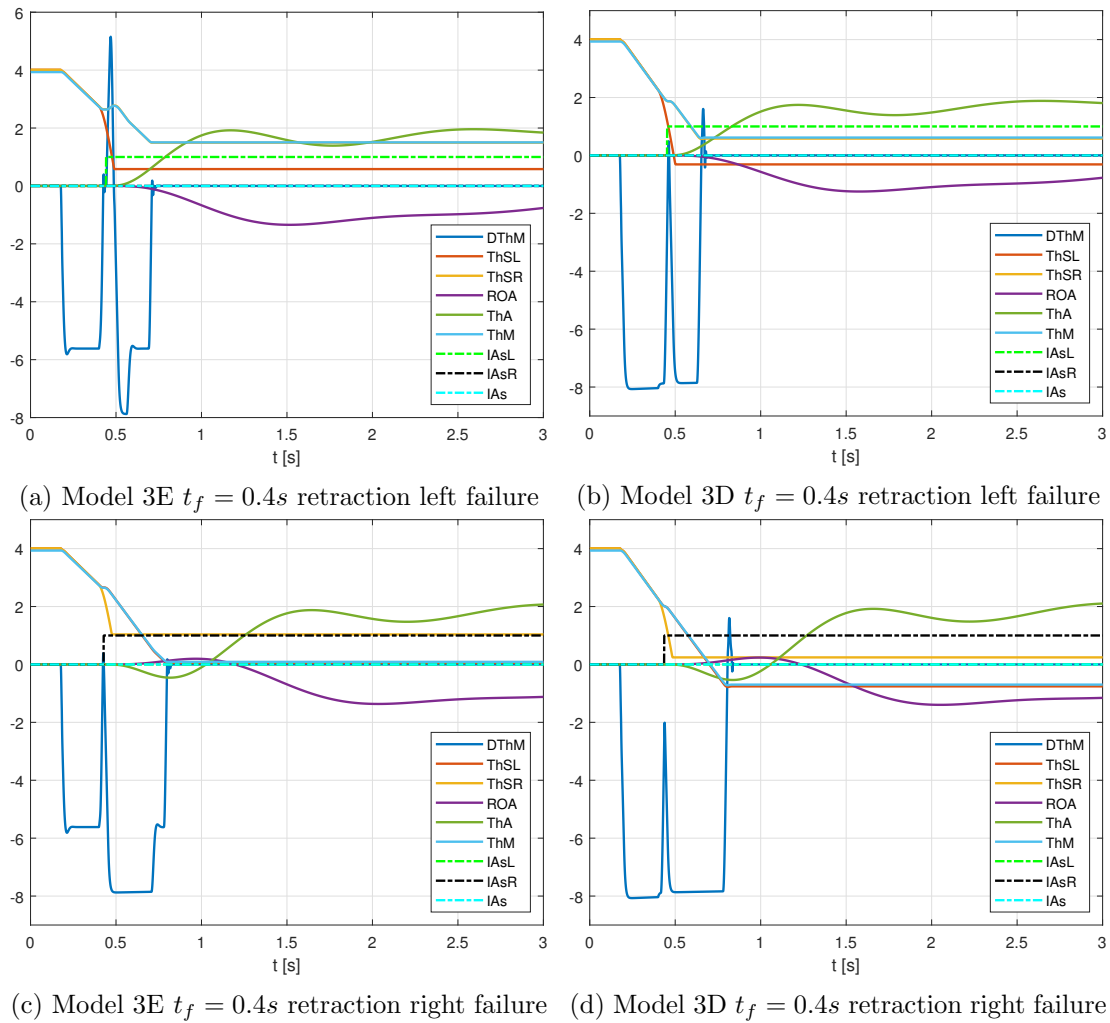


Figure 68: Model 3E vs 3D bord case wear-free extension failure at $T_{RC} = 10000Nm$ (detail)

As with the so-called *regular conditions*, a general overview of the active monitoring techniques has been performed in the previous pages according to the input signal. However is also important to analyze the active techniques behaviour according to the effect of the position anticipation term, considering models with the same input signal. Therefore, a comparison of the active models behaviour according to the *dynamic position* effect for equal input signal models will be performed in the following pages.

In contrast to the *regular conditions* general overview, in aerodynamic wear-free borderline cases only one aerodynamic load case was considered: high T_{RC} . In effect, the aerodynamic wear-free borderline scenarios are characterized by the effect high aerodynamic loads and wear-free actuators performance. Hence, only the high aerodynamic load cases will be considered.

Follows the aforementioned general overview focusing on the position anticipation performance for equal input signal active models.

7.6.1 Step-input models behaviour on wear-free borderline conditions

Firstly, the active technique *3D* behaves much better the new model 3 in any scenario of such borderline conditions. As mentioned in 7.2, the model *3D* presents no surface saturation phenomena as a consequence of the combined effect of both the “dynamic” term that anticipates the asymmetry failure and the reference position θ_M of the step-input models.

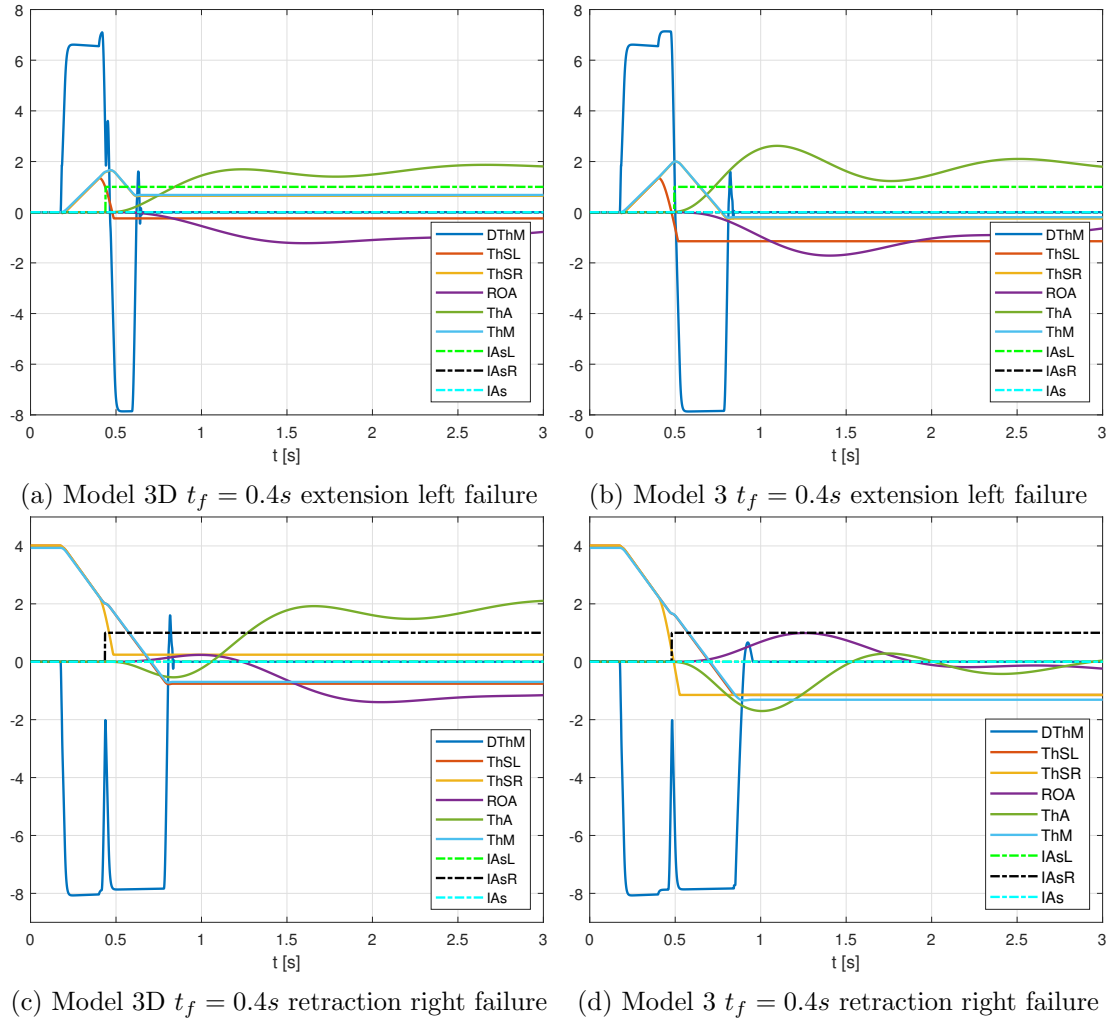


Figure 69: Overview 3D vs 3 bord case wear-free extension failure at $T_{RC} = 10000Nm$ (detail)

In fact, the model *3D* improves all the negative consequences the new model 3 presented. In effect, the combined effect of both a faster asymmetry failure detection due to the anticipation term and the lack of saturation phenomena on model *3D* leads to interesting improvements:

- Should a failure arise when extending the flaps, at least the operative surface would reach an extended position after failure, $\theta_i > 0$. This solves part of the problem that arose in the previous model since some lift will be provided by the high-lift devices during landing. Nonetheless, the ailerons would both correct the rolling moment and provide the extra lift necessary for landing if possible. Otherwise, longer landing field lengths would be necessary.

- Should a failure arise when retracting the surfaces, the steady-state position consequences might be less critical than in the previous model. This improvement is especially important if very small flap retraction are commanded, in which case the right surface may reach not significantly differ from commanded position.
- Regarding the system structural integrity (aerodynamic surfaces, mechanical transmissions...), there will be no impacts if the mechanical lower limit switch of the flap is reached. Therefore, no further damages critical condition will be added to the position asymmetry problem.

All these considerations can be noted in Figure 69.

Thus, the model $3D$ is better than 3 on aerodynamic wear-free borderline scenarios since:

1. The stability margin of the aircraft rolling response is higher on model $3D$ than on model 3 .
2. The maneuverability after failure using model $3E$ is higher than in case of model $3D$.
3. No flap saturation phenomena are present on model $3D$, unlike on model 3 , with which at least one surface saturates in every extension and retraction failure case.

7.6.2 Ramp-input models behaviour on wear-free borderline conditions

Secondly, the active technique $3E$ also behaves much better the new model $3C$ in any scenario of such borderline conditions.

As happened the model $3D$, $3E$ helps to prevent the saturation phenomena by an early failure anticipation by means of the *dynamic position* control logic. In this case the effect of the $\theta_{M,max}$ is not present since $3E$ is a ramp-input control algorithm but the effect of the “dynamic term” is enough to prevent almost every surface saturation scenario. In fact, the model $3E$ only presents saturation in the right failure during extension case due to the adverse effect of $\theta_{Os,Ti}$, as mentioned in 7.5. There are no other saturation cases using model $3E$ with the extension and extraction maneuvers considered for this aerodynamic wear-free borderline case.

Analogously to model $3D$, the fact that the failure surface is braked earlier increases the stability margin of the aircraft rolling dynamic response. Moreover, the aircraft maneuverability after failure also increases, since the failure surface deflection at the braking time $\theta_i(t = t_{br})$ does not significantly differ from the initial position.

In addition, the *false multiple asymmetry failure declaration* disappears with the anticipating effect of the *dynamic position*.

These considerations are relevant to compare the active models $3E$ and $3C$. All these are all illustrated in Figure 70.

Thus, the model $3E$ behaves better than $3C$ on aerodynamic wear-free borderline scenarios since:

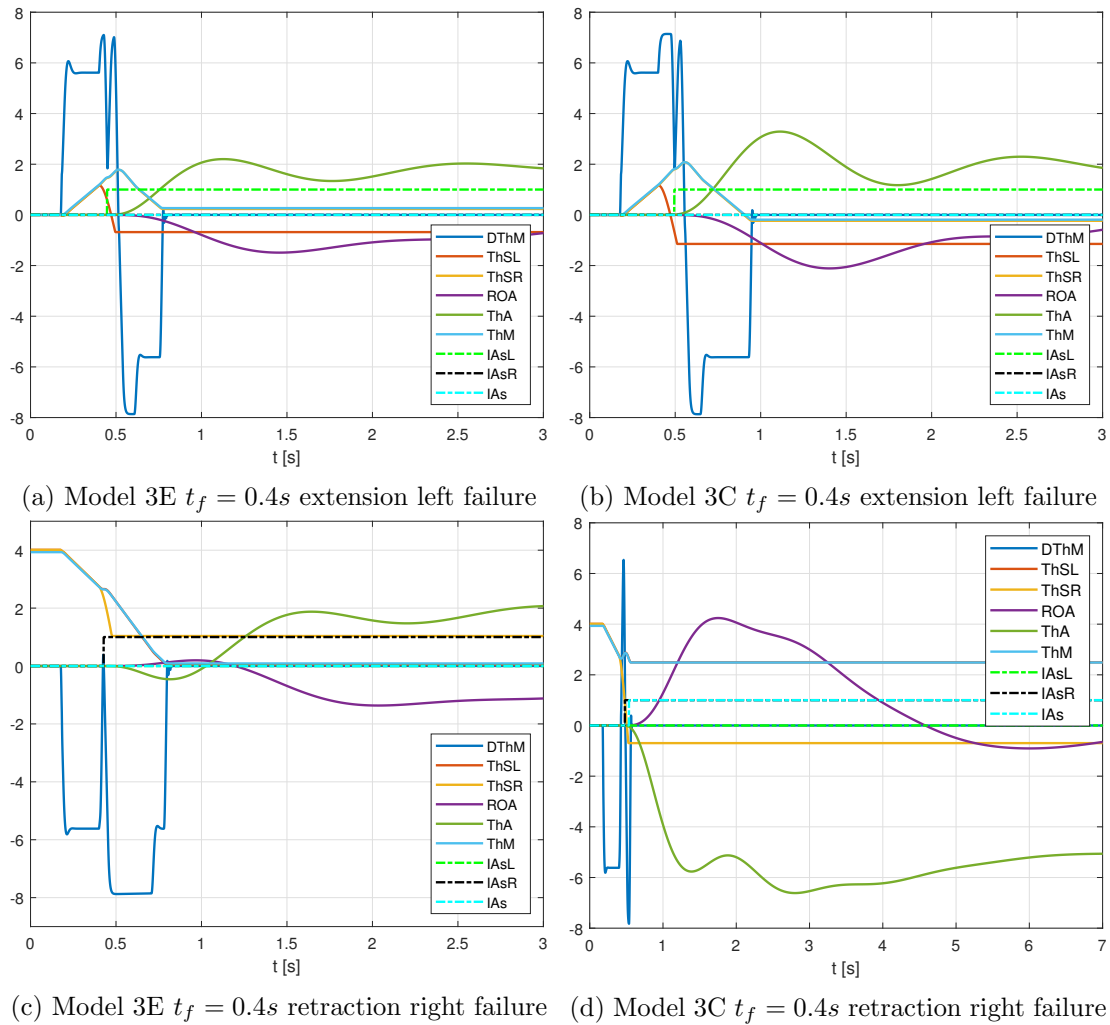


Figure 70: Overview 3E vs 3C bord case wear-free extension failure at $T_{RC} = 10000Nm$ (detail)

1. The stability margin of the aircraft rolling response is higher on model 3C than on model 3.
2. The maneuverability after failure using model 3C is higher than in case of model 3D.
3. Fewer flap saturation cases are present on model 3E, unlike on model 3C.

7.6.3 Summary table of active models in wear-free borderline conditions

As in *regular conditions*, the summary table hereunder compares all the active models on the aerodynamic wear-free borderline conditions studied in this chapter in order to analyze which active monitoring technique behaves better in each situation (see Table 2). This table classifies both the active step-input and ramp-input monitoring techniques in aerodynamic wear-free borderline conditions according to the different surface deflection maneuvers (extension and retraction), always under high aerodynamic loads.

The both the numerical classification and the color coding that measure the active models effectiveness both quantitatively and qualitatively on the current borderline con-

	Step-input models		Ramp-input models			
	3	3D	3A	3C	3E	
High T_{RC}	3	1	4	4	2	Extension
	3	2	5	4	1	Retraction

Table 2: Models efficiency classification on aerodynamic wear-free borderline conditions

ditions follow the same rules than the previous *regular conditions* analysis (see 6.5.3).

In the light of the test results on the current borderline conditions, some considerations should be made:

1. The active monitoring techniques that consider an anticipation term by means of the *dynamic position*, behave much better than the non *dynamic position* active models in case of high aerodynamic loads.
2. The step-input active models seem to behave better than the ramp-input models under equal position anticipation control logic, except from the surface retraction between *dynamic position* control algorithms scenario, on which the model 3E presents the best behaviour.
3. Great behaviour improvements can be noted between the active models marked in green & orange and orange & red.
4. Behavioural improvements between models with the same color might be significant, which is quantitatively measured by the number inside the cell.
5. The only red cell classified with a 5 represents the unacceptable loss of control of model 3A should a right failure arise during retraction.

It seems that the models that behave better on aerodynamic wear-free borderline conditions are:

- The *model 3D* when a flap extension maneuver is commanded.
- The *model 3E* when a flap retraction maneuver is commanded.

Thus, in contrast to what stated for the active techniques behaviour on *regular conditions*, the best model choice for the current borderline conditions depends on the flap deflection maneuver commanded: either extension or retraction.

Follows a summary of the main reasons why each model presents the best behaviour on their specific flap deflection scenario.

- In case of **failure during extension**, the effect of the peak that the reference position θ_M presents on model 3D due to the engine speed $\dot{\theta}_M$ variation, quickly increases the speed difference after failure between the inoperative surface and the reference position. Consequently, the *dynamic position* increases considerably, leading to an earlier failure declaration using model 3D, increasing the rolling response margin of stability and the aircraft maneuverability after failure. On the contrary, the constant slope of model 3E reference position Dem delays the position anticipation effect of the *dynamic position*, delaying the asymmetry failure declaration.

- In case of failure during retraction, the constant and controlled ramp slope Dem of model $3E$ reduces the retraction speed before failure and leads to a higher speed difference after failure between the reference position and the inoperative surface. Hence, the asymmetry failure is declared earlier on the ramp-input model $3E$ than in the active step-input models as a result of the *dynamic position* anticipation effect. Thus, the active technique $3E$ presents higher rolling response stability and aircraft maneuverability after failure. On the contrary, the fast surface retraction speed before failure of model $3D$ prevents the speed difference after failure from growing enough to let the *dynamic position* perform an efficient position anticipation as in the previous case ($\theta_{M,max}$ is too small or even inexistent), which delays the failure declaration.

Nonetheless, the actuators usually deteriorate due to some degradation processes and random shocks, which increases the friction forces of their internal mechanism. Worn-out actuators conform the last borderline case considered in this project. These will be carefully studied in the following section.

8 Simulation results on wear-out conditions

The wear-out cases study the system time response condiering worn out actuators. This increases the friction forces inside the actuators, seriously affecting their performances and, therefore, the surfaces deflection.

It should be reiterated that the actuators considered in this project are **reversible**, which means that the actuator internal friction force is small enough to let them move forward and backwards. This is why the extending flap does not stop after an asymmetry failure under high aerodynamic load conditions in opposing. In effect, the internal friction force does not brake the failure surface as on flap deflection with loew arodynamic load, but it lets the inoperative flap change the sense of motion (from extension to retraction). Nonetheless, such phenomenon would not happen with irreversible actuators since changing the sense of motion is not permtted with those actuators.

In this section, the actuators are still *reversible*, but very close to the irreversibility. Both the aiding and opposing friction efficiencies in dynamic conditions are considerably reduced in order to increase the internal friction force both in case of aiding and opposing aerodynamic load. The physical explanation of these efficiencies was studied in section 3. Nonetheless, their practical effect is commented hereunder:

- The opposing friction efficiency η_{OS} tries to stop the surfaces after a failure during extension, regardless the aerodynamic load.
- The aiding friction efficiency η_{AS} may affect the system in two possible ways:
 - In case of failure during retraction for any aerodynamic load, η_{AS} tries to stop the surface after failure.
 - In case of high aerodynamic load scenarios, either during flap extension or retraction maneuvers, η_{AS} prevents the failure surface from retracting when pulled back by the effect of the high T_{RC} .

Therefore, η_{AS} quantifies the degree of actuators reversibility. In fact, the lower η_{AS} is, the less reversible the actuators will be, since their friction force *in aiding* would be important, preventing the surface from being pulled back by a strong aerodynamic load. Should $\eta_{AS} < 0$, the actuators would be considered *irreversible*. This is not the case of this project, in which both efficiencies are positive.

The Table 3 hereunder illustrates the friction efficiency reduction:

	Wear-free actuators	Worn-out actuators	Efficiency reduction
η_{OS}	0.84	0.6	-28,57%
η_{AS}	0.6	0.1	-83.33%

Table 3: Friction force efficiencies of the original and the worn-out actuators

As shown in Table 3, the friction efficiency reduction is significant, especially on η_{AS} , which will determine the behaviour of the active models on wear-out conditions.

Thus, the actuators remain reversible ($\eta_{OS} > 0$; $\eta_{AS} > 0$) but their behaviour on wear-out conditions presents some typical problems of the *irreversible* actuators, since

low values of η_{AS} reduce the degree of reversibility, as explained before.

This *wear-out* condition conforms an entire new study case. In fact, any flap deflection under either low or high aerodynamic loads can be analyzed with the new and higher friction forces similarly to the *regular conditions* of section 6. In addition, new *wear-out* “extreme conditions” can be studied, similarly to the aerodynamic wear-free cases analyzed in section 7.

Thus, in the current section the *regular wear-out conditions* (also *wear-out conditions*) will be discussed.

These are those that consider:

- Reversible worn out actuators. These are still *reversible* but will present high internal friction forces due to the current wear and tear conditions.
- Low external (aerodynamic) loads when deflecting from an angular position that is close from the maximum flap retraction.

Analogously to what discussed in section 6, the second condition can be written as shown in Equation (6.1).

In addition, a test campaign performed to study the active models behaviour in these conditions considers the following actions, either for left and right surface failures:

- Extraction from 0 to 0.07 rad at $T_{RC} = 0Nm$.
- Retraction from 0.07 to 0 rad at $T_{RC} = 0Nm$.
- Extraction from 0.4 to 0.5 rad at $T_{RC} = 10000Nm$.
- Retraction from 0.5 to 0.4 rad at $T_{RC} = 10000Nm$.

The first two cases are considered to be *maneuvers at low aerodynamic load*. On the other hand, the last two cases are considered to be *maneuvers at high aerodynamic load*.

In the following pages, the test results of the asymmetry active monitoring techniques on *wear-out conditions* will be studied. Similarly to the simulation results in *regular wear-free conditions*, each active monitoring technique will be analyzed both under low and high aerodynamic torques T_{RC} .

8.1 New model 3 results on wear-out conditions

In general, the new asymmetry active monitoring technique 3 performs better on wear-out conditions than in wear-free cases, especially in case of failure during extension under high aerodynamic torques T_{RC} . Indeed, the effect of a high friction force due to the worn out actuators helps the asymmetry control algorithm to detect eventual asymmetry failures, which improves the system performance after failure, as discussed below.

Nonetheless, it should be noted that the actuators are working on wear-out conditions, which deteriorates their performance in many ways: kinetic energy loss during the motion transmission, considerable reduction of the actuators reliability affecting

the entire system reliability as well, among others.

Follows the analysis of the new model 3 both under high and low aerodynamic loads on wear-out conditions.

8.1.1 Low T_{RC} case results

In regard to the active new model 3 on *wear-out conditions* under low aerodynamic torque T_{RC} , the effect of the friction force determines the surface braking after failure, similarly to the wear-free cases.

The results of both extension and retraction for both surfaces are shown in figures 71 and 72.

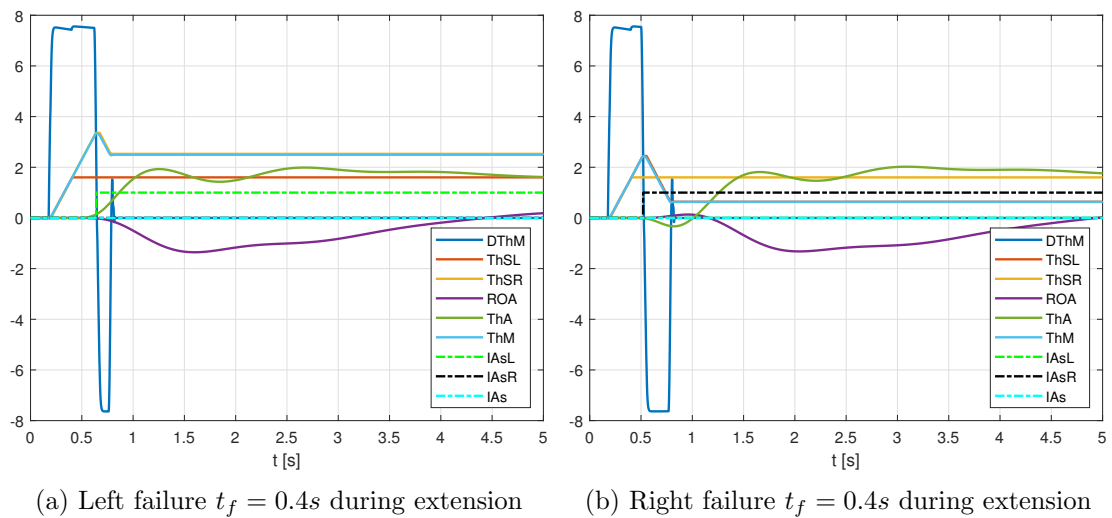


Figure 71: New model 3 failure extension from 0-0.07 rad at $T_{RC} = 0Nm$ wear-out

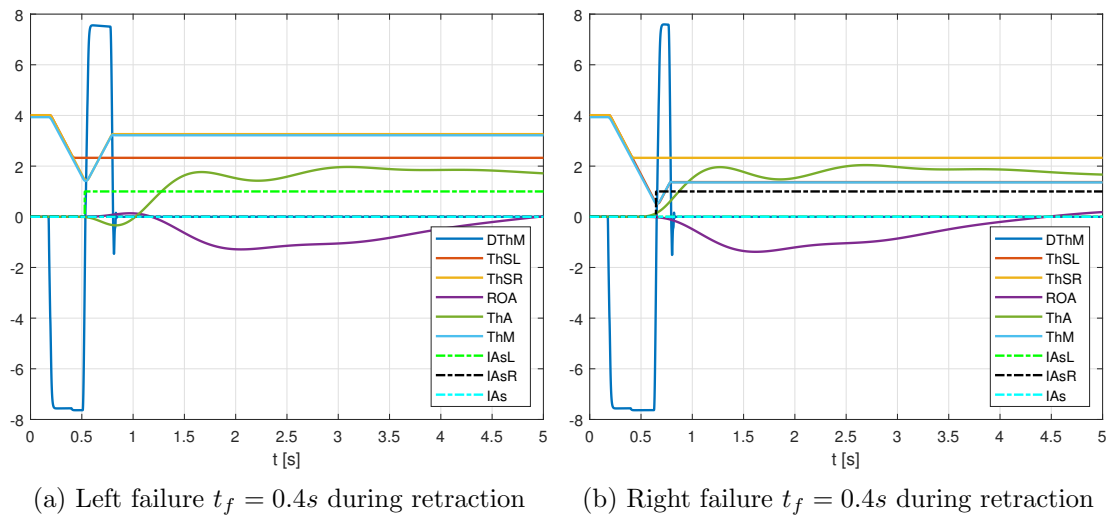


Figure 72: New model 3 failure retraction from 0.07-0 rad at $T_{RC} = 0Nm$ wear-out

In effect, there is little difference between the new model 3 results *regular wear-free conditions* and *wear-out conditions*. Indeed, the braking time after failure t_{br} is slightly

shorter on *wear-out conditions* in the absence of aerodynamic torque, due to the higher friction of the worn-out actuators. Consequently, the broken surface stops earlier and the asymmetry detection delay decreases, reducing the overshoot of the aircrafts rolling parameters and increasing the response stability. On the other hand, the high friction force slows the flap dynamic response, increasing the time-to-peak of the aircraft rolling response and reducing the response stability.

Thus, the worn out actuators reduce the failure declaration delay but slow the flap deflection due to the high friction force. These both reduces the overshoot of the aircraft rolling response and increases its time-to-peak. Consequently, the stability margin of the system time-dependant output remain almost invariant both on wear-free and wear-out conditions.

Nonetheless, the overshoot and time-to-peak variations are almost imperceptible between wear-free and wear-out conditions. In effect, it seems that the regular friction forces inside the actuators brakes the failure flap almost instantaneously and little variations can be noted on model 3 results on both operating conditions.

Regarding the aircraft maneuverability after failure on wear-out conditions, it presents a slight increase since the braking position after failure is a bit less deflected than on wear-free conditions. However, there is little difference between both study cases, almost imperceptible from what illustrated in the aforementioned figures.

In conclusion, the model 3 seems to behave almost in the same way wear-free and wear-out operating conditions in regard to stability and maneuverability. In addition, it should be reiterated that the worn out actuators are not operating at full performance, since higher η_{OS} and η_{AS} increase the energy loss during the motion transmission.

8.1.2 High T_{RC} case results

In case of high T_{RC} torque, the high friction of the worn out actuators, especially *in aiding*, brakes the surfaces almost instantaneously, reducing considerably the braking time after failure t_{br} with respect to the wear-free cases. The extension and retraction results for both surfaces are shown in Figures 73 and 74.

As previously mentioned, the high friction efficiency in aiding η_{AS} prevents the failure surface from retracting when pulled back by the effect of the high T_{RC} in any high aerodynamic load scenario. The high friction efficiency in aiding η_{AS} helps the braking system to stop the failure surface, which can be clearly appreciated in the figures.

Moreover, further considerations should be done in regard to the effect of the high friction force in the time-dependant surface response.

Should a failure arise during extension, the slow extraction before failure due to the friction force is compensated with the fast braking of the inoperative surface after failure, so the system time-response is not delayed with respect to what shown in the wear-free cases. In other words, the time-to-peak remains almost constant. On the other hand, the system presents a less deflected failure position, which leads to a lower rolling response overshoot and a higher maneuverability after failure of model 3. In addition, the combination of an almost constant time-to-peak and a lower overshoot on the aircraft rolling response increases the system stability when using model 3.

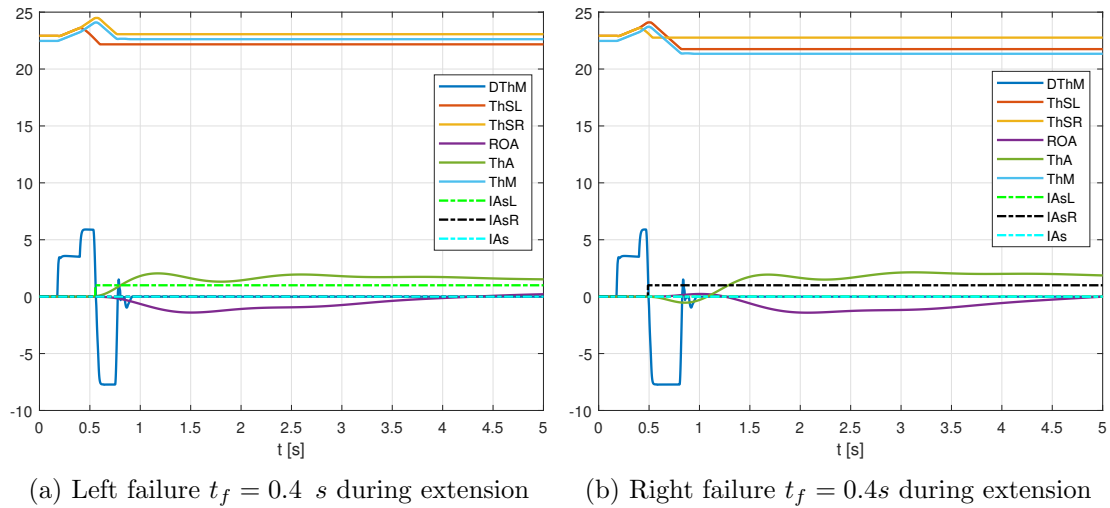


Figure 73: New model 3 failure extension from 0.4-0.5 rad $T_{RC} = 10000Nm$ wear-out

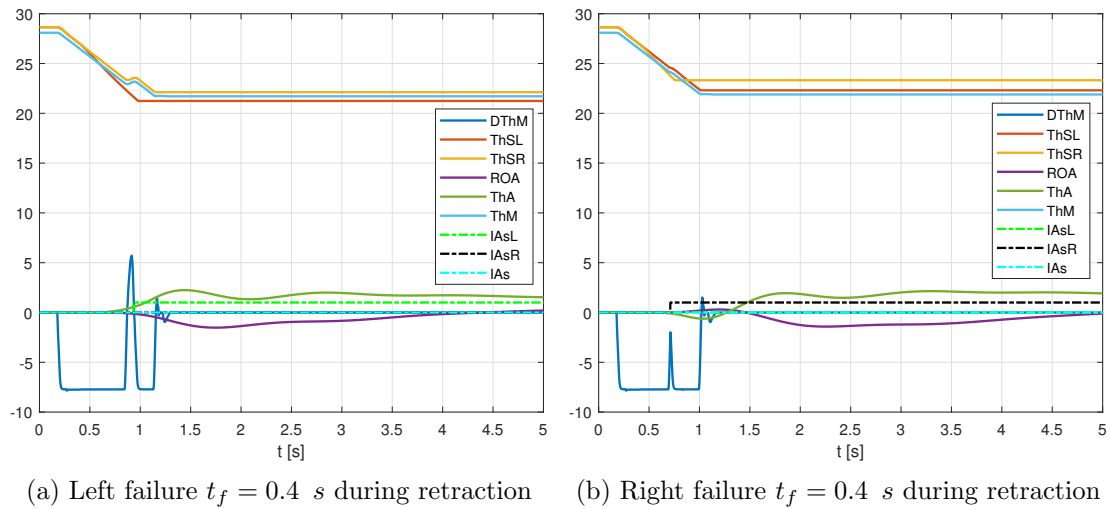


Figure 74: New model 3 failure retraction from 0.5-0.4 rad $T_{RC} = 10000Nm$ wear-out

Should a failure arise during retraction, the slow retraction before failure is *not* compensated with the fast braking of the inoperative surface after failure, so the time-to-peak will be longer in wear-out cases, deteriorating the response stability. Nonetheless, the system presents a less deflected failure, which leads to a lower overshoot of the aircraft rolling response, increasing the system response stability. Consequently, the margin of stability of the time-response on model 3 would be affected by a higher time-to-peak and a lower overshoot. In addition, the aircraft maneuverability when using model 3 after failure increases considerably due to the great reduction of the failure declaration delay and the consequent little flap deflection on steady state.

Consequently, the aircraft maneuverability after failure of model 3 increases in every case on wear-out conditions with respect to the wear-free cases due to the substantial reduction in failure declaration delay. On the other hand, the rolling response stability of model 3 increases in extension cases and remains almost constant in retraction cases.

8.2 Model 3D results on wear-out conditions

8.2.1 Low T_{RC} case results

The results of the asymmetry active monitoring technique $3D$ under low aerodynamic loads on wear-out conditions present no differences with respect to model 3. In effect, the anticipation term is not activated for low aerodynamic torques, regardless the actuators friction efficiencies.

The results of both extension and retraction, either for left or right failures, are shown in figures 71 and 72.

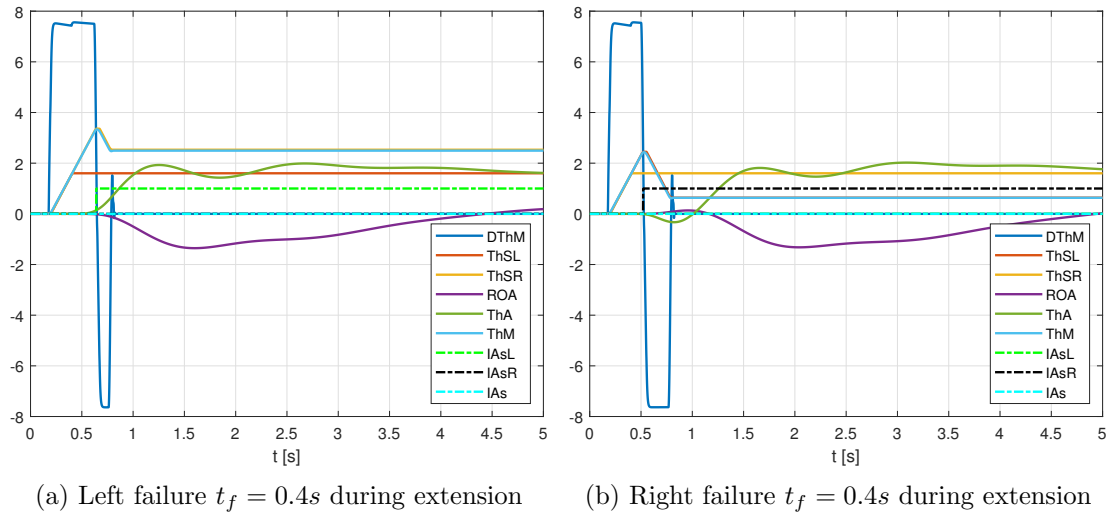


Figure 75: Model 3D failure extension from 0-0.07 rad at $T_{RC} = 0Nm$ wear-out

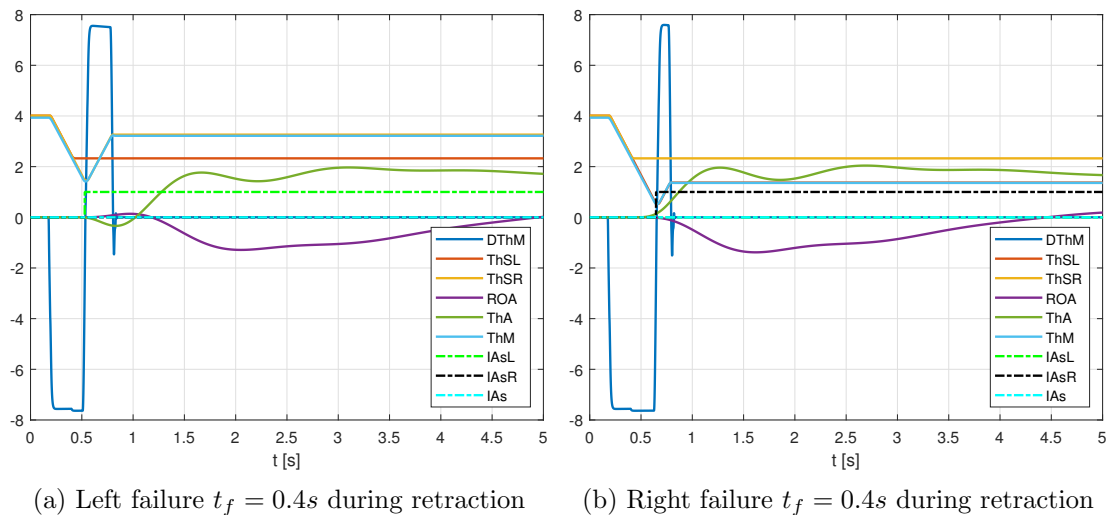


Figure 76: Model 3D failure retraction from 0.07-0 rad at $T_{RC} = 0Nm$ wear-out

Analogously, all the previous considerations made on model 3 in section 8.1.1 on wear-out conditions under low aerodynamic loads, with respect to the wear-free case, also apply to model $3D$.

8.2.2 High T_{RC} case results

The results of the asymmetry active monitoring technique $3D$ under high aerodynamic loads on wear-out conditions present great improvements with respect to model 3, especially in case of failure during retraction. In this case, the combined effect of both the *dynamic position* of the model $3D$ and high friction force of the worn out actuators are the cause of such improvements.

Nonetheless, the *dynamic position* on wear-out conditions will always work with lower surface speeds, even after failure, when the failure surface is not powered anymore by the engine. Therefore, it is expected that the model $3D$ behaves better the model 3 on the aforementioned conditions. However, there will be significant differences with respect to model $3D$ on wear-free conditions.

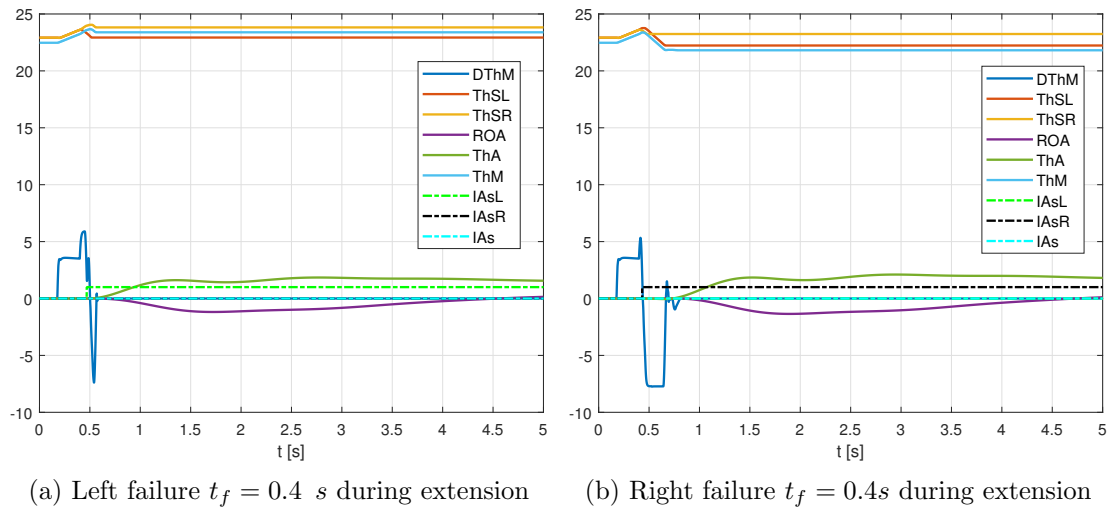


Figure 77: Model 3D extension from 0.4-0.5 rad $T_{RC} = 10000Nm$ wear-out

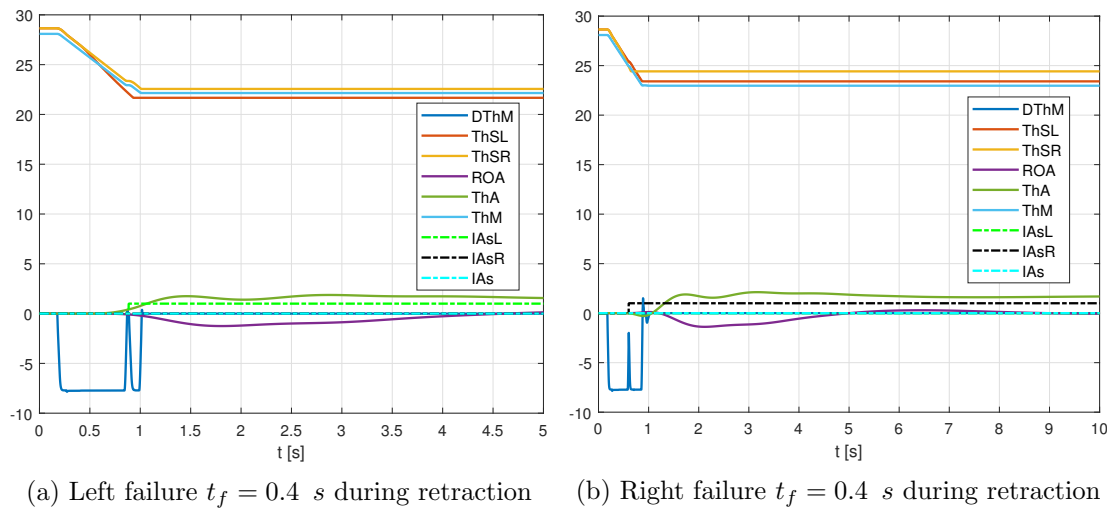


Figure 78: Model 3D retraction from 0.5-0.4 rad $T_{RC} = 10000Nm$ wear-out

The results of both extension and retraction for both surfaces are shown in figures 77 and 78.

The aforementioned resultant effect of both the dynamic position and the high friction force of the worn out actuators depends on the deflection maneuver performed under high aerodynamic load.

In case of failure during extension, the slow extraction before failure due to the friction force is again compensated with the fast braking of the inoperative surface after failure, as happened on model 3. In addition to this, the *dynamic position* anticipates the asymmetry failure detection, which leads to a great reduction on the braking time. In other words, the model 3D exploits all the benefits of an anticipated braking action that helps the braking system and a the beneficial effect of the high friction force that reduced the failure surface speed before it increases excessively. On the other hand, the system presents a less deflected failure position.

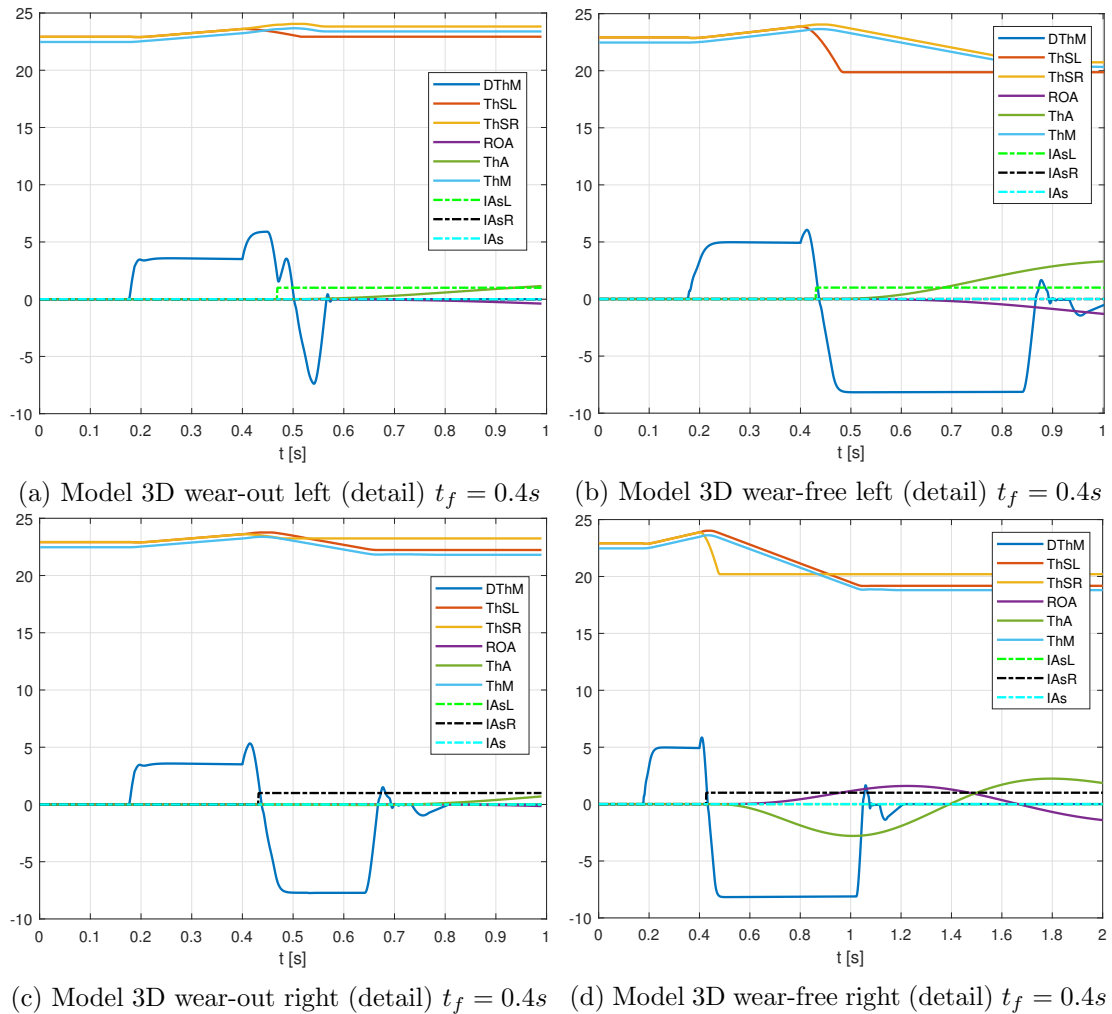


Figure 79: Model 3D wear-out vs wear-free fail extension 0.4-0.5rad $T_{RC} = 10000Nm$

From a control perspective, the little failure surface deflection leads to a lower rolling response overshoot and a higher maneuverability after failure. In addition, the time-to-peak remains almost invariant since the slow extension speed of both flaps is compensated with the exceptionally short t_{br} . Consequently, the model 3D during extension under high aerodynamic load present a high time-response stability and a high maneuverability after failure. These are greater than in case 3 on wear-out conditions and,

consequently, notably greater than those of the active models on wear-free conditions (both 3 and 3D).

All these considerations are illustrated in Figure 79.

On the other hand, in case of failure during retraction, the model 3D improves the model 3 behaviour under the current aerodynamic load conditions, increasing both stability and maneuverability after failure. Nonetheless, the variations respect to the model 3D on wear-free conditions will be discussed below.

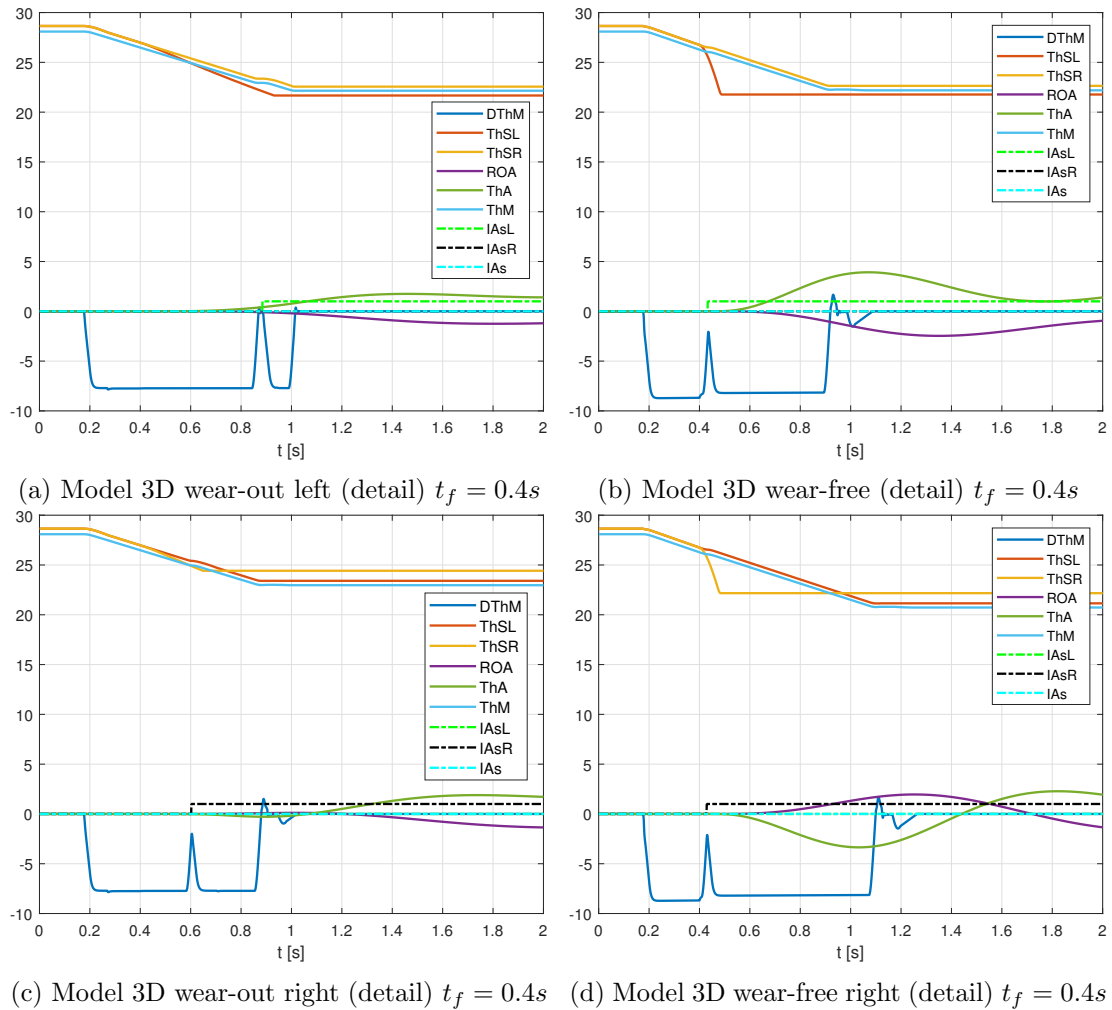


Figure 80: Model 3D wear-out vs wear-free fail retraction 0.5-0.4rad $T_{RC} = 10000Nm$

The slow retraction before failure delays the failure retraction since it slows the surface speed before and after failure. Hence, the *dynamic position* always manages lower surface speeds, as mentioned above. The resultant effect depends on the failure side:

- In left failure cases, both the failure declaration delay and the braking time after failure t_{br} notably increases by the combined effect of both a high friction force that slows the flap retraction and the unfavourable transducer offset position of the left surface. This compromises the aircraft maneuverability after failure and

increasing the time-to-peak of the aircraft roll angle ϕ . However, the slow retraction after failure before the braking instant reduces the rolling response overshoot. Hence the margin of stability of the system time response will be calculated regarding the opposite effects of both overshoot and time-to-peak variations, while the aircraft maneuverability after failure.

- In right failure cases, braking time after failure t_{br} decreases while the failure declaration delay still increases as in the previous case by the same reasons. In addition, the slow retraction after failure before the braking instant reduces the rolling response overshoot, while the time-to-peak remains almost invariant. Therefore, the overall behaviour of model 3D on wear-out conditions leads to a better aircraft maneuverability after failure and a rillong time response stability.

Analogously, all these can be noted in Figure 80.

Thus, regarding the failure during retraction case, the model 3D behaves better than model 3, both of them on wear-out conditions, and presents its advantages and weaknesses with respect to model 3D in wear-free regular conditions.

8.3 Model 3A results on wear-out conditions

The asymmetry active monitoring technique 3A, from where the active model 3C comes, presents an satisfactory behaviour on wear-out conditions, except in retraction cases under high aerodynamic loads.

The satisfactory behaviour cases, which are both the extraction scenarios, regardless the aerodynamic load, and the retraction cases under high aerodynamic loads, each one of those for both left and right failure, are shown in Figure 111.

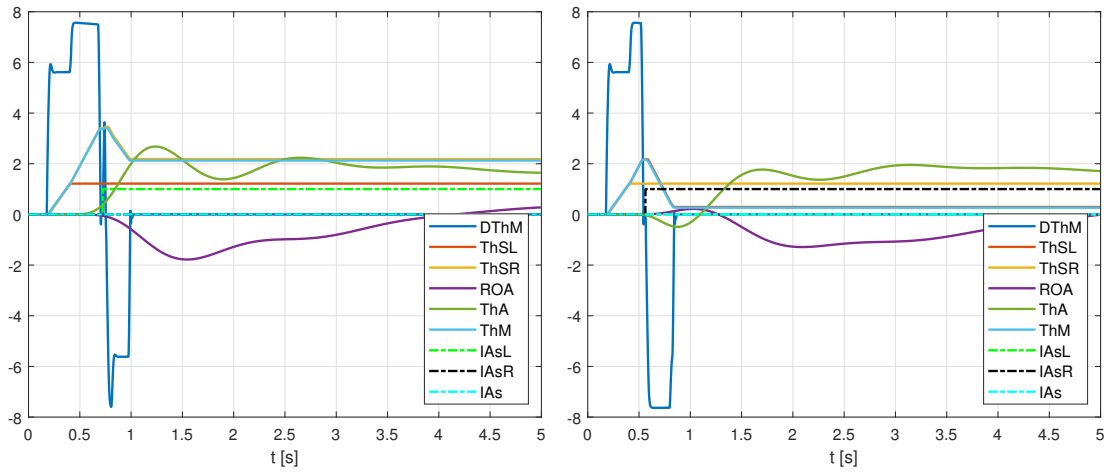
Nonetheless, the behaviour of the active model 3A in retraction cases under high aerodynamic loads, both in left and right failure cases, shows some relevant aspects of the wear and tear conditions that should be analyzed separately, since they lead to a *false multiple asymmetry failure* declaration.

Firstly, the left failure during retraction case is illustrated in Figure 82.

Far from the position divergence that lead to a complete loss of control, discussed above in section 7.3, the current *false multiple asymmetry failure* declaration is caused by the slowing down effect of the high friction force.

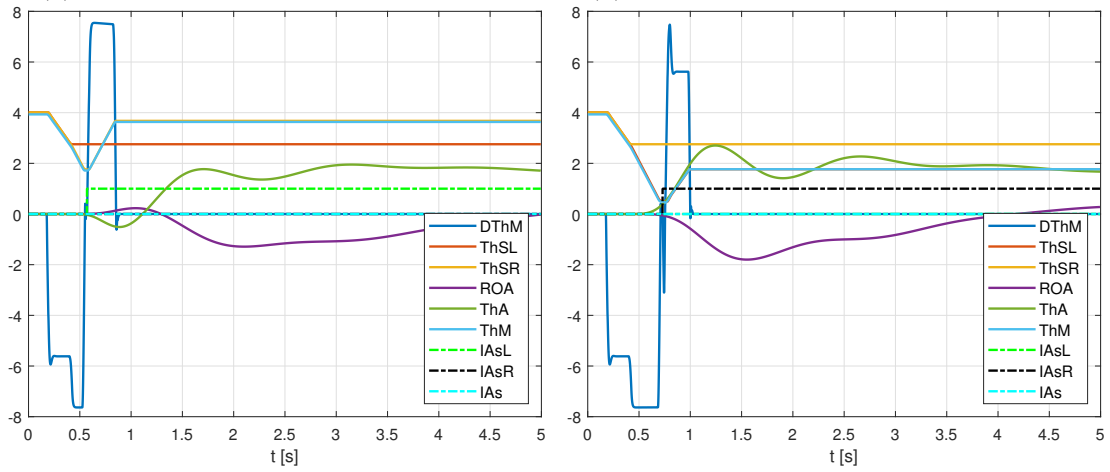
In effect, when the failure surface starts the retracting motion ($t \geq t_f$), the operative right surface starts to break its retraction in order to reduce the error signal ϵ . This is illustrated in the aforementioned Figure 82 as the typical “angular position inversion” between both the left and the right surface minimize ϵ .

Once both surfaces start to diverge form the demand reference position Dem , the operative surface, which is still powered by the engine, presents a faster divergence form the reference position Dem , which leads to a *false asymmetry failure* declaration of the operative right surface. In addition, once the the right partial asymmetry failure counter reaches the corresponding thresholds, the *Slow* parameter shuts the electric current Cor so the right surface quickly stops ($t \cong 0.8s$) by the effect of the high fric-



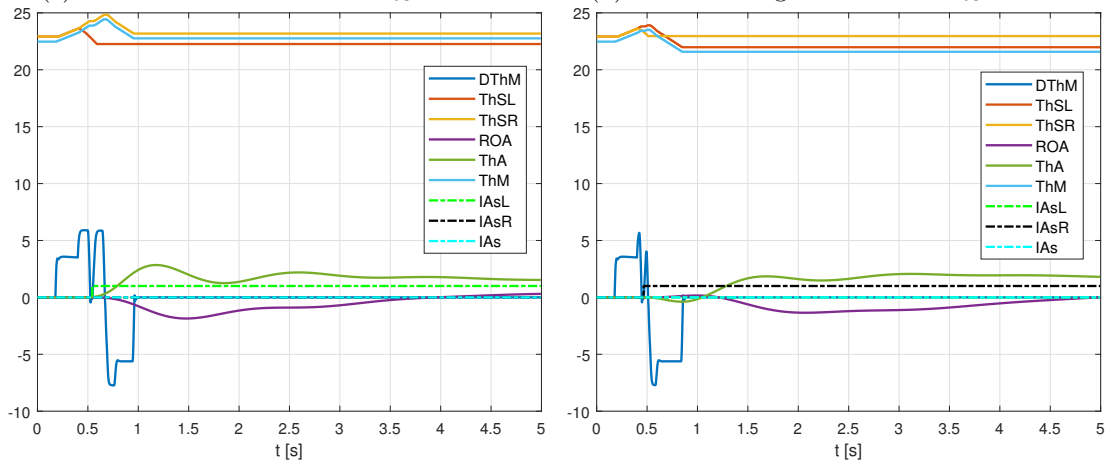
(a) Model 3A left 0-0.07rad $T_{RC} = 0Nm$

(b) Model 3A right 0-0.07rad $T_{RC} = 0Nm$



(c) Model 3A left 0.07-0rad $T_{RC} = 0Nm$

(d) Model 3A right 0.07-0rad $T_{RC} = 0Nm$



(e) Model 3A left 0.4-0.5rad $T_{RC} = 10000Nm$

(f) Model 3A right 0.4-0.5rad $T_{RC} = 10000Nm$

Figure 81: Model 3A satisfactory behaviour cases - wear-out failure $t_f = 0.4s$

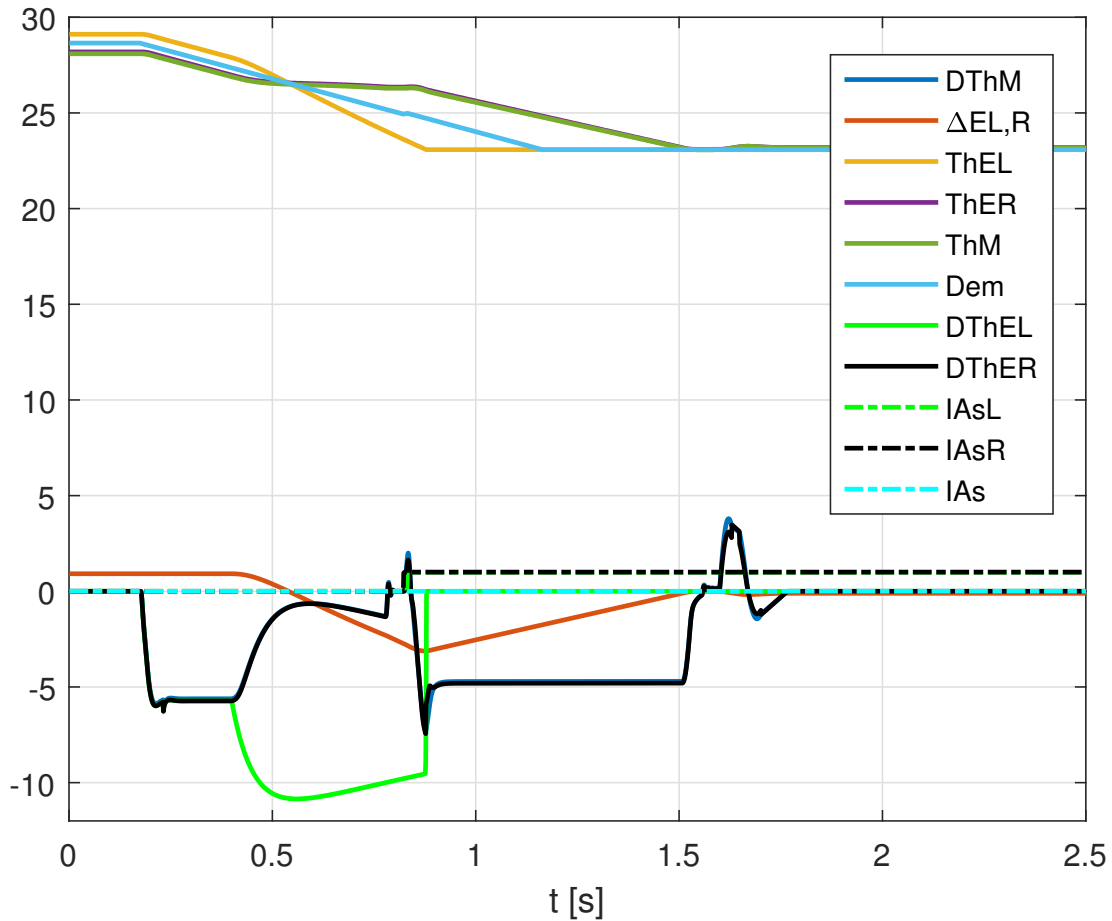


Figure 82: Model 3A (electrical) left failure retraction (detail) wear-out

tion force.

From the moment in which the false right asymmetry failure is declared, the right relative position starts to drop (due to the raising demand signal towards the braked right surface). Consequently, the partial asymmetry failure declaration is produced on the left inoperative surface, which leads to the aforementioned emphfalse multiple asymmetry failure.

As is well known, in case of emphfalse multiple asymmetry failure, the sequential exclusive logic of the asymmetry failure correction algorithm give preference to left failures. Fortunately, it corresponds to the current asymmetry case, so the asymmetry failure correction maneuver will be correctly performed. In effect the inexistent right asymmetry failure is not even considered by the sequential exclusive logic when performing the asymmetry correction.

Nonetheless, the asymmetry correction logic would not have corretctly performed the asymmetry correction in case of right failure. This is the main problem of the right failure during retraction scenario, which is illustrated in Figure 83.

Similarly to the previous case, the error signal ϵ is minimized before failure by the initial both surface divergence from the reference demand position Dem (there is no angular position inversion in this case due to right the position transducer offset $\theta_{Os,TR}$).

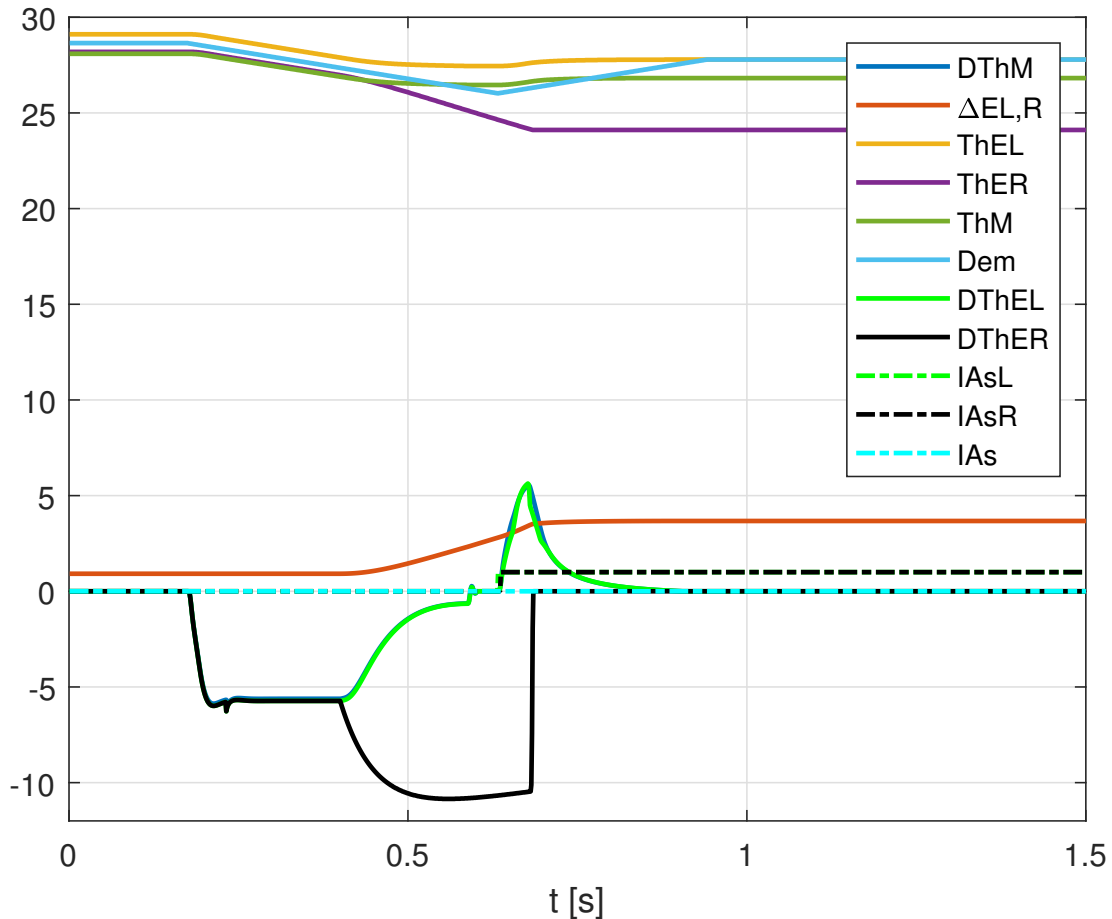


Figure 83: Model 3A (electrical) right failure retraction (detail) wear-out

Then, the *false asymmetry failure* declaration of the operative left surface is produced since the high friction force and the *Slow* parameter quickly stop the operative left surface.

Analogously to the left failure case, the left relative position starts to drop from the moment in which the false left asymmetry failure is declared (due to the dropping demand signal towards the braked left surface). Consequently, the partial asymmetry failure declaration is produced on the right inoperative surface, which leads again to a *false multiple asymmetry failure*.

However, in this case the asymmetry correction logic does not perform the asymmetry correction as expected, since it always gives preference to the left “failure” surface, which is not the one that presents the mechanical transmission problem. Consequently, the asymmetry correction maneuver is similar to what discussed in section 7.3 on aerodynamic borderline wear-free conditions, in which the active model 3A caused to a flap asymmetry loss of control which led to a unstable aircraft rolling steady-state dynamics. In effect, the current time response shows a clear mis-correction of the asymmetry failure, since the right surface cannot reach the left one since it has been braked by the braking system. Consequently, the reference position reaches the left surface which would be its steady-state angular position.

Although the behaviour of model 3A on wear-out conditions presents the same char-

acteristics than in wear-free conditions, no position divergence can be noted. This is caused by the extremely high friction force (actuators involuntary braking torque) of the worn out actuators, which added to applied torque of the braking system $T_{br,i}$, compensates the engine torque applied on the left surface. Consequently, the aforementioned surface cannot diverge but remain braked by *resultant braking torque* ($F_{f,R} + T_{br,R}$).

It should be noted that no *general asymmetry failure* has not been declared since the model 3A only considers *partial asymmetry failures*. In fact, *general asymmetry failure* declaration seems not to be necessary on wear-out conditions since the aforementioned combination of “*braking torques*” prevents the operative surface from diverging. As a consequence, the loss of control scenario will not be presented with the active model 3A.

8.4 Model 3C results on wear-out conditions

The results of the active monitoring technique 3C on wear-out conditions suffer the effect of a high friction force of the worn out actuators. This is the main difference with respect to the corresponding results on wear-free conditions.

Nonetheless, in general, the behaviour of model 3C with respect to the rest of the active models on wear-out conditions is quite similar to what discussed on wear-free regular conditions. This is reasonable, since nothing changed but the actuators performance and the control logic algorithms are the same.

As indicated above in 8.1, it should be reiterated that the actuators are working on wear-out conditions, which deteriorates their performance in many ways. Therefore, all the test results hereunder discussed may improve or deteriorate the active asymmetry detection and correction but the actuators and the entire system will suffer a non-negligible mechanical energy loss.

8.4.1 Low T_{RC} case results

The results of the asymmetry active monitoring technique 3C on *wear-out conditions* under low aerodynamic torque T_{RC} will be again determined by the high internal friction force of the worn out actuators. In addition, the effect of the reduced and controlled demand slope $\left. \frac{d Dem}{dt} \right|_{max}$ will be present again, contributing to slow down the system output dynamics. The combined effect of both the high friction force and the ramp input slope will define the model 3C results on wear-out conditions.

Some differences can be noted when comparing the model 3C with both 3 and 3A under high friction forces, as well as with 3C on wear-free conditions. All these will be studied in below.

The results of both extension and retraction for either left or right failure are shown in figures 84 and 85.

Firstly, the model 3C should improve again the flaws of model 3A, from which it comes, similarly to what described above in section 6.3.2 on wear-free conditions. However, there are not significant variations between two ramp-input models on wear-out conditions under low aerodynamic loads. Similarly to what discussed in this chapter in section 8.1.1 about model 3, the presence of a non-zero friction force inside the ac-

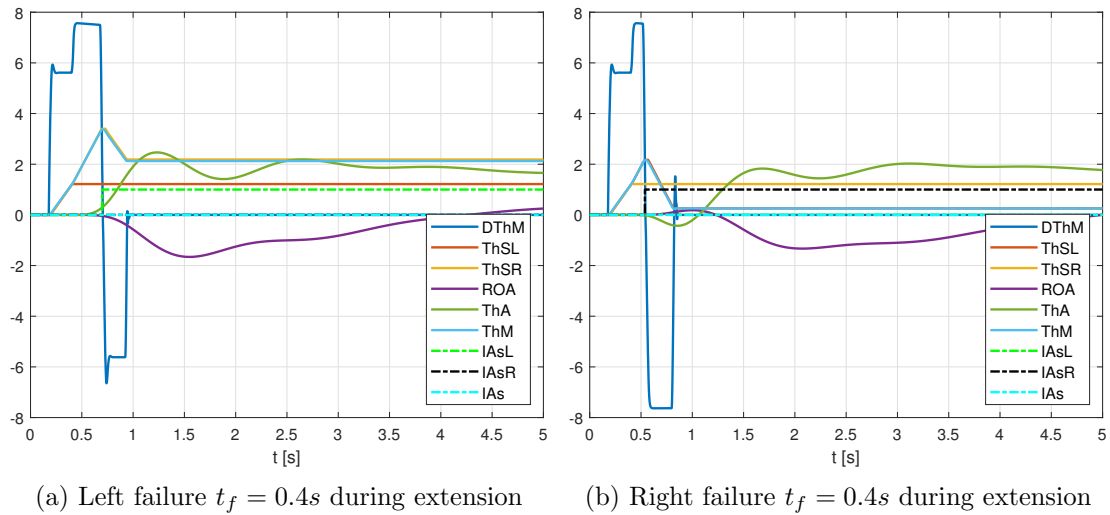


Figure 84: Model 3C failure extension from 0-0.07 rad at $T_{RC} = 0Nm$ wear-out

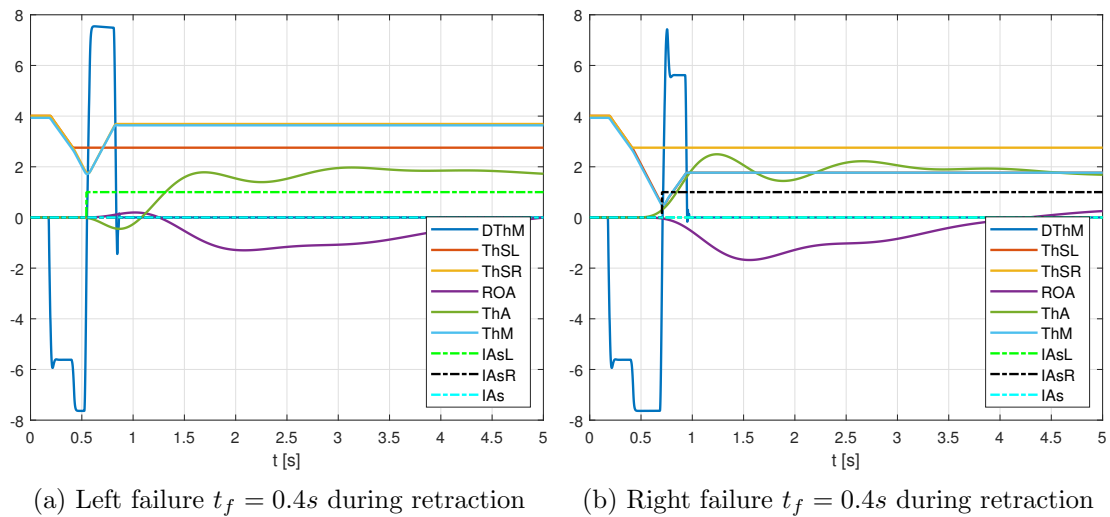


Figure 85: Model 3C failure retraction from 0.07-0 rad at $T_{RC} = 0Nm$ wear-out

tuators, together with a low enough aerodynamic torque, always leads to an almost instantaneous braking of the failure surface, regardless how large the friction value is.

All these can be noted in Figure 86.

Thus, there are not relevant changes in terms of stability and maneuverability after failure between the active techniques 3A and 3C.

Secondly, comparing the results of model 3C on wear-out conditions with those in regular wear-free cases, subtle improvements can be noted due to the high level of wear and tear present in the actuators. Such improvements are similar to those discussed earlier in section 8.1.1 referred to the behaviour model 3 under wear-out conditions.

In effect, as a consequence of the actuators wear and tear conditions, it can be noted both an overshoot reduction of the aircrafat rolling response and the corresponding time-to-peak increases, which necessarily leads to a longer braking time after failure t_{br} . As a

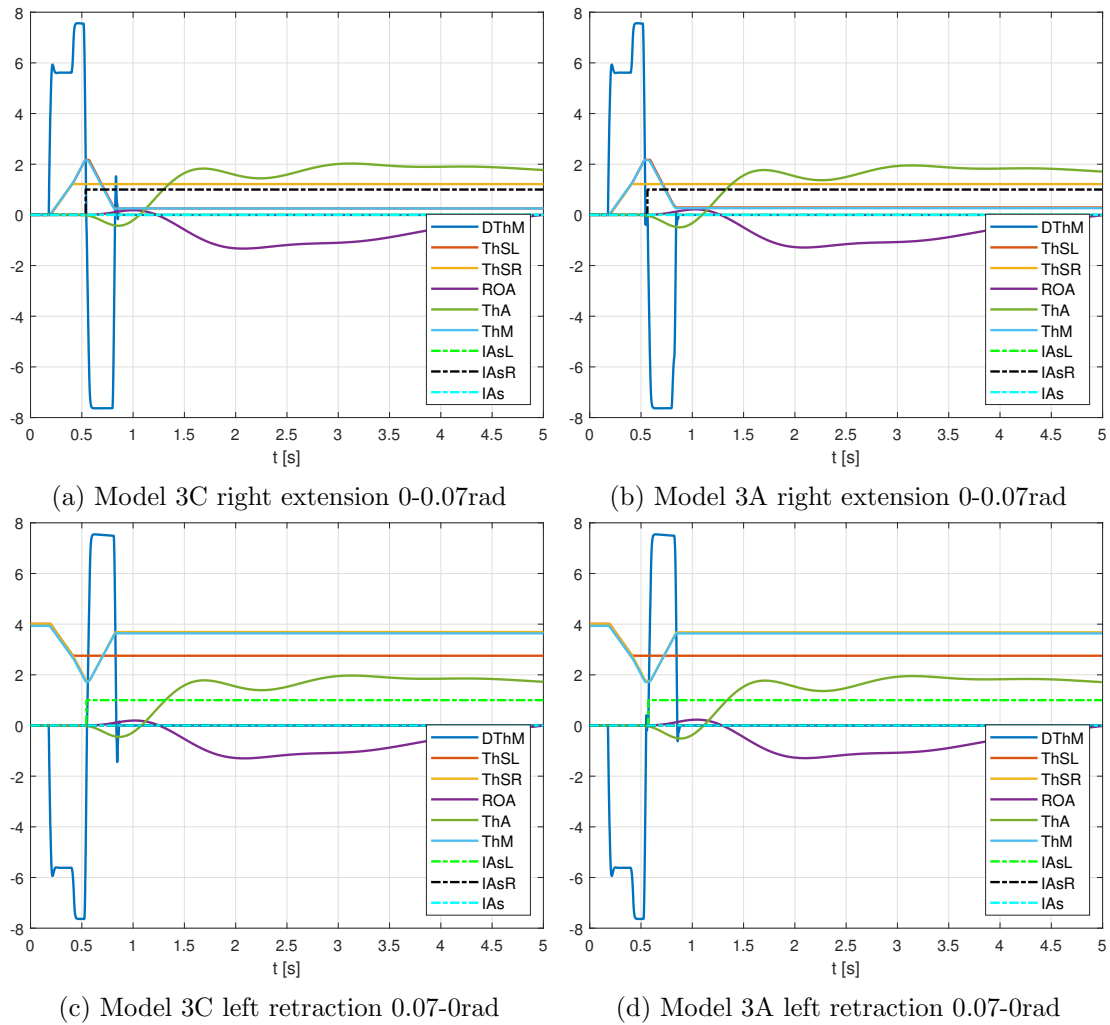


Figure 86: Model 3C vs 3A wear-out failure $t_f = 0.4s$ at $T_{RC} = 0Nm$

consequence of this delay, the maneuverability after failure decreases since the braking position after failure $\theta(t = t_{br})$ is greater on wear-out conditions. On the other hand, the aircraft maneuverability after failure on wear-out conditions, it presents a slight increase since the braking position after failure is a bit less deflected than on wear-free conditions.

Nonetheless, the overshoot and time-to-peak variations are almost imperceptible between wear-free and wear-out conditions. Similarly to the model 3, it seems that the regular high friction forces brakes the failure flap almost instantaneously and little variations can be noted on model 3C results on both operating conditions.

Consequently, the model 3C on wear-out conditions presents a slightly better aircraft maneuverability after failure and an almost invariant roll response stability.

Thirdly, the comparison between the active models 3C and 3, both on wear-out conditions is analogous to the corresponding comparison in case of regular wear-free conditions. In effect, the consideration at the end of section 6.3.3, apply also in the current case considering higher friction forces in the actuators due to the wear and tear conditions.

Thus, the stability margin of time response slightly decreases and the aircraft maneuverability after failure presents a slight increase.

8.4.2 High T_{RC} case results

Greater changes can be noted in the results of the active technique 3C under high aerodynamic loads on wear-out conditions. In fact, extension and retraction scenarios shall be discussed separately to better understand the aforementioned model performances during retraction under high aerodynamic loads.

The results of both extension and retraction for either left or right failure are shown in figures 87 and 88.

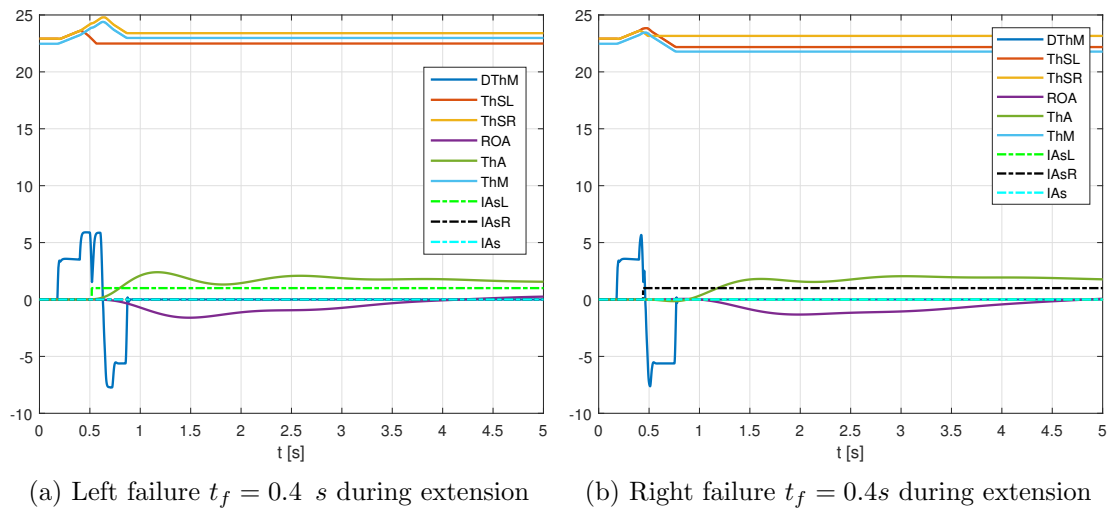


Figure 87: Model 3C extension from 0.4-0.5 rad $T_{RC} = 10000Nm$ wear-out

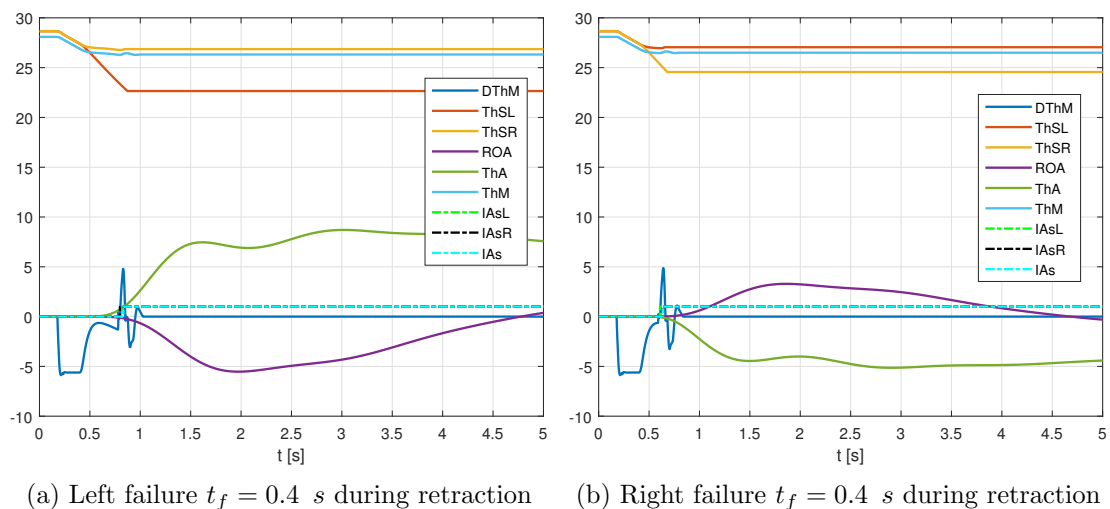


Figure 88: Model 3C retraction from 0.5-0.4 rad $T_{RC} = 10000Nm$ wear-out

In general, the model 3C on wear-out conditions under high aerodynamic loads presents an acceptable extension behaviour (see Figure 87) but some problems arise in case of failure during retraction, when either the left or the right surface fail (see

Figure 88). In fact, the behaviour of model 3C in retraction scenarios under high aerodynamic loads on wear-out conditions seems to be even worse than in aerodynamic borderline wear-free conditions, since both side failures lead to general asymmetry failure declarations.

In regard to the results of model 3C with respect to model 3A under high aerodynamic loads, both of them on wear-out conditions, the former behaves slightly better due to the earlier *partial asymmetry failure* declaration (the counter upper threshold of model 3C halves the corresponding of model 3A). Consequently, both the time response stability and the aircraft maneuverability after failure slightly increase. This is illustrated in Figure 89.

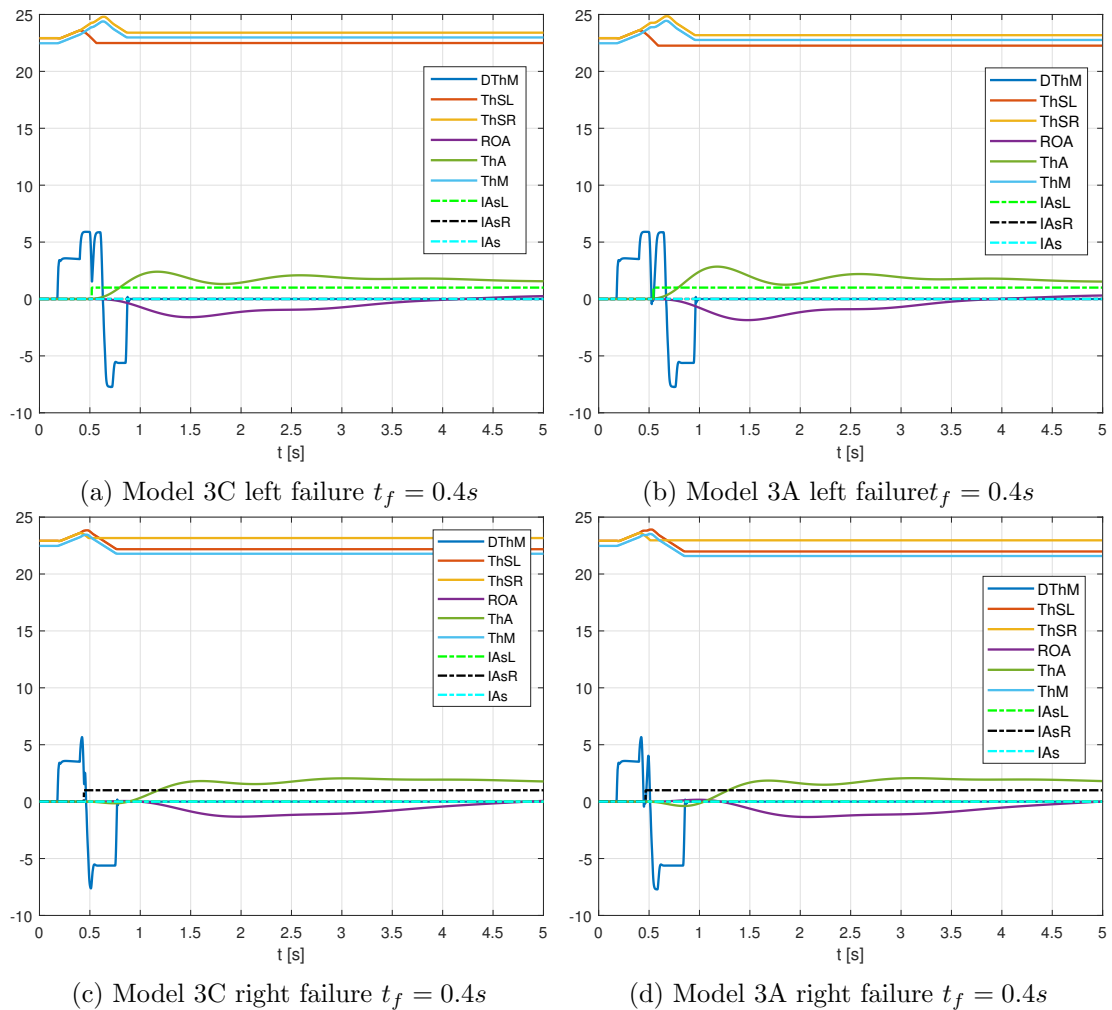


Figure 89: Model 3C vs 3A wear-out failure 0.4-0.5rad at $T_{RC} = 10000Nm$

Great improvements regarding both the time response stability and the aircraft maneuverability after failure may be noted when can also be noted when comparing the same model 3C both on wear-out and wear-free conditions. Again, the effect of the high friction force makes the difference, leading both to a more controlled retraction maneuver after failure and an earlier failure surface braking position $\theta_i(t = t_{br})$.

However, the stability and maneuverability would remain almost invariant when com-

paring 3C with the active model 3 under the same wear and tear conditions. At equal high friction force, the slow demand slope $\left. \frac{d Dem}{dt} \right|_{max}$ makes the difference between both models, as always happens between the aforementioned active models under the same operating conditions. From the control perspective, the stability remains almost the same and the maneuverability after failure increases on wear-out conditions, since lower deflection will be produced as a consequence of the slow and more controlled demand slope.

Nonetheless, important considerations should be done regarding the behaviour on retraction maneuvers of model 3C with worn out actuators.

Similarly to what discussed above in section 8.3 about model 3A, the active model 3C presents a *false multiple asymmetry failure* in retraction cases under high aerodynamic loads, always on the current wear-out conditions. Both the *general asymmetry failure* declaration and an earlier partial asymmetry failure declaration are the main differences between the active model 3C and 3A.

Both the left and the right failure during retraction maneuvers are illustrated in Figure 90. It shows the main characteristics of the electric time response when retracting the flaps using the active model 3C.

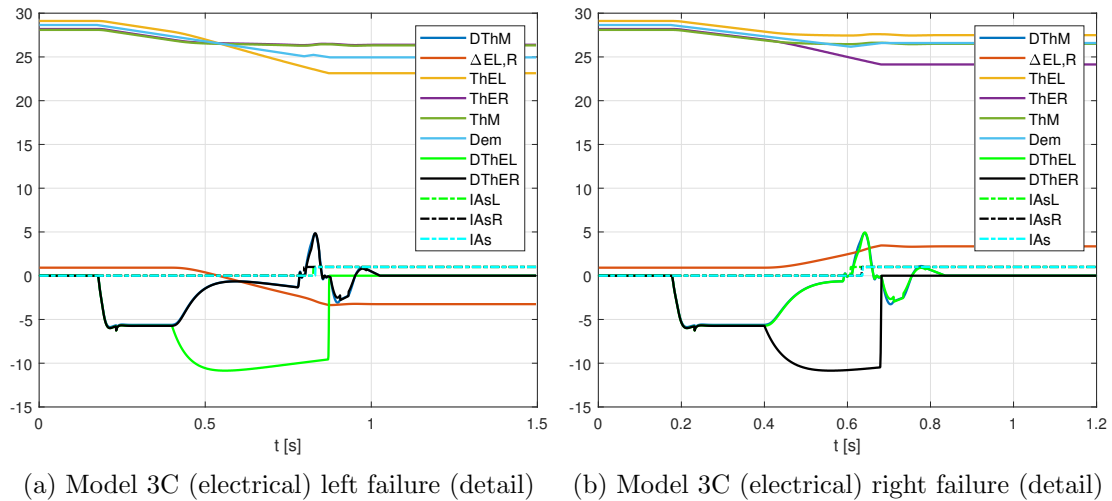


Figure 90: Model 3C electric left & right failure retraction 0-0.07 rad $T_{RC} = 10000Nm$ wear-out

The comparison in case of the left failure during retraction is illustrated in Figure 91. On the other hand, the comparison in case of the right failure during retraction is illustrated in Figure 92.

In case of left failure during retraction (see Figure 91), Notice that the *general asymmetry failure* declaration of model 3C causes a greater position asymmetry on steady state between the left and the right surface. In consequence, a rolling moment would be created, which should be compensated by a greater steady state roll angle $\phi_{A,ss}$. In addition, it should be noted that the *general asymmetry failure* declaration leads to

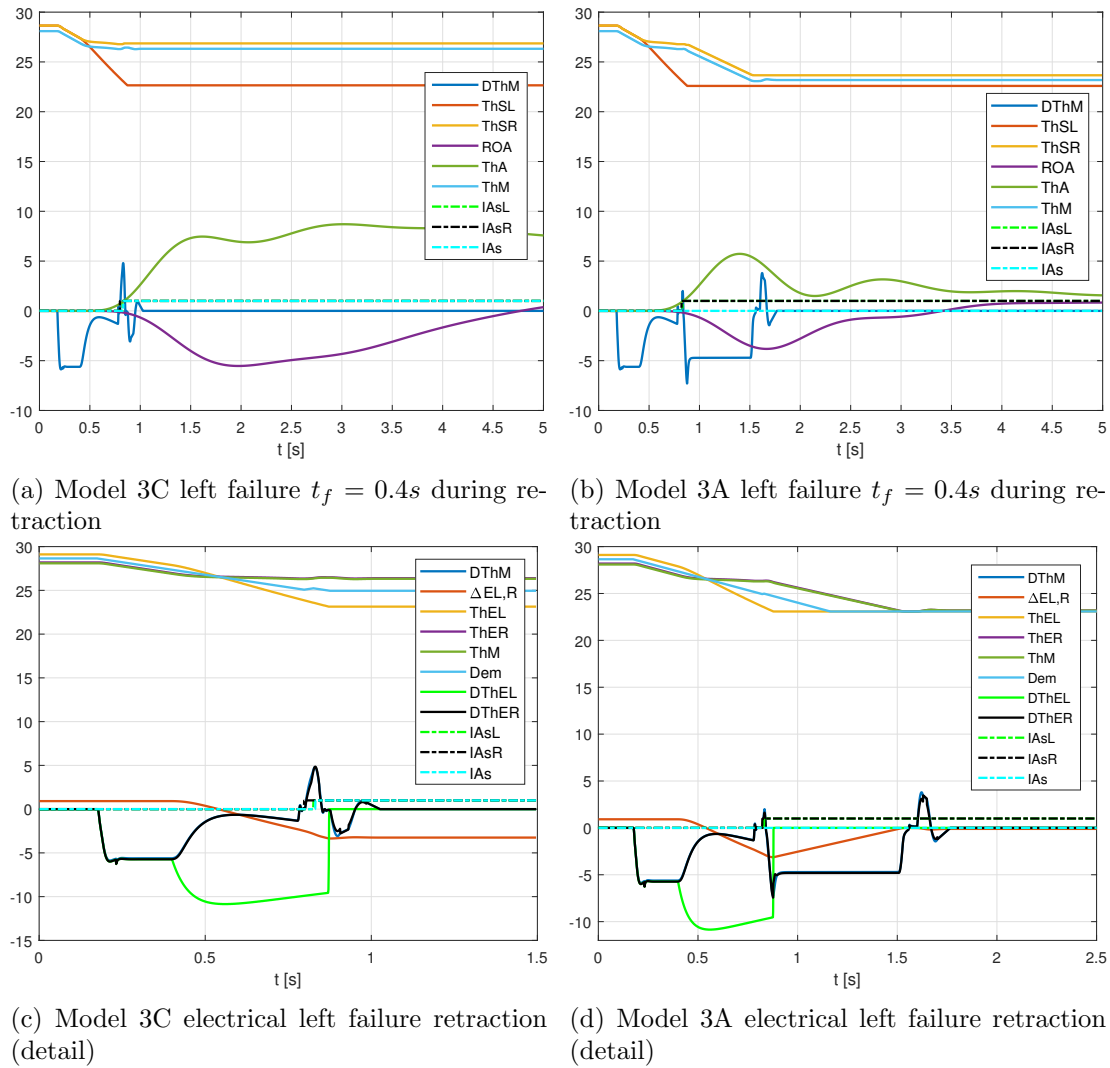


Figure 91: Model 3C vs 3A right failure retraction from 0.5-0.4 rad $T_{RC} = 10000Nm$ wear-out

earlier steady state conditions, so the the aforementioned significant and lasting asymmetry failure conditions are present sooner. All these reduce both the stability of the roll response and the aircraft maneuverability after failure.

On the other hand, little differences may be noted in the time response of both active models in case of right failure during retraction (see Figure 92). It seems that the right *general asymmetry failure* declaration during retraction does not significantly modify the aircraft rolling stability and maneuverability after failure. In effect, the *general asymmetry failure* on model 3C has a similar effect than the *resultant braking torque* $F_{f,R} + T_{br,R}$ on the asymmetry correction using model 3A. Thus, the aforementioned time responses of the both active models will be very similar both regarding the aircraft roll response stability and maneuverability after failure (slightly less on model 3C in both cases).

It should be reiterated that the *general asymmetry failure* declaration seems not to be necessary on wear-out conditions since the aforementioned combination of “*braking torques*” prevents the operative surface from diverging. In other words, there is no need

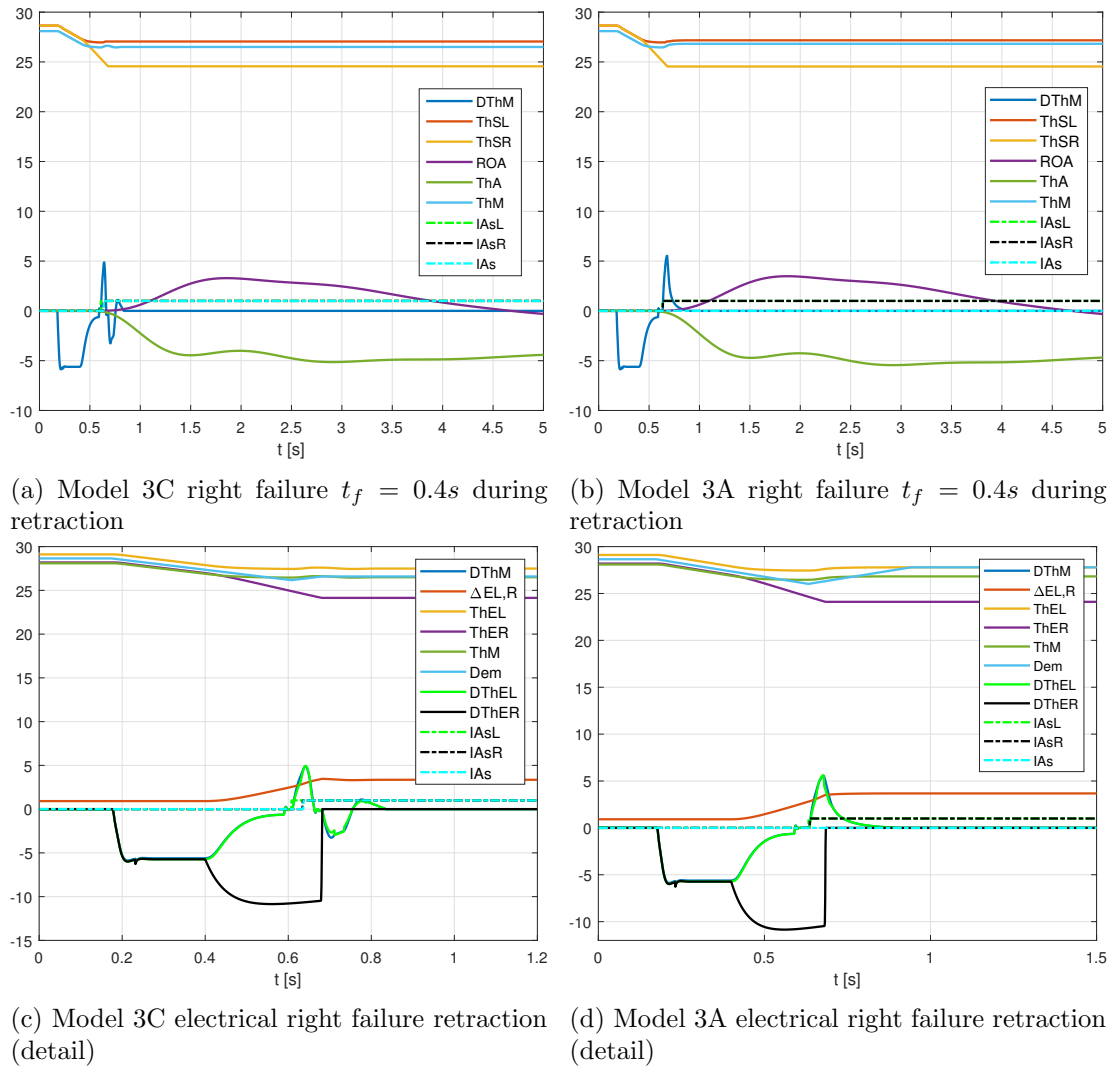


Figure 92: Model 3C vs 3A right failure retraction from 0.5-0.4 rad $T_{RC} = 10000Nm$ wear-out

to declare the *general asymmetry failure* on the active model 3C since no uncontrolled divergence scenario is present on 3A.

The *false multiple asymmetry failure*, both in left and right failure cases, deteriorates both the rolling time reponse stability and the aircraft maneuverability after failure. However, these are still higher than those of the same model 3C on wear-free conditions.

Nonetheless, both maneuverability and controllability are considerably worse on model 3C than on model 3 for given worn out actuators on flap retraction maneuvers.

8.5 Model 3E results on wear-out conditions

8.5.1 Low T_{RC} case results

The asymmetry active monitoring technique 3D under low aerodynamic loads on wear-out conditions present no differences with respect to model 3C, since the anticipation term of the dynamic position will be cancelled, $\xi = 0$. It is analogous to what discussed

in section 6.4.1 about model 3E on wear-free conditions.

The results of both extension and retraction, either for left or right failures, are shown in figures 93 and 94.

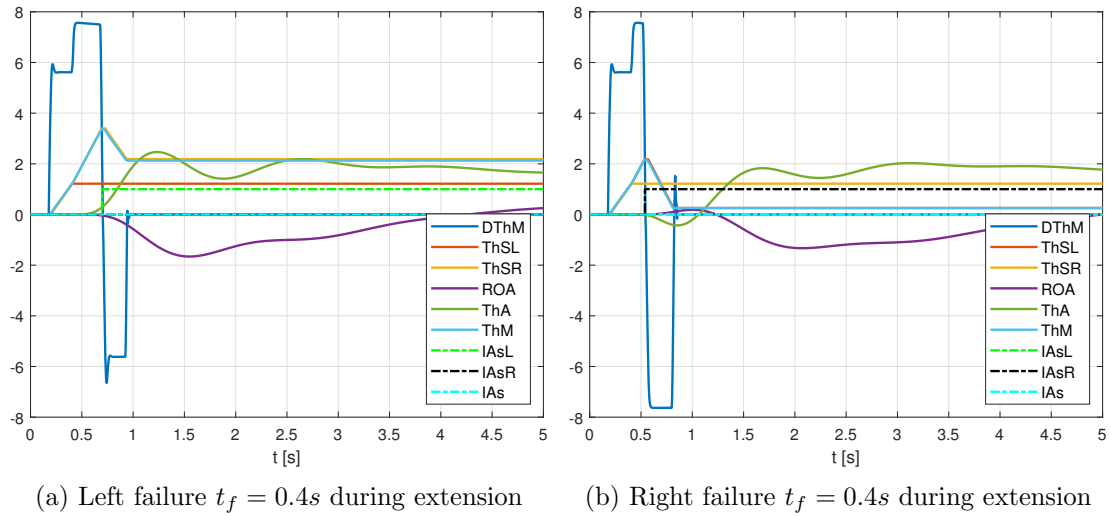


Figure 93: Model 3E failure extension from 0-0.07 rad at $T_{RC} = 0Nm$ wear-out

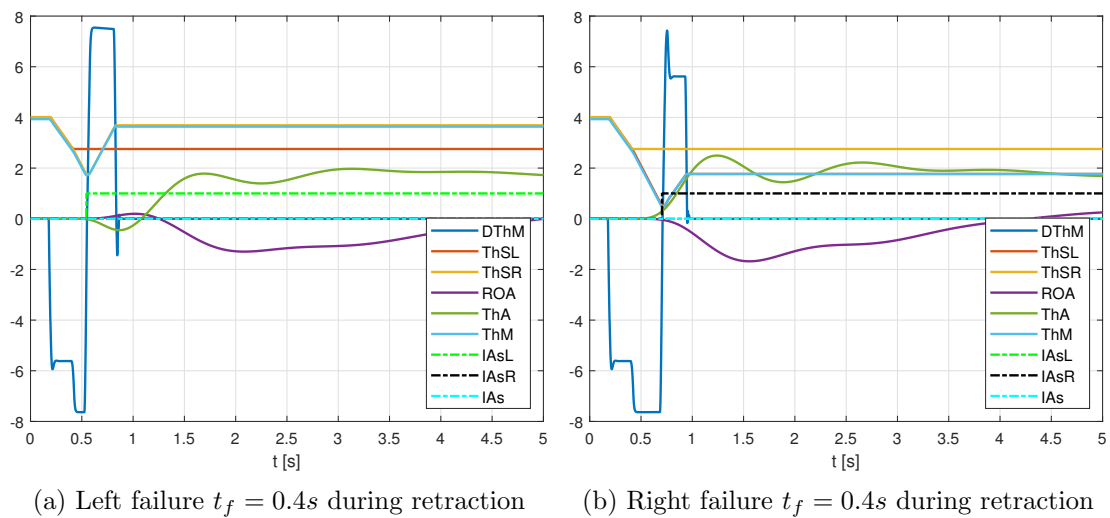


Figure 94: Model 3E failure retraction from 0.07-0 rad at $T_{RC} = 0Nm$ wear-out

As illustrated in the aforementioned figures, the behaviour of model 3E with respect to the model 3D on *worn-out conditions*, both on flap extension and retraction maneuvers, is governed again by the effect of the ramp slope, for given worn out actuators on flap retraction maneuvers.

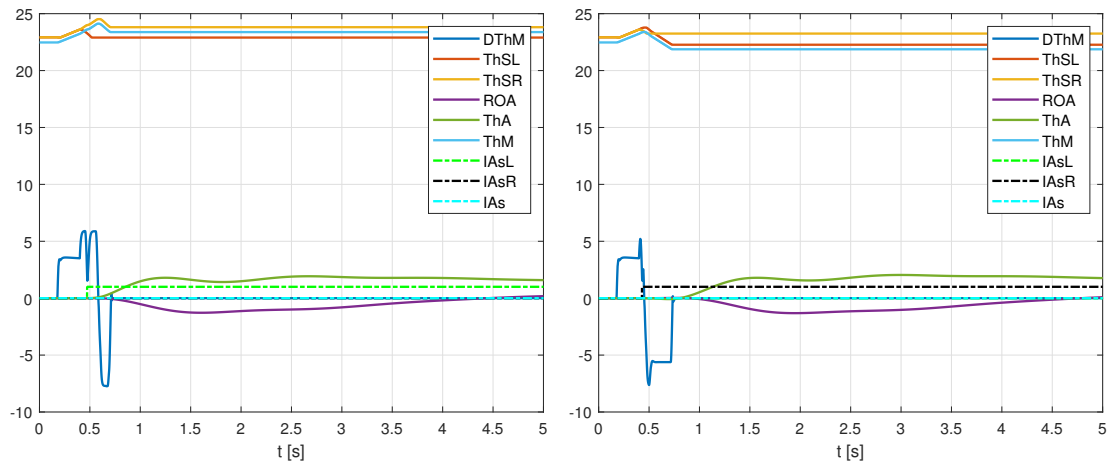
Thus, all the considerations made in section 6.4 are applicable in the current study case. In effect, the differences in the system output dynamics are similar between *dynamic position* models for a given degree of actuators wear and tear. Consequently, the aircraft rolling time response has decreased and the aircraft maneuverability after failure increases on model 3E with respect with model 3D on qwear-out conditions.

Nonetheless, these are considered as *moderate* changes, so neither the stability nor the maneuverability after failure would be seriously affected in any case.

8.5.2 High T_{RC} case results

The asymmetry active monitoring technique 3E presents an excellent behaviour in every high aerodynamic load scenario on wear-out conditions, both in left and right and right failures. Unlike the previous model 3C, the active technique 3E never presents *false multiple asymmetry failures*. Again, the combined effect of both the *dynamic position* of the model 3E and high friction force of the worn out actuators are decisive to obtain the aforementioned improvements, analogously to what mentioned on model 3D in section 8.2.2.

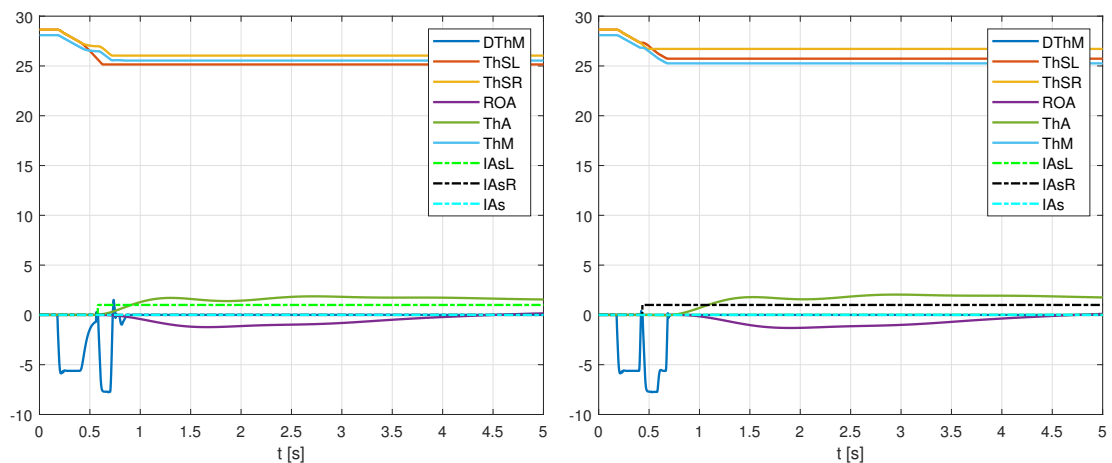
The results of both extension and retraction for either left or right failure are shown in figures 95 and 96.



(a) Left failure $t_f = 0.4s$ during extension

(b) Right failure $t_f = 0.4s$ during extension

Figure 95: Model 3E extension from 0.4-0.5 rad $T_{RC} = 10000Nm$ wear-out



(a) Left failure $t_f = 0.4s$ during retraction

(b) Right failure $t_f = 0.4s$ during retraction

Figure 96: Model 3E retraction from 0.5-0.4 rad $T_{RC} = 10000Nm$ wear-out

The active model $3E$ improves the behaviour of model $3D$ at high aerodynamic loads in failure during retraction cases. Indeed, the slow but controlled demand ramp slope of model $3E$ cause slower flap retraction and more retracted failure surface braking positions $\theta_i(t = t_{br})$ for a given worn out actuators friction force. All these lead to slightly better stability of the aircraft rolling time response and a significantly higher aircraft maneuverability after failure.

These improvements in retraction cases can be noted in Figure 97.

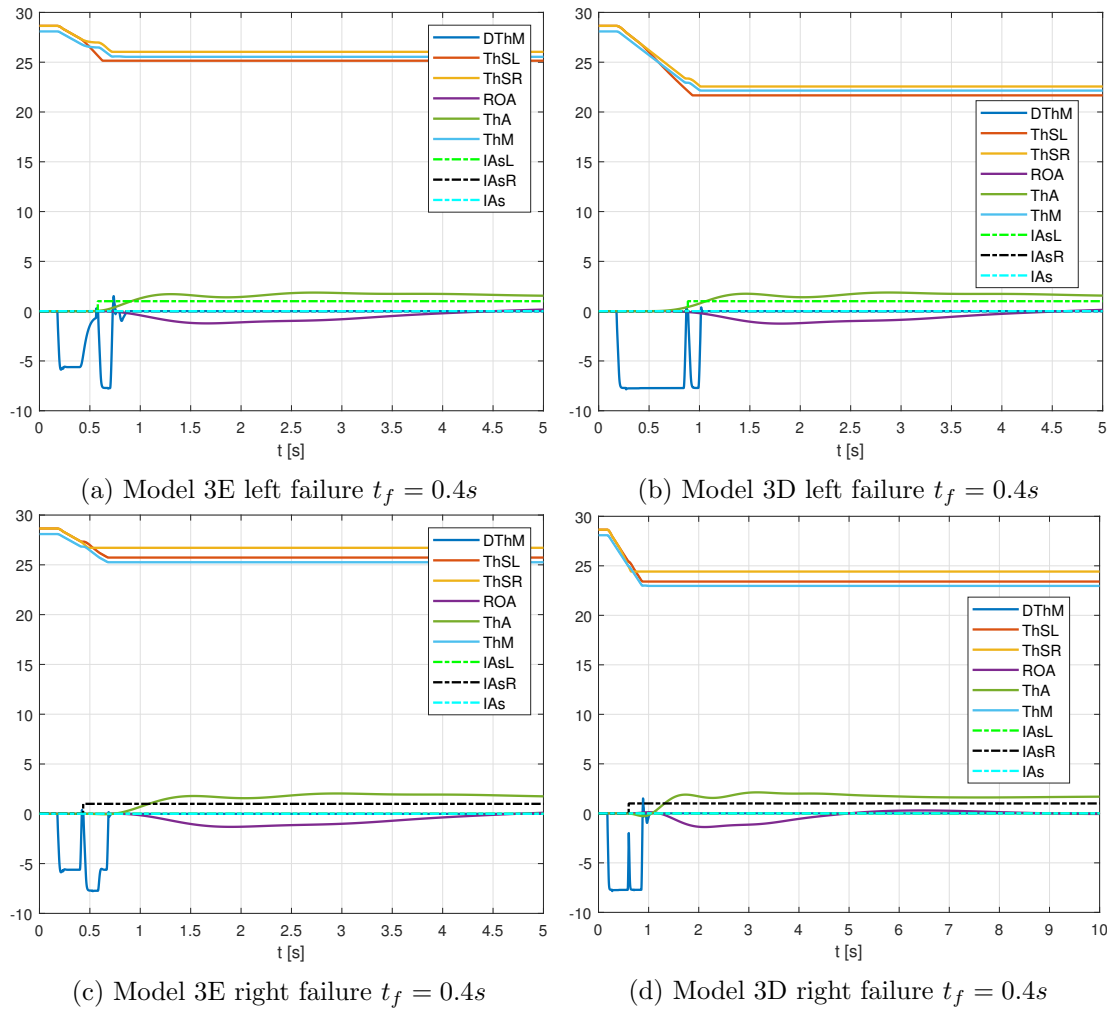


Figure 97: Model 3E vs 3D wear-out failure retraction 0.5-0.4rad at $T_{RC} = 10000Nm$

Moreover, $3E$ presents almost the same stability and maneuverability after failure in extension scenarios compared to model $3D$ on wear-out conditions. In effect, the system output in case of failure during flap extension are almost identical on these two active models. In this case, the effect of the slow but controlled demand ramp slope of model $3E$ will not be as decisive as the slowing down effect of the high friction force for the dynamic system response after failure. In consequence, the stability and maneuverability of both active models will be almost identical in case of failure during extraction under high aerodynamic loads.

Finally, the comparison between the same active model $3E$, both on wear-out and

wear-free conditions, shows a that it behaves much better on wear-out conditions. The decisive effect of the high friction forces inside the actuators caused by the wear and tear conditions, for equal *dynamic position* anticipation term on both models, lead to higher time response stability and maneuverability after failure, regardless the surface maneuver and the failure flap.

Indeed, the high friction force makes the difference between both tests. It slows down the system output dynamics, leading to lower overshoots in the aircraft roll responses, and lower flap retractions after failure, improving the braking position $\theta_i(t = t_{br})$ and the aircraft maneuverability after failure.

8.6 Comparison of active models on wear-out conditions

Analogously to what discussed for the *regular* and *borderline* wear-free cases, a general overview of the active monitoring techniques has been performed in the previous pages according to the input signal. However is also important to analyze the active techniques behaviour according to the effect of the position anticipation term, considering models with the same input signal. Therefore, a comparison of the active models behaviour on wear-out conditions according to the *dynamic position* effect for equal input signal models will be performed in the following pages.

8.6.1 General overview of low T_{RC} case results

The asymmetry active monitoring models may be grouped in two big categories to compare their behaviour on wear-out conditions under low aerodynamic loads, similarly to what discussed in section 6.5.1.

- Step-input monitoring techniques (3 & 3D)
- Ramp-input monitoring techniques (3C & 3E)

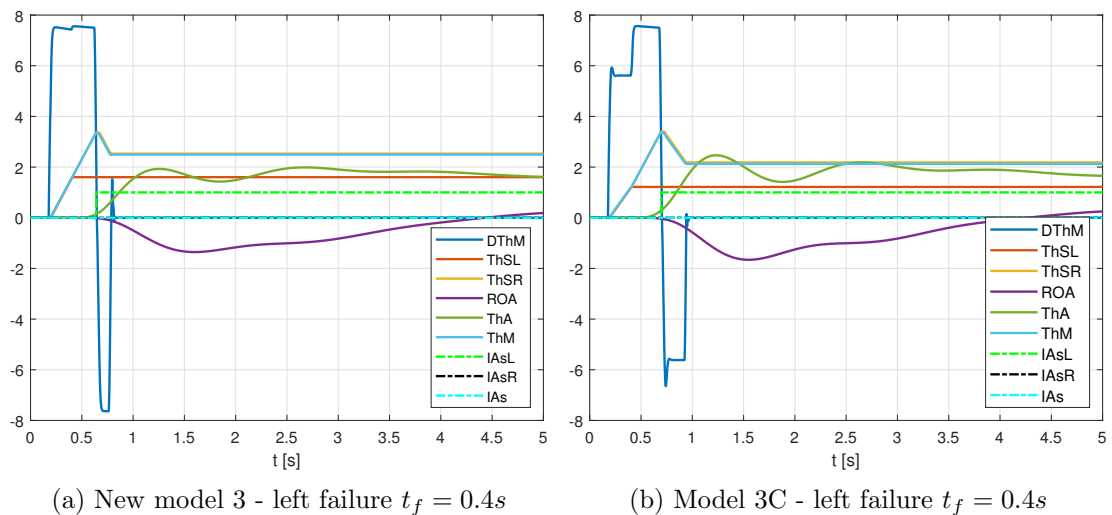


Figure 98: General overview at $T_{RC} = 0 Nm$ - failure extension from 0 to 0.07 rad wear-out

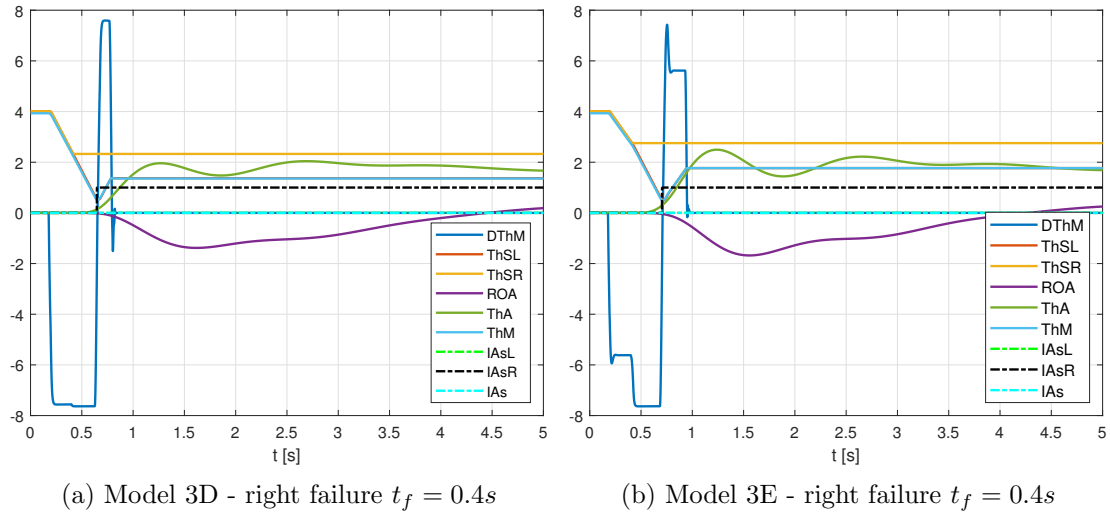


Figure 99: General overview at $T_{RC} = 0 \text{ Nm}$ - failure retraction from 0.07 to 0 rad wear-out

Again, the anticipation logics do not apply when considering low T_{RC} since the control parameter cancels the anticipation term, $\xi = 0$.

In general, the behaviour of the active models on wear-out conditions under low aerodynamic load is satisfactory and very similar to what studied in wear-free conditions. Little difference can be noted between the aforementioned conditions, especially after failure, since even regular actuators friction force values can compensate the low aerodynamic loads and quickly stop the failure surface.

As shown in figures 98 and 99:

- The step-input models responses are slightly more stable since their overshoot is a bit more damped.
- The ramp-input models responses lead to slightly more maneuverable aircrafts. This is because the position at the failure time $\theta_i(t = t_f)$ is reached with little flap deflections, which entails a smaller τ_{br} .

These considerations can be clearly noted both in case of left failure during flap extension and right failure during retraction, in which the effects of both the left and right position offset set on the electrical transducers are more evident.

These considerations can be clearly noted both in case of left failure during flap extension and right failure during retraction since the effects of both the left and right position offset set on the electrical transducers are more evident in such maneuvers

In any case, the response difference between active models is, again, minimal. Thus, all the asymmetry active monitoring techniques are satisfactory in regular conditions.

8.6.2 General overview of high T_{RC} case results

In regard to the system response under high aerodynamic loads, a deep analysis has been done in 8.4.2 and 8.5.2 between active monitoring techniques with the same input signal.

However, in contrast to the low T_{RC} scenarios, the *dynamic position* is relevant to determine the system response, since $\xi = 1$ when T_{RC} is high enough, analogously to what discussed on wear-free conditions in section 6.5.2. In fact, the main response difference between models lies, again, in the position anticipation logic.

Hence, similarly to the previous load scenario discussed above, the asymmetry active monitoring techniques could be grouped in two big categories, regardless the input signal:

- *Dynamic-position* active monitoring techniques (3D & 3E).
- *Non dynamic-position* active monitoring techniques (3 & 3C).

The results of the dynamic-position active monitoring techniques under high aerodynamic loads, either for extension and retraction cases are illustrated in figures 100 and 101.

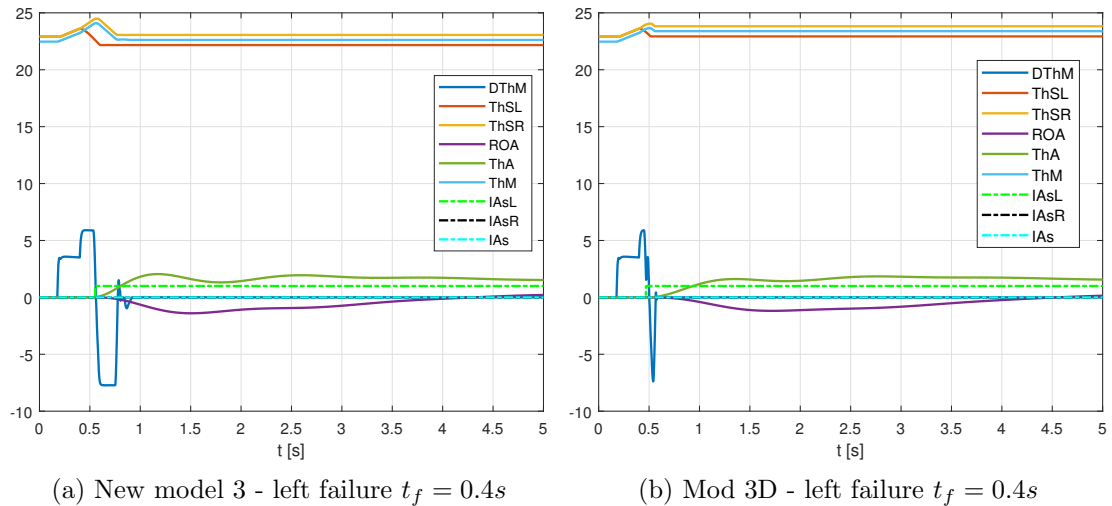


Figure 100: Overview step-input at $T_{RC} = 10000Nm$ - failure extension 0.4-0.5 rad wear-out

In general, the behaviour of the active models under low aerodynamic loads is acceptable. Nonetheless, the response of the dynamic-position active monitoring techniques is much better than those that do not consider any position anticipation logic.

As shown in figures 100 and 101, there is a slight behaviour improvement on model 3D due to the effect of the *dynamic position*. In effect, it could be noted that:

- The response stability using model 3D has slightly increased since the overshoot is a little bit more dumped, due to the combined effect of both a high actuators internal friction force and the effect of the anticipation term of the *dynamic position*.
- The aircraft maneuverability after failure increases in every case. Nevertheless, greater improvements are present on retraction maneuvers where, again, the combined effect high friction force and the *dynamic position* are determinant to achieve less retracted inoperative surface failure positions $\theta_i(t = t_{br})$. In effect,

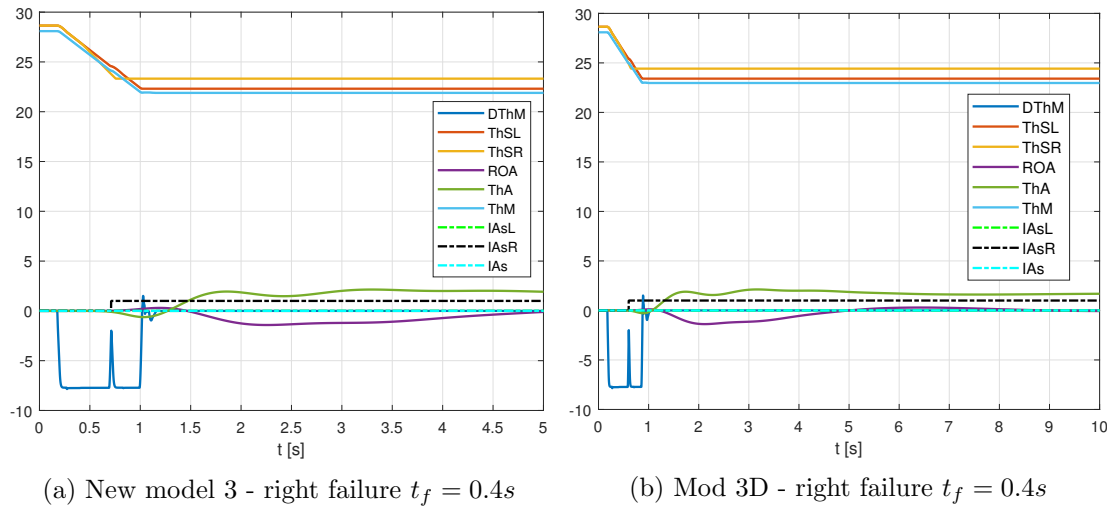


Figure 101: Overview step-input at $T_{RC} = 10000Nm$ - failure retraction 0.5-0.4 rad wear-out

smaller dimensionless braking time τ_{br} lead to smaller braking times after failure t_{br} , which contributes to reduce the aforementioned failure position.

Analogously, in regard to the ramp-input active monitoring techniques, the active model $3E$ also presents relevant improvements regarding stability and maneuverability after failure, as shown in figures 102 and 103.

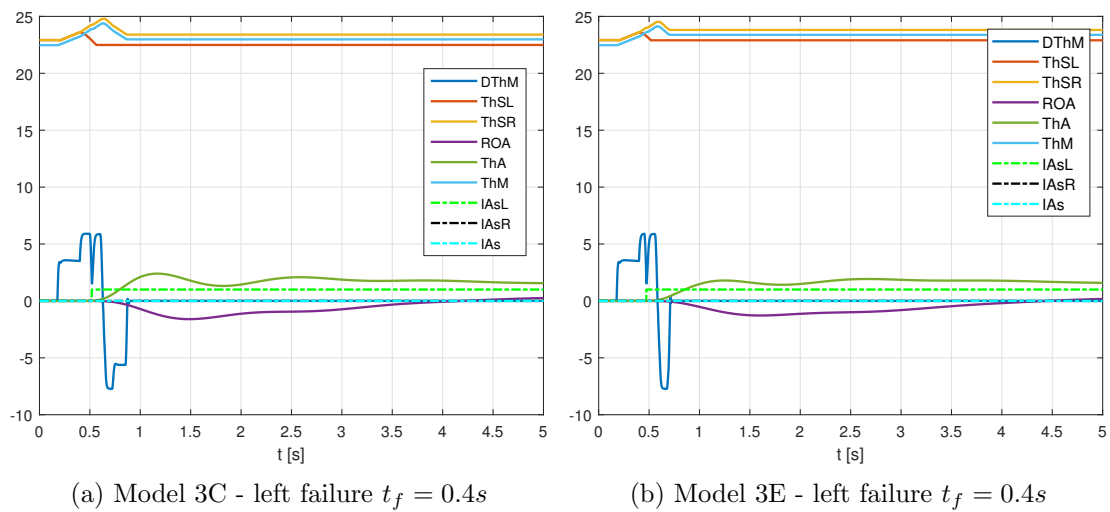


Figure 102: Overview ramp-input at $T_{RC} = 10000Nm$ - failure extension 0.4-0.5 rad wear-out

Similarly to what discussed above, the figures 102 and 103 illustrate again a some behaviour improvements on the active *dynamic position* model, $3E$ regarding the ramp-input models, to the effect of the *dynamic position* together with the worn out actuators high friction forces. Indeed, it could be noted that:

- Slight stability and maneuverability improvements can be noted on model $3E$ in extension cases with respect to model $3C$. Indeed, the effect of the high friction force controls the flap extension before failure and retraction after failure,

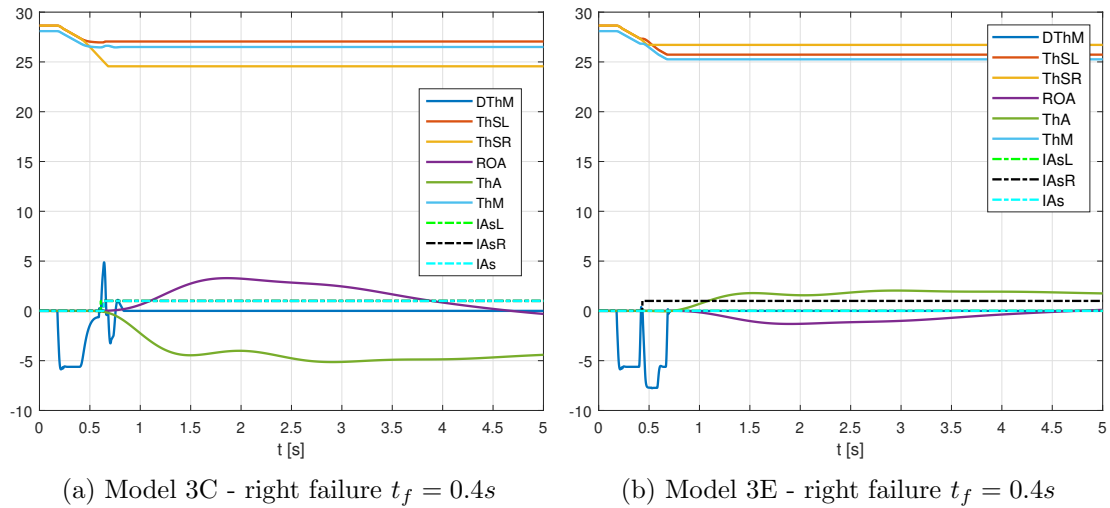


Figure 103: Overview ramp-input at $T_{RC} = 10000Nm$ - failure retraction 0.5-0.4 rad wear-out

always reducing the flap travelling speed, increasing the rolling transient response stability. In addition, lower retracted failure positions $\theta_i(t = t_{br})$ are reached by the failure surface, increasing the aircraft maneuverability after failure.

- Significant time response stability improvements are present on retraction maneuvers on model 3E. In contrast to the active model 3C, the ramp-input model 3E does not present any *false multiple asymmetry failures*, so the emergency surface braking is not executed. Consequently, the inoperative surface are always reached by the operative flap at a slower speed, given the high actuators wear and tear. In addition, the aircraft maneuverability after failure will also be higher on model 3E. In effect, the asymmetry between both flaps on steady state conditions will be minimal¹⁶ on model 3C and the aircraft maneuverability would be higher, even if the both flap braking emergency maneuver after the *general asymmetry failure* declaration causes less retracted failure positions $\theta_i(t = t_{br})$ on model 3C.

8.6.3 Summary table of active models on worn-out conditions

Finally, the summary table hereunder compares all the active models on the wear-out conditions conditions discussed in this chapter in order to analyze which presents the best behaviour in each situation (see Table 4). This table classifies both the active step-input and ramp-input monitoring techniques on wear-out conditions according to the different aerodynamic load cases, either in extension or retraction cases.

	Step-input models		Ramp-input models			
	3	3D	3A	3C	3E	
Low T_{RC}	2	2	3	1	1	Extension
	2	2	3	1	1	Retraction
High T_{RC}	3	1	4	3	1	Extension
	3	2	3	4	1	Retraction

Table 4: Models efficiency classification on *wear-out conditions*

¹⁶set by the angular offset of the electrical transducers position between both surfaces θ_{O_s, T_i}

To such purpose, analogously to what discussed on *regular wear-free conditions* in section 6.5.3, a numerical classification was used to quantitatively evaluate these models. These are ranked on a scale 1 to 5, 1 being the most efficient model and 5 the less efficient one. These numbers indicate the best-intermediate-worst model comparing all the active techniques according both to their dynamic response stability and the aircraft maneuverability after failure. Since the number is the result of the crossed comparison of all the active monitoring techniques, this is considered to be a numerical **relative** scale.

In addition, a color coding was also implemented to give a general overview of the active models behaviour in the considered regular conditions. Similarly, the color coding is based on three colors, green, orange and red. Green represents the most efficient models, orange the less efficient models, in both cases with satisfactory results, and red being the unsatisfactory models in terms of efficiency, always for the considered worn-out conditions.

In the light of the test results, some additional comments should be made:

1. The active monitoring techniques that consider an anticipation term by means of the *dynamic position*, behave better than the non *dynamic position* active models in case of high aerodynamic loads.
2. Minor differences can be noted between the active models according to the input signal in case of low aerodynamic loads. Nevertheless, there is an exception with active model *3A*, due to both its poor robustness and its intrinsically slower dynamics.
3. There are no differences between the same input-signal models in case of low aerodynamic load, with the exception again with the active model *3A* regarding the ramp-input models.
4. Great improvements can be noted between the active models marked in green and orange. Similarly, minor differences can be noted between the active models marked with the same color.

Finally, it seems that the asymmetry active monitoring techniques models that behave better on worn-out conditions are:

- The *active models 3D and 3E* in low aerodynamic load cases.
- The *active model 3E* in high aerodynamic load cases.

Thus, in general, the *model 3E* is considered the *best* model to manage any load and deflection scenario due to the main following characteristics:

- **The slow and controlled flap extension/retraction due to the demand ramp slope that, together with the high friction force of the worn out actuators, cause a more stable system time response.** Indeed, the little speed travel in each surface does not create a great asymmetry in the transient flap response and more dumped overshoot will be present in the roll responses. Hence, the system time output will be more stable.

- **The combined effect of high friction force, slow and controlled demand ramp input and the *dynamic position* anticipation logic leads to an increase of the aircraft maneuverability after failure.** In effect, the slow and controlled system response reduces the dimensionless braking time τ_{br} , which leads to a lower flap extension/retraction $\theta_i(t = t_{br})$ to achieve by the operative surface on the asymmetry correction maneuver. Consequently, lower aileron deflection angles on steady state conditions $\phi_{A,ss}$ will be necessary to compensate the rolling moment induced by the final braked position of both surfaces.
- **The lack of *false multiple asymmetry failure* declarations in flap retraction scenarios, unlike the ramp input $3C$ from where it comes, increases the active model reliability and increases the aircraft maneuverability after failure.** The beneficial effect of the *dynamic position* anticipates the partial asymmetry failure declaration, which prevents from any *false multiple asymmetry failure* declaration case. In consequence, the asymmetry between both flaps on steady state conditions will be minimal (set by the angular offset of the electrical transducers position between both surfaces $\theta_{Os,Ti}$) and the aircraft maneuverability would be higher, even if $\theta_i(t = t_{br})$ would be more extended than in case $3C$.

Nevertheless, aerodynamic borderline conditions can also be present on wear-out conditions. These will introduce relevant instabilities in the system output which will seriously affect the engine speed $\dot{\theta}_M$ and, consequently, the stability margin of the entire system time response stability. This issue, among others, will be discussed in the following section.

9 Aerodynamic wear-out borderline conditions

9.1 Combined effect of aerodynamic load and friction force

The combined effect of both the aerodynamic load and the friction force of the actuators is essential to study the behaviour of the active monitoring techniques on wear-out borderline conditions. The aim of this section is to study the asymmetry monitoring problems that arise from combining both high aerodynamic torques and high friction forces due to the actuators wear-out and compare the results with the other study cases.

Thus, the new study case is called *aerodynamic wear-out borderline conditions*. They include:

- High external (aerodynamic) loads when deflecting from an angular position that is close to the minimum flap retraction. This operating condition considers a combination of both the aircraft speed V and angle of attack α that leads to a high T_{RC} ¹⁷.
- Reversible worn out actuators.

Firstly, the sign convention for the surfaces travel speed and the constant aerodynamic load T_{RC} is the following:

- Positive flap travel speeds $\dot{\theta}_i > 0$ are those present during extension.
- Positive constant aerodynamic load T_{RC} are those that induce a retracting torque on the surfaces.

Let the passive torque vector $\vec{T}_{pass,i}$ be the sum of the aerodynamic torque and the friction (dissipative) torque. It can be written as:

$$\vec{T}_{pass,i} = \vec{T}_{RC,i} + \vec{F}_{f,i} \quad (9.1)$$

where $\vec{F}_{f,i}$ is the friction torque vector and $\vec{T}_{RC,i}$ is the vector of the resistive torque constant component. All these are referenced to the surface i .

On the other hand, let the active torque be:

$$\vec{T}_{act,i} = \frac{\vec{T}_{G,i}}{Z_S} - c_S \vec{\theta}_i \quad (9.2)$$

where $\vec{T}_{G,i}$ is the gear transmission torque, which is transmitted to the surface, and $c_S \vec{\theta}_i$ is the viscous dumping component of the active torque (proportional to the surface speed). Again, these are referenced to the surface i . In addition, the net torque (also named *effective* torque) would be the sum of both the active and the passive torque:

$$\vec{T}_{eff,i} = \vec{T}_{act,i} + \vec{T}_{pass,i} \quad (9.3)$$

Thus, according to the Newton's second law for rotation, the acceleration of the surface i would be:

$$\vec{\ddot{\theta}}_i = \frac{\vec{T}_{eff,i}}{J_S} \quad (9.4)$$

¹⁷linear aerodynamics may be considered in a first approximation

where J_S is the moment of inertia of the surfaces, assuming they are identical.

In regard to the friction force *in opposing*, it satisfies the following expression, as indicated in section 3:

$$\vec{T}_{RC} \cdot \vec{\dot{\theta}}_i \geq 0 \Rightarrow \vec{T}_{RC} \cdot \vec{F}_{f,i} \leq 0 \quad (9.5)$$

so \vec{T}_{RC} and $\vec{F}_{f,i}$ present the same signs. According to the sign convention discussed above, it means that the active torque will always have to compensate the sum of both the aerodynamic torque and the friction force.

In consequence, higher friction force values, due to worn out actuators would increase the passive torque by the increase of the dissipative component. Hence, the dynamic system response would be slower in case of worn out actuators with respect to the wear-free conditions.

Thus, the combination of high aerodynamic torques T_{RC} and high friction forces $F_{f,i}$ *in opposing* due to the friction efficiency reduction η_{OS} causes low net torques $T_{eff,i}$. This may lead to control instabilities when using dynamic position active monitoring techniques (3D and 3E) on wear-out borderline conditions.

In effect, the anticipation term of the *dynamic position* will always be active $\xi = 0$ since it is set according to T_{RC} . Hence, the very slow dynamics are controlled by a “PS” controller, which causes dynamic instabilities such as limit cycles on the engine speed $\dot{\theta}_M$.

It should be noted that the friction forces *in opposing* correspond to extension flap maneuvers. In effect, both positive flap travel speeds $\dot{\theta}_i$ and positive constant aerodynamic loads T_{RC} are only present during flap extensions.

On the other hand, in case of friction force *in aiding*, it satisfies:

$$\vec{T}_{RC} \cdot \vec{\dot{\theta}}_i < 0 \Rightarrow \vec{T}_{RC} \cdot \vec{F}_{f,i} > 0 \quad (9.6)$$

as also indicated in section 3. Hence, both \vec{T}_{RC} and $\vec{F}_{f,i}$ have opposite signs, so there friction force will compensate the aerodynamic torque *in aiding* according to the sign convention.

Similarly to what discussed *in opposing*, higher friction force values would increase the passive torque by the increase of the dissipative component. Again, the dynamic system response would be slower in case of worn out actuators with respect to the wear-free conditions.

Therefore, the combination of high aerodynamic torques T_{RC} and high friction forces $F_{f,i}$ *in aiding* due to the drastic friction efficiency η_{AS} causes low net torques $T_{eff,i}$. This may lead again to control instabilities when using dynamic position active monitoring techniques (3D and 3E) on wear-out borderline conditions. Again, the system very slow dynamics are regulated by a “PS” controller, which is always active since the control parameter ξ depends on the always high aerodynamic torque T_{RC} on borderline conditions.

Moreover, η_{AS} is an important parameter to determine both the degree of the actuators reversibility after failure and the system performances in flap retraction maneuvers, either before and after failure.

In conclusion, particular instability problems will arise both *in opposing* (extension) and *in aiding* (retraction) before failure. In contrast to the wear-free borderline conditions, in which $F_f \ll T_{RC}$, the friction force on wear-out conditions can compensate or amplify the passive torque leading to important failure surface decelerations causing an notable slowdown of the dynamic system response. These should not be controlled by a “PS” controller, which might produce certain instabilities on the system time response.

The algorithms of *3D* and *3E* were not changed to perform the test campaign on the aforementioned current borderline conditions. This allows both an analysis of the models effectiveness on the current conditions and a behaviour comparison with respect to the previous study cases. However, future projects may consider the net torque \vec{T}_{eff} instead of the aerodynamic torque T_{RC} to define the control parameter ξ that activates/deactivates the anticipation term of the *dynamic position*.

The current borderline study case will be called *aerodynamic wear-out borderline conditions*. It considers:

- High external (aerodynamic) loads when deflecting from an angular position that is close to the minimum flap retraction.
- Reversible worn out actuators.

The active asymmetry monitoring techniques will be tested in different aerodynamic torque and flap deflection scenarios with worn out actuators that present the friction efficiencies indicated in table 3. The test campaign considers:

- Extraction from 0 to 0.07 rad at $T_{RC} = 10000Nm$: extraction from a retarded position in flight.
- Retraction from 0.07 to 0 rad at $T_{RC} = 10000Nm$: retraction from a retarded position in flight.

Both cases are considered *maneuvers under high aerodynamic loads*, which was one of the two assumption of the *aerodynamic wear-out borderline conditions*. The Equation (7.1) is applicable in this section.

Follow the analysis of the tests results on aerodynamic wear-out borderline conditions.

9.2 New model 3 results - wear-out borderline case

The behaviour of the new model 3 on aerodynamic borderline cases with worn out actuators is similar to what discussed above on “regular” wear out condition in section 8.1. It is shown in figures 104 and 105.

In effect, little differences may be noted between these two operating conditions, where the main difference is the aerodynamic load T_{RC} value, which will higher on borderline conditions. Hence, the net torque $T_{eff,i}$ is higher on borderline conditions for a given friction force of the worn out actuators, since $T_{eff,i}$ will only depend on

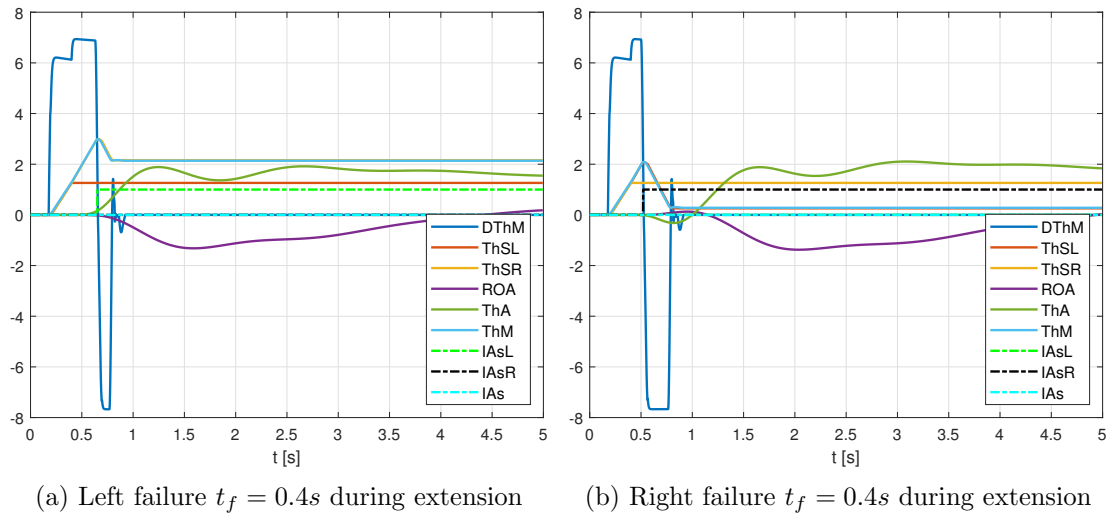


Figure 104: New model 3 - bord. case wear-out failure ext 0-0.07 rad $T_{RC} = 10000Nm$

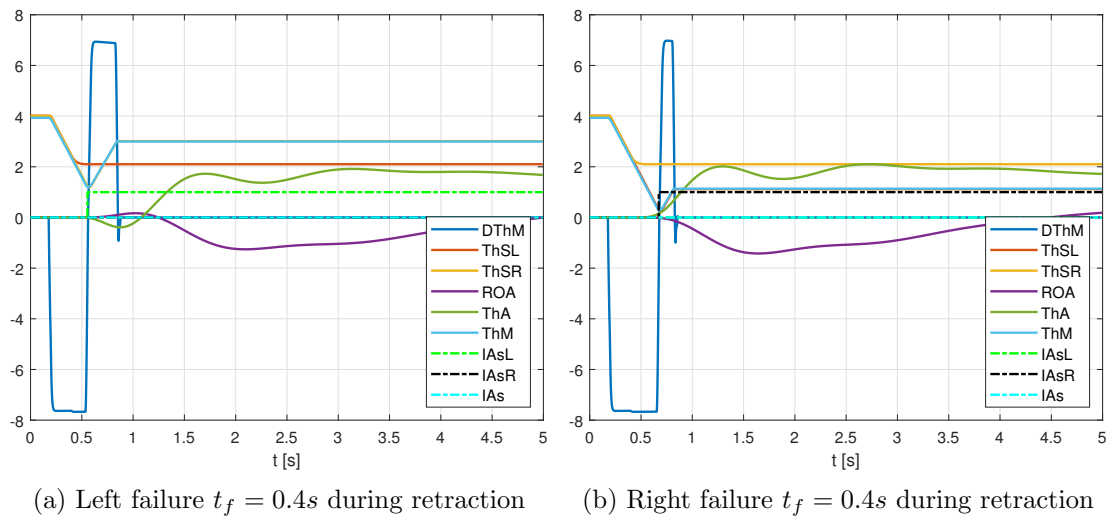


Figure 105: New model 3 - bord. case wear-out failure retr 0.07-0 rad $T_{RC} = 10000Nm$

T_{RC} . Follow the main effects of the high aerodynamic load on wear-out conditions in regard to the flap deflections.

Firstly, both slower extensions and faster retractions are present before failure with respect to the “regular” wear-free conditions. In effect, the aerodynamic resistive torque T_{RC} either “decelerates” the flap extension or “accelerates” it during retraction, varying the surfaces travel speed before failure.

Secondly, the failure surface braking moment is slightly different with respect to the “regular” wear-out cases, in which lower aerodynamic loads were considered. Indeed, the failure surface braking position $\theta_i(t = t_f)$, affected by the high aerodynamic torque T_{RC} , is described as follows:

- Slightly more retracted in extension cases, due to the high aerodynamic torque T_{RC} that helps the braking system to stop the failure surface.
- More retracted in retraction cases, due to the high aerodynamic torque T_{RC} that

“accelerates” the failure retracting surface, delaying the braking moment after failure.

Nonetheless, these differences are subtle, so both the stability margin of the roll response and the aircraft maneuverability after failure do not change significantly between the new model 3 results on wear-out conditions, either “regular” or “borderline”.

On the other hand, notable differences are present between the behaviour on model 3 between both wear-out and wear-free aerodynamic borderline conditions. The effect of the high friction forces inside the worn out actuators prevents the surfaces from reaching the saturation limit θ_{min} .

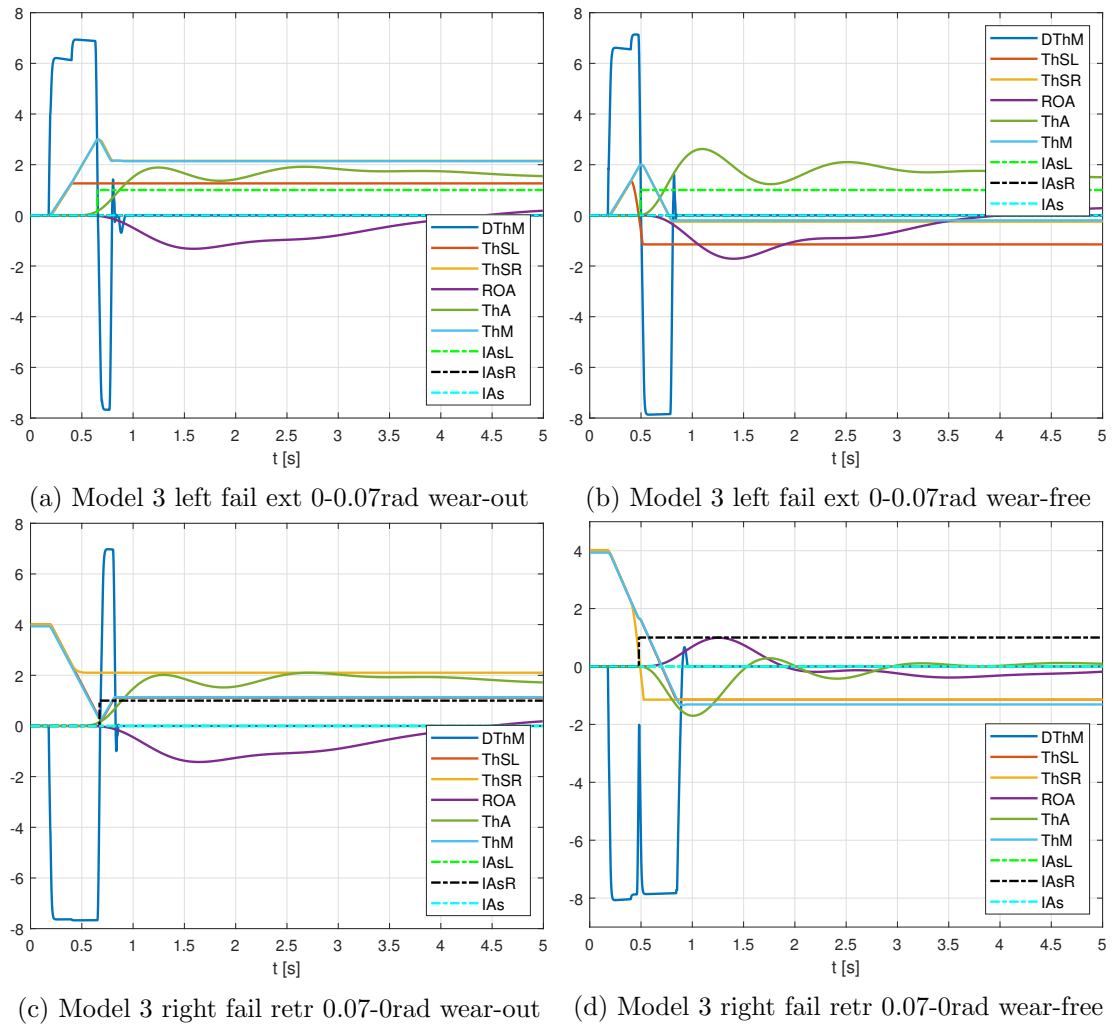


Figure 106: Model 3 wear-out vs wear-free borderline cond $t_f = 0.4s$ $T_{RC} = 10000Nm$

In effect, the friction force *in opposing* during extension reduces the final value of the net torque $T_{eff,i}$. This leads to a deceleration of the failure surface $\ddot{\theta}_i > 0$, helping the braking system to stop the failure surface. On the other hand, the friction force *in aiding* during retraction increases the final value of the net torque $T_{eff,i}$. This causes a positive acceleration on the failure surface $\ddot{\theta}_i < 0$ that brakes the retracting surface. In effect, the sign convention set a negative travel speed on the retracting flap, so positive acceleration may lead to a failure surface braking. All these is illustrated in Figure 106.

In addition, the reduction of the failure surface travel speed is higher in retraction maneuvers, since the actuators efficiency reduction *in aiding* $\Delta\eta_{AS}$ is notably higher than *in opposing* $\Delta\eta_{OS}$. This is essential, since the saturation phenomena may occur after failure, when the inoperative surface is operating in retraction (*aiding*). Hence, the especially high braking of the failure surface in retraction will prevent eventual saturation phenomena on wear-out borderline conditions.

9.3 Model 3D results - wear-out borderline case

Similarly to what discussed in section 7.2 about the wear-free borderline conditions, the anticiaption term is always active on models 3D and 3E. In effect, the control parameter is always $\xi = 1$ activating the position anticipation term of the *dynamic position* given the high aerodynamic load T_{RC} .

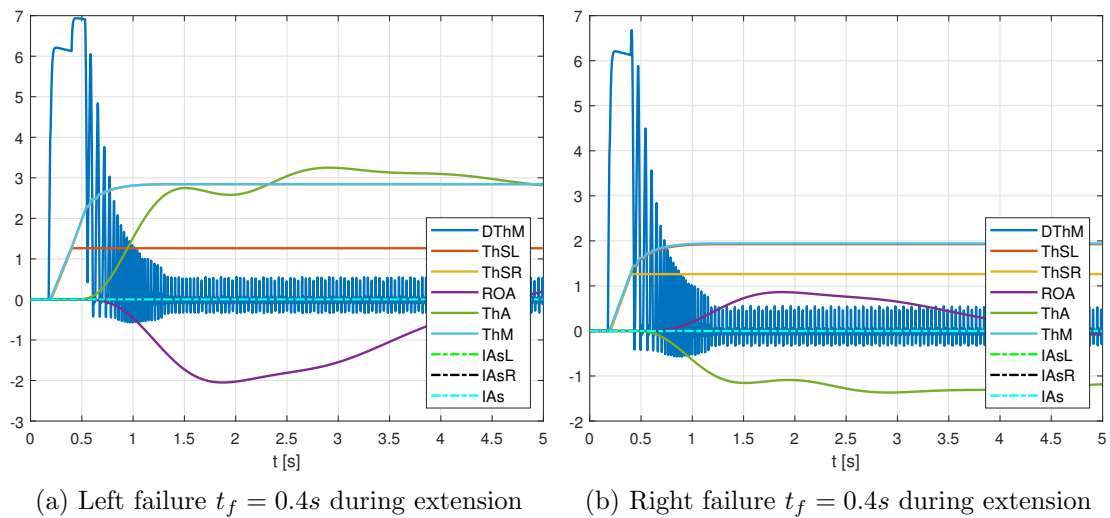


Figure 107: Model 3D - bord. case wear-out failure ext 0-0.07 rad $T_{RC} = 10000Nm$

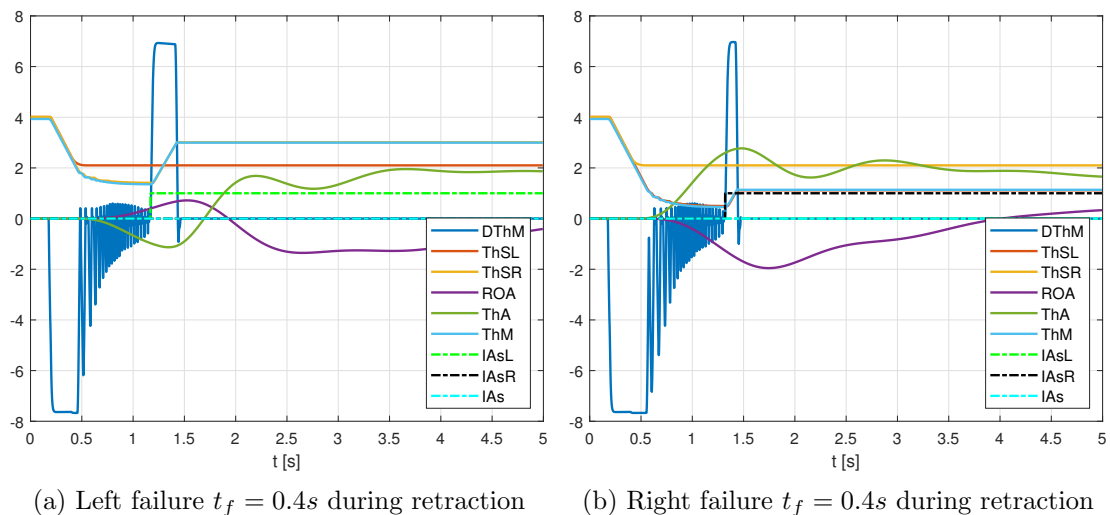


Figure 108: Model 3D - bord. case wear-out failure retr 0.07-0 rad $T_{RC} = 10000Nm$

Nonetheless, this time the anticipation term of the *dynamic position* will be a potential source of instability. As discussed at the beginning of this section, the combination

of high aerodynamic loads and very high friction forces inside the worn out actuators may lead to low values of the net torque $T_{eff,i}$ on the surfaces. In consequence, there is no need to activate the anticipation term, since it is necessary only in those scenarios in which higher retraction speeds may be reached by the inoperative surface after failure. In fact, the activation of the unnecessary anticipating term will cause important instabilities as illustrated in figures 107 and 108.

As shown in the aforementioned figures, there is a clear unstable dynamic response of the system. Notice that two different scenarios are possible when using the active model 3D on borderline wear-out conditions:

- Instabilities during flap extension maneuvers, in which there are no asymmetry failure declarations, regardless the failure side. These are shown in Figure 107.
- Instabilities during flap retraction maneuvers in which, nevertheless, the correct *partial asymmetry failure* is declared, regardless the failure side. These are shown in Figure 108.

A deep analysis of these instabilities should be done. To that end, each scenario will be discussed regarding the instability source and its consequences on the asymmetry failure detection and control.

Firstly, the instabilities during flap extension maneuvers are illustrated in Figure 109. It shows the behaviour of model 3D in case of left failure during extension on the current wear-out borderline conditions.

As shown in Figure 109, the engine speed $\dot{\theta}_M$ goes back and forth, accelerating and decelerating the operative surface (right). The reason why these oscillations appear lies in the fact that the system output dynamics are too slow for a *speed control* (“PS” controller). In other words, the position anticipation term of the *dynamic position* is active $\xi = 1$ in borderline scenarios. In contrast to the wear-free borderline conditions, in which $F_f \ll T_{RC}$, the friction force on wear-out conditions can compensate or amplify the passive torque leading to important failure surface decelerations causing a notable slowdown of the system time response.

The disastrous combination both the slow dynamic system response, due to the high friction force, and the flipping behaviour of the *Slow* parameter lead to the aforementioned instabilities.

The Figure 109 illustrates the engine speed $\dot{\theta}_M$ necessary to extend both surfaces, reaching a sort of steady state conditions before failure. Once the left failure is produced, the engine speed bound can be noted, which powers the right surface that also accelerates, as well as the failure surface speed drop due to the braking of the failure (left) surface. This “perturbation” of the steady conditions before failure increases the relative position of the failure left surface with respect to the *reference position*, which is the engine angular position θ_M on step-input active models such as 3D. At a certain point, the partial asymmetry failure counter reaches the *Slow* parameter upper threshold (empirically set in 1000), activating the aforementioned parameter, which shuts the electric current of the valve. In consequence, the engine speed drops reducing the aforementioned left relative position, which reactivates the the *Slow* parameter, that becomes 1 again. Once this parameter is active, the engine speeds up again, reaccelerating the

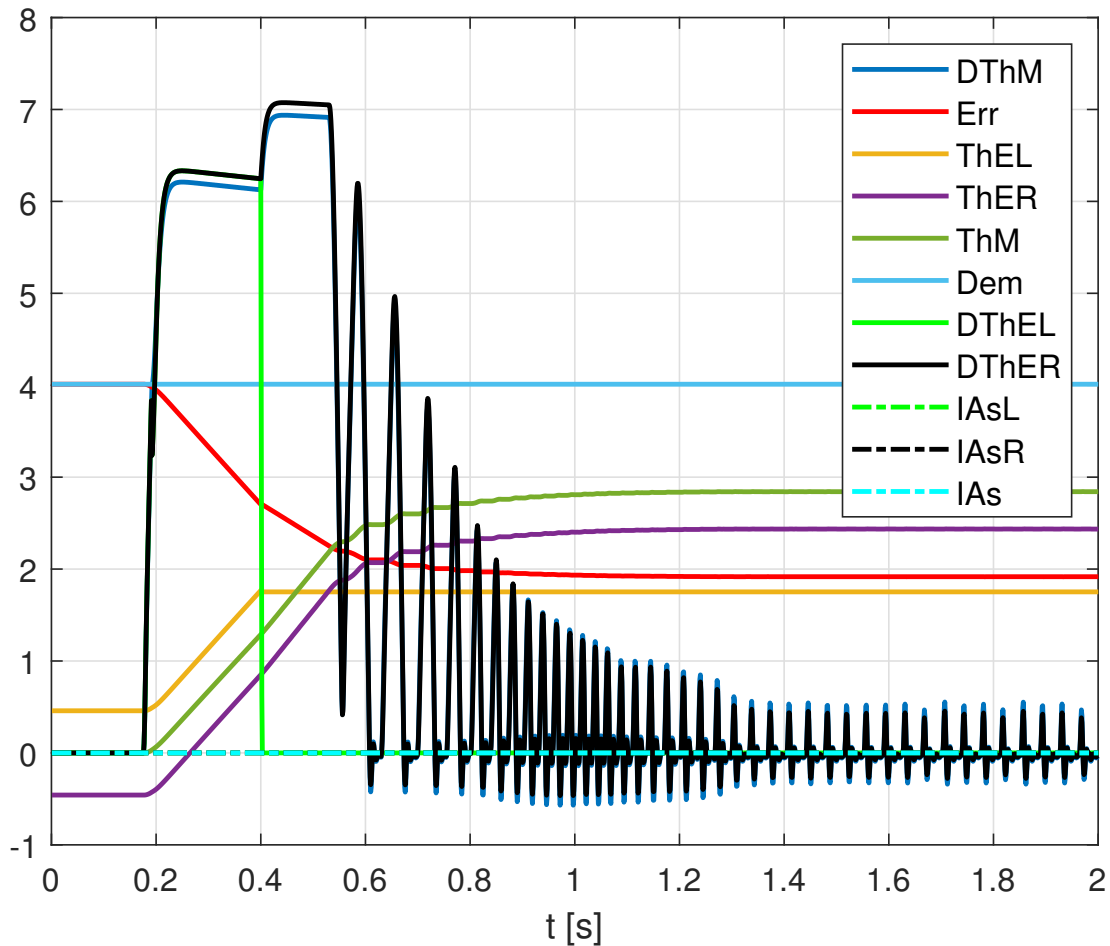


Figure 109: Model 3D (electrical) left fail extension 0-0.07 rad wear-out borderline

operative (right) surface.

Consequently, this flipping between 0 to 1 activates and deactivates the electric current Cor of the valve, causing a limit cycle of the engine speed time output that affects both the electrical and physical surface angular positions.

Notice that the *Slow* parameter flipping effect is similar to what described in section 5.4. Indeed, the engine speed variation $\dot{\theta}_M$ suffers the aforementioned limit cycle, causing an important instability in the system response. It prevents the declaration the left *partial asymmetry failure* and the system will reach a peculiar steady state, caused by the flipping of the electric current that “artificially brakes” the operative surface during the rest of the flight.

This “artificially braking” of the operative surface has significant consequences. These are discussed below:

- Since the *partial asymmetry failure* is never declared, the engine (and also the flapper nozzle) will be in charge of ‘artificially braking’ the operative surface. In consequence, both components may suffer from fatigue when operating under overload conditions, which would increase the high wear and tear conditions of the system and even break down either the components or the mechanical

transmissions.

- There is no asymmetry failure declaration, so no failure notification will be given to the cockpit crew. Consequently, further flap extensions or retractions may be commanded to the system, leading to a further deterioration of the system performance. In effect, the new command may increment the asymmetry between both flaps increasing the steady state roll angle of the aircraft $\phi_{A,ss}$, which may seriously compromise the aircraft maneuverability after failure. In conclusion, it is necessary that the cockpit crew becomes aware to the asymmetry failure to correct it manually, activating the braking system by taking off the pressure of the shutoff valve.

Secondly, the instabilities during flap retraction maneuvers are illustrated in Figure 110. It shows the behaviour of model 3D in case of left failure during retraction on the current wear-out borderline conditions.

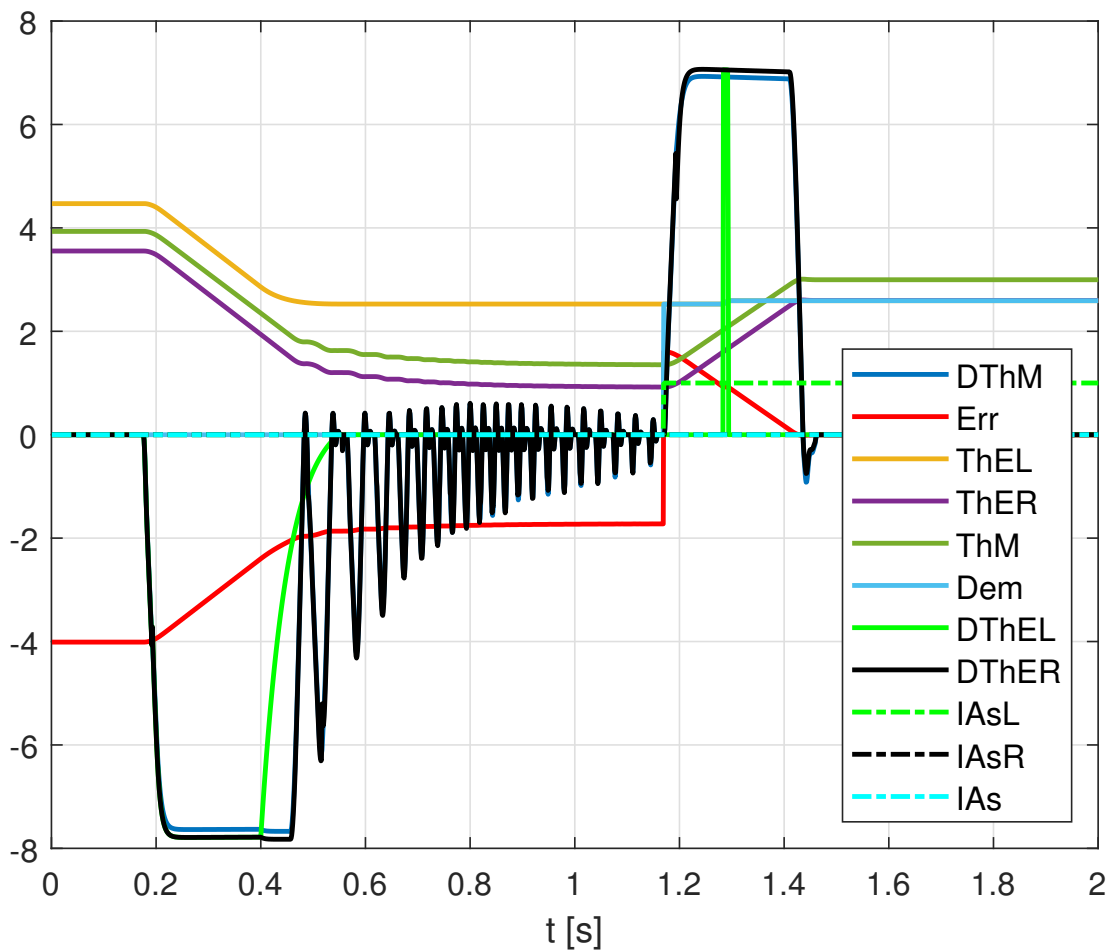


Figure 110: Model 3D (electrical) left fail retraction 0.07-0 rad wear-out borderline

Similar to the left failure during extension discussed above, the engine speed $\dot{\theta}_M$ goes back and forth again, accelerating and decelerating the operative surface (right). The reason why these oscillations appear lies, again, in the fact that the system output dynamics are too slow to activate the position anticipation term of the *dynamic position* to declare the asymmetry failure.

The combination effect of both the slow dynamics of the system and the flipping behaviour of the *Slow* parameter on retraction cases is analogous to what described above for extension scenarios. Again, the reason why these oscillations appear lies in the fact that the system output dynamics are too slow for a speed control (“*PS*” controller).

However, in case of failure during retraction, the correct *partial asymmetry failure* is declared, regardless the failure side, as shown in Figure 110.

The reason why the *partial asymmetry failure* is declared only in retraction cases seems to lie in the friction efficiency reduction when either extending or retracting the surfaces. In case of surface retraction, the actuators efficiency reduction $\Delta\eta_{AS}$ is higher than in case of flap extension $\Delta\eta_{OS}$. This leads to higher friction forces *in aiding* than *in opposing*, that directly affect the deceleration of the operative surface. Therefore the engine speed has to compensate higher friction forces when powering the operative flap, so $\dot{\theta}_M$ decreases. Hence, the amplitude of the limit cycle oscillation decreases, allowing the *partial asymmetry failure* counter to declare the failure on the correct side. Thus, the actuators efficiency reduction determines the partial asymmetry failure declaration.

All these can be summarized as follows:

1. The high friction forces of the worn out actuators slow down the dynamic system response, making the anticipation term of the *dynamic position* unnecessary. In fact, its activation by means of the control parameter $\xi = 1$ will be the source of the aforementioned instabilities.
2. High friction forces produced by a notably reduction of the actuators efficiency reduction causes a limit cycle instability with no *partial asymmetry failure* declaration. Important consequences may derive from this situation, as discussed above.
3. Extremely high friction forces produced by a notably reduction of the actuators efficiency reduction cause a limit cycle instability but the correct *partial asymmetry failure* will be eventually declared.

Comparing the behaviour of models 3D and 3 on wear-out borderline conditions, some important aspects can be noted:

- The system output dynamics are slower on model 3D, as a consequence of the limit cycle which is not always eliminated in steady state conditions. In consequence, the time-to-peak of the roll response will be higher on model 3D, deteriorating the stability margin.
- The engine and the flapper nozzle valve suffer a lot on model 3D when “artificially” braking the operative surface in extension cases, in which no *partial asymmetry failure* is declared on model 3D. This might compromise the system reliability and even the flight safety if the cockpit crew does solve the problem activating the shutoff valve.
- In case of failure during retraction, the overshoot of the roll response is similar on both active models. In addition, the aircraft manoeuvrability after failure is also similar on both active models on wear-out borderline condition, since the steady state flap asymmetry between the position of both surfaces is similar on both models.

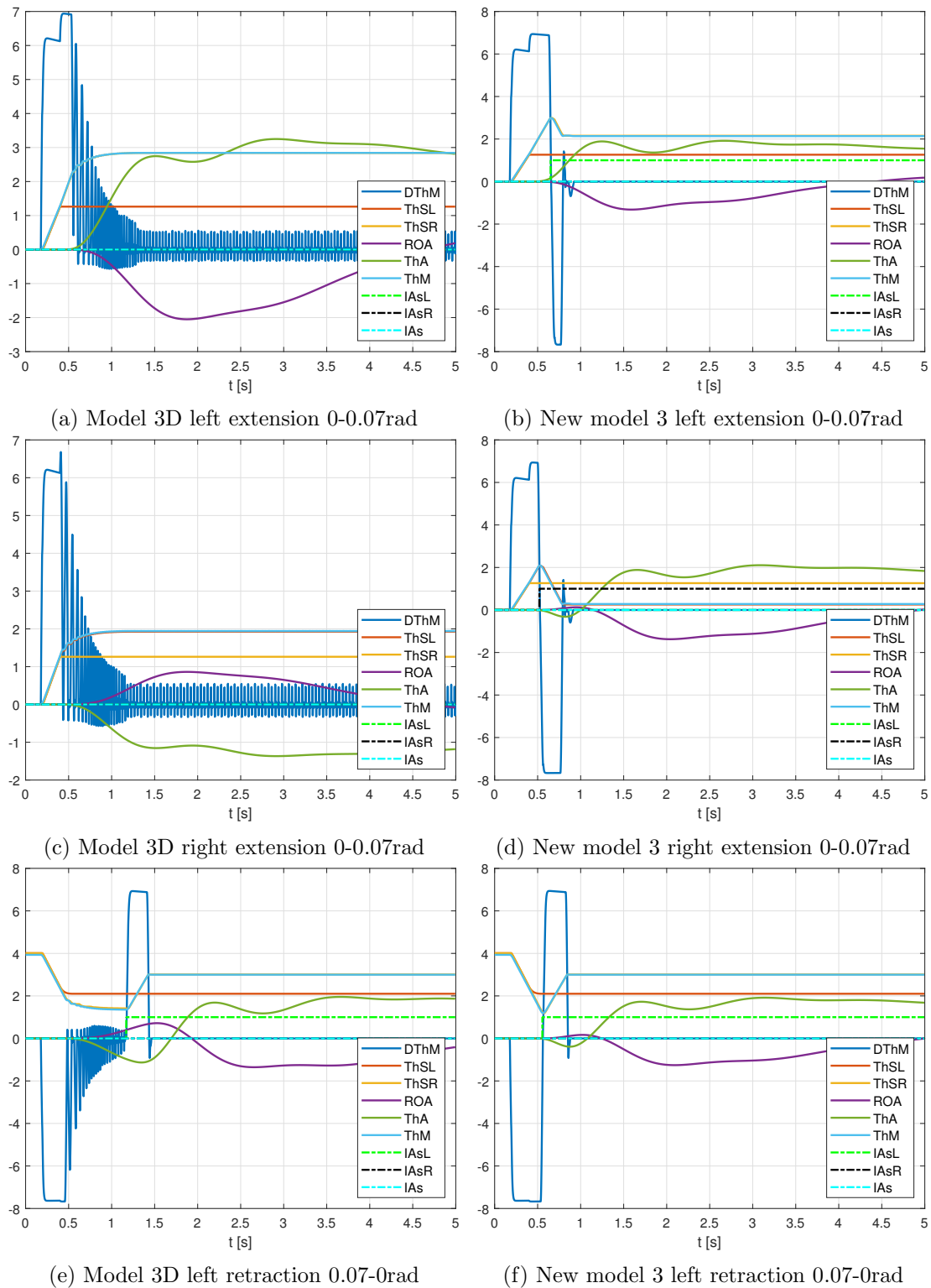
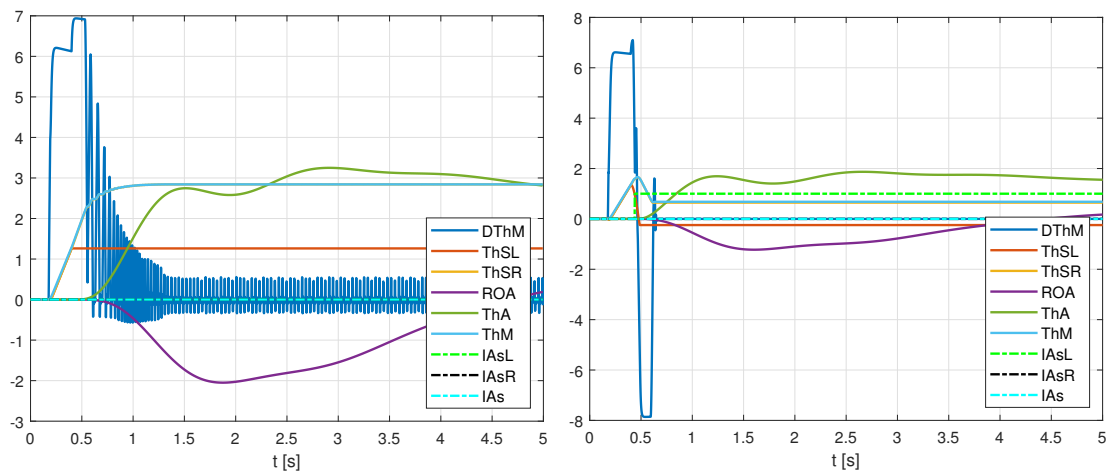


Figure 111: Comparison model 3D vs new model 3 wear-out borderline $t_f = 0.4s$
 $T_{RC} = 10000Nm$

- In case of failure during retraction, both stability and maneuverability after failure are significantly compromised in case of left failure on model 3D. On the other hand, in the right failure scenario on model 3D, the steady state flap asymmetry is similar to what shown on model 3, so both active models will present similar values of aircraft maneuverability after failure.

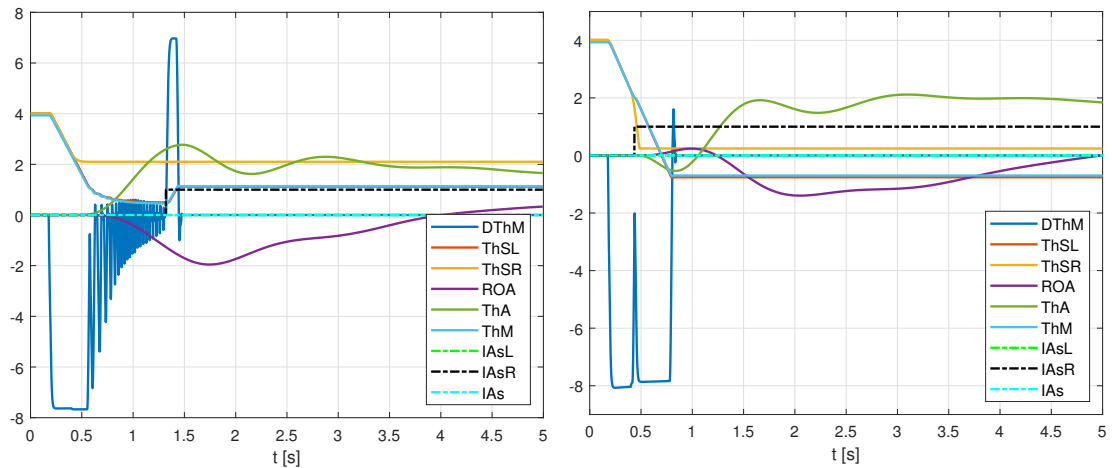
Consequently, the stability of the system output is always higher on the new active model 3. On the other hand, the aircraft maneuverability after failure is similar on both models except in case of left failure during retraction, in which the new model 3 leads to a higher maneuverability.

All these consideration are illustrated in Figure 111.



(a) Model 3D left fail extension 0-0.07 rad wear-out bord

(b) Model 3D left fail extension 0-0.07 rad wear-free bord



(c) Model 3D right fail retraction 0.07-0 rad wear-out bord

(d) Model 3D right fail retraction 0.07-0 rad wear-free bord

Figure 112: Comparison model 3D wear-out vs wear-free borderline $t_f = 0.4s$ $T_{RC} = 10000Nm$

In regard to the behaviour of the active model 3D on borderline conditions, either with wear-free or wear-out actuators, notice that the failure surface retraction on wear-free borderline conditions contrasts to the quickly braking action of the failure surface

in wear-out borderline scenarios. This is the result of the *resultant braking torque* $F_{f,R} + T_{br,R}$, discussed in section 8.4.2.

In general, the consideration highlighted in the previous comparison also apply in the current analysis.

These aspects are illustrated in Figure 112.

9.3.1 Possible solutions to prevent the limit cycle instabilities

There are different ways to prevent the limit cycle insabilities discussed above on the active monitoring technique 3D.

From a control perspective, the *dynamic position* algorithm of model 3D is the source of this instability, since a “PS” controller governs the very slow dynamics of the system. As discussed in section 5.3.2, the control algorithm of model 3D in case of partial asymmetry failure can be written as shown in Equation (5.7):

$$|\theta_M Z_M Z_S - \theta_{E,i}| + \xi \left(\dot{\theta}_M Z_M Z_S - \dot{\theta}_{E,i} \right) T_i S_y > \Delta \theta_E$$

where $\xi = 1$ in every test case on wear-out borderline conditions.

Nonetheless, should the “weight” $T_i S_y$ of the *dynamic position* speed term (anticipation term) be small enough, the “PS” controller would behave similar to a “P” controller (only proportional). The less the control algorithm depends on the failure surface speed θ_i , the better the controller will behave in systems with considerably slow dynamics, as the current case.

In fact, from a control perspective, $T_i S_y$ is the *speed gain* of the *dynamic position* active models. Hence, smaller values of $T_i S_y$ may prevent the limit cycle instability on the engine speed θ_M , increasing both the stability and the reliability of the active model 3D on wear-out borderline conditions.

A significant reduction of the *speed gain* $T_i S_y$ was considered to test the active monitoring technique 3D. This reduction is reflected in Table 5.

Previous $T_i S_y$ [s]	New $T_i S_y$ [s]	$T_i S_y$ reduction [-]
0.1	0.03	-70%

Table 5: *Speed gain* $T_i S_y$ reduction

Such drastic reduction of the asymmetry anticipation time $T_i S_y$, the *speed gain* of the “PS” controller, prevents the limit cycle instability on steady state conditions, as shown in figures 113 and 114.

Notice that the *partial asymmetry failure* is correctly declared on each flap maneuver in every failure side case. It is possible since the controller behaves similarly to a “P” controller due to the low *speed gain* of the anticipation term, which is ideal for those systems which present very slow dynamics.

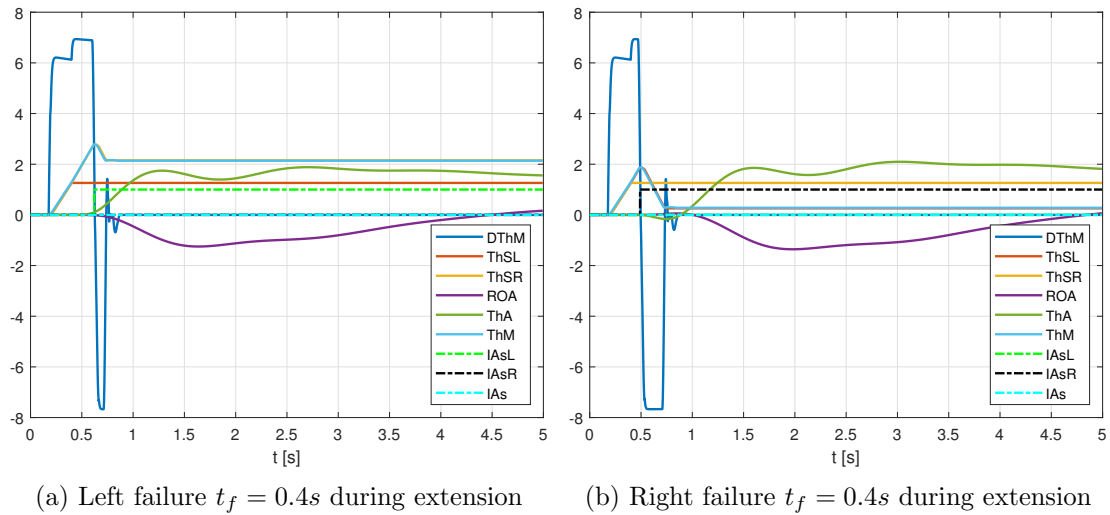


Figure 113: Model 3D - $T_i S_y = 0.03s$ bord. case wear-out ext 0-0.07rad $T_{RC} = 10000Nm$

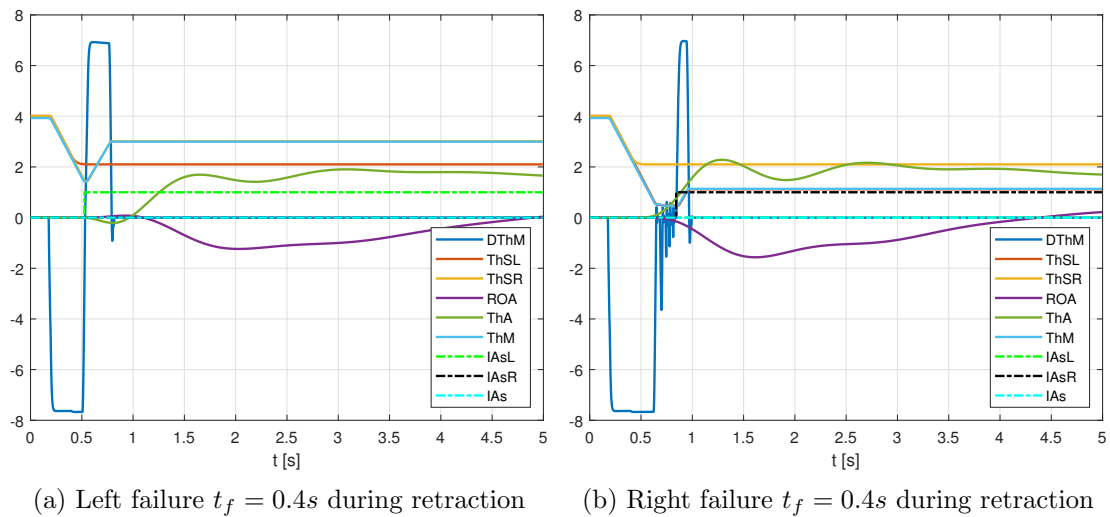


Figure 114: Model 3D - $T_i S_y = 0.03s$ bord case wear-out retr 0.07-0rad $T_{RC} = 10000Nm$

Nonetheless, little instabilities can still be noted, as the oscillation shown in right failure during retraction scenarios. Fortunately, these do not prevent the correct *partial asymmetry failure* declaration, as discussed above.

Thus, the reliability of the active model 3D increases and the operative life both the engine and the flapper nozzle valve. In addition, both the time answer stability and the aircraft maneuverability after failure are higher than those with higher values of $T_i S_y$. All these considerations can be noted in Figure 115, where the electrical variables are represented.

Nevertheless, it should be reiterated that $T_i S_y$ is working as the *speed gain* of the *dynamic position* control algorithms (“PS” controller), so reducing $T_i S_y$ may have negative consequences on wear-free conditions, both in regular or borderline conditions, and even “regular” wear-out conditions that do not consider the borderline scenarios

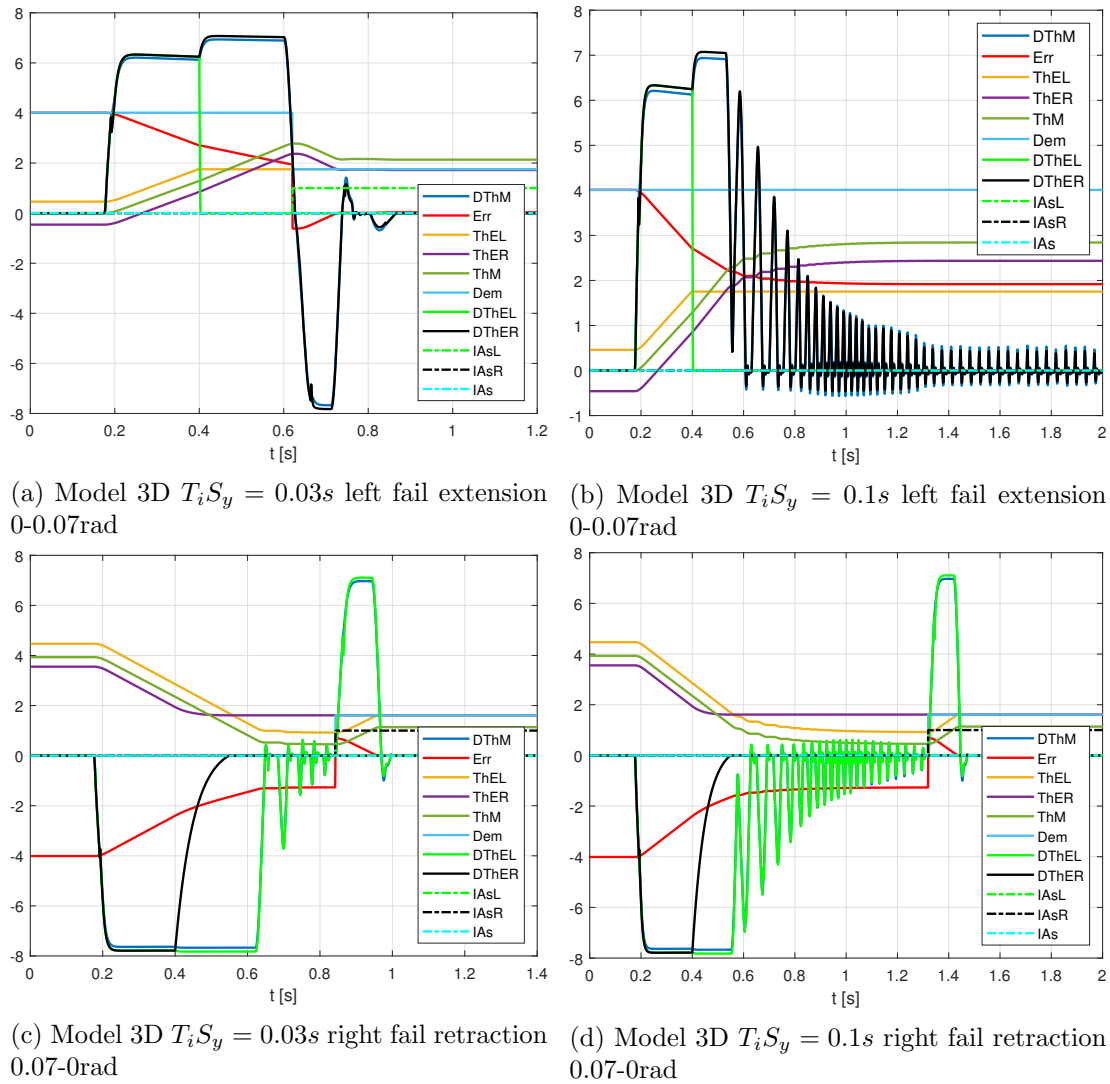


Figure 115: Comparison model 3D $T_i S_y$ variation $t_f = 0.4s$ $T_{RC} = 10000Nm$

assumptions.

In effect, should the anticipation term of the dynamic position algorithm be active $\xi = 1$, the failure surface under high aerodynamic loads experiments high retraction speeds. Hence, fast system dynamics should be considered after failure, which need the anticipation effect of the “PS” controller to both detect and correct the asymmetry maintaining acceptable levels of the active models reliability, dynamic response stability and aircraft maneuverability after failure.

In regard to the lack of *partial asymmetry failure* declaration in case of limit cycle instabilities with the previous *speed gain* value $T_i S_y = 0.1s$, further simulations have been perform to study the effect of a second command on the system that works under the effect of such instabilities.

The behaviour of model 3D working under limit cycle oscillations that receives a second command is illustrated in Figure 116c, where the electrical variables are represented.

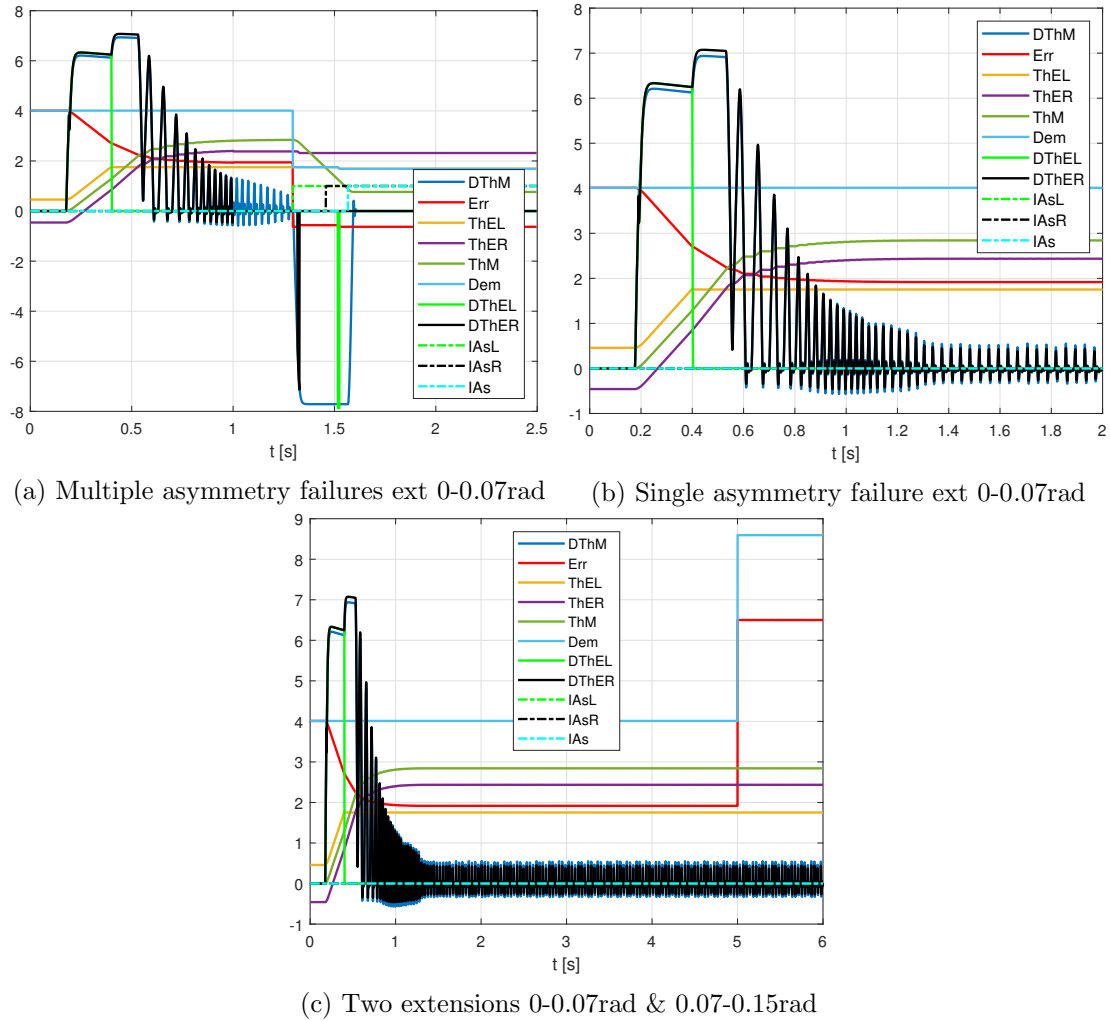


Figure 116: Model 3D multiple vs single failures wear-out bord $T_{RC} = 10000Nm$

In the light of the test results, the system time response presents no changes with respect to the single command cases, which shows the low aircraft controllability caused by the limit cycle instabilities on model 3D. In effect, notice that:

- The system limit cycle still prevents any *partial asymmetry failure* declaration.
- The new command will never be reached, since the system steady state response does not change with the second command.

Nonetheless, simulating **two failures** is a peculiar way to finish the limit cycle oscillation on model 3D without reducing the asymmetry anticipation time $T_i S_y$, *speed gain* of the “PS” controller. In this case, these two failures lead to a **real multiple asymmetry failure** situation, which seem to allow a correct *partial asymmetry failure* declaration. Therefore, the active model 3D seem to improve its behaviour in terms of reliability, stability and maneuverability after failure in case of **real multiple asymmetry failures**.

The multiple failure test conducted to illustrated whats discussed above is: an *extension maneuver* in which two failure have been simulated:

1. A *left failure* at $t_f = 0.4s$.
2. A *right failure* at $t_f = 1s$.

The comparison between the aforementioned test to what obtained with the *single failure* case at $t_f = 0.4s$ is shown in figures 116a and 116b where, again, the electrical variables are represented. However, further tests should be performed to confirm the *real multiple asymmetry failure* effect on the limit cycle instabilities on model 3D.

9.4 Model 3A results - wear-out borderline case

The asymmetry active monitoring technique 3A presents a satisfactory behaviour on wear-out borderline conditions, as shown in figures 117 and 118.

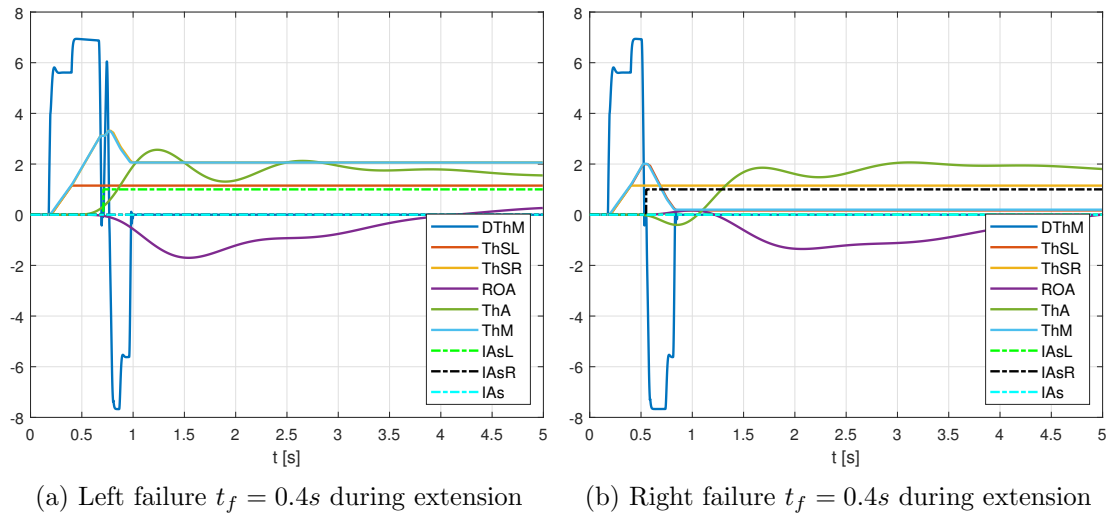


Figure 117: Model 3A - bord. case wear-out failure ext 0-0.07 rad $T_{RC} = 10000Nm$

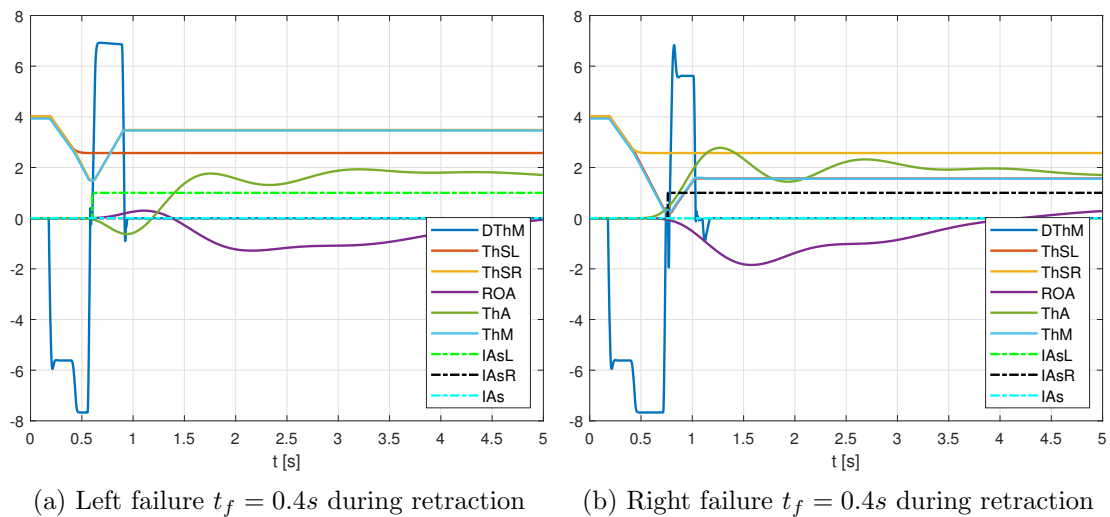


Figure 118: Model 3A - bord. case wear-out failure retr 0.07-0 rad $T_{RC} = 10000Nm$

In contrast to what discussed in aerodynamic borderline cases with wear-free actuators, the active model 3A on wear-out borderline conditions will not present any *lack*

of control in right failure during retraction scenarios. In addition, the double-surface saturation of model 3A in case of right failure during extension discussed in section 7.3 is solved on borderline wear-out conditions.

Furthermore, no limit cycle instabilities appear in any test, since 3A does not consider any dynamic position logic in its control algorithm.

All these considerations are illustrated in Figure 119.

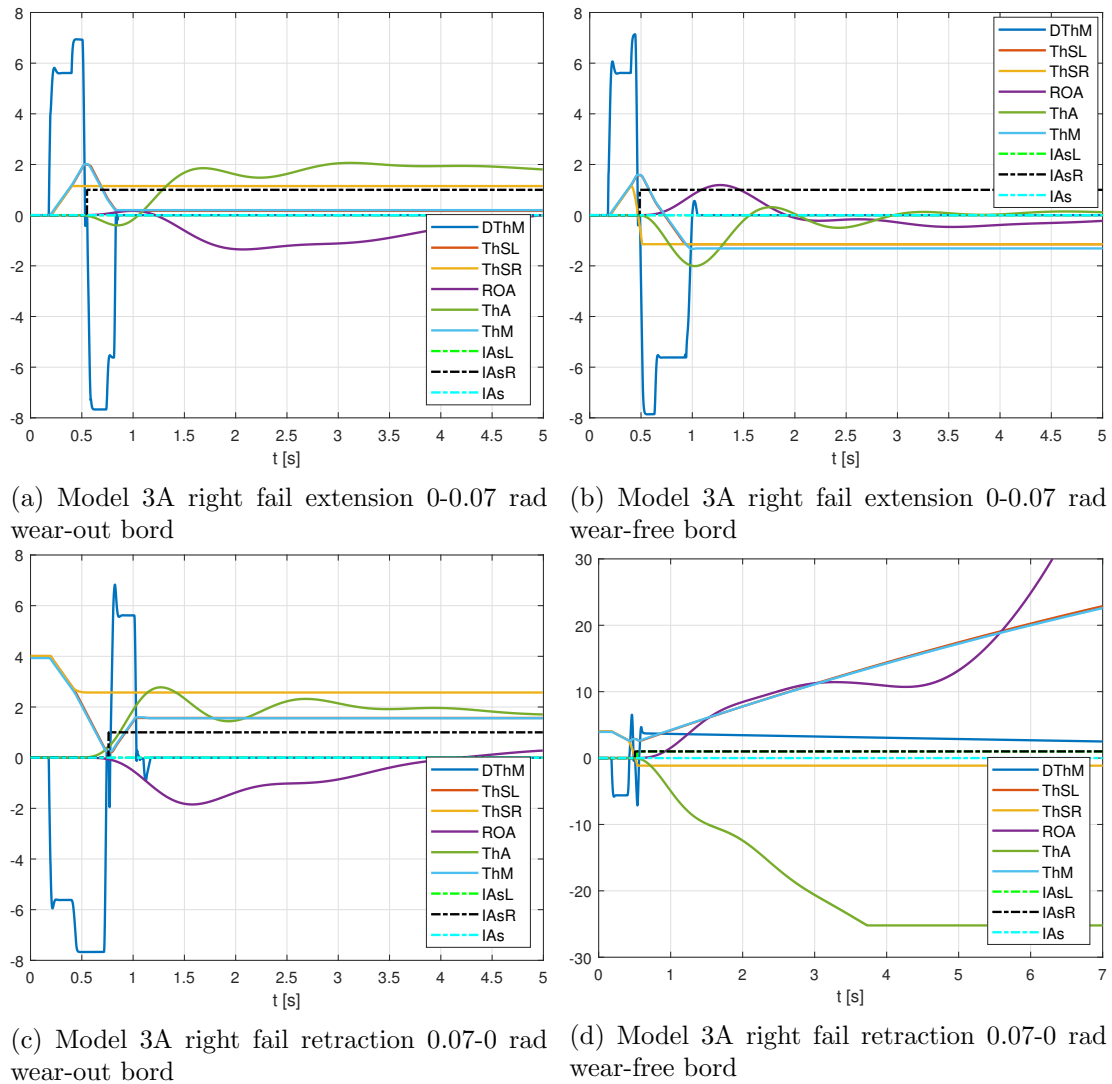
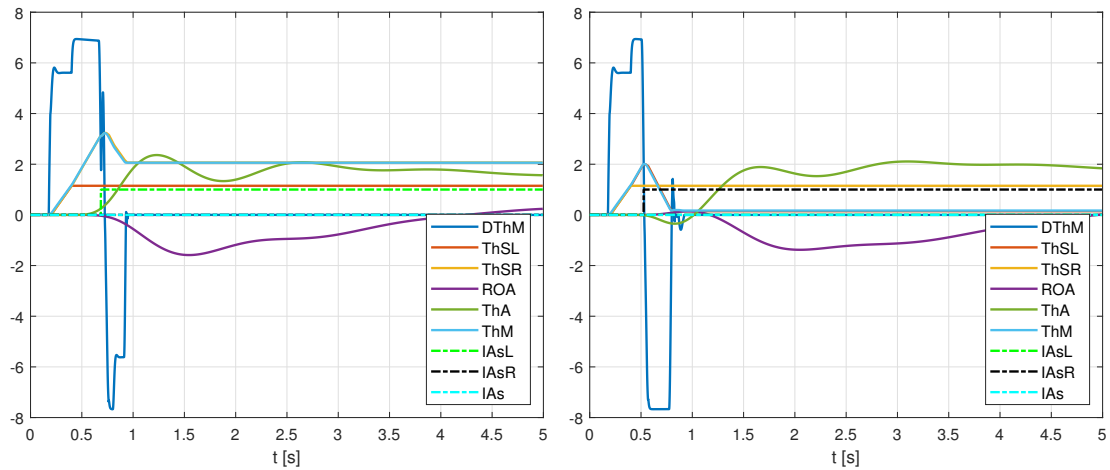


Figure 119: Comparison model 3A wear-out vs wear-free borderline condition $t_f = 0.4s$
 $T_{RC} = 10000Nm$

9.5 Model 3C results - wear-out borderline case

The asymmetry active monitoring technique 3C behaves satisfactorily on wear-out borderline conditions, analogously to what stated above in regard to the model 3A.

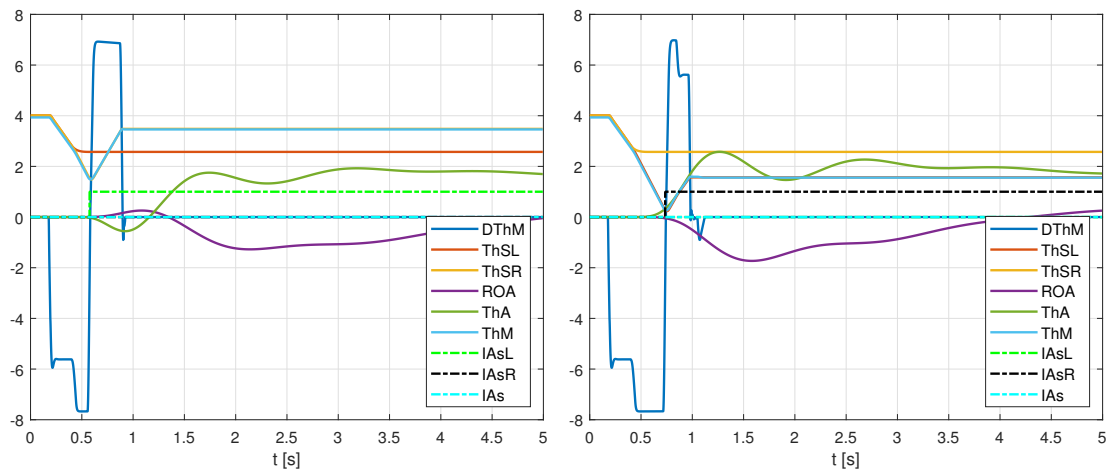
As commented about model 3A, 3C does not consider any dynamic position logic in



(a) Left failure $t_f = 0.4s$ during extension

(b) Right failure $t_f = 0.4s$ during extension

Figure 120: Model 3C - bord. case wear-out failure ext 0-0.07 rad $T_{RC} = 10000Nm$



(a) Left failure $t_f = 0.4s$ during retraction

(b) Right failure $t_f = 0.4s$ during retraction

Figure 121: Model 3C - bord. case wear-out failure retr 0.07-0 rad $T_{RC} = 10000Nm$

its control algorithm, so no limit cycle instabilities will appear in any test case.

The results of both extension and retraction for either left or right failure are shown in figures 120 and 121.

The behaviour of the active models 3C and 3A on wear-out borderline conditions, regarding both the roll response stability and aircraft maneuverability after failure, is:

- Better on model 3C both on left failure during extension and right failure during retraction. Nonetheless, these are all slight improvements, as can be noted in Figure 122.
- Almost identical on both active models in the rest of the test cases (right failure during extension and left failure during retraction), regardless the intrinsic delay of model 3A to declare the *partial asymmetry failure*¹⁸.

¹⁸Remember that the *partial asymmetry failure* counter threshold of model 3A doubles the corresponding threshold of model 3C

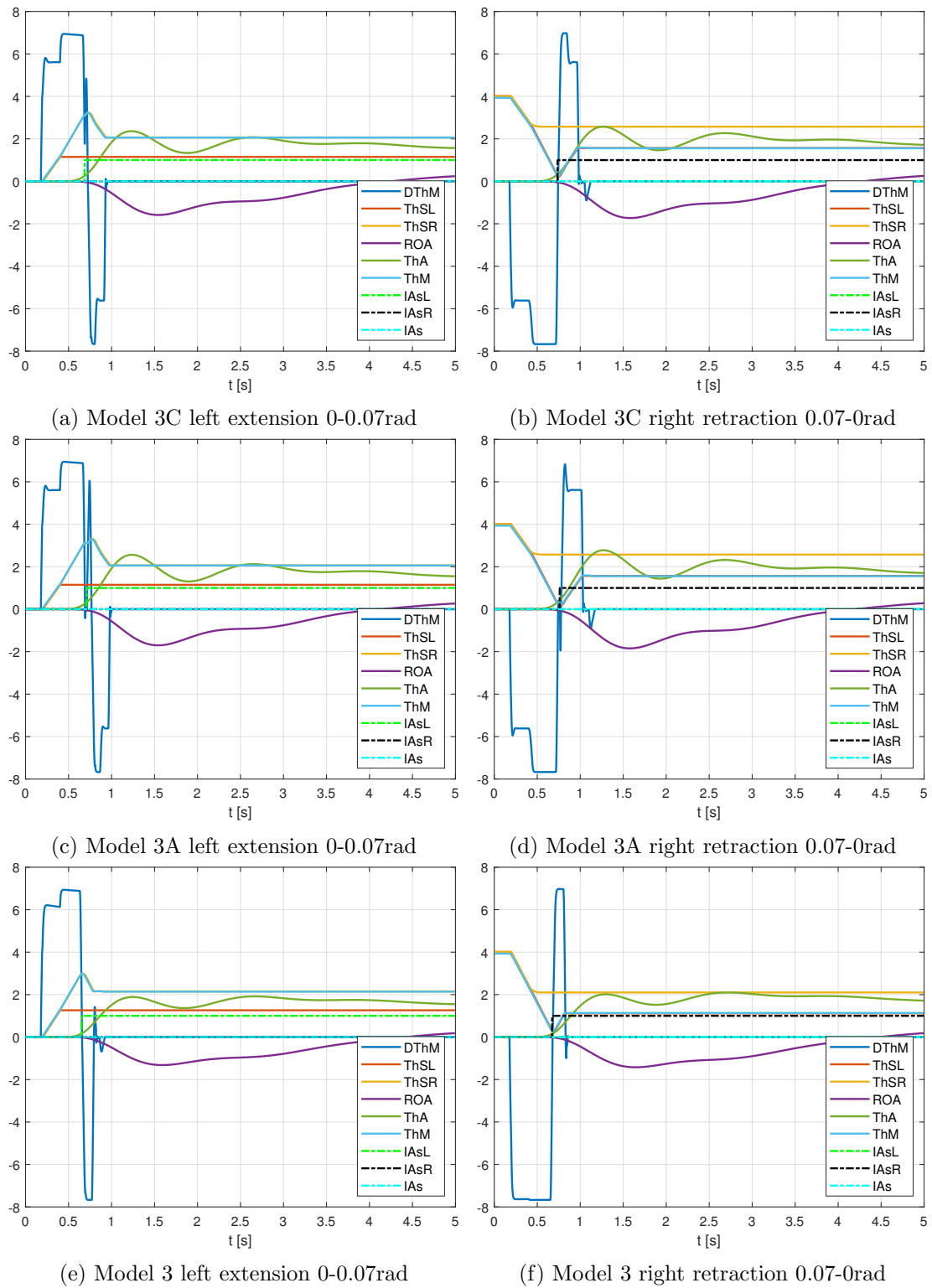


Figure 122: Comparison between models 3C, 3A, 3 wear-out borderline $t_f = 0.4s$
 $T_{RC} = 10000Nm$

Similarly, the active model 3C presents analogous behaviour improvements with respect to the new model 3, both of them on borderline wear-out conditions.

As listed above, these considerations can be clearly noted both in case of left failure during flap extension and right failure during retraction, in which the effects of both the left and right position offset set on the electrical transducers are more evident.

All these aspects are illustrated in Figure 122.

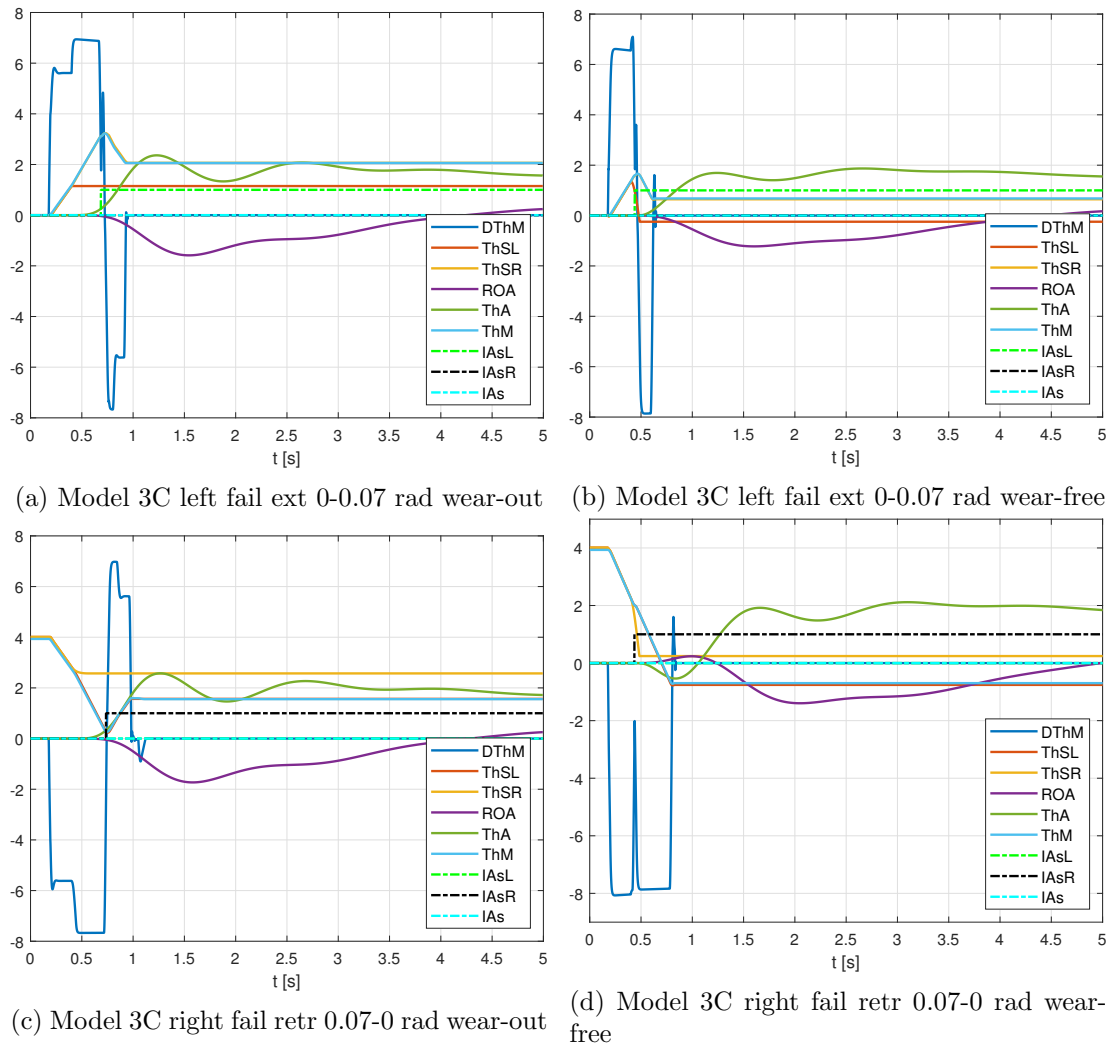


Figure 123: Model 3C wear-out vs wear-free borderline cond $t_f = 0.4s$ $T_{RC} = 10000Nm$

Finally, the model 3C on borderline conditions behaves notably better in wear-out than in wear-free cases in regard to both the roll response stability and aircraft maneuverability after failure. Analogously to what discussed above on model 3D, the failure surface retraction on wear-free borderline conditions contrasts to the quickly braking action of the failure surface in wear-out borderline scenarios.

In addition, the left failure during retraction on wear-out borderline conditions does not declare the *partial asymmetry failure* of the right surface, as in the case of wear-free borderline scenarios (see section 7.4), since no *false multiple asymmetry failures* have

been declared.

Consequently, the active model $3C$ on wear-out borderline conditions presents higher values of both roll response stability and aircraft maneuverability after failure with respect to the same model in borderline wear-free cases.

These considerations are illustrated in Figure 123.

9.6 Model 3E results - wear-out borderline case

Analogously to the other *dynamic position* active models in any borderline scenario, the anti-captation term is always active on model $3E$ on wear-out borderline conditions $\xi = 1$. Nonetheless, the asymmetry active monitoring technique $3E$ presents a quite satisfactory behaviour despite combination of a high friction torque, a high aerodynamic torque and $\xi = 1$, that activates the “*PS*” controller.

The results of both extension and retraction for either left or right failure are illustrated in Figure 124.

Firstly, the active model $3E$ behaves notably better than $3D$. Follow a main improvement of the ramp-input model $3E$ with respect to the corresponding step-input technique $3D$:

- No oscillations are present in the results of model $3E$ except in case of left failure during retraction, which they do not last long allowing the *partial asymmetry failure* declaration. Hence, no differentiation can be made between extension and retraction scenarios regarding the failure declaration, as in the case of model $3D$.
- The *partial asymmetry failure* is always correctly declared on model $3E$. Therefore, all the consequences of not declaring the *partial asymmetry failure* correctly disappear. In effect, the engine and the flapper nozzle valve suffer would **not** brake “artificially” the operative surface in any case and there is no need to implement any additional system to both detect and alert the cockpit crew about the failure situation. In effect, *resultant braking torque* ($F_{f,R} + T_{br,R}$) will stop first the failure surface, and later on the operative surface after reaching the operative one.

The reason why the model $3E$, in general, does not present limit cycle instabilities, as model $3D$, is the kind of *reference position* chosen both on step input and ramp-input models. The former use the engine position θ_M as *reference position*, which is influenced by the engine speed $\dot{\theta}_M$ that suffers from the limit cycle by means of both the *Slow* parameter and the “*PS*” controller. Nevertheless, the latter use demand Dem as *reference position*, which is only affected by the demand ramp slope $\left. \frac{d Dem}{dt} \right|_{max}$. Since the ramp slope is not influenced by the limit cycle on the engine speed $\dot{\theta}_M$, the ramp-input models are ideal to (almost) prevent any limit cycle instabilities when choosing *dynamic position* active models.

Nonetheless, short limit cycles may also arise on model $3E$. These might be caused by the slow system dynamics consequence of the combination of both high friction

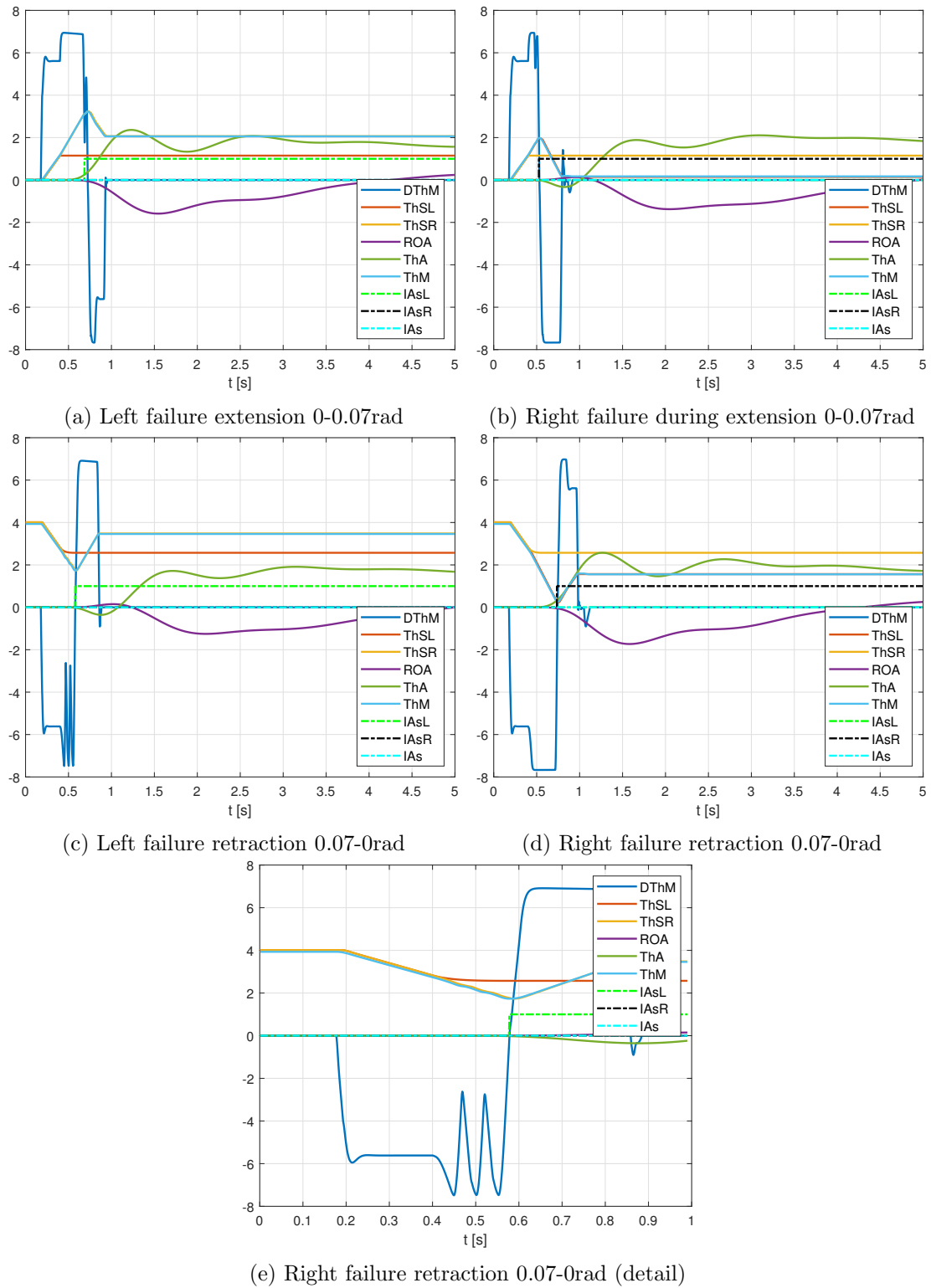


Figure 124: Model 3E - borderline case wear-out failure $t_f = 0.4s$ $T_{RC} = 10000Nm$

torques and the slow but controlled demand ramp input, together with the always active “PS” controller. Fortunately, only the left failure during retraction scenarios present limit cycles instabilities, which seem to be short and allow the correct partial asymmetry failure declaration.

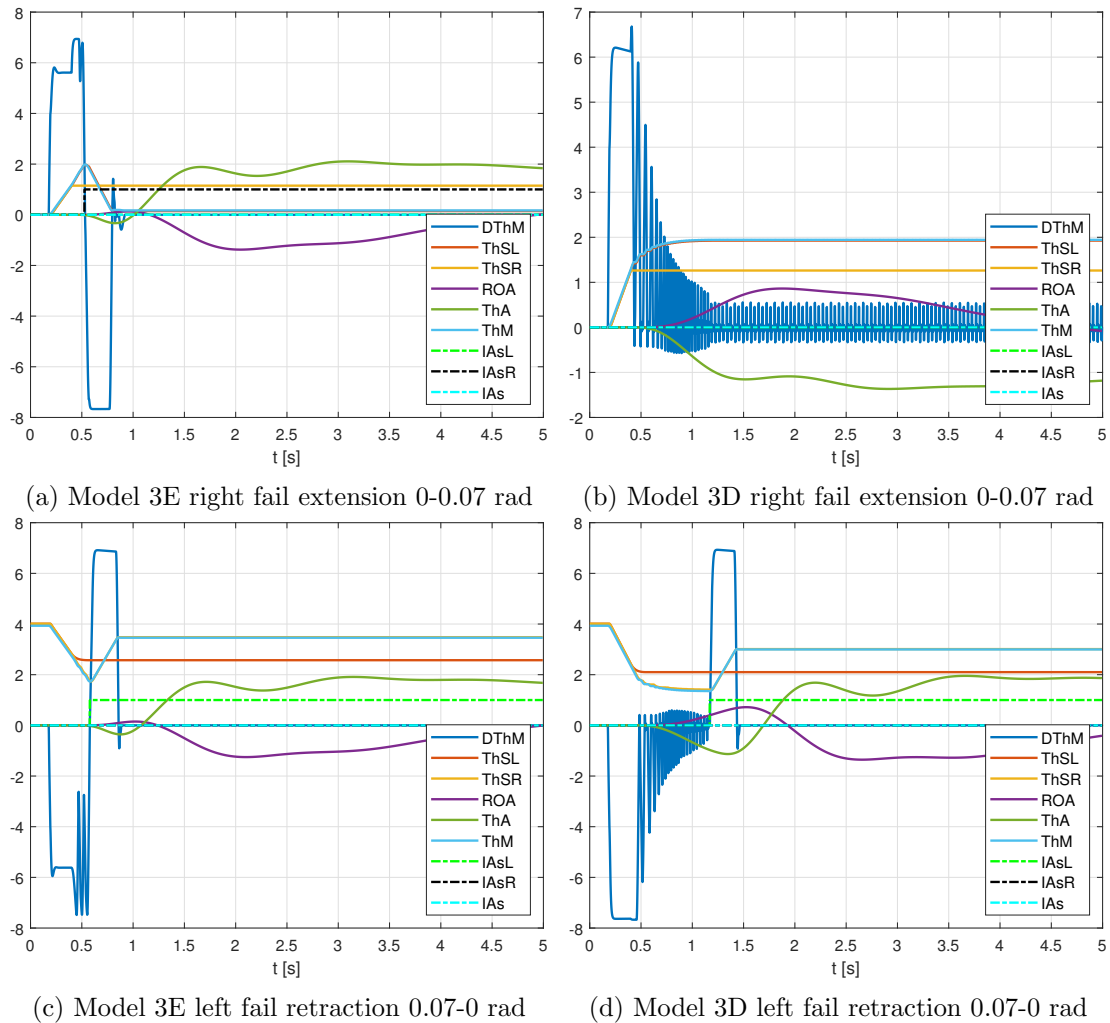


Figure 125: Comparison model 3E vs 3D wear-out bord $t_f = 0.4s$ $T_{RC} = 10000Nm$

In consequence, both the roll response stability and the aircraft maneuverability after failure are:

- Notably better in extension cases. In effect, the lack of limit cycles on model 3E on flap extension maneuvers improves both the stability and maneuverability after failure.
- Better in retraction cases, especially in right failure during extension scenarios. Indeed, either the short or inexistent limit cycles on retraction maneuvers, together with the slow but controlled demand ramp slope improve both the stability and maneuverability after failure.

In addition, the reliability is higher on model 3E than on model 3D due to that *resultant braking torque* ($F_{f,R} + T_{br,R}$) that effectively brakes the surfaces without compromising both the integrity and performance of both the engine and the flapper nozzle

valve.

All these considerations are shown in Figure 125.

Secondly, the active models 3E and the new model 3 is practically the same. Both models behave much better with respect to model 3D since they prevent the limit cycles instabilities but in different ways.

As discussed above, the step-input active models without a *dynamic position* logic use the same reference position as 3D, which is the engine position θ_M , but they use a proportional control logic to detect and correct the flap asymmetry (“P” controller). Therefore, no dynamic instabilities will manifest on the engine speed $\dot{\theta}_M$ preventing the limit cycle on the operative surface.

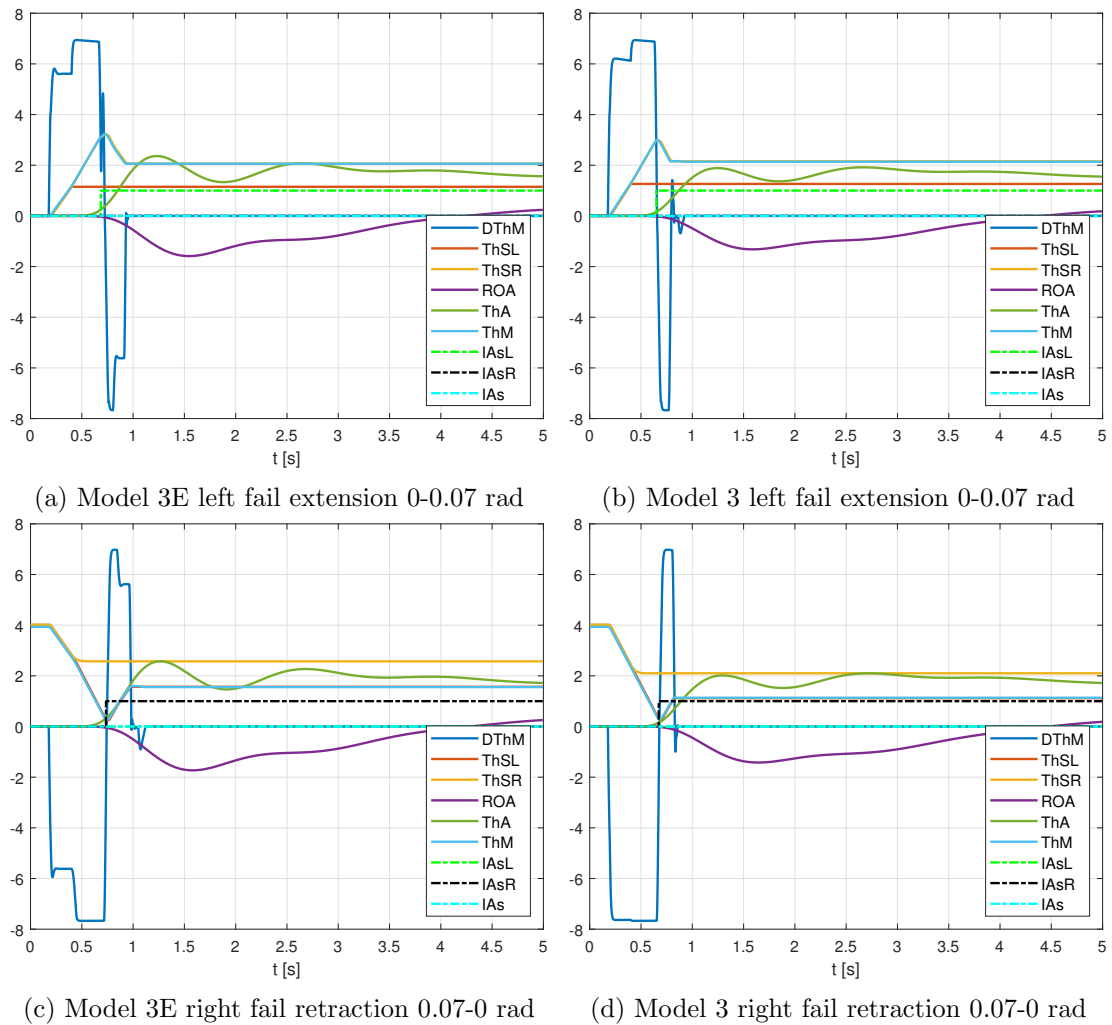


Figure 126: Comparison model 3E vs 3 wear-out bord $t_f = 0.4s$ $T_{RC} = 10000Nm$

On the other hand, the ramp-input active models, either with or without a *dynamic position* logic, use the demand signal Dem as the reference position, which is governed by the demand ramp slope, a fixed simulation parameter that only depends on the command input signal. Hence, it is invariant with the engine speed so:

1. No limit cycles instabilities will be present on ramp-input active model without a *dynamic position* asymmetry control logic (model 3C).
2. It is quite rare to find a limit cycle instability on ramp-input active model that use a *dynamic position* asymmetry control logic (model 3E).

Consequently, the behaviour of the active monitoring technique 3E with respect of the ne active model 3 is almost the same in any test case. Nonetheless slight differences can be noted both on left failures during flap extension and right failures during retraction maneuvers.

These considerations are illustrated in Figure 126.

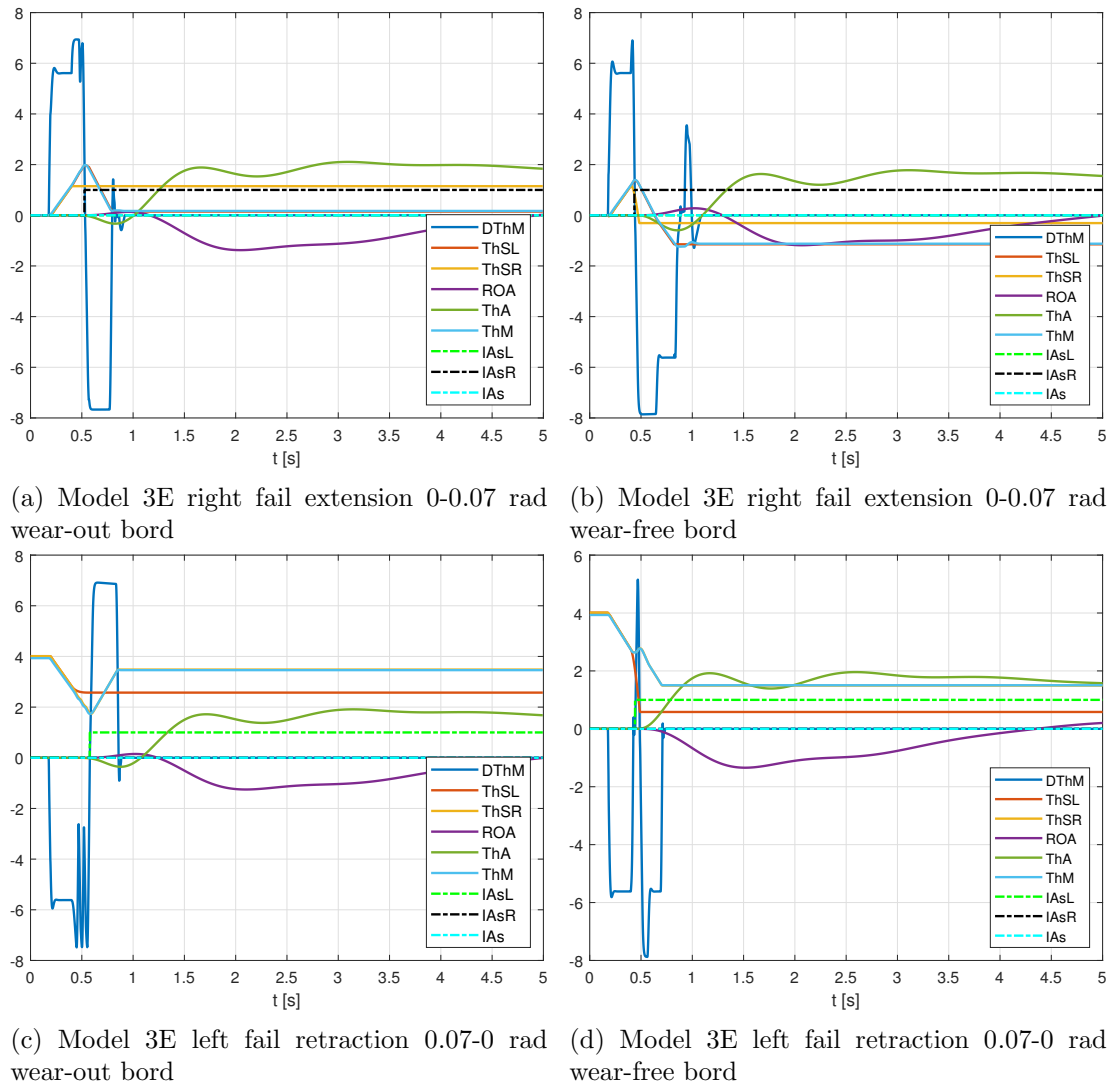


Figure 127: Comparison model 3E wear-out vs wear-free borderline $t_f = 0.4s$ $T_{RC} = 10000Nm$

Finally, the active model 3E on borderline conditions behaves, in general, better in wear-out than in wear-free cases. In effect, the high *resultant braking torque* ($F_{f,R} + T_{br,R}$) on wear-out borderline conditions prevents the braking surface from re-

tracting, as in wear-free borderline scenarios.

On the other hand, no limit cycle instabilities arise on wear-free conditions, since the regular values of the friction force do not decelerate the failure surface as much as in the case of wear-out scenarios, so the dynamic system response will be fast enough to be controlled by the “*PS*” controller. Nonetheless, the model *3E* on borderline wear-out conditions prevents the limit cycle instabilities by means of the *reference position*, invariant with the engine speed instabilities, as discussed above.

Although little changes can be noted regarding both the roll stability and the aircraft maneuverability after failure (which seems to be slightly better in borderline wear-free cases), the test results on wear-out conditions do not show any failure surface braking position under 0 rad, which is quite normal on flap extension maneuvers on wear-free borderline cases. Again, the high *resultant braking torque* ($F_{f,R} + T_{br,R}$) on wear-out conditions brakes earlier the failure surface.

Summarizing, the active technique *3E* on borderline conditions behaves better in wear-out scenarios, even though both roll stability and aircraft maneuverability after failure are similar. Nevertheless, special attention should be paid to limit cycles instabilities, such as in right failure during retraction cases, since they can delay the partial asymmetry failure declaration affecting the system time response stability.

These considerations can be noted in Figure 127.

9.7 Comparison of active models on wear-out conditions

In general, the asymmetry active monitoring techniques seem to behave correctly in aerodynamic wear-out borderline cases except the active model *3D*, which presents a detrimental behaviour in terms of roll stability and maneuverability after failure in any flap maneuver test.

Analogously to the previous study cases, a general overview of the active monitoring techniques has been performed in the previous pages according to the input signal. However is also important to analyze the active techniques behaviour according to the effect of the position anticipation term, considering models with the same input signal.

Similarly to what discussed on wear-free conditions in section 7.6, only one aerodynamic load case was considered in aerodynamic wear-out borderline cases: high T_{RC} . In effect, the aerodynamic wear-out borderline scenarios are characterized by the effect high aerodynamic torques and worn out actuators performace (high friction torques). Hence, only the high aerodynamic load cases will be considered.

The comparison of the active models behaviour on wear-out borderline conditions according to the *dynamic position* effect for equal input signal models will be performed in the following pages.

9.7.1 Step-input models behaviour on borderline wear-free conditions

The active technique *3D* behaves much worse the new model 3 in any scenario of such borderline conditions. As mentioned in 9.3, the model *3D* manifests limit cycle insta-

bilities in every test case. On the contrary, the *non dynamic position* new active model 3 presents a satisfactory behaviour with high time response stability margin and high aircraft maneuverability after failure.

All these considerations are illustrated in Figure 128.

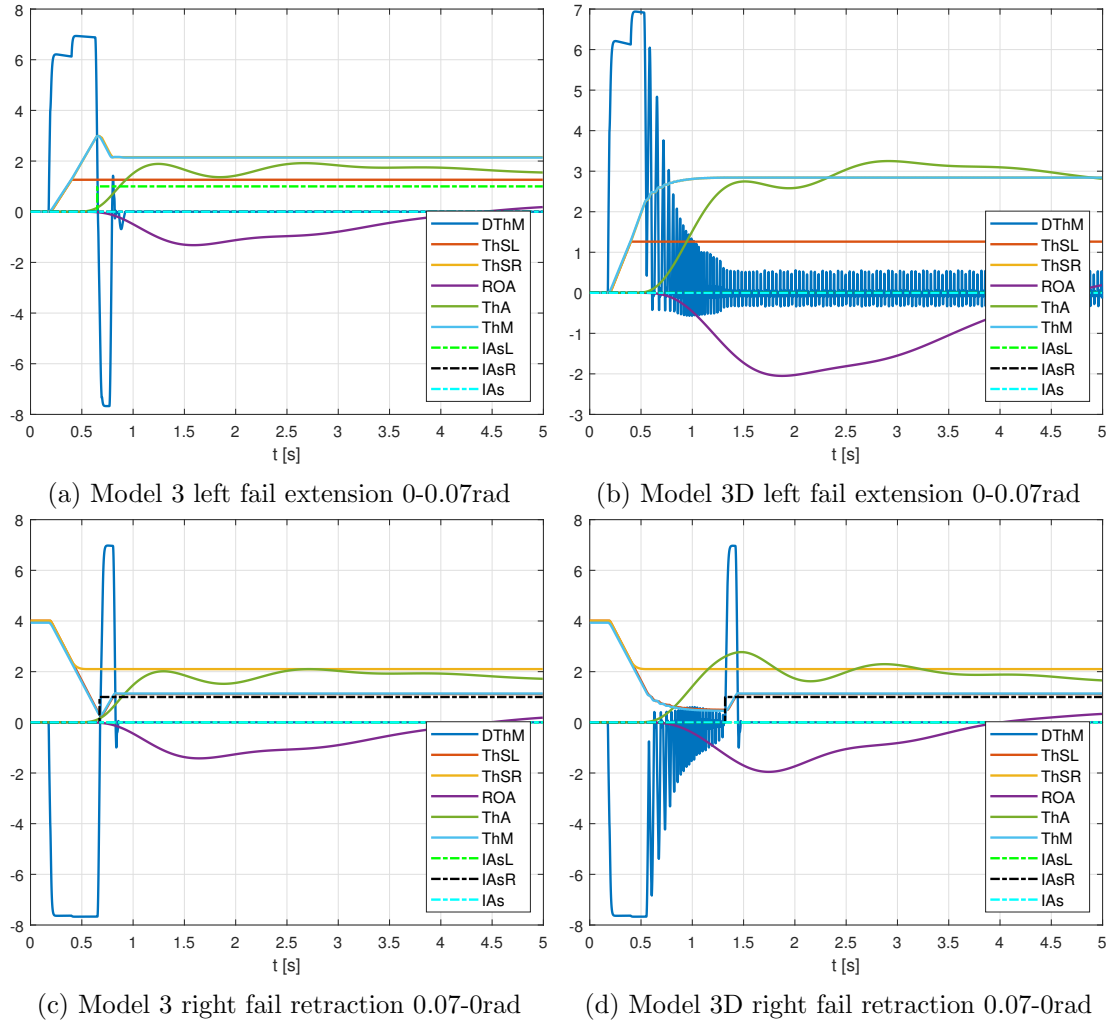


Figure 128: Overview 3 vs 3D bord case wear-out failure $t_f = 0.4s$ at $T_{RC} = 10000Nm$

9.7.2 Ramp-input models behaviour on borderline wear-free conditions

The active technique $3E$ present almost the same behaviour as $3C$ in any scenario of such borderline conditions.

In fact, almost no difference can be noted between the test cases analyzed in this section except on left failure during retraction on model $3E$, which presents the short limit cycle discussed in section 9.6. However, it does not significantly delay the left *partial asymmetry failure* declaration, so both stability and maneuverability after failure are similar and satisfactory on both ramp-input active models, either with or without a *dynamic position* control logic.

These considerations are illustrated in Figure 129.

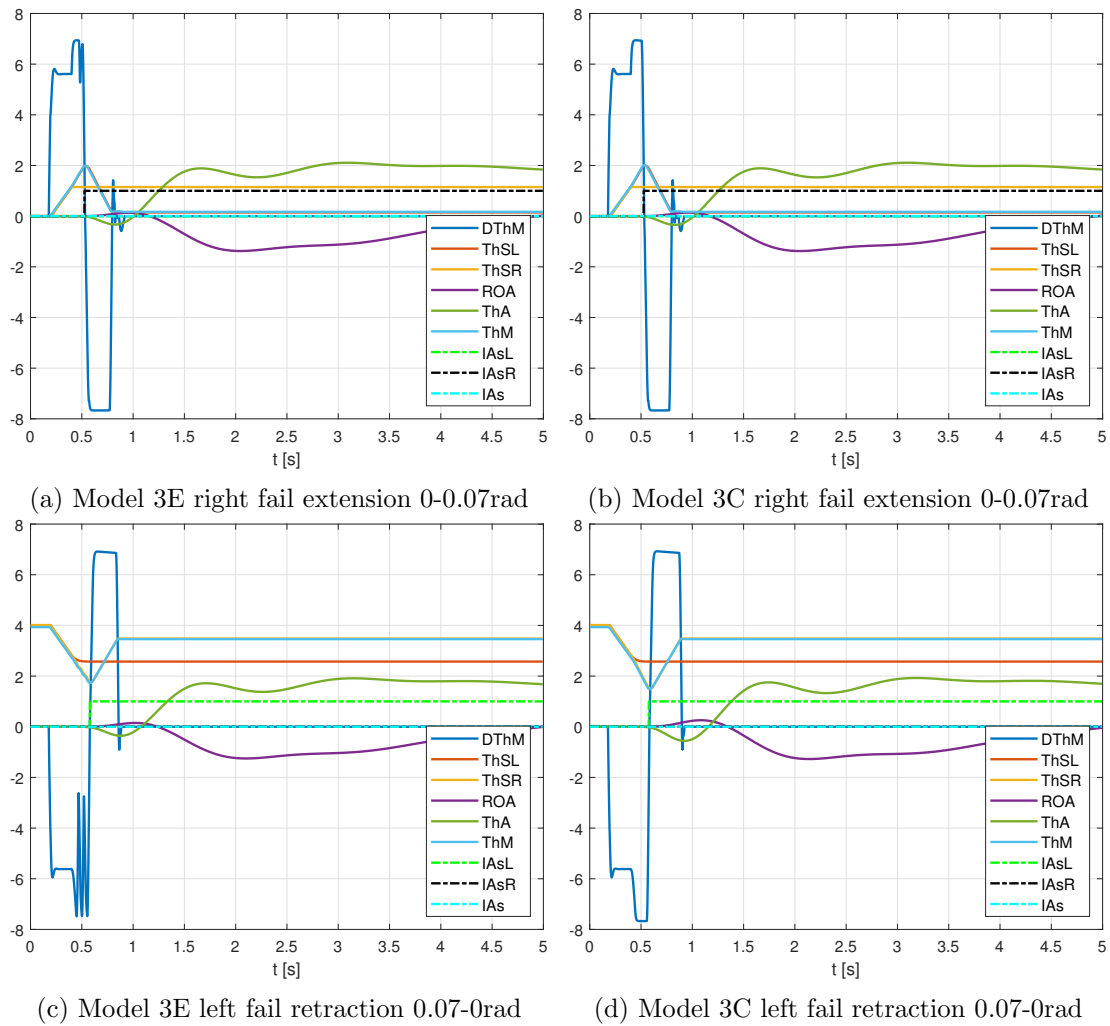


Figure 129: Overview 3E vs 3C bord case wear-out failure $t_f = 0.4s$ at $T_{RC} = 10000Nm$

9.7.3 Summary table of active models in wear-free borderline conditions

Analogously to what stated on wear-free borderline conditions, the summary table hereunder compares all the active models on the aerodynamic wear-out borderline conditions of this chapter in order to analyze which active monitoring technique behaves better in each situation (see Table 6). This table classifies both the active step-input and ramp-input monitoring techniques in aerodynamic wear-out borderline conditions according to the different surface maneuvers, both extension and retraction, always under high aerodynamic loads.

The both the numerical classification and the color coding that measure the active models effectiveness both quantitatively and qualitatively on the current borderline conditions follow the same rules than in case of the previous “regular” worn-out conditions scenarios (see 8.6.3).

In the light of the test results on the current borderline conditions, some considera-

	Step-input models		Ramp-input models			
	3	3D	3A	3C	3E	
High T_{RC}	1	5	3	1	1	Extension
	1	4	3	1	2	Retraction

Table 6: Models efficiency classification on aerodynamic wear-out borderline conditions

tions should be made:

1. The active monitoring techniques that consider an anticipation term by means of the *dynamic position*, may present either the same or notably **worse** behaviour than the non *dynamic position* active models on wear-out borderline conditions.
2. In general, the *new* ramp-input active models seem to behave better than the step-input models.
3. Great behaviour improvements can be noted between the active models marked in green & orange and orange & red. On the current borderline conditions, these improvements refer to the presence of limit cycle instabilities in the test case results.
4. Little behaviour improvements are present between the active models in green.
5. Significant behaviour improvements are present between models either in orange or in red are significant, which is quantitatively measured by the number inside the cell. On the current borderline conditions, these are related to the *partial asymmetry failure* detection ability when limit cycles instabilities are present.
6. The only red cell classified with a 5 represents the unacceptable lack of *partial asymmetry failure* declaration in every extension scenario on model *3D* due to a limit cycle dynamic instability.

It seems that the models that behave better on aerodynamic wear-free borderline conditions are the active **models 3, 3C & 3E** both in flap extension and retraction scenarios.

Thus, in contrast to what stated for the active techniques behaviour on “regular” wear-out conditions, there are **three ideal models** to use both in flap extension and retraction cases: **3, 3C & 3E**. Nevertheless, the ramp-input active models seems to behave better than the step-input techniques on wear-out borderline conditions

Follows a summary of the main reasons why the aforementioned active models presents the best behaviour both on extension and retraction maneuvers.

- The **ramp-input active models** will **rarely present limit cycle instabilities, regardless of whether the presence of a dynamic position control logic or not**. In effect, these models, either with or without a *dynamic position* logic, use the demand signal Dem as the reference position, which is governed by the demand ramp slope, a fixed simulation parameter that only depends on the command input signal. Hence, it is invariant with the engine speed so:
 - No limit cycles instabilities will be present on ramp-input active model without a *dynamic position* asymmetry control logic (model *3C*).
 - It is quite rare to find a limit cycle instability on ramp-input active model that use a *dynamic position* asymmetry control logic (model *3E*).

- The **step-input active models will prevent the limit cycle instabilities only in case of non dynamic position asymmetry control logic**, this means a proportional logic (P controller). In effect, the proportional controller logic does not consider any speed loop, which prevents the limit cycle instabilities of the “ PS ” controllers in case of very slow dynamics, characteristic of aerodynamic wear-out borderline conditions.

10 Conclusions

The present section highlights the behaviour of the four asymmetry active monitoring techniques developed in this project, which are *new model 3*, *3D*, *3C* and *3E*, in order to decide which behaves the best in operating case. In the light of the results, some observations will be made regarding active models control logic.

Briefly, to recapitulate, four different asymmetry active monitoring techniques have been developed from zero in this project. These are:

1. ***New model 3***. It is a non dynamic-position step-input asymmetry active monitoring technique.
2. ***Model 3D***. It is a dynamic-position step-input asymmetry active monitoring technique.
3. ***Model 3C***. It is a non dynamic-position ramp-input asymmetry active monitoring technique.
4. ***Model 3E***. It is a dynamic-position ramp-input asymmetry active monitoring technique.

All these active models are based on a a differential position control logic.

The four asymmetry active monitoring techniques have been tested in different operating environments, both in extension and retraction maneuvers and both in left and right failure scenarios. The different operating environments are:

- a. *Regular wear-free conditions*.
- b. *Aerodynamic borderline wear-free conditions*.
- c. *Wear-out conditions*.
- d. *Aerodynamic borderline wear-out conditions*.

Considering the summary tables used to compare the active models with one another on certain operating conditions, some remarks have to be made regarding which active asymmetry monitoring technique behaves better in each operating environment:

- a. Regarding the ***regular conditions***, the active models ***3D & 3E*** behave the best in low aerodynamic loads, while the model ***3D*** presents the best behaviour in high aerodynamic load cases. Thus, the asymmetry active monitoring technique ***3D*** seems to be behave the best on regular conditions.
- b. In regard to the ***aerodynamic borderline wear-free conditions***, the active model ***3D*** presents the best behaviour when a flap extension maneuver is commanded, while the active model ***3E*** behaves better in retraction maneuvers. Therefore, there is not a predominant active model on high borderline wear-free conditions but it depends on the specific flap deflection maneuver.
- c. With regard to ***wear-out conditions***, both active models ***3D & 3E*** behave the best in extension maneuvers. On the other hand, the active model ***3E*** manages the best the flap retraction scenarios. Thus, the active model ***3E*** seems to be the best model on wear-out conditions.

d. The models **3**, **3C** & **3E** manage the best the *aerodynamic borderline wear-out conditions*.

In light of the above, some remarks have to be made.

Firstly, notice that, in general, the *dynamic-position* active monitoring techniques **3D** and **3E** seem to behave better than those that do not anticipate the position asymmetry failure declaration, **3** and **3C**. The speed loop of the “*PS*” controller that all the dynamic-position active models present makes the difference in case of failure under high aerodynamic loads.

In effect, the failure surface will manifest high retraction speeds, so the speed loop inside the controller leads to an earlier asymmetry condition verification, which anticipates the failure surface braking. Consequently, in general, the *dynamic-position* active monitoring techniques improve both the asymmetry identification and correction, which leads to more stable aircraft roll response, as well as a better aircraft maneuverability after failure.

Nonetheless, these are not true when operating on *aerodynamic borderline wear-out conditions*. These combine both worn out actuators, which present high internal friction forces, and high aerodynamic loads when the flap are positioned very closed to their lower mechanical end-of-travel. These extreme aerodynamic conditions in wear-out scenarios are special, since the speed loop of the “*PS*” controller is not necessary, since little surface deflection speeds will be manifested on these conditions. However, both **3D** and **3E** always activate the speed loop under high aerodynamic loads, since high failure surface retraction speeds close enough to the lower mechanical end-of-travel may have serious consequences.

In that regard, the speed loop of both **3D** and **3E** may cause limit cycle instabilities. These affect the engine speed and can be found when the friction forces slow down the system dynamic response while the speed loop is active. The instabilities are present on the dynamic-position active models in following two situations:

1. When deflecting the control surfaces under low aerodynamic loads, regardless the degree of the actuators wear and tear.
2. When deflecting the control surfaces on *aerodynamic borderline wear-out conditions*. These regard only the aerodynamic extreme operating condition using worn out actuators.

The limit cycle instabilities are especially critical on model **3D** since it suffers its reference position $\dot{\theta}_M$ instabilities and less common on model **3E**, which depends on the constant ramp-input signal.

Secondly, the *demand input signal* is important to determine the active model behaviour on any operating condition. In general, the step-input active monitoring techniques seem to behave better on wear-free conditions, while the ramp-input models seem to handle very well the wear-out conditions.

The system dynamic response shortly after failure on wear-free conditions is faster than in wear-out scenarios. Hence, the active models should be able to adapt the steady

state conditions before failure to the rapidly changing conditions directly after failure. It depends strongly on the active models *reference position*. In effect, the faster the reference position varies directly after failure, the sooner the correction action will start.

In this regard, the reference position on step-input models is the engine speed $\dot{\theta}_M$. It depends on the engine acceleration $\ddot{\theta}_M$, which adapts itself to the new flap load conditions after failure following to a second-order time response. The reference position rapid adaptation to the new conditions after failure allows the operative surface to reach faster failure flap. In addition, the maximum position asymmetry between both flaps will be reduced.

Thus, both the aircraft roll dynamic response will be more stable. Moreover, the aircraft maneuverability after failure will higher since less aileron deflections will be necessary to correct the induced roll moment caused by the control surfaces position asymmetry.

This is the reason why both 3 and especially 3D behave better than the ramp-input models on wear-free conditions.

On the other hand, the ramp-input models reference position is the demand input signal Dem , which is limited by both the maximum and minimum ramp slope, empirically set as:

$$\left. \frac{d Dem}{dt} \right|_{max} = \pm 0.1 rad/s$$

Note that this is a constant function which, in general, would lead to slightly slower but more controlled system time responses. This is not a problem on wear-out conditions since the high friction forces inside the worn out actuators will already slow down the system time response. However, the ramp input signal will be essential to prevent the limit cycle instabilities since these affect the engine speed. Fortunately, the reference position of the ramp-input models does not depend on the engine speed but on a constant ramp slope.

Thus, the ramp-input models are ideal to operate on wear-out conditions.

To sum up, the asymmetry active monitoring techniques that behave the best on each operating condition are:

- The active model 3D and 3E on wear-free conditions.
- The active model 3E on wear-out conditions.

In the light of the above, it seems that the active model 3E presents either an acceptable or excellent behaviour according to the operating condition analyzed in this project.

Nomenclature

Acronyms

Symbol	Description	Units
BS	Ballscrew actuators	–
CAS	Control Augmentation System	–
$CSAS$	Control and Stability Augmentation Systems	–
CTT	Critical torque tube (also drive shaft torsion bars)	–
ECU	Electrical Control Unit	–
FBW	Fly By Wire	–
PCU	Power Control Unit	–
PDU	Power Drive Unit	–
PT	Position Transducers	–
SAS	Stability Augmentation System	–
SV	Servo valve	–

Physical Magnitudes

Symbol	Description	Units
t_f	Failure time	s
α	Angle of attack of the aircraft	rad
β	Bulk modulus	N m^{-2}
$\ddot{\theta}_M$	Motor angular acceleration (on fast shaft)	rad s^{-2}
$\ddot{\theta}_{L,R}$	Left/right control surface acceleration (on slow shaft)	rad s^{-2}
$\ddot{\theta}_{SL,R} \equiv \ddot{\theta}_i$	Control surfaces physical (real) angular acceleration (on slow shaft)	rad s^{-2}
$\Delta\eta_{AS}$	Actuators efficiency reduction <i>in aiding</i>	–
$\Delta\eta_{OS}$	Actuators efficiency reduction <i>in opposing</i>	–
$\Delta\tau$	Integration time step	–
$\Delta\theta_E$	Angular position threshold to define the flap asymmetry condition	rad s^{-1}
$\Delta\theta_{asym}$	Control surface asymmetry measure	rad
$\Delta\theta_{asym}$	Differential position asymmetry of the control surfaces (on slow shaft)	rad

$\Delta\theta_{BL}$	Drive shaft backlash (or gear backlash)	rad
ΔN	Step increment/decrement	–
ΔP	Servo valve pressure increment	N m^{-2}
ΔQ	Servo valve volumetric flow rate increment	$\text{m}^3 \text{s}^{-1}$
Δr	Servo valve radial clearance	m
ΔZ_S	Actuator gear ratio increment	–
$\dot{\theta}_A$	Aileron deflection speed	rad s^{-1}
$\dot{\theta}_E$	Control surfaces electrical speed (on slow shaft)	rad s^{-1}
$\dot{\theta}_i$	Control surface travel speed on slow shaft	rad
$\dot{\theta}_M$	Motor angular speed (on fast shaft)	rad s^{-1}
$\dot{\theta}_{L,R}$	Left/right control surface speed (on slow shaft)	rad s^{-1}
ϵ	Error	rad
ϵ_{ss}	Steady state error	rad
η_m	Mechanical efficiency	–
η_v	Volumetric efficiency	–
η_{AS}	Actuators friction efficiency <i>in aiding</i> considering dynamic conditions	–
η_{OS}	Actuators friction efficiency <i>in opposing</i> considering dynamic conditions	–
$\frac{d Dem}{dt}$	Ramp slope	rad s^{-1}
$\frac{d}{dt}(X_S)$	Servo valve spool speed	m s^{-1}
$(\frac{d Dem}{dt})_{max}$	Ramp slope	rad s^{-1}
μ	Oil dynamic viscosity	N s m^{-1}
ω_M	Angular velocity in <i>rad/s</i>	rad s^{-1}
ϕ_A	Aircraft roll angle	rad
$\phi_{A,ss}$	Steady state roll angle	rad
ρ	Oil dynamic viscosity	kg m^{-3}
τ_{br}	Dimensionless braking time	–
$\theta \equiv \theta_i$	Control surface deflection angle on slow shaft	rad
θ_A	Aileron deflection	rad

θ_E	Control surfaces electrical position (on slow shaft)	rad
θ_G	Drive shaft torsional deformation	rad
$\theta_i(t = t_f)$	Failure surface braking position	rad
$\theta_i(t = t_{br})$	Braking position after failure	rad
θ_M	Engine position (on fast shaft)	rad
$\theta_{A,max}$	Aileron mechanical upper end-of-travel	rad
$\theta_{A,min}$	Aileron mechanical lower end-of-travel	rad
$\theta_{E,av}$	Average electrical position	rad
$\theta_{E,i}$	Failure surface electrical position or electrical $\theta_{L,R}$	rad
θ_{EL}	Left control surface electrical position	rad
θ_{ER}	Right control surface electrical position	rad
$\theta_{i,br} \equiv \theta(t = t_{br})$	Failure surface braking position	rad
$\theta_{i,ss}$	Steady state control surface position (on slow shaft)	rad
θ_{IT}	Position upstream of the position transducer (also position on intermediate shaft)	rad
$\theta_{L,R}$	Control surfaces physical (real) angular position (on slow shaft)	rad
$\theta_{M,max}$	Maximum engine position (on “fast” shaft)	rad
θ_{max}	Control surface mechanical upper end-of-travel	rad
θ_{min}	Control surface mechanical lower end-of-travel	rad
$\theta_{Os,Ti}$	Electrical transducers angular position offset	rad
θ_T	Mechanical position on intermediate shaft with no transducers backlash	rad
φ	Orifice circumferencial amplitude	rad
$\vec{\theta}_i$	Vector of the control surface acceleration on slow shaft	rad s ⁻²
$\vec{\dot{\theta}}_i$	Vector of the control surface travel speed on slow shaft	rad s ⁻¹
$\vec{F}_{f,i}$	Actuators friction torque vector	N m
$\vec{T}_{act,i}$	Active torque vector	N m
$\vec{T}_{eff,i}$	Net torque (also named <i>effective</i> torque) vector	N m

$\vec{T}_{G,i}$	Gear transmission torque	N m
$\vec{T}_{pass,i}$	Passive torque vector	N m
$\vec{T}_{RC,i}$	Resistive torque constant component	N m
ξ	Control parameter	–
A	Passage area	m ²
A_{1R}	Passage area from port 1 to <i>return</i> passage	m ²
A_{1S}	Passage area from <i>supply</i> passage to port 1	m ²
A_{2R}	Passage area from port 2 to <i>return</i> passage	m ²
A_{2S}	Passage area from <i>supply</i> passage to port 2	m ²
A_{min}	Minimum passage area	m ²
A_{SV}	Servo valve second stage end faces	m ²
C_d	Servo valve discharge coefficient (also efflux coefficient)	–
C_m	Aircraft dimensionless pitching moment coefficient	–
c_M	Motor damping coefficient	kg m ² s ⁻¹
c_S	Control surface damping coefficient	kg m ² s ⁻¹
$c_{M,leak}$	Engine leakage coefficient	kg m ² s ⁻¹
C_{m_0}	Aircraft no-lift dimensionless pitching moment	–
C_{m_α}	Aircraft static longitudinal stability derivative	–
$C_{m\delta}$	Derivative of the dimensionless pitching moment coefficient with respect to the flap deflection angle	–
Com	Command input signal	rad
Cor	Electric current	A
D	Displacement	m
Dem	Demand input signal	rad
e	Maximum radial eccentricity	m
F_{DA}	Net dynamic friction force (torque) <i>in aiding</i>	N m ⁻²
F_{DO}	Net dynamic friction force (torque) <i>in opposing</i>	N m
F_{DS}	Control surface constant component of the dynamic friction force (torque)	N m

$F_{f,M}$	Dry (or Coulomb) friction that affects the PDU	N m
$F_{f,S}$	Dry (or Coulomb) friction that affects the control surfaces	N m
$F_f \equiv F_{f,i}$	Modulus of the actuators friction torque vector	N m
FST	Transducer scale factor	–
G_A	Amplification gain	–
G_M	Torque-motor gain	–
G_{QF}	Servo valve volumetric flow rate gain	–
I_A	General asymmetry indicator	–
I_{Ai}	partial asymmetry indicator	–
$I_{Wrn,i}$	Partial asymmetry counter	–
$I_{Wrn,i}^{thr,S}$	<i>Slow</i> parameter threshold	–
$I_{Wrn,i}^{thr}$	Partial asymmetry counter threshold	–
I_{Wrn}^u	Upper asymmetry counter threshold	–
J_S	Moment of inertia of the control surface	kg m ²
K_G	Drive shaft torsional stiffness	N m rad ⁻¹
K_{1G}	Closed loop drive shaft torsional stiffness (upstream of the position transducers)	N m rad ⁻¹
K_{2G}	Closed loop drive shaft torsional stiffness (downstream of the position transducers)	N m rad ⁻¹
K_{SF}	Servo valve spool-flapper stiffness	N m ⁻¹
N	Number of seps of the counter	–
n	Angular velocity in r.p.m	r.p.m
P_1	Inlet pressure	N m ⁻²
P_2	Outlet pressure	N m ⁻²
P_i	Pressure differential between the inlet and the outlet port	N m ⁻²
P_M	Mechanical power	W
P_R	Servo valve return pressure	N m ⁻²
P_S	Servo valve supply pressure	N m ⁻²
P_T	Tank pressure	N m ⁻²
$P_{brL,R}$	Minimum brake releasing pressure	N m ⁻²

$P_{SV,c}$	Minimum permissible system pressure	N m^{-2}
P_{SV}	Servovalve supply pressure (between shutoff valve and servovalve)	N m^{-2}
Q	Volumetric flow rate	$\text{m}^3 \text{s}^{-1}$
Q_{1L}	Maximum volumetric flow rate through the port 1 (to the hydraulic motor)	$\text{m}^3 \text{s}^{-1}$
Q_{1R}	Volumetric flow rate oil flow from port 1 to the <i>return</i> passage	$\text{m}^3 \text{s}^{-1}$
Q_{1S}	Volumetric flow rate from the <i>supply</i> passage and port 1	$\text{m}^3 \text{s}^{-1}$
Q_{2L}	Maximum volumetric flow rate through the port 2 (back from the hydraulic motor)	$\text{m}^3 \text{s}^{-1}$
Q_{2R}	Volumetric flow rate oil flow from port 2 to the <i>return</i> passage	$\text{m}^3 \text{s}^{-1}$
Q_{2S}	Volumetric flow rate oil flow from the supply passage and port 2	$\text{m}^3 \text{s}^{-1}$
Q_M	Volumetric flow rate through the engine	$\text{m}^3 \text{s}^{-1}$
Q_{UM}	Volumetric flow rate proportional to the engine speed	$\text{m}^3 \text{s}^{-1}$
R_{lin}	Servovalve linear coefficient	N s m^{-5}
R_{quad}	Servovalve quadratic coefficient	$\text{N s}^2 \text{m}^{-8}$
Re	Reynolds number	–
$Slow$	<i>Slow</i> parameter	–
T_M	Mechanical torque	N m
T_R	Resistive torque from the external (aerodynamic) loads	N m
$T_{brL,R}$	Wingtip brakes braking torque applied either on the left or right control surface	N m
t_{br}	Braking time after failure	s
t_{dec}	Deceleration time	s
$T_{eff,i}$	Modulus of the net torque (also named <i>effective</i> torque) vector	N m
T_{FDM}	Engine dynamic friction force	N m
$T_{FF,M}$	Friction force torque in the engine $F_{f,M}$ according to the Coulomb friction model	N m
$T_{fL,R}$	Friction torque either on the left or right control surface	N m

T_{FSM}	Engine static friction force	N m
$T_{GL,R}$	Engine torque transmitted to either the left or right actuator	N m
T_{GL}	Engine torque transmitted to the left control surface	N m
T_{GL}	Torque transmitted to the left actuator	N m
T_{GR}	Engine torque transmitted to the right control surface	N m
T_{GR}	Torque transmitted to the right actuator	N m
T_{in}	Inertial torque	N m
$T_i S_y$	Asymmetry anticipation time	s
T_{RC}	Constant component of the resistive torque	N m
T_{RC}^{thr}	Aerodynamic constant torque threshold	–
$T_{RL,R}$	Resistive torque from the external (aerodynamic) loads applied on either the left or right control surface	N m
T_{visc}	Viscous torque, proportional engine angular velocity ω_M	N m
V	Aircraft airspeed	m s^{-1}
V_{ol}	Volume	m^3
X_F	Servo valve flapper displacement	m
X_H	Shutoff valve spool displacement	m
X_O	Servo valve orifice regulation length	m
X_S	Servo valve spool displacement	m
X_{H0}	Shutoff valve spool zero displacement position	m
X_{H1}	Smaller shutoff valve spool displacement that produces P_S	m
X_{HM}	Maximum shutoff valve spool displacement position	m
Z_M	Motor gear reducer or its gear ratio	–
Z_S	Actuator gear reducer or its gear ratio	–
Δt_{fail}	Failure declaration delay	s
C_{Lmax}	maximum lift coefficient	–
X_{O1R}	Servo valve orifice between port 1 and the <i>return</i> passage	m

X_{O1S}	Servovalve orifice between the <i>supply</i> passage and port 1	m
X_{O2R}	Servovalve orifice between port 2 and the <i>re-</i> <i>turn</i> passage	m
X_{O2S}	Servovalve orifice between the <i>supply</i> passage and port 2	m

Bibliography

- Belmonte, D., Dalla Vedova, M., & Quattrocchi, G. (2019, 01). A new active asymmetry monitoring and control technique applied to critical aircraft flap control system failures. *MATEC Web of Conferences*, 304, 04011. doi: 10.1051/mateconf/201930404011
- Borello, L., & Villero, G. (n.d.). An innovative architecture for flap control system of medium/large aircraft. In *Aircraft engineering, technology, and operations congress*. Retrieved from <https://arc.aiaa.org/doi/abs/10.2514/6.1995-3919> doi: 10.2514/6.1995-3919
- Borello, L., & Villero, G. (1998). Mechanical failures of flap control systems and related monitoring techniques. In *21st icas congress*.
- Borello, L., & Villero, G. (2000). Flap control systems actuators: mathematical and computational model for dynamic simulation. In *European congress on computational methods in applied sciences and engineering eccomas 2000*.
- Borello, L., & Villero, G. (2004). Mechanical failures of flap control systems: proposal of advanced monitoring techniques. *International Journal of Mechanics and Control*, 5(2), 9–28.
- Borello, L., Villero, G., & Dalla Vedova, M. (2009). New asymmetry monitoring techniques: effects on attitude control. *Aerospace Science and Technology*, 13(8), 475–487.
- Borello, L., Villero, G., & Dalla Vedova, M. D. (2014). Flap failure and aircraft controllability: Developments in asymmetry monitoring techniques. *Journal of Mechanical Science and Technology*, 28(11), 4593–4603.
- Etkin, B., & Reid, L. D. (1996). *Dynamics of flight: Stability and control*. John Wiley & Sons, Inc.,.
- Flight controls - skybrary aviation safety*. (n.d.). Retrieved 2021-02-21, from https://www.skybrary.aero/index.php/Flight_Controls
- Jacazio, G., & Borello, L. (1986). A non-linear model of an electro-hydraulic servo system with axial piston hydraulic motor. In *7th international fluid power symposium*.
- Jacazio, G., Borello, L., & Villero, G. (1994). Secondary flight controls: mechanical failures of transmission lines and related asymmetry problems. In *Icas proceedings* (Vol. 19, pp. 1386–1386).
- Jacazio, G., et al. (1988). Mathematical models of electrohydraulic servovalves for fly-by-wire flight control systems. *Mathematical and Computer Modelling*, 11, 563–569.
- Joshi, A., & Jayan, P. (2002). Modeling and simulation of aircraft hydraulic system. In *Aiaa modeling and simulation technologies conference and exhibit* (p. 4611).
- Krus, P. (1998). Modelling and simulation of complex fluid and mechanical aircraft systems. In *Aiaa and sae, 1998 world aviation conference* (p. 5560).

